

UNIVERSITY OF NOTTINGHAM

Department of Electrical and Electronic Engineering

ANALYSIS OF THE TAPERED WAVEGUIDE

by

A. BELGHORAF, Ingenieur d'etat

Thesis submitted to the University of Nottingham
for the Degree of Doctor of Philosophy

December 1984

ACKNOWLEDGEMENTS

The author wishes to extend his thanks to Professor R. L. Beurle for the use of University facilities.

The author would like to thank Professor L. B. Felsen for shedding light on some practical computing problems encountered, as well as for the fruitful discussions.

The author is also grateful to the Algerian Government for sponsoring this research.

Last, but by no means least, the author wishes to express his sincere thanks to Dr. J. M. Arnold for his constant encouragement and invaluable suggestions throughout this research.

ABSTRACT

This thesis describes analytical and numerical investigations of tapered waveguide problems, for integrated optics applications.

A plane wave spectral analysis, models the propagation process of the tapered waveguide and introduces the concept of an Intrinsic spectral Integral, which turns out to be in good agreement with calculations in terms of Adiabatic modes. This allows us to extend the Intrinsic mode concept beyond the singularity where the Adiabatic mode concept breaks down.

In this sense, the implementation of the resulting spectral formulation; for the case of homogeneous media, contains all information pertinent to the modal propagation mechanism, inside and outside the tapered waveguide; before and after the singularity caused by cut off of the Adiabatic mode.

The thesis is mainly concerned with implementing the Intrinsic mode theory as a numerical computational tool.

In this respect, very good agreement is demonstrated between this model and calculations performed numerically using the parabolic equation method. On the other hand, the new model contains far greater physical and analytical possibilities than previous methods.

CONTENTS

	<u>Page</u>
CHAPTER 1 : INTRODUCTION	1
1.1. Definition of the tapered waveguide	1
1.2. Formulation of the problem	4
1.3. Presentation of the work	7
CHAPTER 2 : ANALYSIS OF PLANE PARALLEL WAVEGUIDES	9
2.1. Introduction	9
2.2. Cross section field pattern for the single layer structure	13
2.2.1. Guided wave region	13
2.2.2. Leaky wave region	15
2.3. Cross section field pattern for the double layer structure	16
2.3.1. Guided wave region	16
2.3.2. Coupled wave region	17
2.4. Computational results and discussion	19
2.4.1. Single layer problem	19
2.4.2. Double layer problem	21
2.4.3. Discussion	24
CHAPTER 3 : ANALYSIS OF THE TAPERED WAVEGUIDE BY PLANE WAVE TRACKING	26
3.1. Introduction and formulation of the model	26
3.2. Field due to rays free of reflection	27
3.3. Field excited by the upgoing species of rays	28
3.4. Field excited by the downgoing species of rays	31
3.5. Total field contribution	33
3.6. Transformation of the plane wave spectrum by Poisson-Sum-Formulae	33
3.7. Assessment of the local eigenvalue equation	38
3.8. Field analysis in different regions of the tapered waveguide	41
3.8.1. Guided wave region	41
3.8.2. Transition region	43
3.8.3. Radiation region	45

CHAPTER 4 : INTRINSIC SPECTRAL INTEGRAL	46
4.1. Definition of the Intrinsic field	46
4.1.1. Construction of the Spectral Intrinsic Integral	47
4.1.2. Identification of the lateral waves	49
4.1.3. Elaboration of the phase function for the Intrinsic Integral	50
4.2. Application of the Intrinsic Integral to the single layer structure	52
4.2.1. Definition of branch point θ_c	52
4.2.2. Location of saddle points and determination of the steepest descent path (SDP)	53
(a) Definition of SDP	53
(b) Definition of branch cut contour	54
(c) Computational result	55
4.2.3. Intrinsic field in the guided wave region	57
4.2.4. Intrinsic field in the leaky wave region	62
4.3. Application of Intrinsic Integral to the double layer structure	63
4.3.1. Location of saddle point and determination of SDP contour	63
4.3.2. Intrinsic field in the guided wave region	66
4.3.3. Definition of branch point θ'_c	67
4.3.4. Intrinsic field in the coupled wave region	69
CHAPTER 5 : RADIATION SPECTRAL INTEGRALS	72
5.1. Introduction	72
5.1.1. Definition of the Radiation Integral	72
5.1.2. Radiation Integral at bottom interface B_{12}	73
5.2. Parametric eigenvalue equation of the Radiation Integral (5.4)	75
5.3. Integrand variation of the Radiation Integral (5.4) along the real axis	78
5.3.1. Single layer structure	79
(a) θ_q in the guided wave region	79
(b) θ_q in the leaky wave region	80

5.3.2. Double layer structure	81
(a) θ_q in the guided wave region	81
(b) θ_q in the coupled wave region	82
5.3.3. Definition of integration contour along the real axis	83
5.4. Application of the Radiation Integral to the single layer structure	84
5.4.1. Radiation field in the guided wave region	84
5.4.2. Radiation field in the leaky wave region	85
5.5. Radiation Integral for the double layer structure	86
5.5.1. Radiation field in the guided wave region	87
5.5.2. Radiation Integral in the coupled wave region	88
(a) Definition	88
(b) Change from polar to Cartesian co-ordinates	91
(c) Radiation field in the coupled wave region	93
CHAPTER 6 : COMPARISON OF SOME RESULTS WITH OTHER PAPERS	96
6.1. Introduction	96
6.2. Co-ordinate system appropriate to underwater acoustic applications	97
6.3. Co-ordinate system appropriate to integrated optics applications	98
6.4. Total field behaviour inside and outside the tapered waveguide	99
6.5. Contours of constant amplitude patterns	102
6.6. Discussion	104
CHAPTER 7 : CONCLUSION	105
7.1. Summary of results	105
7.2. Suggestions and further work	109
APPENDIX A	111
APPENDIX B	113
APPENDIX C	115
APPENDIX D	120
APPENDIX E	124
APPENDIX F	126
REFERENCES	130

CHAPTER ONE

INTRODUCTION

The tapered waveguide typical of non-uniform problems, has found application in many areas, such as integrated optics, underwater acoustics, tropospheric duct etc.

Exact analytical solution of the mode propagation of such a non-separable structure is impossible. That is why we shall establish systematically approximate solutions for mode propagation in the tapered waveguide, in connection with integrated optics applications.

1.1. Definition of the tapered waveguide

The principle of the tapered waveguide for applications to integrated optics consists of a thin film of refractive index (n_1) that tapers down onto a medium of refractive index (n_2) which could be either infinitely open (Fig.1.1a), or confined within a uniform thickness d (Fig.1.1b).

An incident ray in the tapered waveguide therefore, undergoes multiple reflections whose angle of incidence θ on the tapered waveguide-medium (n_2) boundary increases progressively as the taper narrows down. Successive total and subsequently partial reflections at that bottom interface of the tapered waveguide take place, as the angle of incidence θ increases with consecutive reflections, eventually becoming larger than the critical angle θ_c characterising the structure. Rays which reach any observation point X after many such partial reflections have very small

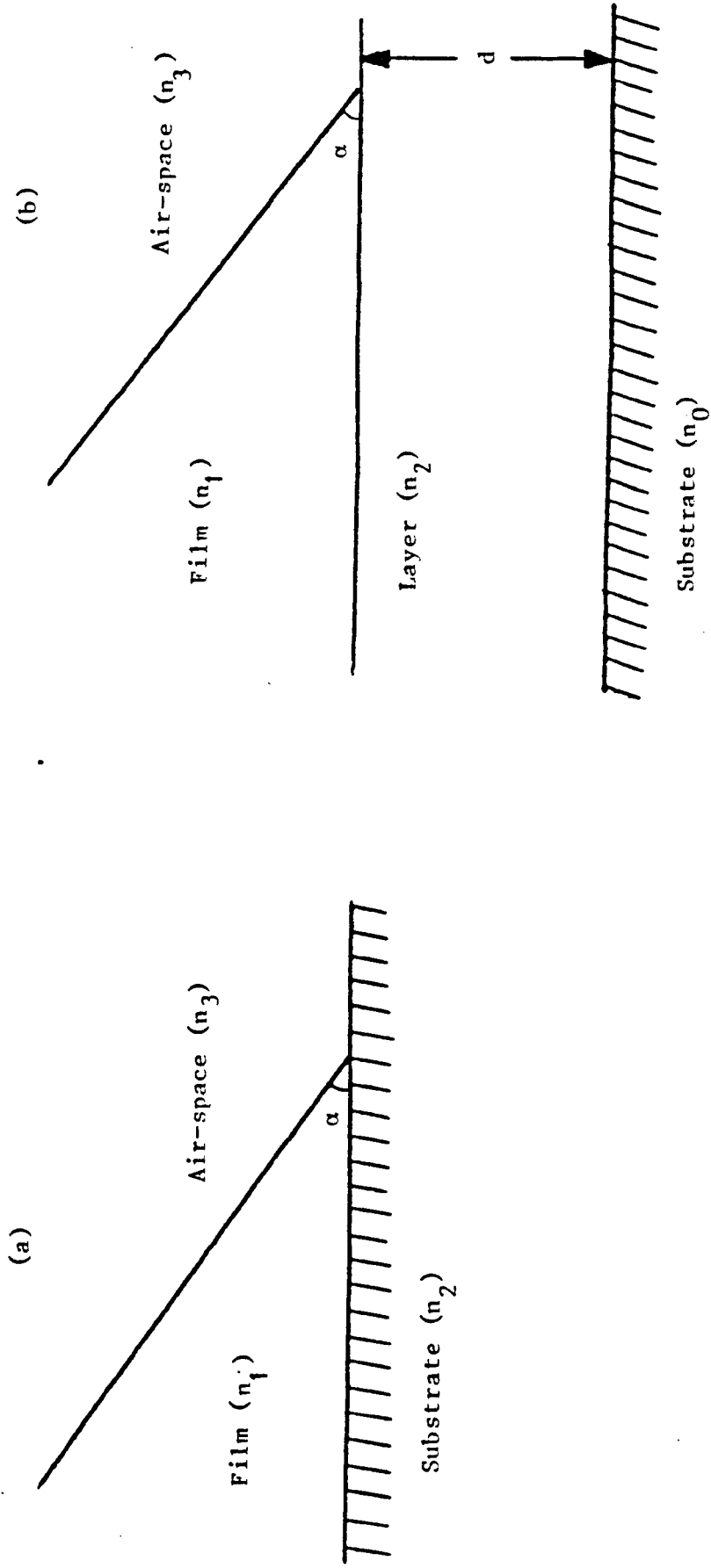


Fig.1.1.1 : Configuration of the two structures to deal with involving the tapered waveguide (n_1) as a main body.

amplitude in comparison to rays which undergo only total reflections along their path to the observation point. Each successive pair of reflections at the top and bottom interface of the tapered waveguide increases the incidence angle θ by twice the wedge angle α . As a result, at some observation point X , the angle of incidence θ becomes higher than the critical angle θ_c of total reflection. Therefore as a consequence, energy starts refracting from the tapered waveguide to its adjacent medium. This energy is augmented by that of subsequent rays, so that ultimately most of the incident energy is transformed into an outgoing beam. The beam formed by a tapered waveguide is produced by many rays that emerge at slightly different angles. The resulting outgoing beam is characterised by a relatively large divergence which may be between 1 to 20 degrees.

Because of this energy refraction from the tapered waveguide to its adjacent medium (n_2), the tapered waveguide could also be characterised as a tapered coupler in addition to its guiding properties, provided that medium (n_2) is bound (Fig.1.1b). Though there are various types of couplers of practical interest developed, such as the prism coupler [1] and the grating coupler [2], the tapered coupler distinguishes itself as it is very simple and compatible with planar device technology having nevertheless a good efficiency.

It has been reported [3] that in order to increase the efficiency of the prism coupler, a tapered coupler can be inserted in the bottom gap of the prism.

Although the coupling efficiency may be higher than 70% as reported by Tien et al [4], the high beam divergence detracts

considerably from the attractiveness of the coupler.

Of course, the tapered coupler can also be used as an input or output coupler; however its efficiency is usually quite small, for it is difficult practically to align and match the form of the incident beam to the divergent shape. In spite of this, the tapered coupler has found applications in cases where this divergence is not objectionable; for example, high detectors [5], mode splitters [6] or mode convertors [6].

The tapered coupler, on the other hand, is also practically useful for the study of semiconductor epitaxial layers. In particular when the refractive index of a film such as GaAs layer is large it becomes difficult to find an appropriate conventional prism coupler having a high refractive index, as well as being transparent to the radiation used to couple light into that layer [7]. In this case, resorting to the tapered coupler will eventually circumvent the difficulty. Another advantage of the tapered coupler is that it avoids the abrupt termination of the coupling that is required in uniform waveguides.

Finally, the structure of a tapered dielectric waveguide, is used to confine and guide energy in guided wave devices and circuits of integrated optics. The simplest fabrication method uses the deposition of films onto another medium of different refractive index. These films can be deposited by evaporation [8], sputtering [9], diffusion [10], ion implantation [11] or by epitaxial growth techniques [12]. The last method is restricted to deposition of thin single crystalline film only.

1.2. Formulation of the problem

The leaky wave theory that has proved to be useful for dealing with couplers such as prisms and gratings [13,14], does not apply to the tapered coupler. The reason is that the incident surface wave is converted rapidly into an outgoing radiation, for the surface wave mode reaches a cut-off condition within the tapered waveguide. Energy is then scattered over a wide spectrum of radiation modes, so that a leaky wave mode can be established.

As a matter of fact, attempts to solve the tapered waveguide by geometrical ray tracing, encounter difficulties too. They are due to multiple reflections of rays near critical incidence at the waveguide boundaries.

As the tapered waveguide has a non-uniform configuration, it does not allow the application of separation of variables; and the lack of symmetry does not guarantee any exact method to solve the problem of non-separability. Inevitably, one must resort to approximate methods.

The most commonly used tool for studying such a case of non-uniform waveguide, has very often been the coupled wave theory. It has systematically been used to study time dependant quantum mechanics. However, when this theory is applied to non-uniform waveguides [15,16,17,18] in integrated optics, then serious defects in connection with the singularity are encountered in the radiated field. For instance, near and beyond a critical region, the adiabatic mode disappears when it should continuously convert into a radiation mode. One recalls the concept of an adiabatic mode, which is considered to be a distribution of

electromagnetic field which, over any given transverse cross section, has the same transverse variation as the normal mode in a uniform waveguide having the same cross section.

Though the adiabatic modes are not exact solutions to Helmholtz' equation, coupling does exist between them. The coupling is formally described by coupled mode theory [18,19,20].

There is no known resolution of the mode cut-off problem, within the coupled mode theory. The coupling cannot be neglected at the critical region where a bound mode converts into a radiation mode. Nonetheless, some recent papers [20,21,22] have successfully constructed solutions of the wave equation describing the propagation of acoustic waves in shallow water ocean, a problem mathematically similar to the tapered waveguide in integrated optics, though different in nature.

Pierce [21] uses the postulative concept of the parabolic equation; Kamel and Felsen [22] describe the propagation of modes by establishing a numerical Green's function; and Evans [20] analyses the structure locally by sectioning it into many steps, and in each step he explores the coupled mode theory.

Those constructed solutions are reported to describe the mode propagation of acoustic waves in ocean. Though they involve a great deal of assumptions, they are still worth referring to, as long as they constitute the only resource to compare with our results, in connection with a non-uniform problem such as the tapered waveguide.

Due to these disadvantages mentioned earlier, little theoretical effort has been spent on investigating the tapered waveguide in integrated optics applications. From this arose the

impetus to carry out such an analysis. We shall henceforth show how a concept of plane wave spectral analysis can be employed for the representation of field distributions in the tapered waveguide, where the wave equation is not separable.

To the lowest order of approximation, validated for sufficiently weak wedge angle α , intermode coupling can be neglected.

Though all the following chapters deal with a TE type of polarisation, a similar treatment could be used in the case of a TM polarisation by using the corresponding magnetic field components.

Finally, one is aware that the concepts of ray optics (geometrical optics), describe the propagation of fields by defining rays as normals to the surfaces of constant phase of the field. Light rays have intuitive appeal since a narrow beam is a good approximation to the more abstract notion of light rays. One need only assume that a light ray in a homogeneous optical medium follows a straight path.

In addition, one needs to know Snell's law, which relates the angle of incidence to the angle of refraction at a dielectric interface, where a ray system passes through it.

Ray optics includes the description of the phase of the field by means of the notion of the optical path length, which is defined by the actual length times the refractive index of the medium, making it easy to attach a phase to the light ray.

1.3. Presentation of the work

Chapter 2 analyses the tapered waveguide using locally the conventional electromagnetic wave theory. Thereby the tapered structure is visualised as a series of uniform steps, in which conventional wave theory for uniform guides holds.

The solution of Helmholtz' equation is accomplished by suggesting in each medium as well as in each region, appropriate solutions of the field which satisfy the local boundary conditions.

Chapter 3 describes an alternative method of studying the tapered waveguide. It makes use of a concept of hybrid ray-mode formalism, where rays and guided mode expansions have been used as alternative methods.

A properly chosen combination of rays and modes can furnish a field representation which to a certain approximation provides basic insight into the propagation process. The resulting hybrid ray-mode representation thereby clarifies the interplay between rays and modes, and lends some basic insight into the propagation mechanism. Criteria for the proper mix of rays and modes are developed and explained on physical grounds in Chapter 3, which gives a remarkably simple and physically appealing mixture of rays and modes.

Chapter 4 expands the hybrid ray-mode spectrum formalism; which leads to the concept of a spectral Intrinsic Integral.

Chapter 5 is also devoted to the concept of a Radiation spectral Integral, constructed from any of the spectra elaborated in Chapter 3. This is achieved by simply associating with each individual spectral plane wave, incident on any boundary, a refracted wave with appropriate transmission coefficient. Both

Intrinsic and Radiation Integrals describe rigorously and systematically a source-free field behaviour, not only before and after the branch point singularity, but also inside and outside the tapered waveguide. Analytically, these Integrals involve contour deformation, steepest descent path (SDP) integration, and possibly residue calculus at poles.

As we shall show, both Integrals, if performed via the steepest descent method, would work well in the guided wave region where the field has an adiabatic behaviour inside the tapered waveguide and exponential outside.

The asymptotic evaluation of both Integrals near the singularity, by the steepest descent path method, delineates the role of saddle point and branch point. The former engenders the adiabatic as well as the radiated field, and the latter engenders the lateral waves launched near the transition region.

However, in the region past the singularity, the variation of the field is no more adiabatic inside the tapered waveguide, and the SDP method fails; for it becomes difficult to estimate the branch cut integral due to the branch point singularity. Thus one is inclined to use other asymptotic methods for evaluation of both Integrals.

Chapter 6 has in fact two purposes. On the one hand, it summarises some computed results of the field distribution (for the single layer structure only), by implementing the spectral analysis method, presented in previous Chapters. On the other hand, it compares those results with other reference papers.

CHAPTER TWO

ANALYSIS OF PLANE PARALLEL WAVEGUIDES

2.1. Introduction

This chapter analyses the plane parallel waveguide by using the conventional electromagnetic wave theory, which provides a framework for comparison with other chapters.

We consider the structure and co-ordinate system shown in Fig.2.1a; where a film of range dependent thickness T and uniform index n_1 is sandwiched between a film of uniform thickness d and a uniform index n_2 , and an air-cover of uniform index n_3 ($n_3=1$). The whole structure rests on a substrate of uniform index n_0 . Such a configuration will be called the 'double layer structure'. Fig.2.1b illustrates a simpler configuration, consisting of the double layer geometry as previously, but the film (n_2), by removal of its lower boundary to infinity, behaves as an infinite substrate so that substrate (n_0) is absent. Such a configuration will be called the 'single layer structure'.

As the light propagating in both structures of Figs.2.1 is confined by total internal reflection, in order to achieve true mode guidance, it is necessary to require that :

$$n_1 > n_2 > n_0 > n_3 . \quad (2.1a)$$

For numerical purposes, we shall mostly fix the indices as follows.

$$n_1 = 2 \quad (2.1b)$$

$$n_2 = 1.76 \quad (2.1c)$$

$$n_0 = 1.50 \quad (2.1d)$$

$$n_3 = 1.0 \quad (2.1e)$$

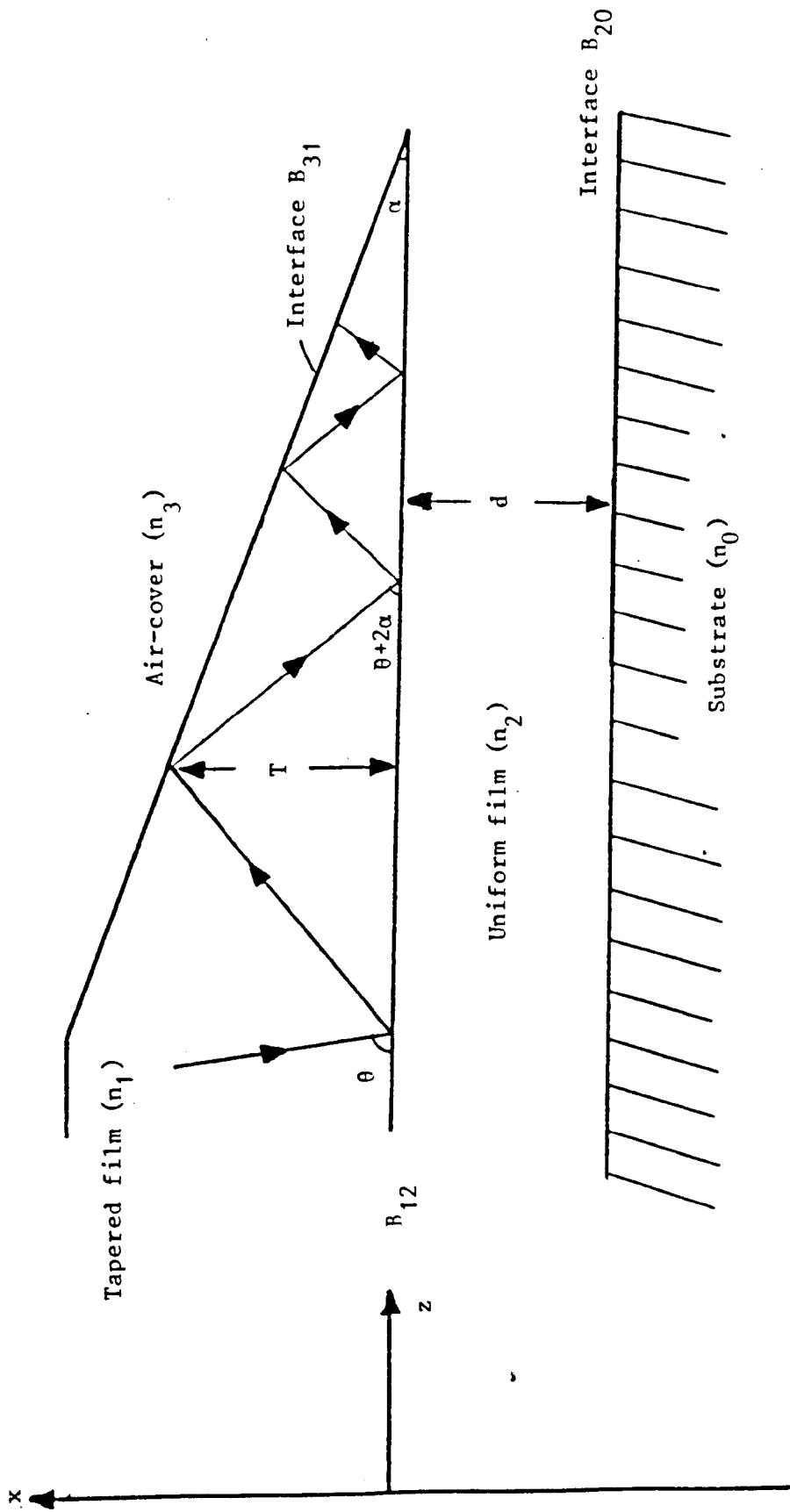


Fig.2.1a: Configuration of the double layer structure

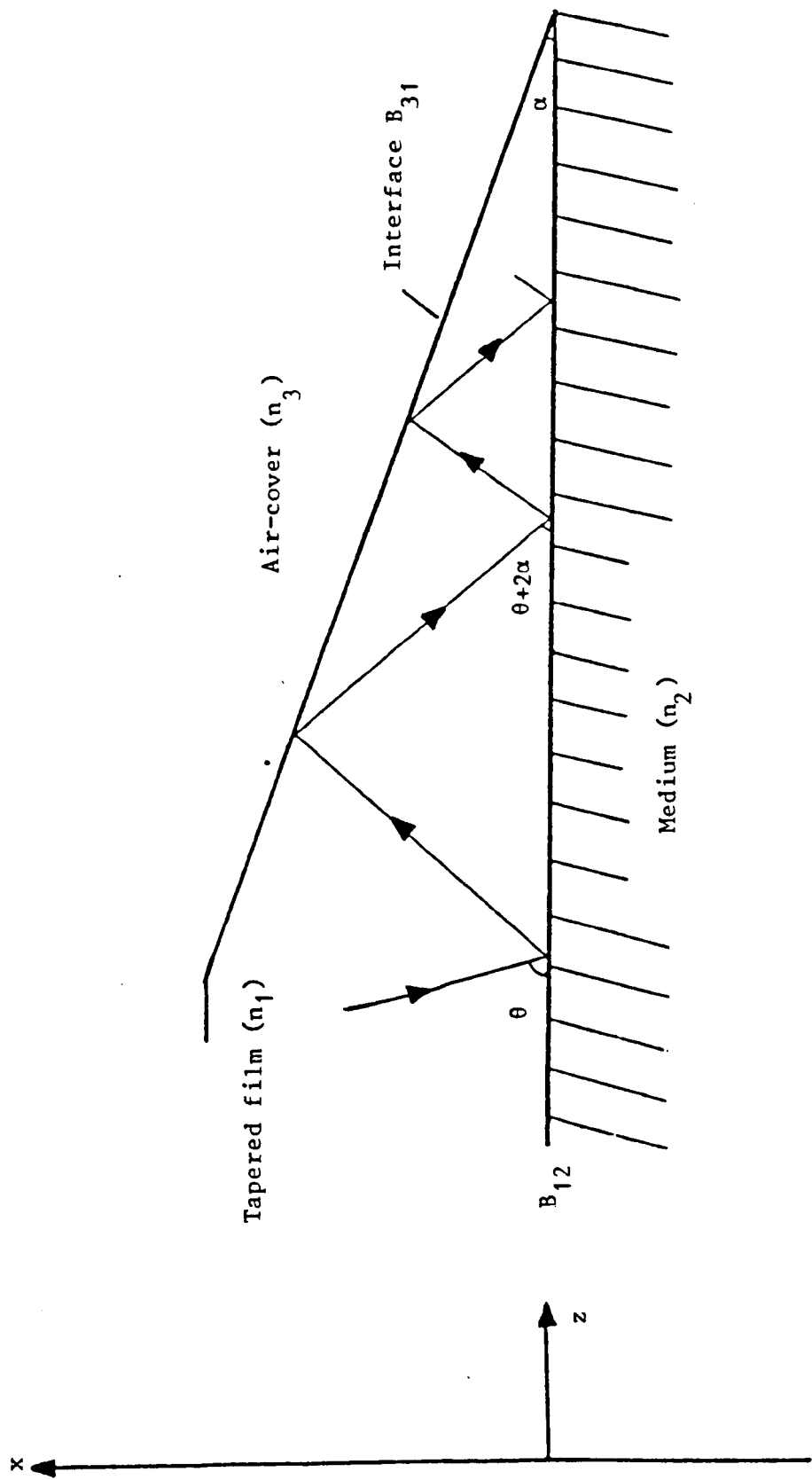


Fig.2.1b : Configuration of the single layer structure

These values are not intended to be exactly typical of integrated optics devices, but have been chosen to permit direct comparison with the results of Jensen and Kuperman [24] in the underwater acoustic case.

We shall assume throughout this chapter as well as in the next chapters that the guided light is coherent and monochromatic, and that the waveguides of Fig.2.1 consist of media which are lossless and isotropic. For a discussion of lossy and anisotropic media, the reader should refer to [25-31].

The physical picture of light guidance is one of the light rays tracing a multiply-reflected path in the tapered film (n_1) as shown in Fig.2.1, with total internal reflection occurring at the top and bottom interfaces of the tapered film (n_1).

We establish the convention that the B_{ij} boundaries refer to the interface between media of refractive index n_i and n_j . As such, zigzag rays propagate into the tapered film (n_1), and each successive pair of reflections at the boundaries B_{12} and B_{31} increase the angle of incidence θ by twice the wedge angle α . Eventually this angle θ will be higher than the critical angle θ_c ($\theta_c = \text{Arccos } n_2/n_1$), for total reflection at B_{12} , and some energy begins to leak into the medium (n_2). Note that the critical angle at B_{31} is higher than the critical angle at B_{12} , as one has appropriately chosen the indices in (2.1).

The tapered waveguide constitutes the main body of both structures of Fig.2.1 to be analysed. In order to enable the derivation of mode characteristics and to analyse both structures, we could approximate the tapered film (n_1) by a sequence of steps that discretely represent the taper of Fig.2.2. Obviously, the

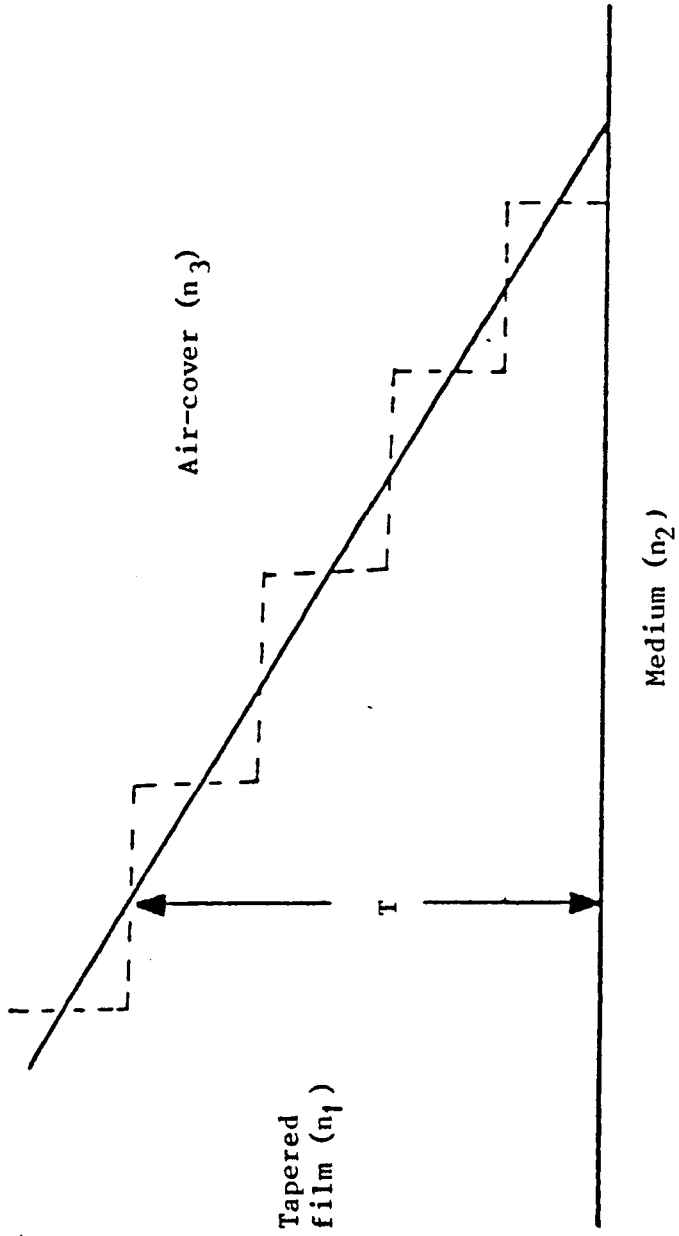


Fig.2.2 : Approximation of the tapered waveguide (n_1) by using a series of steps

result should improve as the steps are made smaller in size and greater in number. Within each step the solutions for the modes are simply those of a waveguide with parallel boundaries. Each step will be characterised by its thickness T . The problem of calculating the amplitude characteristic of the transmitted and reflected modes at each step, for a given incident mode, is done by matching the incident, reflected and transmitted fields components at each step boundary [16,18,20,32].

We shall therefore analyse the structures locally as though they were translation-invariant in configuration. Such planar structures are illustrated in Fig.2.3a and Fig.2.3b corresponding to the single layer problem and the double layer problem respectively. Thereby we define the co-ordinate systems.

We use the conventional electromagnetic wave formalism to introduce the basic concept and terminology of both structures of Fig.2.3, including the nature of mode propagation, waveguide cut-off and propagation constants. We assume invariance of the geometries along the y -axis which symbolically expresses the fact that all derivatives with respect to the y -axis are zero.

When a wave propagates inside the structure, one dimension of the beam cross section is guided by the stratification of the layers in x ; but in the z -direction, the wave can propagate freely. Also fields of the guided modes must vanish at $|x| = \infty$.

An appropriate field pattern is required inside and outside the film (n_1) so that the desired coupling to adjacent layers can be achieved.

The modal field for a plane parallel structure can be derived from the one-dimensional modal equation (for TE modes)

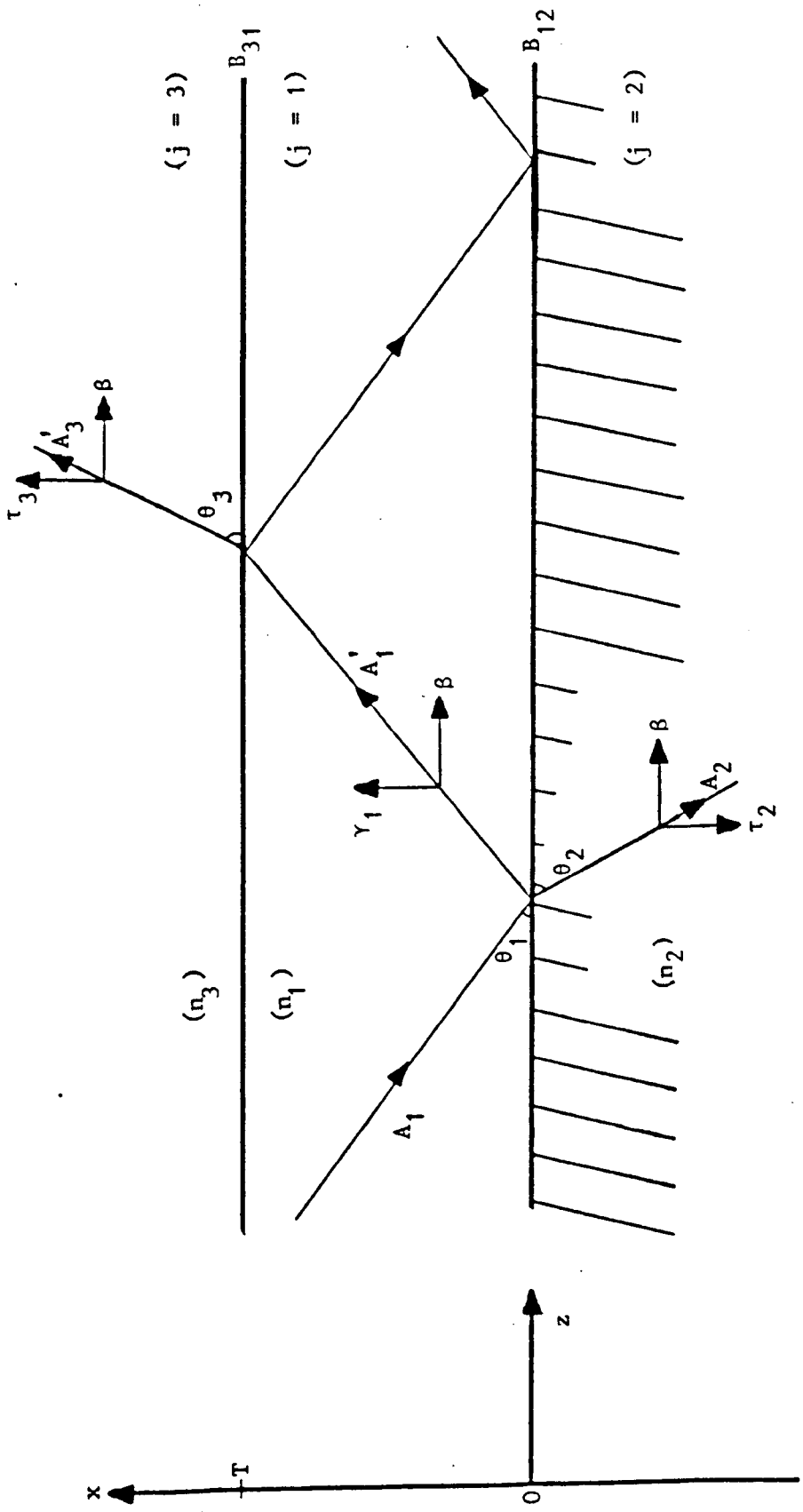


Fig.2.3a : Wave tracking in each medium (j) of the single layer structure at vicinity of a local thickness T, the tapered film (n_1) is seen as a uniform layer

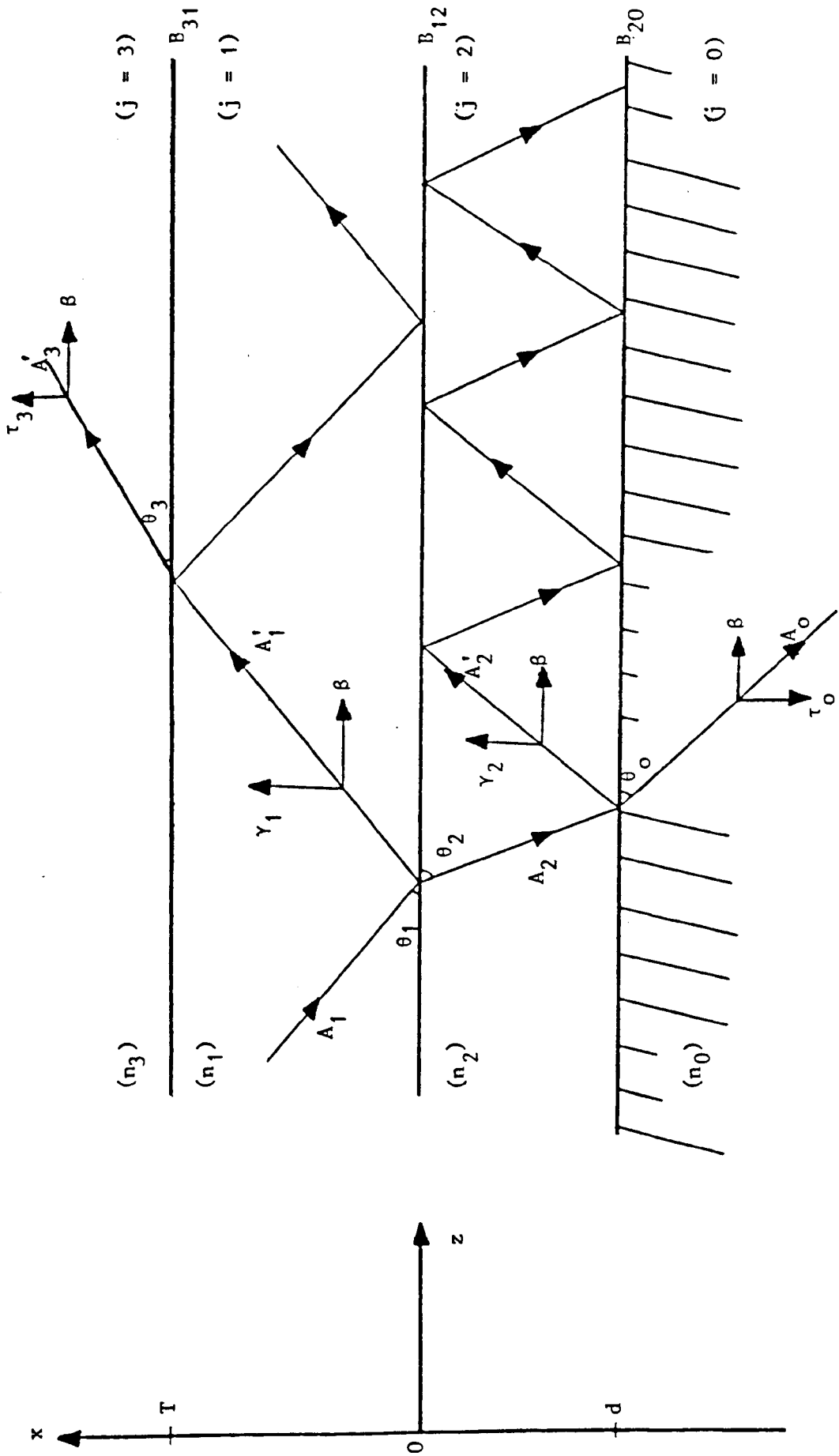


Fig.2.3b : Wave tracking in each medium (j) of the double layer structure at vicinity of a local thickness T , the tapered film (n_1) is seen as a uniform layer (d is negative)

$$\frac{\partial^2 E_y}{\partial x^2} + (n_j^2 k_0^2 - \beta^2) E_y = 0 \quad (2.2a)$$

where :

$$\beta = n_j k_0 \cos\theta_j \quad (2.2b)$$

k_0 is the free-space wave number. The subscripts θ_j and n_j respectively relate to the angle of modal plane wave and the index of the layer concerned. Equation (2.2b) defines the so-called modal propagation constant.

Mathematically, problems involving Maxwell's equation have solutions that match the boundary conditions at interfaces.

Various modes of propagation can be discerned in these geometric configurations of Fig.2.3. In the single layer case, modal fields are either trapped in the film layer (n_1) or are radiation modes in the surrounding materials. In the double layer case, two different types of trapped mode can exist: those trapped in the film layer (n_1) alone, and those distributed between the two adjacent layers (n_1) and (n_2).

In each of the layers of Fig.2.3, we shall postulate plane-wave electric fields E_y . As the TE mode has only three field components, H_x and H_z can be derived straight away from E_y by means of Maxwell's equations.

The customary time dependance in complex notation can be expressed by $\exp(-i \omega t)$, and shall be omitted throughout the equations still to come.

We shall use the subscript $j = 3$ for the quantities that belong to free-space; $j = 2, 1, 0$ for the quantities that belong respectively to the film (n_2), film (n_1) and substrate (n_0), see Fig.2.3.

We shall denote the complex amplitude of the downward and upward plane waves by A_j and A'_j in each medium. Conventionally, all A_j waves propagate towards the lower boundary, and the A'_j towards the upper boundary, see Fig.2.3.

When coupling of waves in each medium occurs, all waves have the same propagation constant β , defined in (2.2b).

2.2. Cross section field pattern for the single layer structure

We shall consider two cases as waves propagate along the parallel films of Fig.2.3a.

2.2.1. Guided wave region

In this region, plane waves in the film ($j = 1$) impinge at an incident angle θ to the boundaries which renders the effective index (defined as $\frac{\beta}{k_0}$) in the interval $n_2 < \frac{\beta}{k_0} < n_1$. The guided wave modes are the transverse electromagnetic waves trapped inside the film ($j = 1$) by total internal reflection between B_{12} and B_{31} boundaries.

Because of the total internal reflection in the film ($j = 1$), the electromagnetic field is non zero in the lower-index regions but, the amplitude of the wave decays exponentially as a function of the cross distance x in those regions.

We define the transverse propagation constants as :

$$\gamma_j^2 = n_j^2 k_0^2 - \beta^2 \quad j = 1 \quad (2.3a)$$

$$\tau_j^2 = \beta^2 - n_j^2 k_0^2 \quad j = 2,3 \quad (2.3b)$$

$$\beta = n_j k_0 \cos\theta_j \quad j = 1,2,3 \quad (2.3c)$$

β is the longitudinal propagation constant,

γ_j is the real transverse propagation constant in a medium where oscillating waves are present,

τ_j is the evanescent transverse decay constant corresponding to a medium where evanescent waves are present.

The distribution of the electromagnetic field component has the form of a standing wave in the film ($j = 1$), and exponential in medium ($j = 2$) and ($j = 3$). That is :

$$E_y = A_3' \exp(-x |\tau_3|) \quad j = 3 \quad (2.4a)$$

$$E_y = A_1 \exp(-i x \gamma_1) + A_1' \exp(i x \gamma_1) \quad j = 1 \quad (2.4b)$$

$$E_y = A_2 \exp(x |\tau_2|) \quad j = 2 \quad (2.4c)$$

We also define the derivatives of the electromagnetic field component as :

$$i \omega \mu H_x = -\partial E_y / \partial z \quad (2.5a)$$

$$i \omega \mu H_z = \partial E_y / \partial x \quad (2.5b)$$

Where ω and μ are the pulsation of the wave and the permeability of the concerned solid media, respectively.

The boundary conditions demand that the field E_y and its normal derivatives be continuous across the boundaries :

$$x = 0, \quad x = T \quad (2.6)$$

where T represents the physical local thickness of the film ($j = 1$).

Normalising the modes to a unit power P , requires :

$$P = \frac{1}{2} \text{Real} \left\{ \int_{-\infty}^{+\infty} E_y H_x^* dx \right\} \quad (2.7)$$

where P represents the total transverse power across the structure,

and the asterisk denotes the complex conjugate of the H_x component defined in (2.5).

Application of (2.4), (2.5), (2.6) and (2.7) leads to the determination of the field amplitudes A_j and A_j^* , and to the characteristic equation which is :

$$\gamma_1 \operatorname{Tan}^{-1} \frac{|\tau_3|}{\gamma_1} - \operatorname{Tan}^{-1} \frac{|\tau_2|}{\gamma_1} = \pi q \quad (2.8)$$

where the integer q is the mode number, and the transverse propagation constants are given by equation (2.3).

Equation (2.8) is the characteristic equation for the single layer structure in the pure guided wave region. Bearing that Tan^{-1} is the inverse tangent function.

2.2.2. Leaky wave region

In this region, the effective index is less than n_2 . That is $\frac{\beta}{k_0} < n_2$. Leaky waves occupy the medium ($j = 2$) which behaves as an infinite substrate.

The transverse propagation constants are defined by :

$$\gamma_j^2 = n_j^2 k_0^2 - \beta^2 \quad j = 1, 2 \quad (2.9a)$$

$$\tau_j^2 = \beta^2 - n_j^2 k_0^2 \quad j = 3 \quad (2.9b)$$

The distribution of the field is a standing wave in the film ($j = 1$), evanescent wave in medium ($j = 3$) and outward propagating wave in medium ($j = 2$). Hence

$$E_y = A_3^* \exp(-x |\tau_3|) \quad j = 3 \quad (2.10a)$$

$$E_y = A_1 \exp(-i x \gamma_1) + A_1^* \exp(i x \gamma_1) \quad j = 1 \quad (2.10b)$$

$$E_y = A_2 \exp(-i x \gamma_2) \quad j = 2 \quad (2.10c)$$

Combining (2.5), (2.6), (2.7), (2.9) and (2.10), one obtains the characteristic equation in the leaky wave region, which is :

$$\gamma_1 T - \text{Atan} \frac{|\tau_3|}{\gamma_1} + \text{Atan} \frac{i \gamma_2}{\gamma_1} = \pi q \quad (2.11)$$

where q still represents the mode number and the transverse propagation constants are given by equation (2.9).

2.3. Cross section field pattern for the double layer structure

Similarly as we did for the single layer problem, we consider two regions as waves propagate along the parallel films of Fig.2.3b corresponding to the double layer structure. The difference here is that the medium ($j = 2$) behaves as a propagating film of thickness d and the substrate ($j = 0$) is present.

2.3.1. Guided wave region

For waves to be trapped in the film ($j = 1$), the effective index is bound in the interval $n_2 < \frac{\beta}{k_0} < n_1$.

We define the transverse propagation constant in each medium to be :

$$\gamma_j^2 = n_j^2 k_0^2 - \beta^2 \quad j = 1 \quad (2.12a)$$

$$\tau_j^2 = \beta^2 - n_j^2 k_0^2 \quad j = 0, 2, 3 \quad (2.12b)$$

We postulate standing wave in the film ($j = 1$), evanescent waves in medium ($j = 2$), ($j = 3$) and in substrate ($j = 0$). The field distribution becomes then :

$$E_y = A_3' \exp(-x |\tau_3|) \quad j = 3 \quad (2.13a)$$

$$E_y = A_1 \exp(-i x \gamma_1) + A_1' \exp(i x \gamma_1) \quad j = 1 \quad (2.13b)$$

$$E_y = A_2 \exp(x |\tau_2|) + A_2' \exp(-x |\tau_2|) \quad j = 2 \quad (2.13c)$$

$$E_y = A_0 \exp(x |\tau_0|) \quad j = 0 \quad (2.13d)$$

The boundary conditions require that the field and its normal derivatives be continuous at boundaries :

$$x = 0, \quad x = T, \quad x = d \quad (2.14)$$

where T still represents the thickness of the film ($j = 1$), and d is the thickness of the film ($j = 2$) as depicted by Fig.2.3b.

Recalling equations (2.5), (2.7), (2.12), (2.13) and (2.14) will establish the characteristic equation which is :

$$\begin{aligned} \gamma_1 T - \text{Atan} \frac{|\tau_3|}{\gamma_1} - \text{Atan} \left\{ i \frac{|\tau_2|}{\gamma_1} \tan \left[i |\tau_2| d + \text{Atan} \frac{|\tau_0|}{i |\tau_2|} \right] \right\} \\ = \pi q \end{aligned} \quad (2.15)$$

The definition of all transverse propagation constants in (2.15) is given by (2.12). The integer q labels the mode to be guided.

2.3.2. Coupled wave region

The effective index in this region ranges in the interval $n_0 < \frac{\beta}{k_0} < n_2$. Guided waves propagate in both layers ($j = 1$) and ($j = 2$).

The transverse propagation constants can be defined as :

$$\gamma_j^2 = n_j^2 k_0^2 - \beta^2 \quad j = 1, 2 \quad (2.16a)$$

$$\tau_j^2 = \beta^2 - n_j^2 k_0^2 \quad j = 0, 3 \quad (2.16b)$$

The electromagnetic field distribution is such that standing waves occur in film ($j = 1$) and film ($j = 2$), while exponential waves occur in medium ($j = 3$) and substrate ($j = 0$). We have then :

$$E_y = A_3' \exp(-x |\tau_3|) \quad j = 3 \quad (2.17a)$$

$$E_y = A_1 \exp(-i x \gamma_1) + A_1' \exp(i x \gamma_1) \quad j = 1 \quad (2.17b)$$

$$E_y = A_2' \exp(i x \gamma_2) + A_2 \exp(-i x \gamma_2) \quad j = 2 \quad (2.17c)$$

$$E_y = A_0 \exp(x |\tau_0|) \quad j = 0 \quad (2.17d)$$

A final recalling of (2.5), (2.7), (2.14), (2.16) and (2.17) makes the characteristic equation in the coupled wave region to be :

$$\gamma_1 T - A \tan \frac{|\tau_2|}{\gamma_1} - A \tan \left\{ \frac{\gamma_2}{\gamma_1} \tan \left[\gamma_2 d + A \tan \frac{|\tau_0|}{\gamma_2} \right] \right\} = \pi q \quad (2.18)$$

The integer q characterises the mode number and the transverse propagation constants are given by (2.16).

A close look at (2.18) reveals that equation (2.11) could have been established differently by taking the limit of equation (2.18) as d tends to infinity. As a matter of fact, equation (2.18), which corresponds to the characteristic equation of the double layer structure in the coupled wave region, entails equation (2.11) by combining medium ($j = 2$) and medium ($j = 0$) into a single infinite medium ($j = 2$) corresponding to the single layer structure and allowing $n_0 = n_2$.

2.4. Computational results and discussion

The numerical solution of all characteristic equations is achieved by executing the Newton-Raphson algorithm.

In order to maintain the same assumptions as in the next chapters, and also for simplicity, the boundary to the free-space medium ($j = 3$) is taken as perfectly reflecting. This can be justified by the fact that $n_3 = 1$ and is largely inferior to n_1 . Such an assumption is equivalent to determining the phase of the Fresnel reflection coefficient at the boundary B_{31} as $-\pi$. Consequently, in all equations, each term like $\text{Atan} \frac{|\tau_3|}{\gamma_1}$ must be substituted by the number $+\frac{\pi}{2}$.

Also as all characteristic equations involve a branch point at $\frac{\beta}{k_0} = n_2$, it is necessary to specify a convention which decides which branch in the computer program to choose. For this purpose we set $\text{Imag} [n_2 - \frac{\beta}{k_0}]^{\frac{1}{2}} > 0$, for an $\exp(-i \omega t)$ time convention.

2.4.1. Single layer problem

We consider the characteristic equation (2.11), also known as the eigenvalue equation, governing the single layer structure of Fig.2.3a. It determines the allowed values of the normalised propagation constant $\frac{\beta}{k_0}$ and describes the modes propagating not only in the guided wave region, but also in the leaky wave region, by solving equation (2.11) for complex β .

The real solutions will mathematically represent the modes in the guided wave region, whereas the complex solutions will represent the modes in the leaky wave region. Consider first the real solutions of the eigenvalue equation (2.11); their computation for the ten lowest modes is depicted by Fig.2.4. It describes the

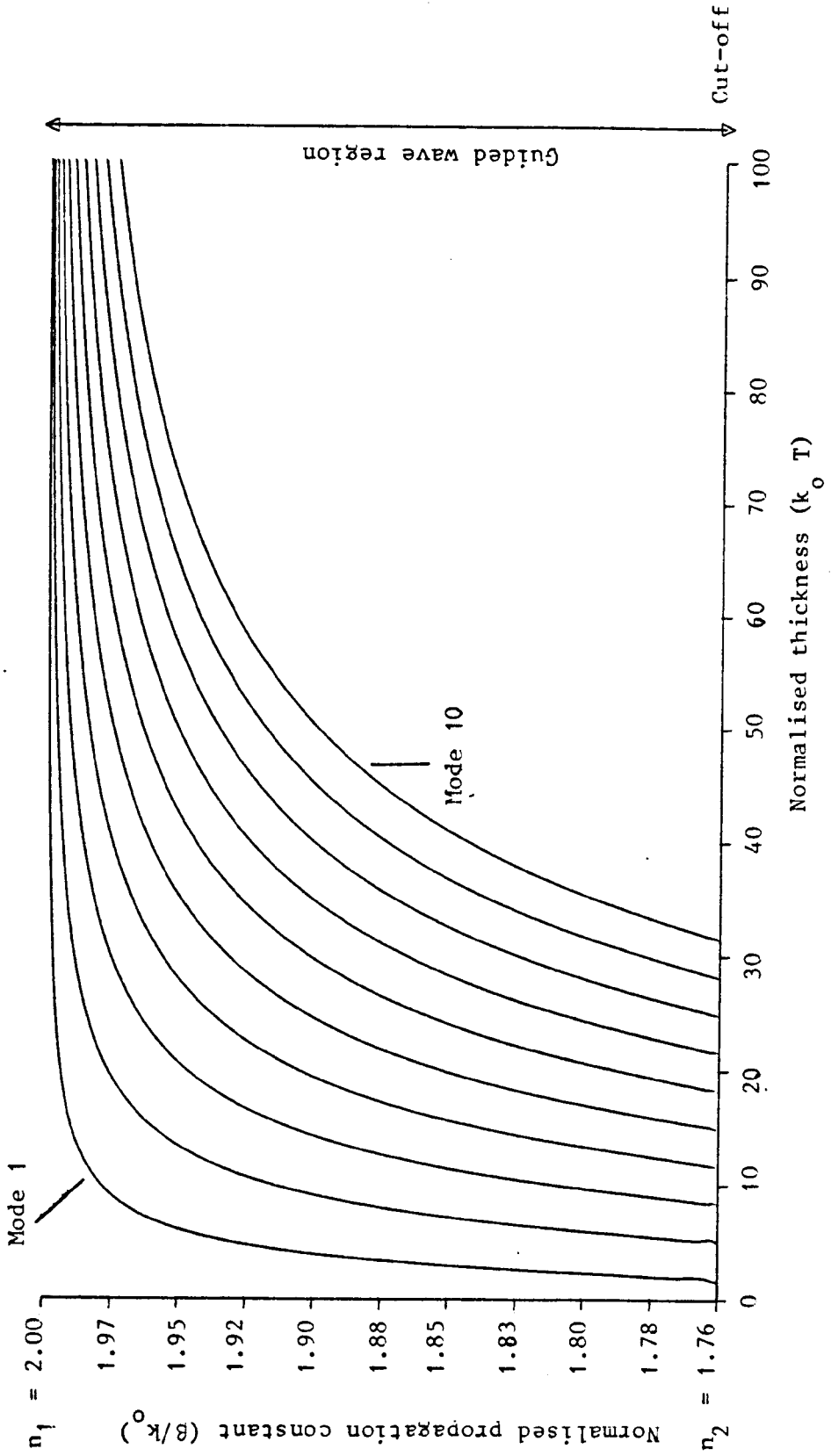


Fig.2.4. Computation of eigenvalue equation in the guided wave region for the 10 lowest modes of the single layer structure. The refractive indices in each medium are $n_1 = 2$; $n_2 = 1.76$; $n_3 = 1$.

possible real normalised propagation constants $\frac{\beta}{k_0}$ ranging in the interval $n_2 < \frac{\beta}{k_0} < n_1$. Such solutions represent the modes in the guided wave region. As the normalised thickness $k_0 T$ of the film ($j = 1$) narrows down, $\frac{\beta}{k_0}$ approaches the cut-off ($\frac{\beta}{k_0} = n_2$).

By further reducing T , complex solutions of (2.11) need to be taken into account; when cut-off occurs, no real solution of the eigenvalue equation is present. Hence $\frac{\beta}{k_0}$ becomes complex with a positive imaginary part. These solutions represent the modes in a new region known as the leaky wave region. It is, however, worth mentioning that in the case of the double layer structure (as will be shown later on), even beyond the transition thickness, $\frac{\beta}{k_0}$ still remains real by the nature of its corresponding eigenvalue equation.

Fig.2.5 shows systematically the behaviour of the trajectory of the leaky wave solutions for the ten lowest modes of the single layer structure in the complex plane as T changes from a maximum value ($k_0 T = 100$) to a minimum value ($k_0 T = 0$). Any real solution of Fig.2.5 represents the guided wave in the interval $n_2 < \frac{\beta}{k_0} < n_1$, whereas complex solutions that exist past the transition region ($\frac{\beta}{k_0} = n_2$) belong to leaky modes. For any modes illustrated in the complex plane of Fig.2.5, it can be observed that the imaginary part of $\frac{\beta}{k_0}$ is positive. This is crucial to the vanishing of such leaky waves away from the transition region. Also, as the thickness T is reduced, each point on the locus sees its imaginary part getting higher in magnitude. This emphasises the fact that as the thickness T of the film ($j = 1$) diminishes, the corresponding leaky wave launched in medium ($j = 2$) decays more rapidly. Physically, the leaky waves describe the radiation which occurs past the transition region as the incident angle θ exceeds the

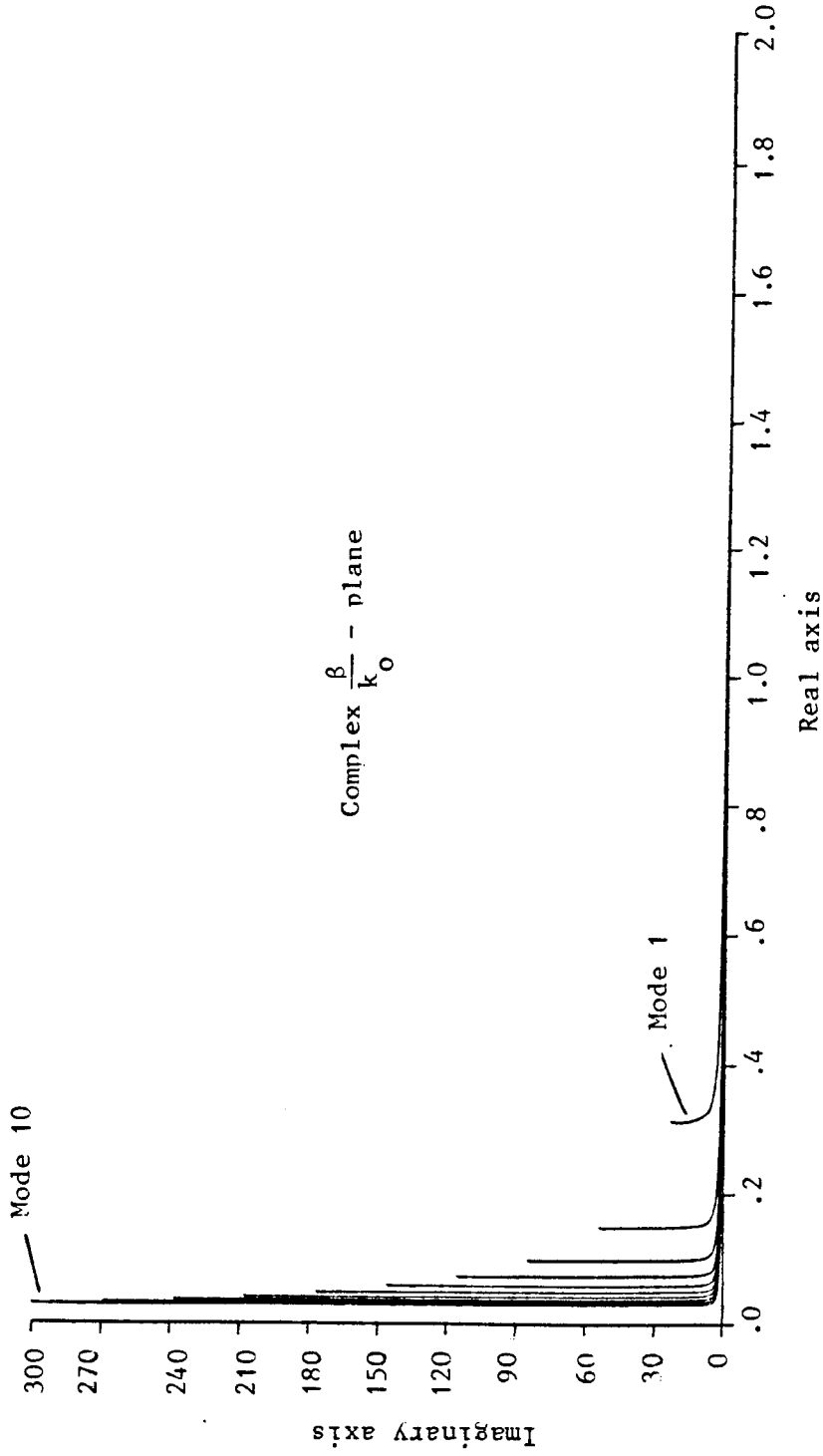


Fig.2.5. Computation of eigenvalue equation in the leaky wave region for the 10 lowest modes of the single layer structure. Solutions are the complex normalised propagation constants (β/k_0) as the thickness of the tapered waveguide T diminishes (from right to left of figure). The refractive indices in each medium are $n_1 = 2$; $n_2 = 1.76$; $n_3 = 1$.

critical angle $\theta_c = \text{Arccos} \frac{n_2}{n_1}$ of the single layer structure. Fig.2.6 illustrates the computation of the incident angle θ defined by $\theta = \text{Arccos} \left(\frac{\beta}{n_1 k_0} \right)$ as the thickness T varies from a maximum to a minimum value, and for the ten lowest modes of the single layer structure. The real solutions of θ corresponding to the guided wave region are restricted in the interval $0 < \theta < \theta_c$, whereas the complex solutions of θ corresponding to the leaky wave region are confined in the interval $\theta_c < \text{Real}(\theta) < \frac{\pi}{2}$.

We compute expressions (2.4) and (2.10) which describe the continuous field distribution in each medium and in each region. It is illustrated by Fig.2.7 and Fig.2.8 that the field patterns corresponding to a few of the lowest modes describe perfectly the field variation assumed earlier in this chapter.

In the guided wave region, the thickness chosen in the film ($j = 1$) is T_g . For $k_0 x > k_0 T_g$ and $k_0 x < 0$, there is an evanescent wave describing the cross section fields in medium ($j = 3$) and medium ($j = 2$) respectively. In the interval $0 < k_0 x < k_0 T_g$ we have a standing wave oscillating in the film ($j = 1$).

In the leaky wave region corresponding to a thickness T_L in the film ($j = 1$); we obtain an evanescent wave in medium ($j = 3$) only for $k_0 x > k_0 T_L$. For $0 < k_0 x < k_0 T_L$, there is a standing wave trapped in the film ($j = 1$); and for $k_0 x < 0$ there is a leaky wave radiating away in medium ($j = 2$).

2.4.2. Double layer problem

As far as the double layer structure of Fig.2.3b is concerned, we refer to the eigenvalue equation (2.18) to describe the modes covering the guided wave region and the coupled wave

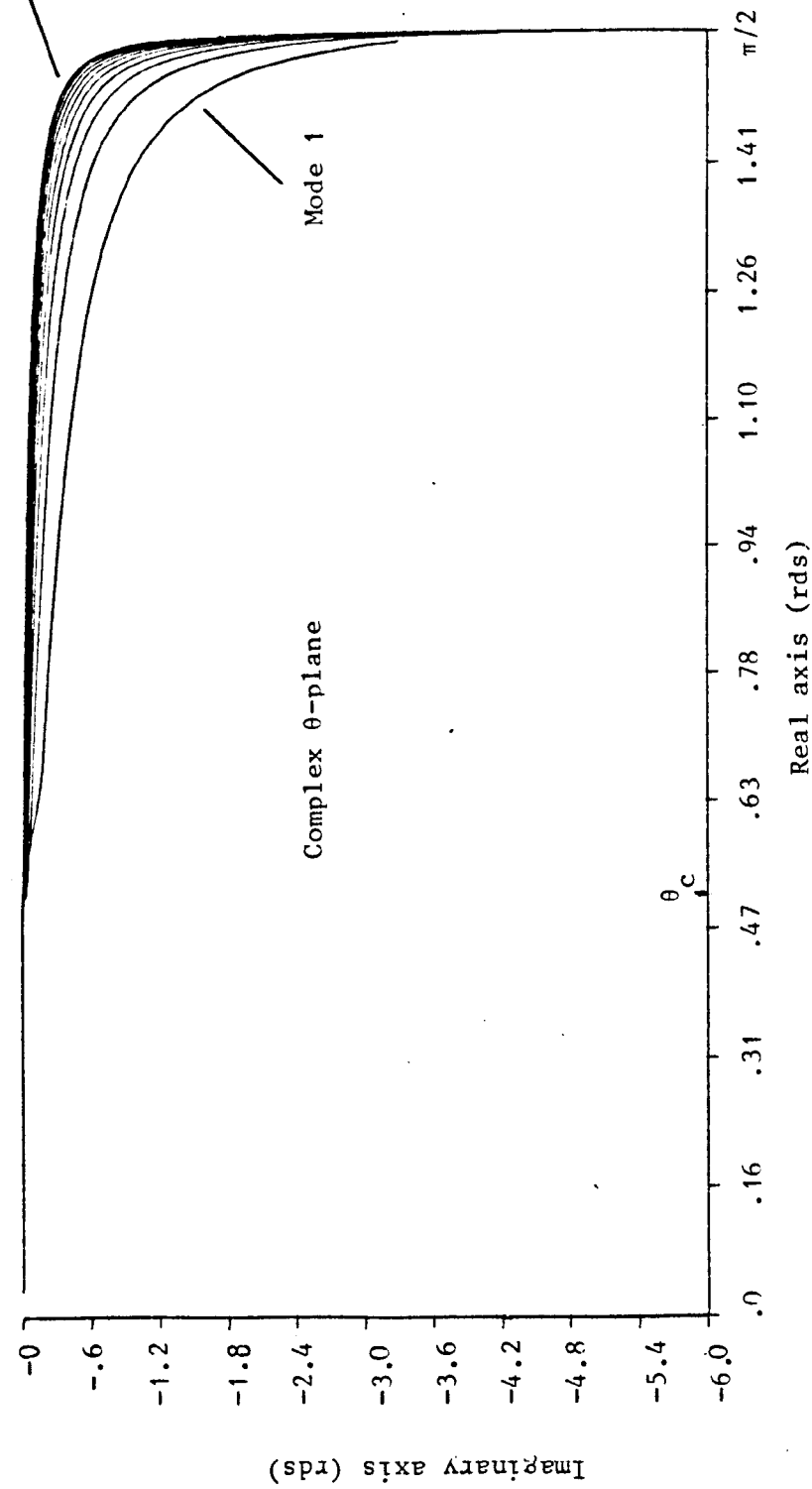


Fig.2.6. Computation of eigenvalue equation in the leaky wave region for the 10 lowest modes of the single layer structure. Solutions are the complex incident angles (in rds) as the thickness π is reduced (from left to right of figure). The refractive indices in each medium are $n_1 = 2$; $n_2 = 1.76$; $n_3 = 1$

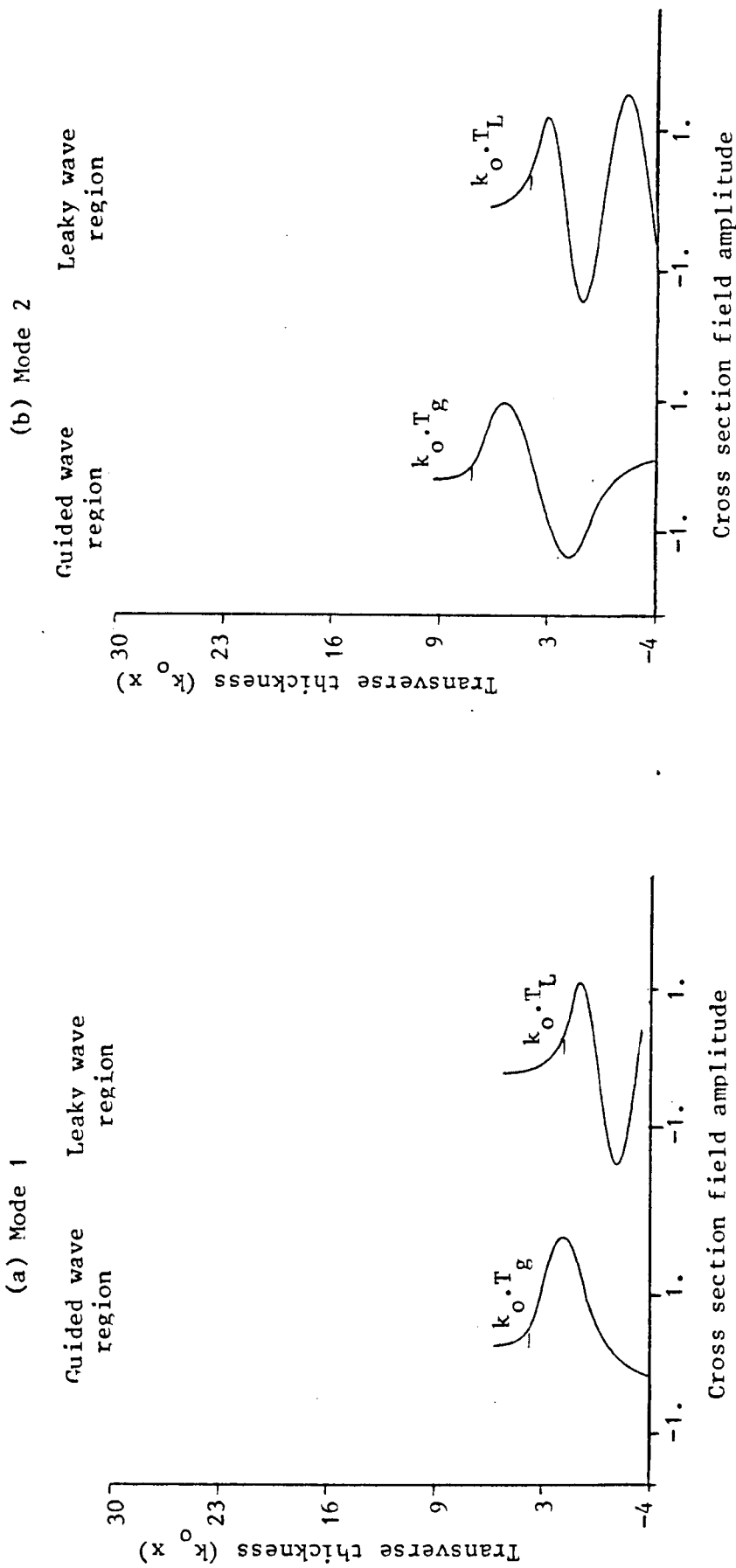
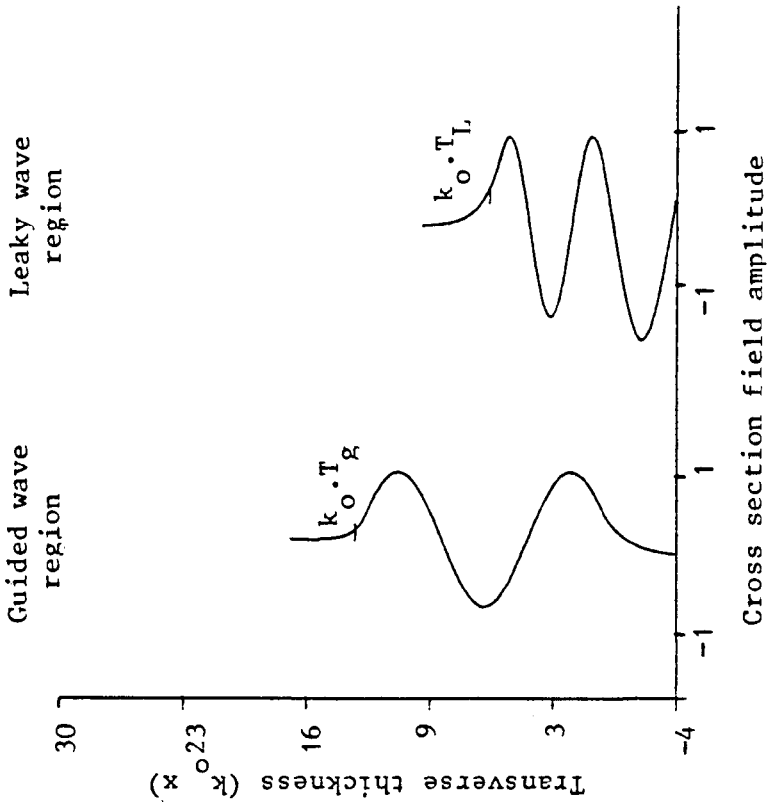


Fig.2.7. Computation of the normalised cross section field pattern in each medium versus the normalised transverse thickness ($k_0 x$), for the single layer structure. The refractive indices in each medium are $n_1 = 2$; $n_2 = 1.76$; $n_3 = 1$

(a) Mode 3



(b) Mode 4

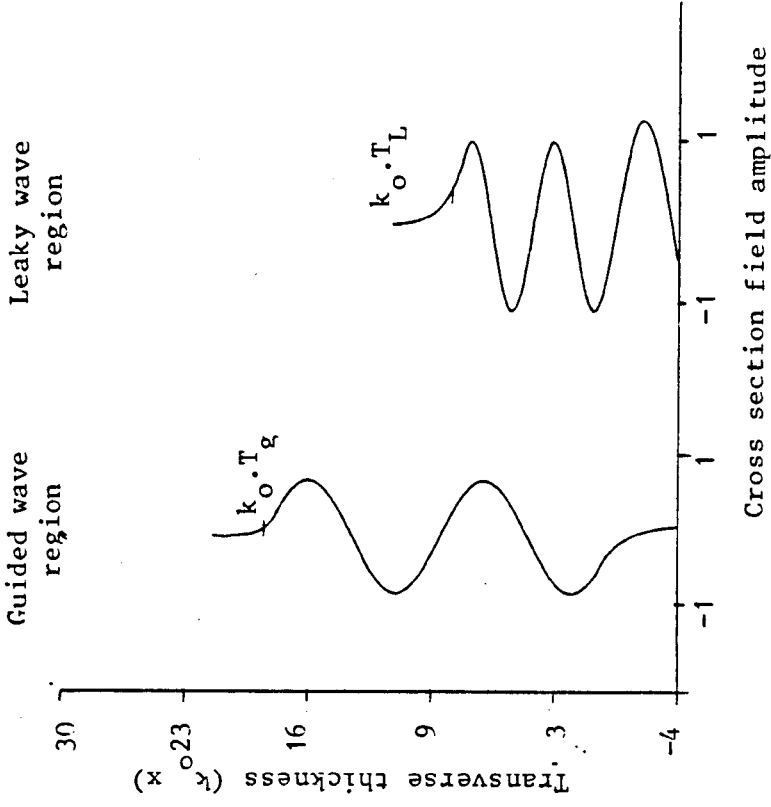


Fig.2.8. Computation of the normalised cross section field pattern in each medium versus the normalised transverse thickness ($k_0 x$), for the single layer structure. The refractive indices in each medium are $n_1 = 2$; $n_2 = 1.76$; $n_3 = 1$

region at the same time. Of course one could have used equation (2.15) to analyse the modes in the guided wave region, but computational results have proved it to be similar to equation (2.18). So for convenience and continuity reasons, we shall essentially solve the general eigenvalue equation (2.18) to mathematically represent the modes in the guided wave region as well as in the coupled wave region.

For numerical purposes, we fix the normalised thickness of the uniform film ($j = 2$), $k_0 d$, to be a certain value adequate to allow the propagation of a desired mode.

Practically, the eigenvalue equation (2.18) turns out to comprise real solutions which are of interest only, in the guided region as well as in the coupled wave region. The reason for that is essentially due to the analytical nature of equation (2.18). Consequently, unlike the single layer problem, leaky waves which are characterised by complex propagation constants do not exist in these regions where solutions are real for the double layer problem. However, the presence of the uniform film ($j = 2$) traps and guides the waves in the coupled wave region. In order to obtain information about the eigenvalue solutions, one should refer to the plotting of Fig.2.9. It shows the computation of eigenvalue equation (2.18) for the ten lowest modes of the double layer structure. Thereby the two regions are clearly distinguished. The guided wave region is described by the normalised propagation constant in the interval $n_2 < \frac{\beta}{k_0} < n_1$; whereas the coupled wave region is described in the interval $n_0 < \frac{\beta}{k_0} < n_2$. In the transition region corresponding to $\frac{\beta}{k_0} = n_2$, continuity is clearly seen.

The computer plot of Fig.2.9 describes clearly the general

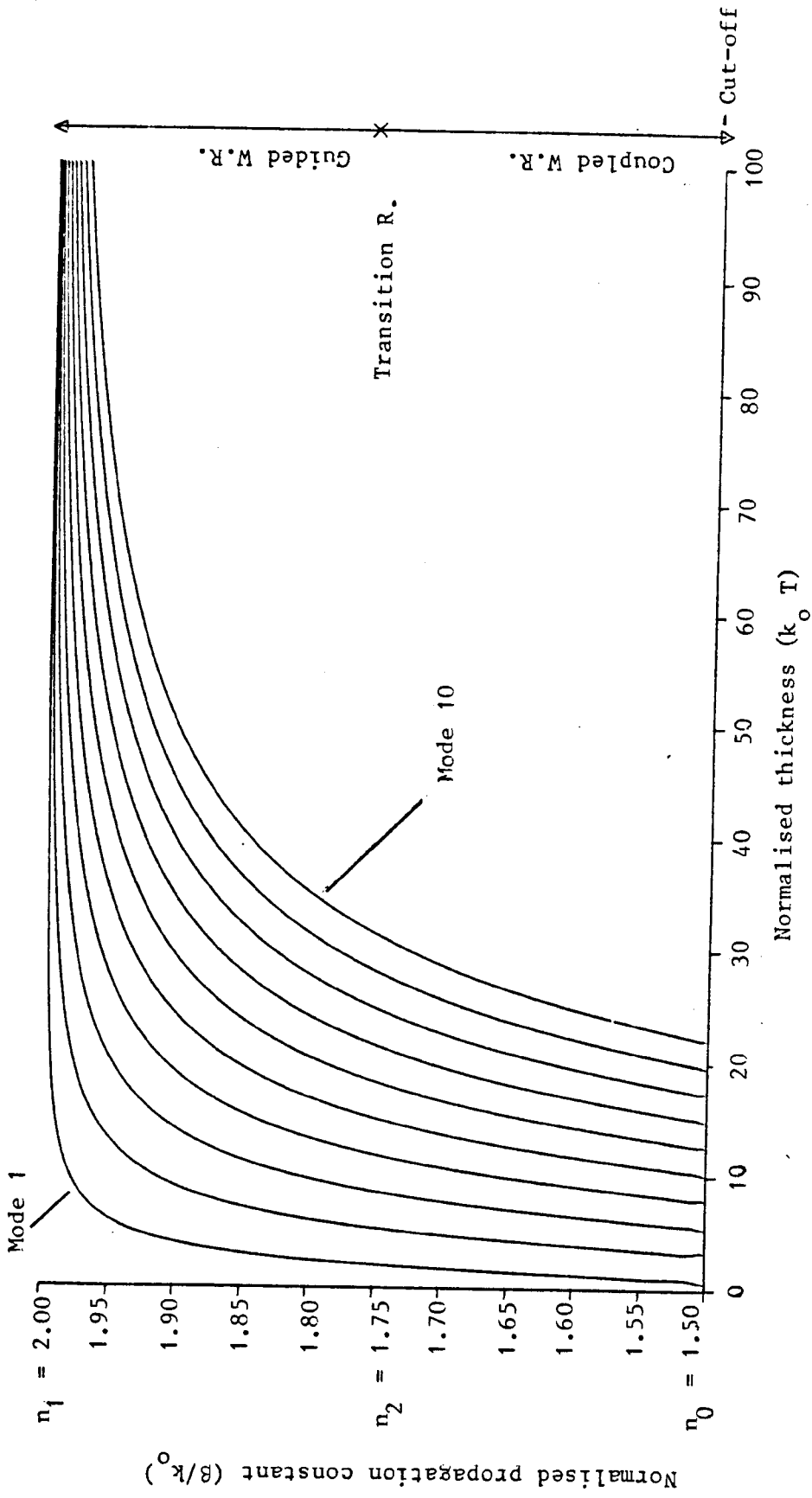


Fig.2.9. Computation of eigenvalue equation for the double layer structure and for the 10 lowest modes. The refractive indices in each medium are $n_0 = 1.5$; $n_1 = 2$; $n_2 = 1.76$; $n_3 = 1$. The normalised thickness of the uniform film (n_2) is : $k_0 d = -5$

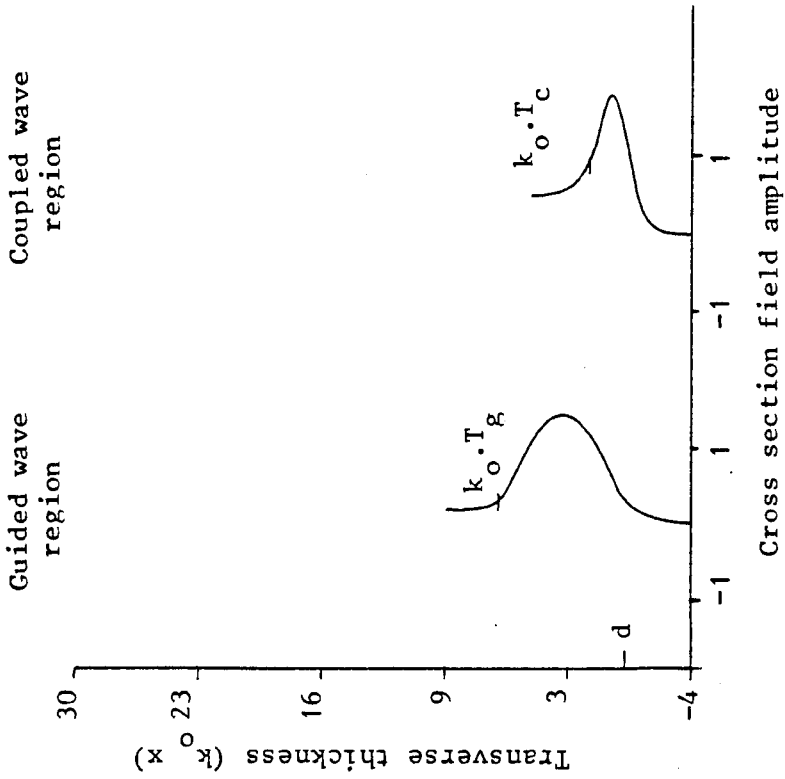
behaviour as the propagation constant β goes from one region to the other, as T diminishes. The two regions are described at the same time and continuity at the transition thickness is satisfied. When the normalised thickness $k_0 T$ is maximum, $\frac{\beta}{k_0}$ approaches the local index of the film ($j = 1$). To this degree the film ($j = 1$) acts as a bulk medium and all energy is contained within the same film ($j = 1$), which constitutes the source where all energy emanates from. When $\frac{\beta}{k_0}$ varies from n_1 to n_2 and as T decreases continuously, the field extends more outside the film ($j = 1$) as it approaches the transition thickness ($\frac{\beta}{k_0} = n_2$). At this stage light exits the guided wave region and is no more trapped. It then enters a new region known as the coupled wave region. For $\frac{\beta}{k_0}$ varying from n_2 to n_0 , coupled waves propagate along the film ($j = 1$) and the film ($j = 2$) having the same propagation constant β . At the cut-off point ($\frac{\beta}{k_0} = n_0$), the coupled waves in the film ($j = 1$) and the film ($j = 2$) become at least cut-off as all energy is leaked from film ($j = 2$) to substrate ($j = 0$). In this case, solutions of (2.18) become complex and the problem would be similar to the single layer structure when leaky waves are present; the treatment would be similar to subsection 2.4.1.

Finally, the computation of equations (2.13) and (2.17) which assess the cross section field pattern distribution in each medium and in each region is shown by Fig.2.10 and Fig.2.11 for a few of the lowest modes.

For each mode, one distinguishes the two regions and their continuity at each interface as postulated beforehand in previous section .

In the guided wave region, we choose a thickness T_g of the

(a) Mode 1



(b) Mode 2

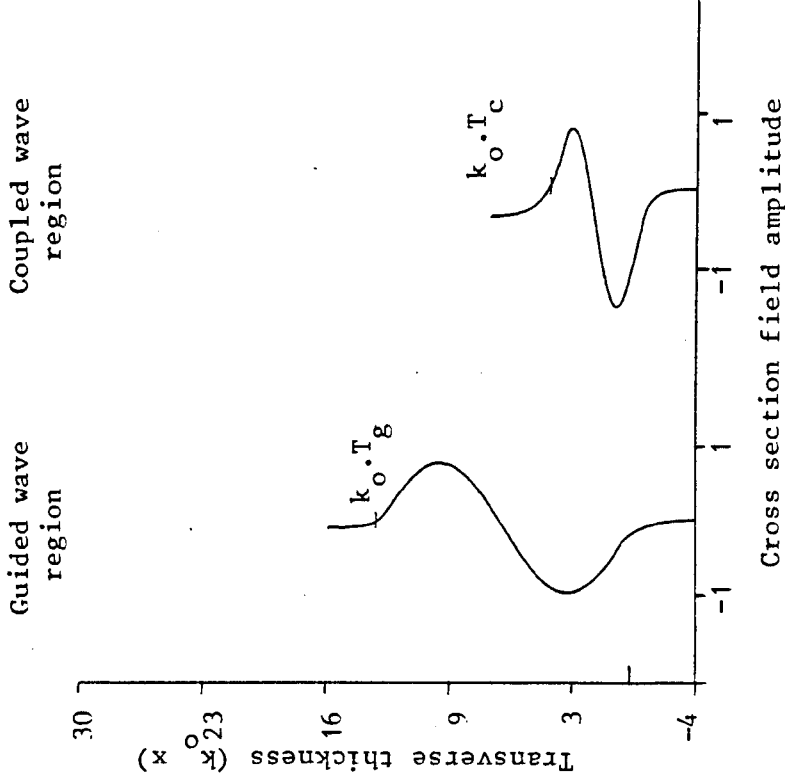
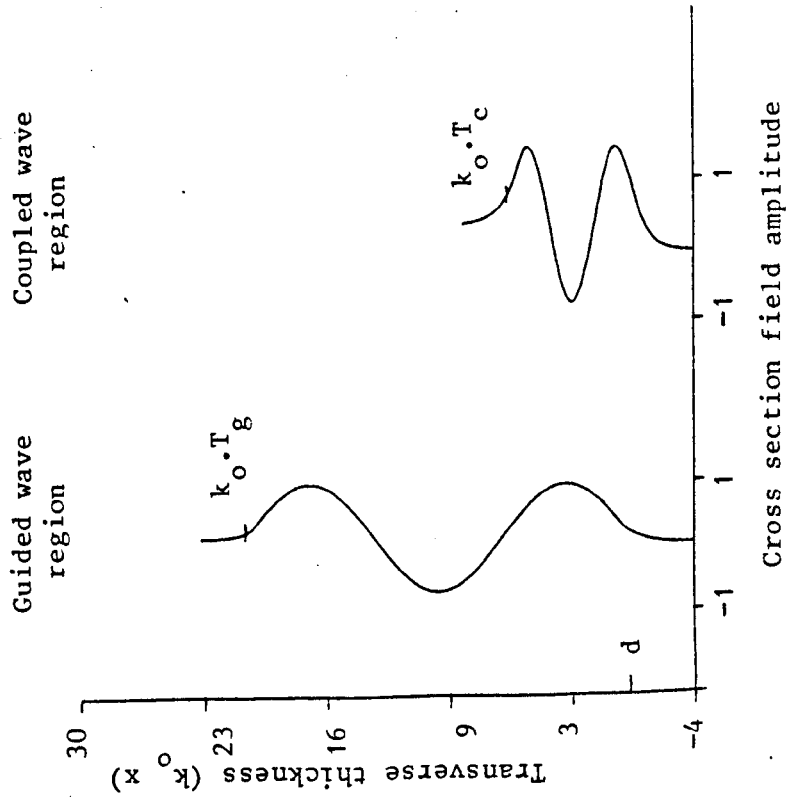


Fig.2.10. Computation of the normalised cross section field pattern in each medium versus the normalised transverse thickness ($k_0 x$), for the double layer structure. The refractive indices in each medium are $n_0 = 1.5$; $n_1 = 2$, $n_2 = 1.76$; $n_3 = 1$. The normalised thickness of the uniform film (n_2) is: $k_0 d = -5$

(a) Mode 3



(b) Mode 4

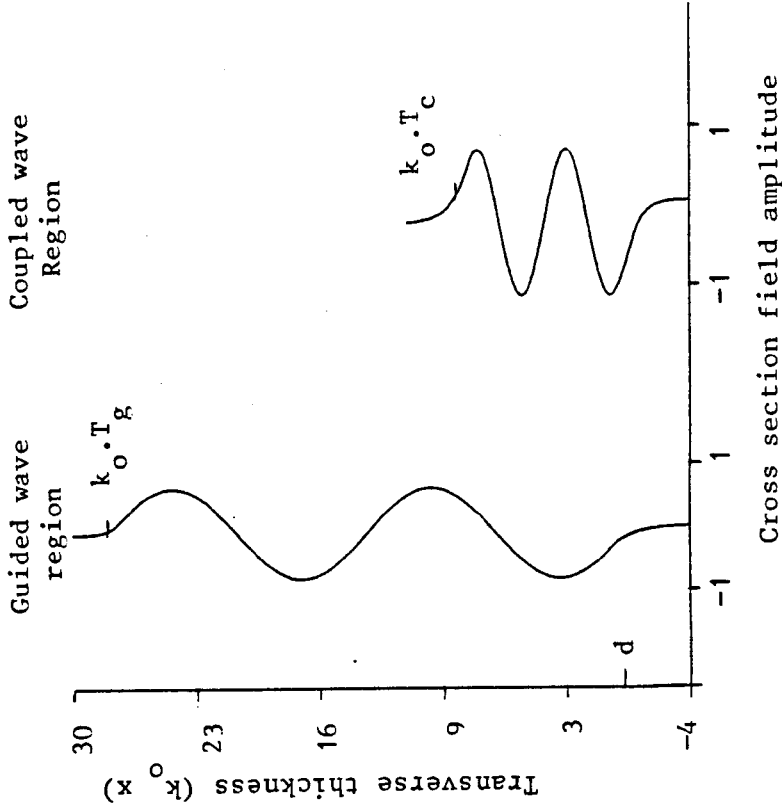


Fig.2.11. Computation of the normalised cross section field pattern in each medium versus the normalised transverse thickness ($k_0 x$), for the double layer structure. The refractive indices in each medium are $n_0 = 1.5$; $n_1 = 2$, $n_2 = 1.76$; $n_3 = 1$. The normalised thickness of the uniform film (n_2) is : $k_0 d = -5$

film ($j = 1$). When the normalised cross section variable k_0x is such that $k_0x > k_0T_g$, the cross section field describes an evanescent wave in medium ($j = 3$). For $0 < k_0x < k_0T_g$, the field represents a standing wave within the film ($j = 1$). As $k_0x < 0$, the field extends to an evanescent wave in the film ($j = 2$) and substrate ($j = 0$).

Ultimately, in the coupled wave region which is characterised by a thickness T_c in the film ($j = 1$), $k_0x > k_0T_c$ gives an evanescent wave in medium ($j = 3$). We get an oscillating standing wave in the film ($j = 1$) for $0 < k_0x < k_0T_c$; and in the film ($j = 2$) for $k_0d < k_0x < 0$. For $k_0x < k_0d$, an evanescent wave describes the field distribution in substrate ($j = 0$). As the modes in Fig.2.10 and Fig.2.11 propagate along the film ($j = 1$) ($k_0x > 0$), the modes are pushed down as they get nearer and beyond the transition region; there they finally become coupled and trapped once again by the film ($j = 2$) ($0 > k_0x > k_0d$).

2.4.3. Discussion

In subsections 2.4.1. and 2.4.2., we have been able to present interesting numerical results for the two configurations of Fig.2.3, by investigating the mode propagation in plane parallel waveguides, as the thickness T diminishes. Such a requirement is accommodated by the natural geometrical configuration of the tapered waveguide, which constitutes the main body of both structures in Fig.2.1. In this sense, one can unquestionably apply all numerical results of subsections 2.4.1 and 2.4.2 to the single layer problem as well as to the double layer problem respectively.

The phenomenon observed in Fig.2.7 and Fig.2.8 and which

describes the radiation transfer from the tapered waveguide to its adjacent medium, has found application not only in integrated optics, but also in any type of longitudinal non-uniform disturbances, such as underwater acoustics, tropospheric ducts etc. That illustrated in Fig.2.10 and Fig.2.11, which couples efficiently and continuously energy from the tapered waveguide to its adjacent film, has considerable interest mainly in integrated optics.

CHAPTER THREE

ANALYSIS OF THE TAPERED WAVEGUIDE

BY PLANE WAVE TRACKING

3.1. Introduction and formulation of the model

This chapter describes a method for analysing the tapered waveguide, which constitutes the main body of the structures given in Figs.2.1, by tracking the plane wave spectrum as energy propagates along the tapered waveguide. The method here, for integrated optics applications, follows the procedure described by Arnold and Felsen [23] in which they analyse acoustic propagation in shallow ocean water. Such an approach is provided by the ray optical method, whereby the field from a source point \underline{X}_0 (or line source) to an observation point \underline{X} , is tracked along ray paths that obey the rules of geometrical optics.

For analysis, one should refer to Fig.3.1 where a more basic geometry of the tapered waveguide is illustrated. The tapered waveguide itself is characterised by a dielectric material of refractive index (n_1) and is enclosed above and below, by media of indices (n_3) and (n_2) respectively.

There is assumed to be no variation of the field in the direction parallel to the tapered waveguide apex; also, the only component of the electric field is assumed to be along this direction, characteristic of TE polarisation. We shall throughout this chapter, omit the time dependence $\exp(-i \omega t)$. We locate a harmonic line source at \underline{X}_0 . Rays originating from \underline{X}_0 propagate at different directions perpendicular to the source.

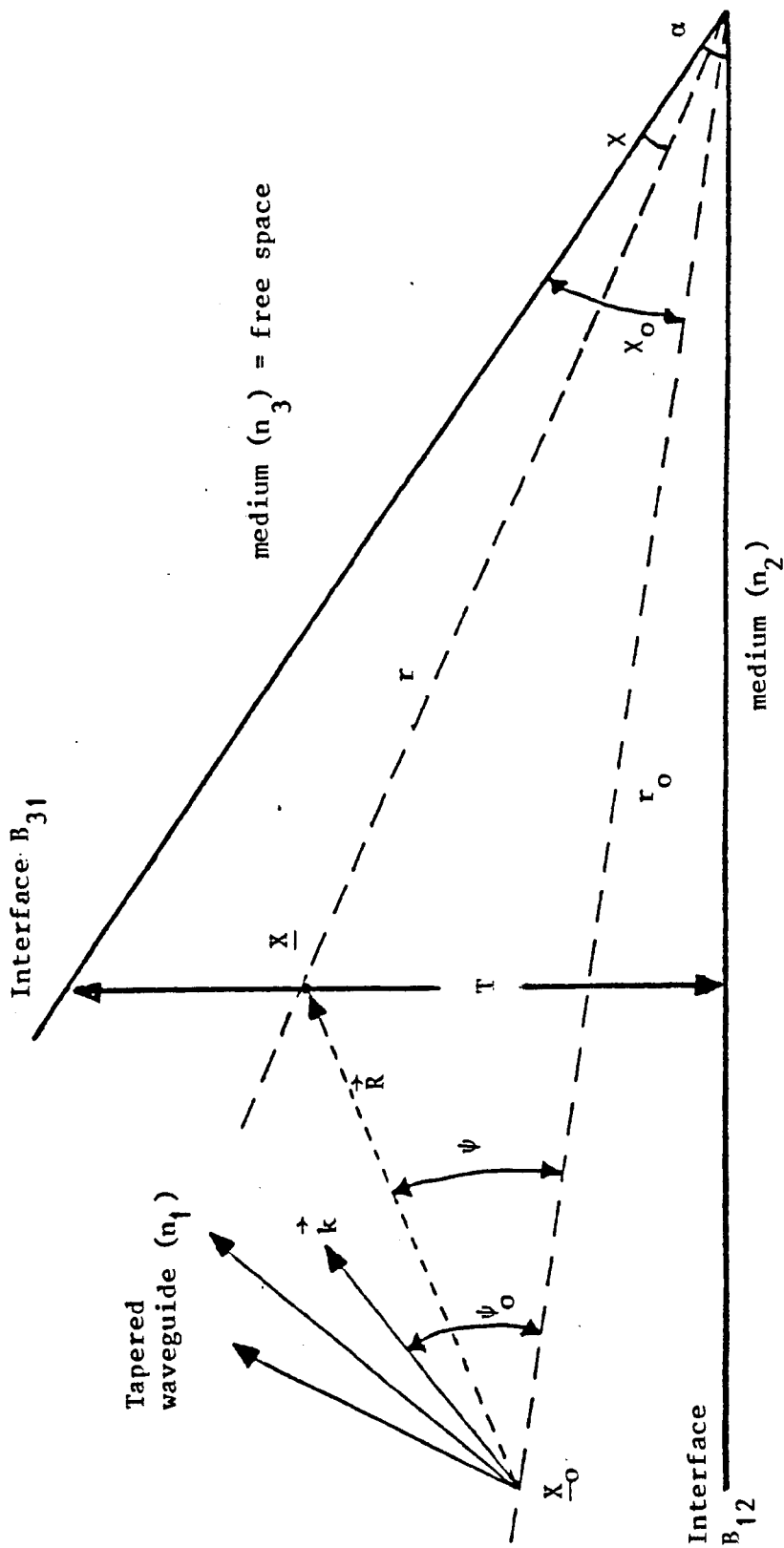


Fig.3.1 : Reference system in the tapered waveguide :
 Observation point $\underline{X} \equiv (x, r)$ at a local thickness T
 Source point $\underline{X}_0 \equiv (x_0, r_0)$

In such an approach, a discrete number of rays reach the observation point located at \underline{X} ; each such ray can be identified by the number of times it has been reflected at the bottom interface B_{12} . Consequently, we must partition the rays emanating from the source \underline{X}_0 into two categories :

- * Upgoing rays, which impinge at the interface B_{31} first.
- * Downgoing rays, which impinge at the interface B_{12} first.

These two types of ray are then tracked through multiple reflections, and each type of ray is further split into those undergoing an even or odd number of reflections at B_{12} boundary, see Fig.3.2. In this case, any ray reaching the observation point \underline{X} belongs to one of the four species of rays mentioned above.

3.2. Field due to rays free of reflection

We consider first the direct contribution of waves that emanate from the source \underline{X}_0 , without any reflection at either interface of the tapered waveguide occur. The wave number k related to the tapered film (n_1) propagates at an angle $\psi - \psi_0$ from the line joining the source \underline{X}_0 to the observation point \underline{X} , (see Fig.3.1). \underline{X}_0 and \underline{X} are characterised by their polar co-ordinates (χ_0, r_0) and (χ, r) respectively, with respect to the wedge apex.

The geometrical path length R represents the distance separating the source and the observation point.

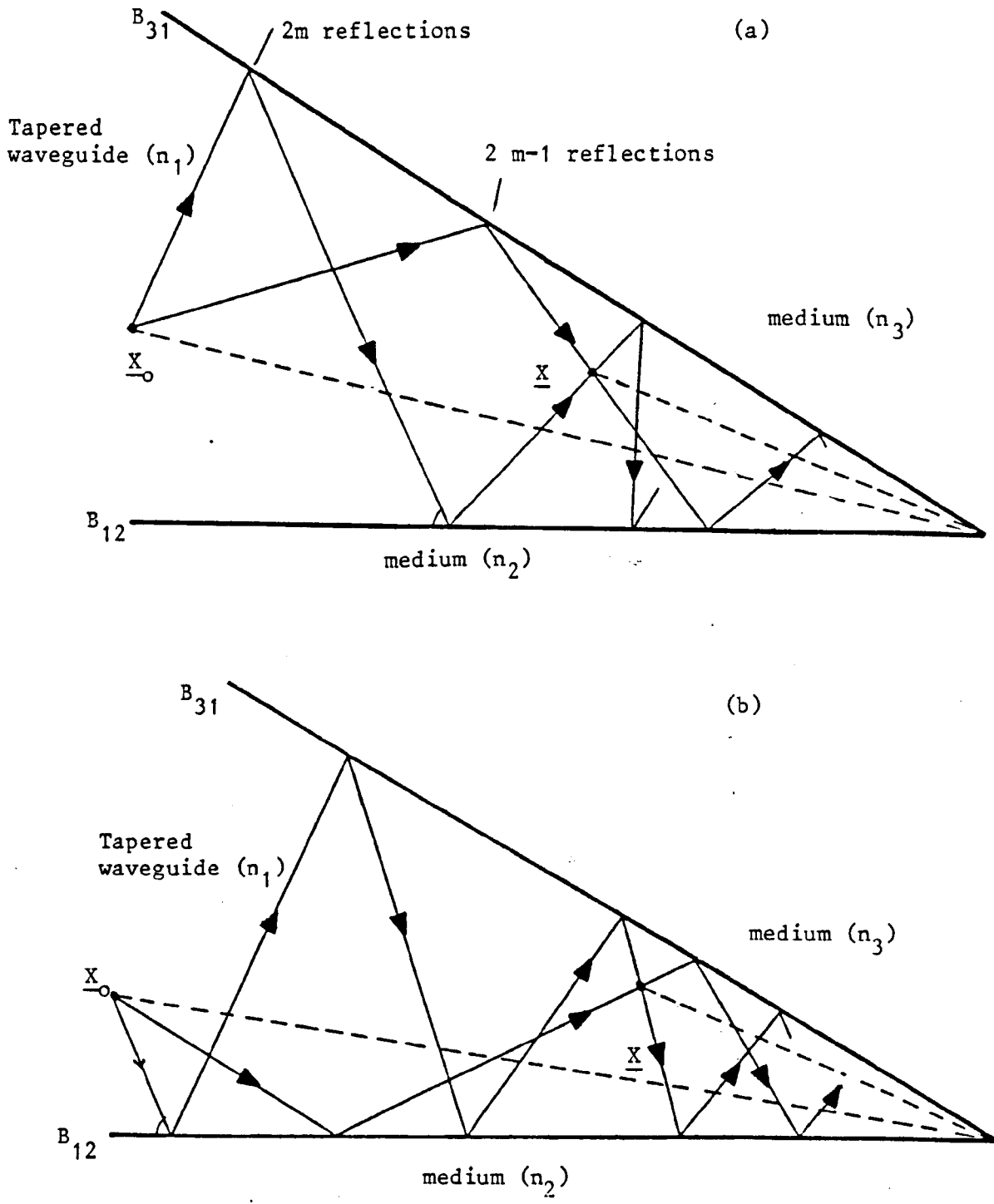


Fig.3.2 : (a) shows the upgoing waves undergoing $2m$ or $2m-1$ reflections from \underline{X}_0 to \underline{X}
 (b) shows similarly the downgoing waves

Each plane wave in the source spectrum, contributes to the field at \underline{X} by a term given by :

$$\exp(i \vec{k} \cdot \vec{R}) = \exp[i k R \cos(\psi - \psi_0)] \quad (3.1a)$$

where the phase quantity of the term on the left of the expression (3.1a), is the dot product between the wave vector \vec{k} and the geometrical path vector \vec{R} . The moduli k and R are defined as :

$$k = |\vec{k}|, \quad R = |\vec{R}| \quad (3.1b)$$

Physically, (3.1a) represents a single plane wave propagating with a wave number $k = n_1 k_0$, where n_1 is the tapered waveguide's refractive index, and k_0 is the free-space wave number. The total contribution of the field due to waves undergoing no reflection at a given observation point \underline{X} is taken as a full spectrum, as ψ_0 ranges over visible and invisible angles. In terms of a Green's function, the total field obtained will be :

$$g^o(\underline{X}, \underline{X}_0) = \frac{i}{4\pi} \int_C \exp[i k R \cos(\psi - \psi_0)] d\psi_0 \quad (3.2)$$

The contour (C) of integration in the complex ψ_0 -plane, is depicted by Fig.3.3.

3.3. Field excited by the upgoing species of rays

Here, we consider the type of waves that hit the B_{31} boundary first. Such rays, depicted by Fig.3.2a consist of two categories. Those undergoing an even number ($2m$) of reflections at each interface of the tapered waveguide are denoted by G_e^u ; and those which follow an odd number ($2m-1$) of reflections are denoted by G_o^u .

A single plane wave, originating from the source \underline{X}_0 contributes to the observation point \underline{X} by the term :

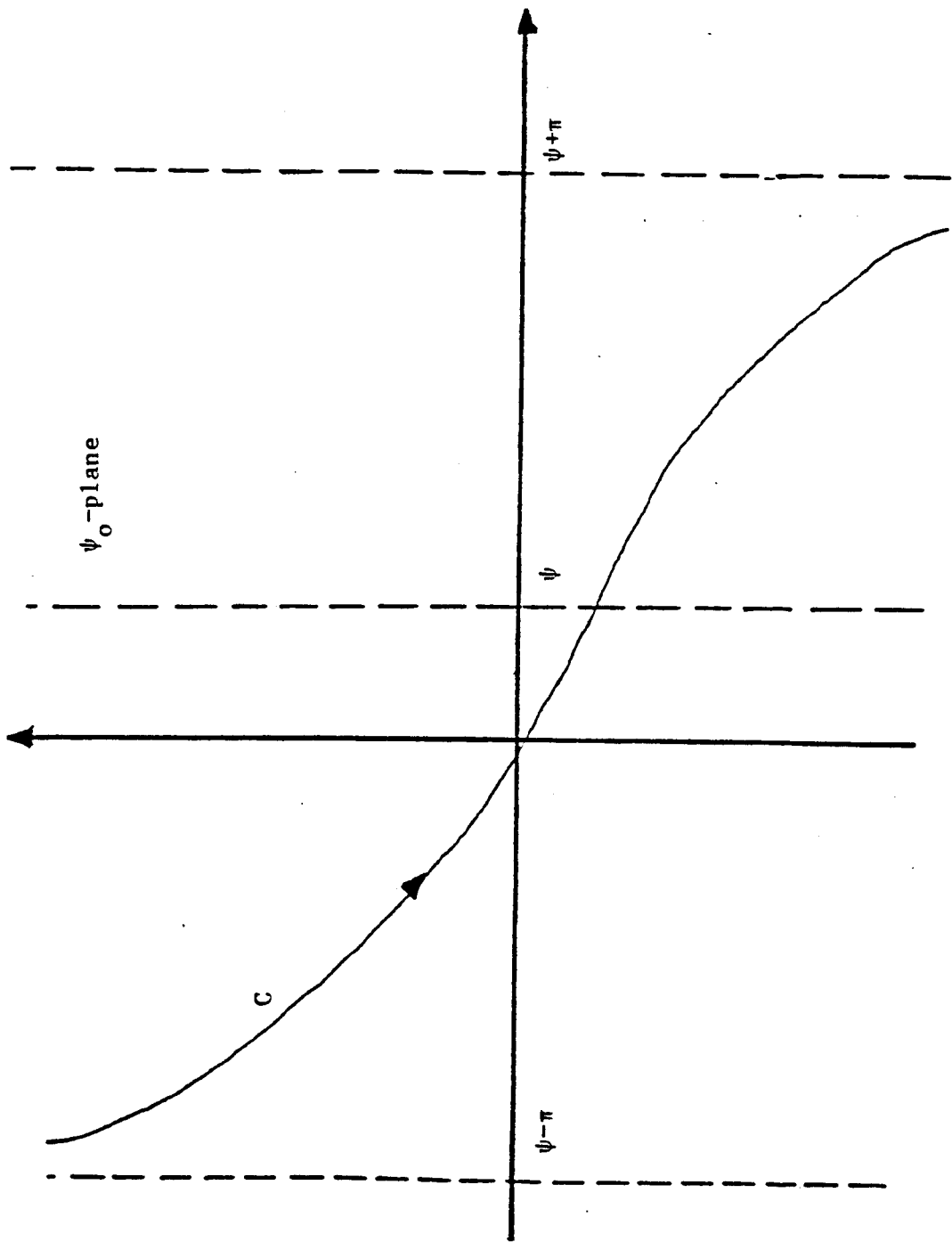


Fig.3.3 : $-\pi < \psi_0 - \psi < \pi$ corresponding to the total contribution of the spectrum along the contour (C)

$$G_e^u(\theta_m, \theta_o) = \exp[i \phi_e^u(\theta_m, \theta_o) + i k R_e^u(\theta_m, \theta_o)] \quad (3.3a)$$

after an even number of reflections; and

$$G_o^u(\theta_m, \theta_o) = \exp[i \phi_o^u(\theta_m, \theta_o) + i k R_o^u(\theta_m, \theta_o)] \quad (3.3b)$$

after an odd number of reflections.

The subscripted ϕ_e^u and ϕ_o^u , refer to the accumulated phase change of plane waves introduced after an even (2m) or odd (2m-1) number of reflections respectively.

Similarly, the subscripted R_e^u and R_o^u represent respectively, the geometrical path measured from \underline{X}_o to \underline{X} after an even or odd number of reflections.

The integer m ranges in the interval $1 < m < M$, where $m = 1$, corresponds to the first reflected ray impinging at an incidence angle θ_o , and $m = M$ corresponds to the maximum reflected ray whose incident angle is θ_M . Consequently, one expects the incident angle θ at boundary B_{12} , after m reflections occur, to be limited within the interval : $\theta_o < \theta < \theta_M$. (3.4)

The total field contribution due to the upgoing species of waves, following an even or odd number of reflections, can be expressed in terms of a Green's function as :

$$g^u(\underline{X}, \underline{X}_o) = \frac{i}{4\pi} \int_C \sum_{m=1}^M [G_e^u(\theta_m, \theta_o) + G_o^u(\theta_m, \theta_o)] d\theta_o \quad (3.5)$$

The contour (C) of integration is shown in the complex ψ_o -plane on Fig.3.3, after mapping the ψ_o -plane into the θ_o -plane through the equation $\psi_o = \theta_o^{-\alpha} \chi_o$.

Fig.3.4a and Fig.3.4b show the geometrical constructions, developed by the image method, which facilitates the tracking of

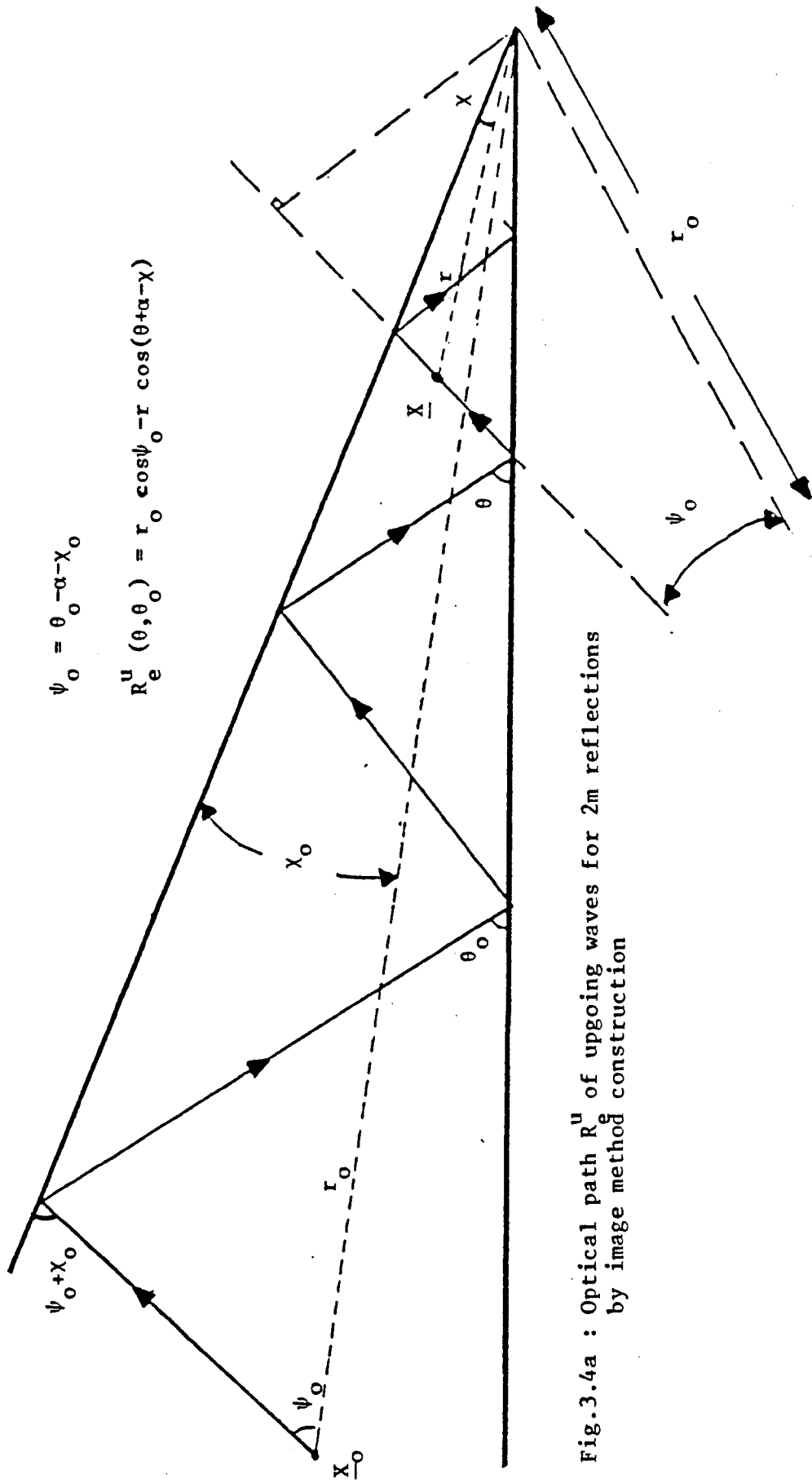


Fig.3.4a : Optical path R_e^u of upgoing waves for 2m reflections by image method construction

waves, after an even or odd number of reflections respectively. They also give the previous geometrical expression that maps ψ_o into θ_o .

Following the image tracking of plane waves in Figs.3.4, one defines :

$$\phi_e^u(\theta_m, \theta_o) = m \pi + \sum_{\ell=1}^m \phi(\theta_\ell) \quad (3.6a)$$

$$\phi_o^u(\theta_m, \theta_o) = \phi_e^u(\theta_m, \theta_o) - \phi(\theta_m) \quad (3.6b)$$

Where $\phi(\theta_\ell)$ is the phase of the plane wave reflection coefficient at bottom interface B_{12} , corresponding to the ℓ^{th} reflection. Each species of wave strikes B_{12} at an angle θ_m . After each pair of reflections, the incidence angle θ_m is augmented by twice the wedge angle α . Therefore at the m^{th} reflection, the incidence angle θ_m will be :

$$\theta_m = \theta_o + 2 \alpha (m-1) \quad (3.7a)$$

Because of the one-to-one relationship between the number of reflections m and the incident angle at B_{12} ; one can drop the subscript m on θ and write (3.7a) as follows :

$$\theta = \theta_o + 2 \alpha (m-1) \quad (3.7b)$$

Continuation of the discrete sum in (3.6) is vital to further analysis. It is achieved by application of the Euler-MacLaurin formulae (given by expression A.4 in Appendix A) to equations (3.6) and (3.7); one obtains then :

$$\begin{aligned} \phi_e^u(\theta, \theta_o) &= \left(\frac{\theta - \theta_o}{2\alpha}\right) \pi + \pi + \frac{1}{2\alpha} \int_{\theta_c}^{\theta} \phi(\theta') d\theta' - \frac{1}{2\alpha} \int_{\theta_c}^{\theta_o} \phi(\theta') d\theta' \\ &\quad + \frac{1}{2} \phi(\theta) + \frac{1}{2} \phi(\theta_o) + \text{Error} \end{aligned} \quad (3.8a)$$

$$\phi_o^u(\theta, \theta_o) = \phi_e^u(\theta, \theta_o) - \phi(\theta) \quad (3.8b)$$

where the Error term is neglected as postulated in Appendix A. The interface B_{31} is assumed perfectly reflecting, for the presence of π in some quantities in (3.8a), which accounts for the phase change accumulated after m reflections at that interface.

$\phi(\theta)$ is the phase of the reflection coefficient at the bottom boundary B_{12} of the tapered waveguide. It is given straight away by the Fresnel equation for the single layer problem and by Appendix D for the double layer problem.

The expressions for the path length are given by reference to Fig.3.4a and Fig.3.4b. They are :

$$R_e^u(\theta, \theta_o) = r_o \cos(\theta_o - \alpha - \chi_o) - r \cos(\theta + \alpha - \chi) \quad (3.9a)$$

$$R_o^u(\theta, \theta_o) = r_o \cos(\theta_o - \alpha - \chi_o) - r \cos(\theta - \alpha + \chi) \quad (3.9b)$$

3.4. Field excited by the downgoing species of rays

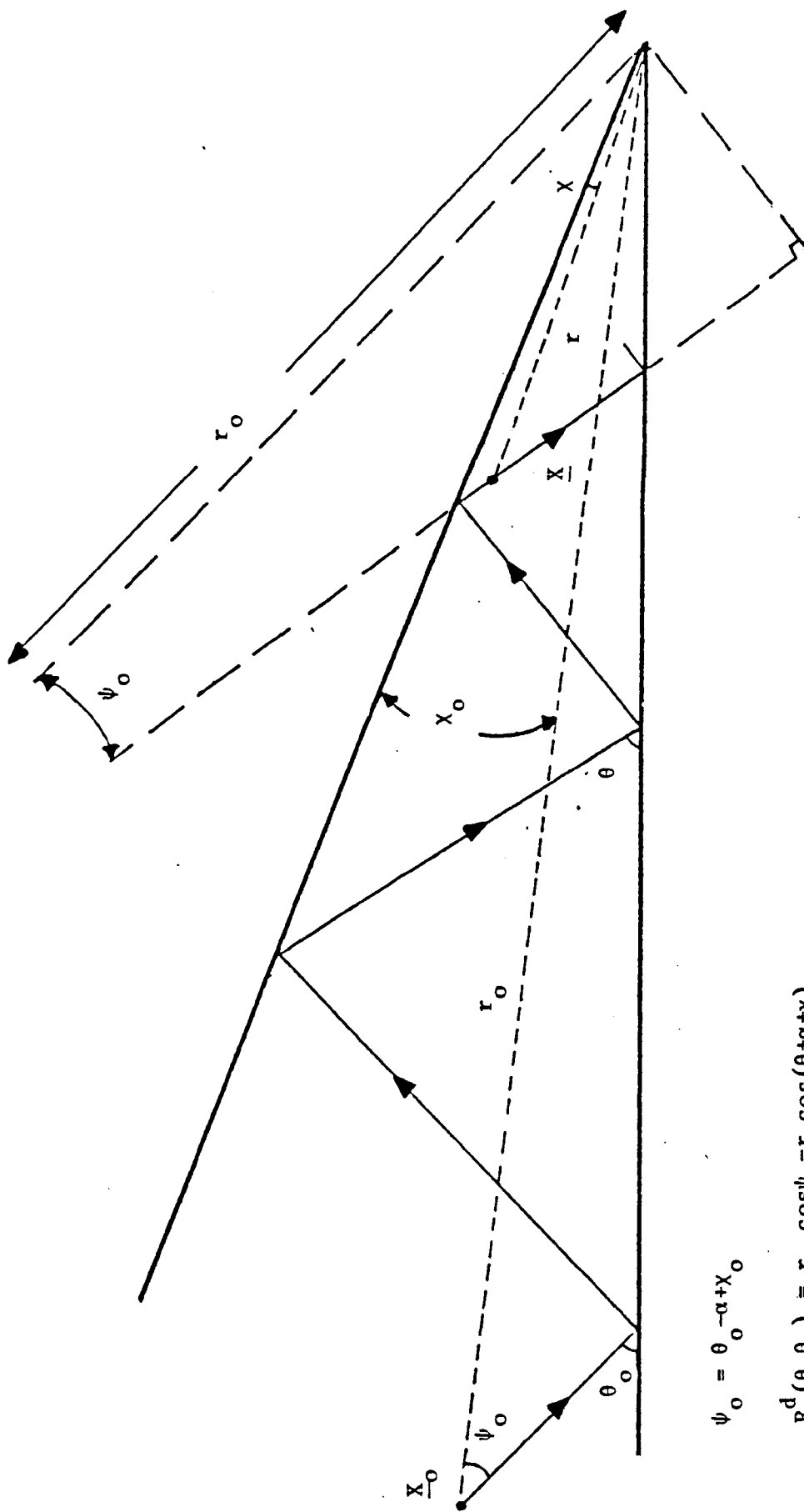
An exactly similar reasoning as in the previous section will give similar expressions for the field due to the downgoing part of the spectrum, as depicted by Fig.3.2b. In terms of a Green's function, the total field contribution is then :

$$g^d(\underline{x}, \underline{x}_o) = \frac{i}{4\pi} \int_C \sum_{m=1}^M [G_e^d(\theta_m, \theta_o) + G_o^d(\theta_m, \theta_o)] d\theta_o \quad (3.10)$$

The contour (C) is given by Fig.3.3, after mapping ψ_o into θ_o through equation $\psi_o = \theta_o - \alpha + \chi_o$, which is geometrically found by reference to Figs.3.5. One also defines :

$$G_e^d(\theta_m, \theta_o) = \exp[i \phi_e^d(\theta_m, \theta_o) + i k R_e^d(\theta_m, \theta_o)] \quad (3.11a)$$

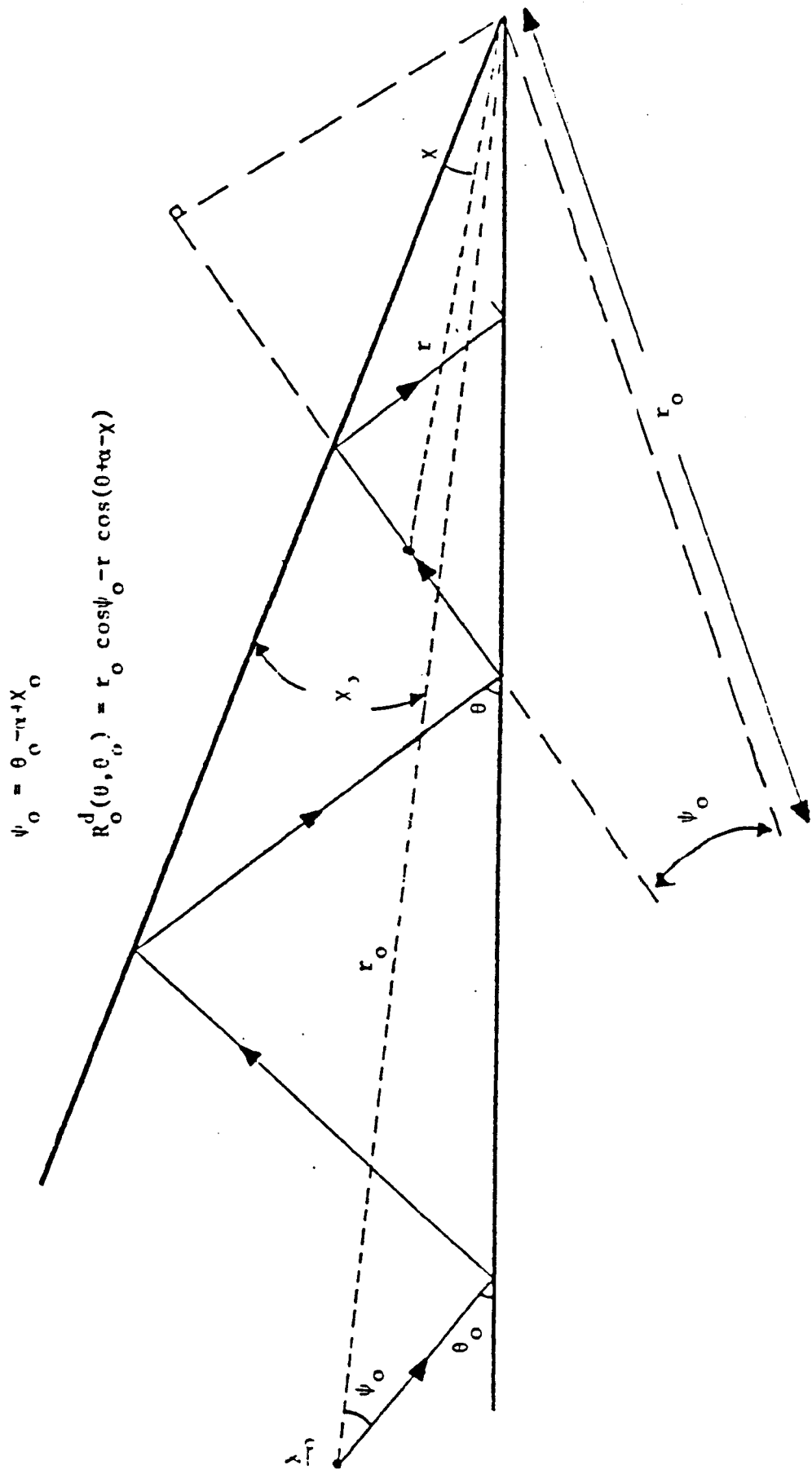
$$G_o^d(\theta_m, \theta_o) = \exp[i \phi_o^d(\theta_m, \theta_o) + i k R_o^d(\theta_m, \theta_o)] \quad (3.11b)$$



$$\psi_0 = \theta_0 - \alpha + \chi_0$$

$$R_e^d(\theta, \theta_0) = r_0 \cos \psi_0 - r \cos(\theta + \alpha + \chi)$$

Fig.3.5a : Optical path R_e^d for downgoing waves for 2m reflections by image method construction



$$\psi_0 = \theta_0 - \pi + X_0$$

$$R_0^d(\theta, \theta_0) = r_0 \cos \psi_0 - r \cos(\theta + \alpha - X)$$

Fig. 3.5b : Optical path R_0^d of downgoing waves for $2m-1$ reflections by image method construction

The phase functions in (3.11) are also defined in a similar manner as done with the upgoing type of waves, by reference to Fig.3.5a and 3.5b. They are :

$$\phi_e^d(\theta_m, \theta_o) = m \pi + \sum_{\ell=1}^m \phi(\theta_\ell) \quad (3.12a)$$

$$\phi_o^d(\theta_m, \theta_o) = \phi_e^d(\theta_m, \theta_o) - \pi \quad (3.12b)$$

After combining A.4 and (3.7) into equations (3.12), we get :

$$\begin{aligned} \phi_e^d(\theta, \theta_o) = & \left(\frac{\theta - \theta_o}{2\alpha}\right) \pi + \pi + \frac{1}{2\alpha} \int_{\theta_c}^{\theta} \phi(\theta') d\theta' - \frac{1}{2\alpha} \int_{\theta_c}^{\theta_o} \phi(\theta') d\theta' \\ & + \frac{1}{2} \phi(\theta) + \frac{1}{2} \phi(\theta_o) \end{aligned} \quad (3.13a)$$

$$\phi_o^d(\theta, \theta_o) = \phi_e^d(\theta, \theta_o) - \pi \quad (3.13b)$$

The presence of the π in (3.12b) and (3.13b), accounts for the fact that for downgoing waves, each even ray has one more reflection on top interface B_{31} than the odd ray. As the top interface is assumed perfectly reflecting, one expects a phase change difference of π , between the two cases.

The geometrical paths are also defined by reference to Figs.3.5 as follows :

$$R_e^d(\theta, \theta_o) = r_o \cos(\theta_o - \alpha + \chi_o) - r \cos(\theta + \alpha + \chi) \quad (3.14a)$$

$$R_o^d(\theta, \theta_o) = r_o \cos(\theta_o - \alpha + \chi_o) - r \cos(\theta + \alpha - \chi) \quad (3.14b)$$

3.5. Total field contribution

The total field contribution at any observation point \underline{X} whose polar coordinates are (χ, r) , is due to both scattered components, plus the incident non-reflected field. Combining then, equations (3.2), (3.5) and (3.10), one obtains :

$$g(\underline{X}, \underline{X}_0) = g^o(\underline{X}, \underline{X}_0) + g^u(\underline{X}, \underline{X}_0) + g^d(\underline{X}, \underline{X}_0) \quad (3.15)$$

In addition to the field contribution in (3.15), additional fields could be added to the total field expression in (3.15). They are due to diffraction at the apex of the tapered waveguide, and also to the type of waves depicted by Fig.3.6, which are rays whose incident angle is higher than $\frac{\pi}{2}$ as they travel past the observation point and return to it after reversal of slope. Such rays carry very small amplitude. For the parameter of interest (α small) in practical integrated optics applications, those additional contributions can largely be neglected numerically.

3.6. Transformation of the plane wave spectrum by Poisson-Sum-formulae

Equations (3.5) and (3.10) may not be well suited to numerical applications, because of the existence of too many dominant terms with similar amplitude but largely varying phases. As the sums in (3.5) and (3.10) are finite, we can suggest the technique of Poisson-summation which transforms any discrete sum, like (3.5) and (3.10), into a sum of continuous spectra. Making use of the result A.3 of Appendix A, its application to the four species of waves in (3.5) and (3.10) gives for the upgoing waves' contribution :

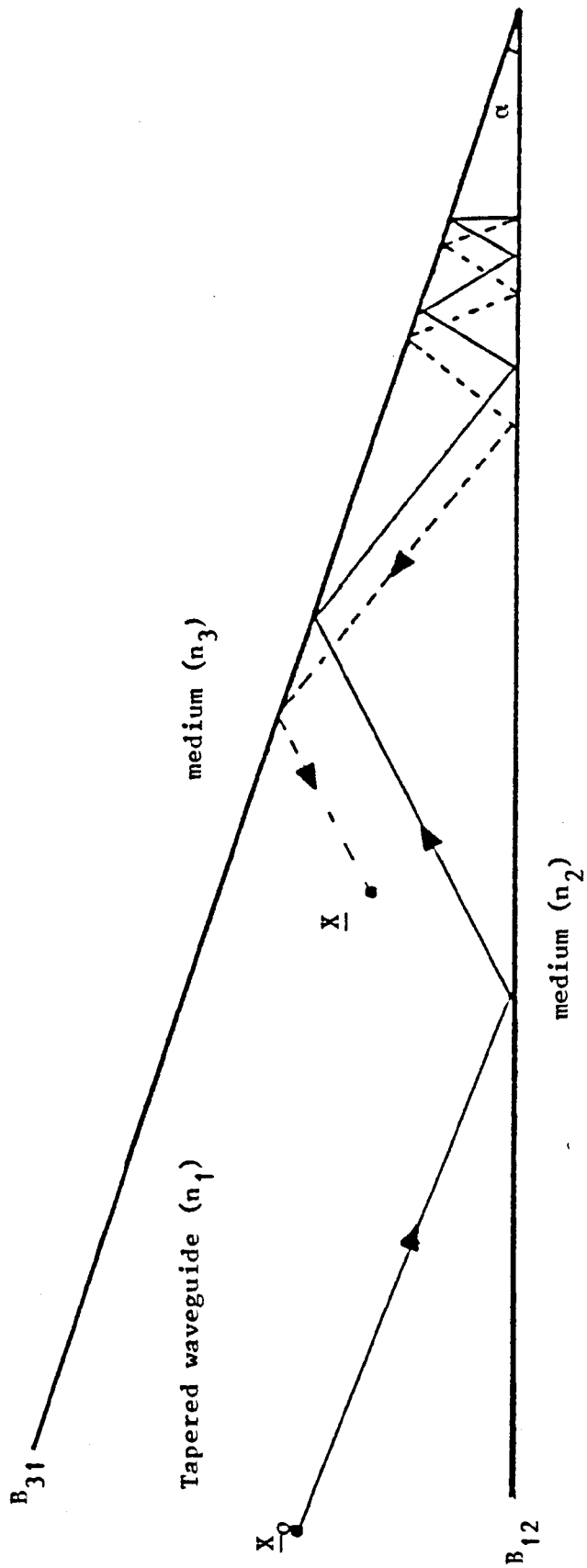


Fig.3.6 : A ray which reaches \underline{X} after reversal of its direction of propagation undergoes many partial reflections and carries small amplitude when it reaches \underline{X}

$$\sum_{m=1}^M [G_e^u(\theta, \theta_o) + G_o^u(\theta, \theta_o)] = \frac{1}{2} [G_e^u(\theta_o, \theta_o) + G_o^u(\theta_o, \theta_o) + G_e^u(\theta_M, \theta_o) + G_o^u(\theta_M, \theta_o)] + \frac{1}{2\alpha} \sum_{q=-\infty}^{+\infty} \int_{\theta_o}^{\theta_M} [G_e^u(\theta, \theta_o) + G_o^u(\theta, \theta_o)] \exp(-2 i \pi m q) d\theta \quad (3.16a)$$

Similarly for the downgoing waves' contribution :

$$\sum_{m=1}^M [G_e^d(\theta, \theta_o) + G_o^d(\theta, \theta_o)] = \frac{1}{2} [G_e^d(\theta_o, \theta_o) + G_o^d(\theta_o, \theta_o) + G_e^d(\theta_M, \theta_o) + G_o^d(\theta_M, \theta_o)] + \frac{1}{2\alpha} \sum_{q=-\infty}^{+\infty} \int_{\theta_o}^{\theta_M} [G_e^d(\theta, \theta_o) + G_o^d(\theta, \theta_o)] \exp(-2 i \pi m q) d\theta \quad (3.16b)$$

In both equations (3.16a) and (3.16b), q is an integer introduced as a consequence of Poisson summation; it characterises physically the mode that propagates along the tapered waveguide. The incident angle θ_o is the equivalent incident angle corresponding to the first reflection ($m = 1$) at B_{12} interface; as for the angle θ_M , it is the incident angle reached when the maximum ($m = M$) reflections occur at B_{12} interface. We recall that the mapping of m into θ is already given by expressions (3.7).

A further integration along the contour (C) in the θ_o -plane lying from $+i\infty$ to $-i\infty$ in (3.5) and (3.10), requires an extra integral sign in both terms of equations (3.16a) and (3.16b).

Combination of (3.2), (3.5), (3.10) and (3.16) leads to the final expression of the field distribution at an observation point \underline{X} :

$$\begin{aligned}
g(\underline{X}, \underline{X}_0) &= g^o(\underline{X}, \underline{X}_0) + \frac{1}{2} [g_1^u(\underline{X}, \underline{X}_0) + g_2^u(\underline{X}, \underline{X}_0) + g_1^d(\underline{X}, \underline{X}_0) \\
&\quad + g_2^d(\underline{X}, \underline{X}_0)] + \frac{i}{4\pi} \sum_{q=-\infty}^{+\infty} [g_e^u(\underline{X}, \underline{X}_0) + g_o^u(\underline{X}, \underline{X}_0) \\
&\quad + g_e^d(\underline{X}, \underline{X}_0) + g_o^d(\underline{X}, \underline{X}_0)] \tag{3.17a}
\end{aligned}$$

$g^o(\underline{X}, \underline{X}_0)$ is defined by equation (3.2). We also define :

$$g_1^u(\underline{X}, \underline{X}_0) = \frac{i}{4\pi} \int_C [G_e^u(\theta_o, \theta_o) + G_o^u(\theta_o, \theta_o)] \tag{3.17b}$$

$$g_2^u(\underline{X}, \underline{X}_0) = \frac{i}{4\pi} \int_C [G_e^u(\theta_M, \theta_o) + G_o^u(\theta_M, \theta_o)] \tag{3.17c}$$

$$g_1^d(\underline{X}, \underline{X}_0) = \frac{i}{4\pi} \int_C [G_e^d(\theta_o, \theta_o) + G_o^d(\theta_o, \theta_o)] \tag{3.17d}$$

$$g_2^d(\underline{X}, \underline{X}_0) = \frac{i}{4\pi} \int_C [G_e^d(\theta_M, \theta_o) + G_o^d(\theta_M, \theta_o)] \tag{3.17e}$$

Where $G_e^u(\theta_m, \theta_o)$, $G_o^u(\theta_m, \theta_o)$, $G_e^d(\theta_m, \theta_o)$ and $G_o^d(\theta_m, \theta_o)$ are defined in (3.3) and (3.11) respectively.

The other quantities in (3.17a) are given by :

$$g_e^u(\underline{X}, \underline{X}_0) = \frac{1}{2\alpha} \int_C \int_{\theta_o}^{\theta_M} \exp[i k S_e^u(\theta, \theta_o)] d\theta_o d\theta \tag{3.18a}$$

$$g_o^u(\underline{X}, \underline{X}_0) = \frac{1}{2\alpha} \int_C \int_{\theta_o}^{\theta_M} \exp[i k S_o^u(\theta, \theta_o)] d\theta_o d\theta \tag{3.18b}$$

$$g_e^d(\underline{X}, \underline{X}_0) = \frac{1}{2\alpha} \int_C \int_{\theta_o}^{\theta_M} \exp[i k S_e^d(\theta, \theta_o)] d\theta_o d\theta \tag{3.18c}$$

$$g_o^d(\underline{X}, \underline{X}_0) = \frac{1}{2\alpha} \int_C \int_{\theta_o}^{\theta_M} \exp[i k S_o^d(\theta, \theta_o)] d\theta_o d\theta \tag{3.18d}$$

The phase functions of the integrands in (3.18) are defined as follows :

$$k S_e^u(\theta, \theta_o) = k S_c(\theta, \theta_o) + \frac{1}{2} \phi(\theta) + k r_o \cos(\theta_o - \alpha - \chi_o) - k r \cos(\theta + \alpha - \chi) \quad (3.19a)$$

$$k S_o^u(\theta, \theta_o) = k S_c(\theta, \theta_o) - \frac{1}{2} \phi(\theta) + k r_o \cos(\theta_o - \alpha - \chi_o) - k r \cos(\theta - \alpha + \chi) \quad (3.19b)$$

$$k S_e^d(\theta, \theta_o) = k S_c(\theta, \theta_o) + \frac{1}{2} \phi(\theta) + k r_o \cos(\theta_o - \alpha + \chi_o) - k r \cos(\theta + \alpha + \chi) \quad (3.19c)$$

$$k S_o^d(\theta, \theta_o) = k S_c(\theta, \theta_o) + \frac{1}{2} \phi(\theta) + k r_o \cos(\theta_o - \alpha + \chi_o) - k r \cos(\theta + \alpha - \chi) - \pi \quad (3.19d)$$

Setting :

$$k S_c(\theta, \theta_o) = \frac{1}{2} \phi(\theta_o) - \frac{1}{2\alpha} \int_{\theta_c}^{\theta} \phi(\theta') d\theta' + \frac{1}{2\alpha} \int_{\theta_c}^{\theta} \phi(\theta') d\theta' + \pi (1-2q) \frac{(\theta - \theta_o)}{2\alpha} + \pi (1-2q) \quad (3.19e)$$

It is numerically anticipated that $g^o(\underline{X}, \underline{X}_o)$, $g_1^u(\underline{X}, \underline{X}_o)$, $g_2^u(\underline{X}, \underline{X}_o)$, $g_1^d(\underline{X}, \underline{X}_o)$ and $g_2^d(\underline{X}, \underline{X}_o)$ are very small compared to the sum in (3.17a). Therefore, we shall neglect all those small contributions in (3.17a)

and only contributions due to the double integrals will be considered in (3.17a). The reason is mainly due to the fact that, when expanding asymptotically any expression from (3.17b) to (3.17e), they exhibit an algebraic decay which, for an observation point \underline{X} sufficiently far from the source \underline{X}_0 , becomes vanishingly small.

In order to simplify the analysis, the phase functions in (3.19) can further be expressed by expanding each phase in terms of $\alpha + \chi_0$, $\alpha - \chi_0$ and $\alpha - \chi$ when appropriate, about the point zero.

Fixing the source point at $\underline{X}_0 \equiv (\chi_0, r_0)$, we obtain the final expressions of the phase functions corresponding to each species of waves :

$$k S_e^u(\theta, \theta_0) = \left\{ \alpha^{-1} Q(\chi_0, \theta_0) - \frac{\partial Q}{\partial \theta_0}(\chi_0, \theta_0) + r_0 \chi_0 k \sin \theta_0 \right\} \\ - \left\{ \alpha^{-1} Q(\chi, \theta) + \frac{\partial Q}{\partial \theta}(\chi, \theta) + r \chi k \sin \theta \right\} \quad (3.20a)$$

$$k S_o^u(\theta, \theta_0) = \left\{ \alpha^{-1} Q(\chi_0, \theta_0) - \frac{\partial Q}{\partial \theta_0}(\chi_0, \theta_0) + r_0 \chi_0 k \sin \theta_0 \right\} \\ - \left\{ \alpha^{-1} Q(\chi, \theta) - \frac{\partial Q}{\partial \theta}(\chi, \theta) - r \chi k \sin \theta \right\} \\ - \pi(2q-1) \quad (3.20b)$$

$$k S_e^d(\theta, \theta_0) = \left\{ \alpha^{-1} Q(\chi_0, \theta_0) - \frac{\partial Q}{\partial \theta_0}(\chi_0, \theta_0) - r_0 \chi_0 k \sin \theta_0 \right\} \\ - \left\{ \alpha^{-1} Q(\chi, \theta) + \frac{\partial Q}{\partial \theta}(\chi, \theta) - r \chi k \sin \theta \right\} \quad (3.20c)$$

$$\begin{aligned}
k S_o^d(\theta, \theta_o) &= \left\{ \alpha^{-1} Q(x_o, \theta_o) - \frac{\partial Q}{\partial \theta} (x_o, \theta_o) - r_o x_o k \sin \theta_o \right\} \\
&\quad - \left\{ \alpha^{-1} Q(x, \theta) + \frac{\partial Q}{\partial \theta} (x, \theta) + r x k \sin \theta \right\} \\
&\quad - \pi(2q-1)
\end{aligned} \tag{3.20d}$$

Where the function $Q(x, \theta)$ is defined as :

$$Q(x, \theta) = \alpha k r \cos \theta - \frac{1}{2} \int_{\theta_c}^{\theta} \phi(\theta') d\theta' + \pi \theta (q - \frac{1}{2}) \tag{3.21}$$

3.7. Assessment of the local eigenvalue equation

In order to evaluate the double integral of equations (3.18), approximate techniques such as the saddle point method must be sought. For that, the inverse of the wedge angle α will be taken as the large parameter.

Because of the double integral of (3.18), two saddle points need to be taken into account. They are θ_{oq} which characterises the saddle point at the source point \underline{x}_o and is itself fixed; and θ_q which is the saddle point at any observation point \underline{x} which is defined by the co-ordinates (x, θ) .

By taking the leading terms in α^{-1} only, in equations (3.20), the saddle points θ_{oq} and θ_q are defined by :

$$\frac{\partial Q}{\partial \theta_o} (x_o, \theta_{oq}) = 0 \tag{3.22}$$

$$\frac{\partial Q}{\partial \theta} (x, \theta_q) = 0 \tag{3.23}$$

Where the function $Q(\chi, \theta)$ is already defined in (3.21).

Inserting (3.21) into (3.22) and (3.23), leads to the local characteristic equations that define θ_{oq} and θ_q respectively.

They are :

$$2 r_o \alpha k \sin \theta_{oq} + \phi(\theta_{oq}) - \pi (2q-1) = 0 \quad (3.24a)$$

$$2 r \alpha k \sin \theta_q + \phi(\theta_q) - \pi (2q-1) = 0 \quad (3.24b)$$

Equations (3.24) are identified as the eigenvalue equations, characterising locally the tapered waveguide at a width $r_o \alpha$ and $r \alpha$ respectively.

The terms $r_o \alpha$ and $r \alpha$ are the local thicknesses of the tapered waveguide ($r_o \alpha = T_o$, $r \alpha = T$), which locally position the source and the observation point respectively, along the tapered waveguide.

As the thickness T ($T = r \alpha$) is reduced, the saddle point θ_q increases until it reaches a critical angle θ_c ($\theta_c = \text{Arccos } n_2/n_1$) where n_1, n_2 are the indices of the media on either side of interface B_{12} . If we express $Q(\chi, \theta)$ in (3.21) in terms of $\theta - \theta_c$ near $\theta = \theta_c$; there appears a term in $(\theta - \theta_c)^{\frac{1}{2}}$ which states that θ_c is a branch point for $Q(\chi, \theta)$ and hence, for all phases of equations (3.20) (in the single layer case only).

Because of the analytical similarity between (3.24a) and (3.24b), only equation (3.24b) will be of interest in the following treatment. The quantity $\phi(\theta)$ which is the phase of the reflection coefficient, introduced at interface B_{12} of the tapered waveguide; can be derived from the Fresnel equation in the case of the single layer structure, which is :

$$\phi(\theta) = 2 \operatorname{Atan} i \frac{n_2 \sin \theta''}{n_1 \sin \theta} \quad (3.25)$$

Where θ and θ'' are respectively, the incident and refracted angle on either side of boundary B_{12} . n_1 and n_2 are the refractive indices of their respective media.

In the case of the double layer structure, $\phi(\theta)$ is given by Appendix D.

Either case of $\phi(\theta)$, substituted into (3.24b), leads exactly to the eigenvalue equations (2.11) and (2.18) respectively; already computed and discussed in section 2.4 of Chapter 2, using a completely different treatment. In section 2.4, the eigenvalue equations have been discussed mainly in terms of the normalised propagation constant $(\frac{\beta}{k_0})$ versus the normalised thickness $k_0 T$. We recall that, according to Fig.3.1, the polar coordinate r of the observation point $\underline{X} \equiv (\chi, r)$ is related to the local thickness T of the tapered waveguide by the approximation $T = r\alpha$ as long as the wedge angle α is small.

Here, the solution of (3.24b), representing the saddle point θ_q for different positions of the observation point (for different value of T), is taken as the inverse cosine of the computed $(\frac{\beta}{k_0})$ in section 2.4.

In the case of the double layer structure, the saddle points θ_q of interest are real in the guided wave region ($\theta_q < \theta_c$) as well as in the coupled wave region ($\theta_q > \theta_c$), by the nature of the characteristic equation (2.18).

In the case of the single layer structure however, the solutions θ_q are real only in the guided wave region ($\theta_q < \theta_c$), becoming complex with negative imaginary part in the leaky wave region

(Real $(\theta_q) > \theta_c$). As a matter of fact, when the saddle point θ_q transits from the guided wave region to the leaky wave region, it is necessary to declare which branch in $(\theta - \theta_c)^{\frac{1}{2}}$ to take. In order to obtain decaying waves in the leaky wave region [for an $\exp(-i \omega t)$ time convention] one chooses $(\theta - \theta_c)^{\frac{1}{2}}$ to remain in a single Riemann Sheet, any time the branch point θ_c is crossed. This has been predicted in the computation of (2.11) and plotted in Fig.2.6 in Chapter 2. Thereby, we notice that the negative imaginary part of solutions θ_q implies that the waves decay exponentially as a consequence of radiation loss as they propagate along the tapered waveguide. The waves that result are leaky.

3.8. Field analysis in different regions of the tapered waveguide

As the observation point \underline{X} moves along the tapered waveguide, there arise three cases when evaluating the asymptotic integrations in (3.18), depending on the location of the saddle point θ_q with respect to the critical angle θ_c .

3.8.1. Guided wave region

The saddle points θ_q and θ_{oq} are chosen in the interval $\theta_{oq} < \theta_q < \theta_c$. In such a region, the two saddle points do not lie near the critical angle θ_c . Each integral of equations (3.18) can be estimated using the method of saddle point.

Applying Appendix B to each species of waves described by (3.18) and recalling (3.17a) leads to the total field approximation in the guided wave region :

$$g(\underline{X}, \underline{X}_o) = i \sum_{q=-\infty}^{+\infty} Y(\chi, \theta_q) Y(\chi_o, \theta_{oq}) \quad (3.26)$$

where

$$Y(\chi, \theta_q) = A(\chi, \theta_q) \sin(r \chi k \sin \theta_q) \exp[-i \alpha^{-1} Q(\chi, \theta_q)] \quad (3.27a)$$

$$Y(\chi_o, \theta_{oq}) = A(\chi_o, \theta_{oq}) \sin(r_o \chi_o k \sin \theta_{oq}) \exp[i \alpha^{-1} Q(\chi_o, \theta_{oq})] \quad (3.27b)$$

The coefficient $A(\chi, \theta)$ is defined in Appendix B and is given by :

$$A(\chi, \theta) = \left\{ k r \alpha \cos \theta + \frac{1}{2} \frac{\partial \phi}{\partial \theta}(\theta) \right\} \quad (3.28)$$

The function $Q(\chi, \theta)$ is defined in (3.21). A close look at (3.26) reveals that the dominant contribution of the field in the guided wave region is represented by a sum of products. One factor depends on the saddle point θ_{oq} at the source \underline{X}_o , and the other on the saddle point θ_q at the observation point \underline{X} .

Equations (3.27) define the so-called adiabatic mode, a field which is characterised by a χ -dependent amplitude and an r -dependent phase.

The adiabatic mode so defined, propagates locally and adapts smoothly to the configuration of the tapered waveguide, in a manner that renders coupling to other modes insignificant.

Each adiabatic mode propagates locally with a local longitudinal propagation constant β , defined here as :

$$\beta = \frac{1}{\alpha} \frac{\partial Q}{\partial r}(\chi, \theta_q) = k \cos \theta_q \quad (3.29a)$$

where $Q(\chi, \theta)$ is given by (3.21).

The local transverse propagation constant will be :

$$\gamma_1 = (k^2 - \beta^2)^{\frac{1}{2}} = k \sin \theta_q \quad (3.29b)$$

Both propagation constants β and γ_1 , characterise the local adiabatic mode propagation at a saddle point θ_q , located by the polar co-ordinates (χ, r) . We notice that β and γ_1 in (3.29), take the values corresponding to a uniform waveguide of width T ($T = r\alpha$) of the tapered waveguide at the saddle point θ_q .

The smallest value of β in this range ($\theta_{oq} < \theta_q < \theta_c$), coincides with the critical angle when $\theta_q = \theta_c$; whereas the largest value of β results in a physical conception of total internal reflection of the guiding mechanism of the adiabatic mode. Such a maximum value of β in this range, coincides with the saddle point $\theta_q = \theta_{oq}$.

We recall the expressions of β and γ_1 in (3.29), which have already been introduced in Chapter 2 via a different approach. The computation of the adiabatic mode at the observation point in (3.27a), will appear in the next chapter, when it will be compared and discussed with another type of newly constructed mode, which is more systematic than the adiabatic mode concept.

3.8.2. Transition region

In this region, the saddle point θ_q is approximately equal to the critical angle θ_c . The saddle point θ_{oq} is still maintained fixed and is lower than both θ_q and θ_c . Mathematically, such a transition region represents the region where the adiabatic mode becomes cut-off. Applying the results of (C.7) and (C.9) of Appendix C into equation (3.17a), the total field contribution of each species of waves in the transition region, where $\theta_q \cong \theta_c$, will be :

$$g(\underline{X}, \underline{X}_0) = i \sum_{q=-\infty}^{+\infty} Y(\chi_0, \theta_{oq}) W(\chi, \theta_c) \quad (3.30)$$

where

$$W(\chi, \theta_c) = F(Z) \sin(r \chi k \sin \theta_c) \exp[-i \alpha^{-1} Q(\chi, \theta_c)] \quad (3.31a)$$

$Y(\chi_o, \theta_{oq})$ and $Q(\chi, \theta)$ are given respectively by (3.27b) and (3.21).

Substitution of Q_1 in (C.11a), into (C.8) in Appendix C; leads to the expression of $F(Z)$, given by :

$$F(Z) = 2 (2 \pi i \alpha)^{-\frac{1}{2}} \Delta^{-2/3} L \quad (3.31b)$$

where Δ and Z are respectively given by (C.10a) and (C.10c). As for L , it is given in terms of Airy's function [23] by :

$$\begin{aligned} L &= \int_{-\infty}^{\infty} e^{i 2 \pi / 3 t} \exp(-t^2 Z \Delta^{-2/3}) \exp(-\frac{t^3}{3}) dt \\ &= -2 \pi \exp[2 i (Z \Delta^{-2/3})^3 / 3] \exp(-i \pi / 3) \\ &\quad \times [Ai'(\epsilon) + e^{i \frac{\pi}{6}} 2 \Delta^{-\frac{2}{3}} Ai(\epsilon)] \end{aligned} \quad (3.31c)$$

With

$$\epsilon = e^{i \frac{\pi}{3}} (Z \Delta^{-\frac{2}{3}})^2 \quad (3.31d)$$

The equations (3.31) make it clear that $W(\chi, \theta_c)$ represents the variation of a local mode, where the saddle point θ_q is near the branch point θ_c . The function $F(Z)$ agrees with a result found by Pierce [21], where he analyses by a different method the sound wave propagation in shallow ocean water at a similar transition region. Though the problem elaborated by Pierce may not be exactly the same as the tapered waveguide in integrated optics, it is mathematically similar in nature, in so far as both cases are concerned with a non-separable problem.

3.8.3. Radiation region

In this region, the saddle point θ_q and critical angle θ_c are no longer confluent. The saddle point θ_q moves around the branch point θ_c to become complex in the case of the single layer problem, but remains real in the case of the double layer problem. In such cases, the critical angle θ_c lies in the interval $\theta_{oq} < \theta_c < \text{Real}(\theta_q)$. An additional branch cut integral needs to be added to the saddle point θ_q contribution. The branch cut integral added to each integral of (3.18), accounts for the lateral waves launched in a region past the critical angle.

Inserting the result (C.12) of Appendix C into equation (3.17a), leads to the total approximated field distribution in a region where $\theta_{oq} < \theta_c < \text{Real}(\theta_q)$, given by :

$$g(\underline{x}, \underline{x}_o) = i \int_{q=-\infty}^{+\infty} Y(\chi_o, \theta_{oq}) \left\{ Y(\chi, \theta_q) + V(\chi, \theta_c) \right\} \quad (3.32a)$$

where $Y(\chi_o, \theta_{oq})$ and $Y(\chi, \theta_q)$ are defined in (3.27); and $V(\chi, \theta_c)$ by :

$$V(\chi, \theta_c) = B(\chi, \theta_c) \sin(k r \chi \sin \theta_c) \exp[-i \alpha^{-1} Q(\chi, \theta_c)] \quad (3.32b)$$

The coefficient $B(\chi, \theta_c)$ and $Q(\chi, \theta_c)$ are given by (C.14) and (3.21) respectively.

The first term in (3.32a) represents the contribution of the adiabatic mode as elaborated in subsection 3.8.1; and the second term accounts for the lateral waves. By inspecting $V(\chi, \theta_c)$ in (3.32b), we notice that it contains a term in $\eta^{-\frac{5}{2}}$, which assesses the algebraic decay of the lateral waves as the observation point \underline{x} moves along the tapered guide towards the apex. Such a term is also in agreement with the result of Pierce [21] in a region past the transition region.

CHAPTER FOUR

INTRINSIC SPECTRAL INTEGRAL

4.1. Definition of the Intrinsic Field

In Chapter 3, the wave tracking formulation allowed us to describe analytically the mode propagation inside the tapered waveguide only. However, owing to the non-existence of the Adiabatic mode past the transition region, the Adiabatic representation only holds in a limited region.

In order to describe the modal field distribution inside the tapered waveguide in all regions with respect to the transition layer; a systematic method is formulated in this chapter. For this, the concept of an 'Intrinsic mode' is introduced, which physically represents an Intrinsic field that satisfies local continuity of the boundary values at the top and bottom interfaces of the tapered waveguide, and is itself a plane wave spectrum [39,40].

Once the Intrinsic field approach is adopted, one is able to analyse the tapered waveguide, not only in the inside, but also outside the wedge, both before and after the transition region.

As will be shown later, the Intrinsic field has properties similar to the Adiabatic field defined in subsection 3.8.1, but it is a more general concept.

4.1.1. Construction of the Spectral Intrinsic Integral

For a suitable contour of integration (C) in the complex θ -plane, an integral $I(\chi, \theta)$ is defined as follows :

$$I(\chi, \theta) = (2 \alpha)^{-\frac{1}{2}} \int_C \exp[i k S(\chi, \theta)] d\theta \quad (4.1)$$

Physically, (4.1) describes a local mode, generated by integration over an angular plane wave spectrum. Such a source-free mode (labelled q) is defined at an observation point \underline{X} and propagates smoothly along the tapered waveguide, with a wave number k . Its characteristic invariant q is maintained during the propagation both before and after the transition region.

In (4.1) θ still remains the incident angle of plane waves with respect to the bottom boundary of the tapered waveguide. The phase function $k S(\chi, \theta)$ in (4.1) could be any phase among the four species introduced in Chapter 3; and which are given by equations (3.19). In this case, the constructed plane wave spectrum (4.1) maintains itself self-consistently with no effect from the source.

The contour (C) could be any arbitrary contour in the complex θ -plane, as long as convergence of (4.1) is guaranteed. See Fig.4.1, whereby the contour (C) can be deformed into 2 separate contours (C') and (C''). The latter is such that $0 < \text{Real}(\theta) < \frac{\pi}{2}$ and the former, $\frac{\pi}{2} < \text{Real}(\theta) < \pi$. As it has been mentioned earlier in section 3.5 and as will be rigorously proved in the next chapter, all plane waves having incident angle $\theta > \frac{\pi}{2}$ (as depicted in Fig.3.6), have their direction of propagation reversed and travel away from the apex. Such rays

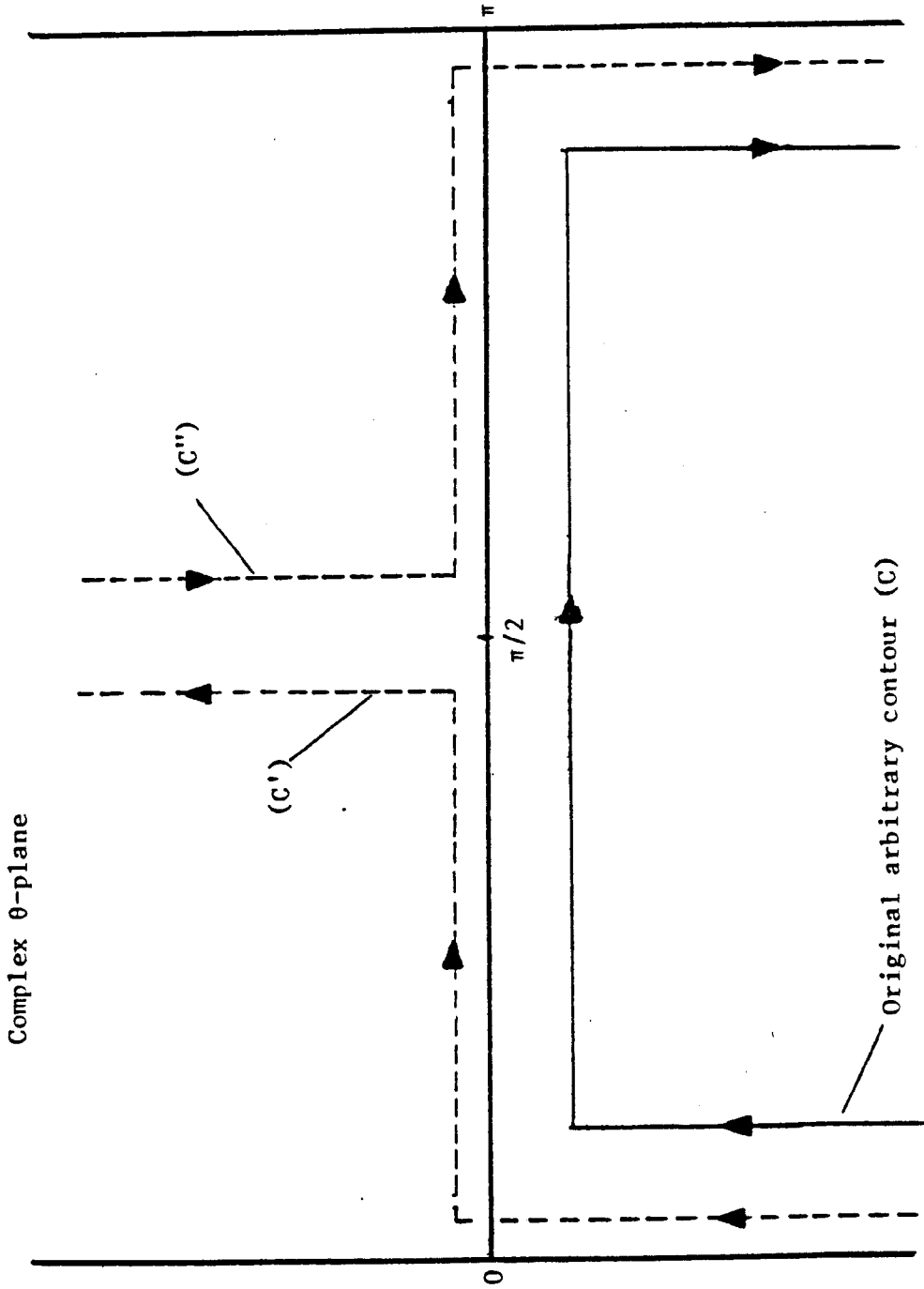


Fig.4.1 : Construction of the contour of integration from the original arbitrary contour in the complex θ -plane

are safely neglected since they carry very small amplitude due to the loss of power incurred in multiple reflection. For this reason, the contour (C'') can be ignored too; and the contour (C') as depicted in Fig.4.1 maintains its dominant contribution to the integral (4.1). In this sense, any integration of (4.1) along (C) will be reduced to an integration along (C').

An asymptotic evaluation of (4.1) by the saddle point method leads to an integration once again along another deformed contour, along a steepest descent path (SDP), related to the phase $S(\chi, \theta)$ and which will be computationally investigated later on. In addition, the presence of any singularity in the integrand of (4.1) may have to be taken into consideration.

The integral in (4.1) may be evaluated by Cauchy's theorem [36], as follows :

$$\int_{C'} = \int_{SDP} + \int_{BRANCH\ CUT} + \text{POLES CONTRIBUTION} \quad (4.2a)$$

As long as there is no pole involved (at least, as far as the single layer problem is concerned) one is left with

$$\int_{C'} = \int_{SDP} + \int_{BRANCH\ CUT} \quad (4.2b)$$

The branch cut integral exhibited in here, contributes to the asymptotic solution only if the singularity θ_c is crossed during the deformation of the contour (C') into the steepest descent path (SDP).

The deformation of (C') into the SDP is performed as desired on a single Riemann sheet. The tracking of the saddle point around the singularity θ_c is accomplished in compatibility

with the above requirement only if proper account of all branches is taken in the computer program.

4.1.2. Identification of the lateral waves

When the saddle point θ_q (which makes the dominant contribution to the integral $I(\chi, \theta)$) lies near the branch point of the phase function (which is to be defined later), it identifies departure directions of laterally shifted rays. These transitions give rise in physical space to excitation of lateral waves, a phenomenon well explored for a single bottom reflection, at a single interface between 2 half-spaces [34].

However, the problem here is much more complicated, because at the transition region the lateral wave itself undergoes multiple reflection between two non-parallel boundaries. Consequently, when the saddle point θ_q moves beyond θ_c , a branch cut integral must be added to the analytically continued saddle point approximation, as stated in (4.2b). The saddle point contribution retains its interpretation as a local mode, which is now leaky; and the branch cut contribution is interpreted as a lateral wave (by analogy to the lateral wave introduced in subsection 3.8.3), excited at the critical transition region.

Physically, the lateral wave corresponds to a shift, which manifests itself in a reflected ray which is laterally shifted; such a shift indicates that the light penetrates to a depth into the bottom adjacent medium, before it is reflected. This phenomenon, called the Goos-Hanschen shift [37] and occurring near the transition region, has turned out to be an important element in integrated optics, in the understanding of the flow of energy.

4.1.3. Elaboration of the phase function for the Intrinsic Integral

Among the four species of waves elaborated in Chapter 3, we consider only two spectra so that each plane wave in one species, reflects into the corresponding plane wave in the other, with the appropriate Fresnel reflection coefficient at the bottom boundary of the tapered waveguide. In this case, those two spectra are undoubtedly self-consistent.

Applying (4.1) to those two categories of waves, after deforming the contour (C') into a steepest descent path (SDP) contour, gives :

$$I_e^u(\chi, \theta) = (2 \alpha)^{-\frac{1}{2}} \int_{SDP} \exp[i k S_e^u(\theta, \theta_0)] d\theta \quad (4.3a)$$

$$I_o^u(\chi, \theta) = (2 \alpha)^{-\frac{1}{2}} \int_{SDP} \exp[i k S_o^u(\theta, \theta_0)] d\theta \quad (4.3b)$$

The assumption that the plane wave spectrum (4.1) is source-free, is equivalent to removing source-dependent terms in the phase expression $S_e^u(\theta, \theta_0)$ and $S_o^u(\theta, \theta_0)$, depending on the polar co-ordinates (r_0, χ_0, θ_0) , as given by (3.19a) and (3.19b) for the two species of waves specified above. Combining the contribution of those two types of waves, the corresponding Intrinsic integral I consists of summing up the two expressions in (4.3), which gives :

$$I(\chi, \theta) = I_e^u(\chi, \theta) + I_o^u(\chi, \theta) \quad (4.3c)$$

By making use of (3.19) and (4.3), the total Intrinsic field at an observation point \underline{X} will, be after omitting the source terms :

$$I(\chi, \theta) = (2 \alpha)^{-\frac{1}{2}} \int_{SDP} 2 \cos[k r \sin \theta \sin(\chi - \alpha) - \frac{\phi(\theta)}{2}] \exp[-i \alpha^{-1} Q(\chi, \theta)] d\theta \quad (4.4)$$

(4.4) describes then the field inside the tapered waveguide, characterised by its wave number k . The coefficient $Q(\chi, \theta)$ is defined in expression (3.21); and χ, r are the polar co-ordinates of any observation point \underline{X} with respect to the wedge angle α , as shown in Fig.3.1.

Further analysis and computation of the Intrinsic Integral (4.4), is accomplished by appropriately substituting the right expression of the phase change $\phi(\theta)$, introduced at the bottom interface of the tapered waveguide. $\phi(\theta)$ is involved directly in the integrand of (4.4) and also through $Q(\chi, \theta)$. We recall that for the single layer problem, $\phi(\theta)$ is derived straightaway from the Fresnel's equation which states :

$$\phi(\theta) = 2 \operatorname{Atan} \left(\frac{i n_2}{n_1} \frac{\sin \theta''}{\sin \theta} \right) \quad (4.5)$$

Where n_1, n_2 are the refractive indices of the tapered waveguide and the adjacent bottom media (n_2) respectively. θ'' is the refracted angle in medium (n_2). The incident angle θ is related to θ'' via Snell's law which is :

$$n_1 \sin \theta = n_2 \sin \theta'' \quad (4.6)$$

For the double layer problem, $\phi(\theta)$ is calculated in Appendix D.

The same process holds for the Adiabatic field, defined in subsection 3.8.1 by equation (3.27), which depends on the appropriate substitution of $\phi(\theta)$ via $Q(\chi, \theta)$.

4.2. Application of the Intrinsic Integral to the Single Layer Structure

After extracting the expression for the phase change $\phi(\theta)$ from the Fresnel's equation (4.5) and inserting it into (4.4), the Intrinsic Integral describing the mode propagation for the single layer problem is complete. Depending on the location of the observation point \underline{X} (or saddle point θ_q), two regions can be analysed. The guided wave region is defined by all observation points \underline{X} such that $\theta_q < \theta_c$; in the leaky wave region, θ_q is located such that $\text{Real}(\theta_q) > \theta_c$.

4.2.1. Definition of branch point θ_c

We recall, that the existence of singularity θ_c ($\theta_c = \text{Arccos} \frac{n_2}{n_1}$), is essentially due to the branch point in $\phi(\theta)$ at the bottom interface of the tapered waveguide, for critical incidence (when the wedge thickness T is near the critical region). This is accommodated by the fact that when one expands $\phi(\theta)$ in θ about θ_c there is a term like $(\theta - \theta_c)^{\frac{1}{2}}$ appearing. This clearly implies that θ_c is a branch point for $\phi(\theta)$, and hence for the phase function of (4.4) via $Q(\chi, \theta)$ as well. Consequently, crossing the branch point θ_c in the complex θ -plane must then be carefully monitored. For that, a branch cut convention needs to be defined so as to keep the expression $(\theta - \theta_c)^{\frac{1}{2}}$ constantly in a single Riemann sheet, and to guarantee the convergence of integral (4.4). We also require $\text{Imag}(\theta - \theta_c)^{\frac{1}{2}} \geq 0$, in order to obtain decaying wave amplitude, as θ_q moves along the tapered waveguide towards the apex in accordance with our time convention $\exp(-i \omega t)$.

It is worth mentioning at this point, that in the case of the double layer structure, $\phi(\theta)$ is defined in Appendix D. The

critical angle θ_c , which is defined earlier above, is not a branch point to $\phi(\theta)$, because of the mathematical nature of $\phi(\theta)$.

4.2.2. Location of saddle points and determination of the steepest descent path (SDP)

(a) Definition of SDP

Asymptotic evaluation of (4.4), by the steepest descent method, requires the exact location of the saddle point θ_q at an arbitrary local thickness T along the tapered waveguide, as well as the locus of the steepest descent path contour.

To investigate the saddle points of (4.4) it is necessary to find the zeros of the derivative of the phase of the integrand, $\frac{\partial Q}{\partial \theta}(\chi, \theta)$, in (4.4). Because the function $Q(\chi, \theta)$ is simply the θ -dependent part of the phase in (4.4), the equation obtained is identical to the characteristic equation (2.11), already introduced and computed in subsection 2.4.1.

Once the saddle point θ_q has been located, the burden of this integration lies in finding the steepest descent path (SDP) of the phase of the integrand function in (4.4). For a specified observation point, as well as for a given mode number, the steepest descent path (SDP) can be constructed via the following equations :

$$\text{Imag} [i S(\chi, \theta)] = \text{Imag} [i S(\chi, \theta_q)] \quad (4.6a)$$

or

$$\text{Real} [S(\chi, \theta)] = \text{Real} [S(\chi, \theta_q)] \quad (4.6b)$$

where $S(\chi, \theta)$ is any phase of the integrand function of equation (4.4).

Along the steepest descent path, the major contribution in the integral (4.4) is dominated by the angles in the vicinity of the saddle point θ_q .

The computer program which has been developed to implement the steepest descent path, consists mainly in determining first the saddle point θ_q at each observation point (at local thickness T and χ) then, using the Newton-Raphson method, having equations (4.6) satisfied.

Appendix E gives a brief flow chart of the computer program 'Saddle point - SDP', implemented to compute the SDP.

In addition, one has to declare clearly in the computer program the principal branch corresponding to different Riemann Sheets of all complex square roots involved in expression (4.6), because of the multiple valued function $\phi(\theta)$ indirectly involved in (4.6).

(b) Definition of branch cut contour

As we have introduced the SDP above, we can define similarly the branch cut contour, which is defined as follows :

$$\text{Real } [S(\chi, \theta)] = \text{Real } [S(\chi, \theta_c)] \quad (4.7)$$

where θ_c is the branch point corresponding to the transition region of the single layer structure. The computation of the branch cut is achieved in an exactly similar manner as done for the SDP, with the only difference that equation (4.6) which defines the SDP should be substituted by equation (4.7) which defines the branch cut contour.

Since the need for a branch cut integral arises only when

θ_q lies past the branch point θ_c , it will not be used in the integration of (4.4).

(c) Computational result

Fig.4.2 depicts the computation of the steepest descent path and the branch cut contour, for three different cases related to the position of the saddle point θ_q with respect to the branch point singularity θ_c .

The branch point is located at a local normalised critical thickness $k_0 T = 1.75$, for the first lowest mode.

Fig.4.2a corresponds to the SDP contour in the guided wave region. The saddle point θ_q is located at a local thickness $k_0 T = 10$. One notices that the SDP contour crosses the real axis at an angle $\frac{\pi}{4}$, which agrees with the theory of functions of complex variable in a region free of singularity. In such a region, the real saddle point θ_q denoted by the x sign in the figure is such that $\theta_q < \theta_c$. In this case, the contribution of integral (4.4) is dominated by the portion of the SDP near the saddle point.

The branch cut contour starting from the branch point θ_c , denoted by the ∇ sign in figure, does not contribute to the integration of (4.4), for in this region the SDP does not cross the branch point yet.

Fig.4.2b represents the SDP contour near the transition region at $k_0 T = 1.8$. The contour tends to surround the branch point θ_c . In this case, saddle point and branch point are confluent and further reduction of T will make the SDP cross θ_c . We then enter a new region known as the leaky wave region.

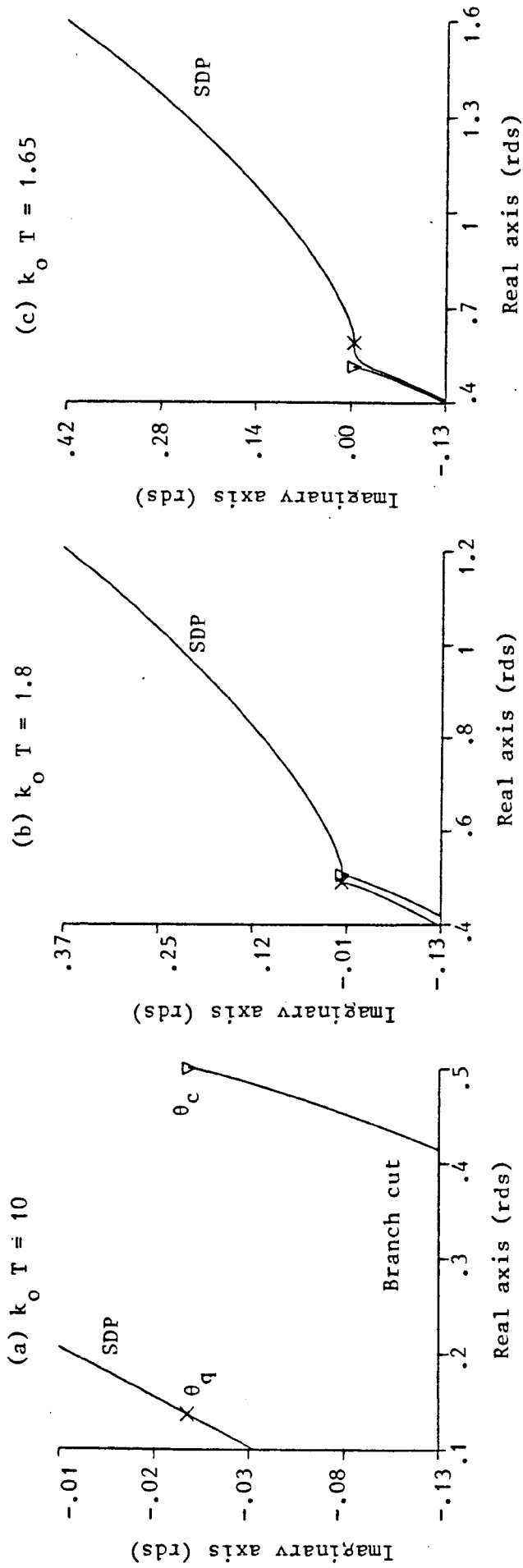


Fig.4.2. Plot in the complex θ -plane of the computed steepest descent path (SDP) and branch cut for Intrinsic Integral of the single layer structure. Three different positions of the observation point are considered : (a) Saddle point located in the guided wave region, (b) Saddle point located near transition region, (c) Saddle point located in the leaky wave region. The refractive indices in each medium are : $n_1 = 2$; $n_2 = 1.76$; $n_3 = 1$. Mode 1, normalised critical thickness = 1.75, $\chi = 0$ rds, $\alpha = 0.02$ rds. x Saddle point θ_q , ∇ Branch point θ_c .

Fig.4.2c corresponds to the SDP contour in the leaky wave region; which locates a saddle point θ_q beyond the branch point θ_c .

The saddle point θ_q is complex in this region, with a negative imaginary part. The local normalised thickness is $k_0 T = 1.65$. It is noticed from Fig.4.2c that the SDP crosses the line $\text{Real}(\theta) = \theta_c$; and it is continuous.

Besides, the branch cut contour is asymptotic to the lower part of the SDP. These are also standard properties of functions of complex variables, in a region beyond the singularity. In such a region, where $\text{Real}(\theta_q) > \theta_c$, the integration of (4.4) is theoretically supposed to be accomplished by the SDP method as well as the branch cut contribution. However, in practice it is difficult to separate the two contributions, and numerical problems arise. This is a major limitation of the saddle point method in the region beyond the singularity. In addition, in such a region it is computationally very difficult to pick up the SDP. For, in the vicinity of saddle point θ_q , the steepest descent path (SDP) and the steepest ascent path (SAP) are difficult to distinguish. The above complications may render the asymptotic evaluation of integral (4.4) impractical. Consequently, one may require direct numerical evaluation of (4.4). Those restrictions will be overcome by suggesting another simpler contour of integration for (4.4) which, as will be shown later, will be valid not only in the guided wave region, but also beyond any singularity.

For any observation point \underline{X} , specified by the polar co-ordinates (χ, r) (where $r = \frac{T}{\alpha}$), inside the tapered

waveguide, one expects the polar variable χ to be in the interval $0 < \chi < \alpha$, where α is the wedge angle. The computer plots of Fig.4.2 have all been carried out for $\chi = 0$ rds only, which corresponds to an observation point situated on the top interface B_{31} of the tapered waveguide, for the first mode $q = 1$. For other χ , as well as for higher modes, the contours obtained (though not represented) are qualitatively similar to the plotting of Fig.4.2, but different quantitatively. For as the mode number q increases, the critical thickness increases, as one can see from the plotting of eigenvalue equation (2.11) in Fig.2.6.

4.2.3. Intrinsic field in the guided wave region

As the Intrinsic field is analysed asymptotically in terms of the saddle point method, we recall that each observation point $\underline{X} \equiv (\chi, r)$ is characterised by the polar variable χ and the range r . To each thickness T ($T = r\alpha$) corresponds one and only one incidence angle (saddle point θ_q); we shall then represent each observation point \underline{X} either, by its co-ordinate $\underline{X} \equiv (\chi, \theta_q)$ or by $\underline{X} \equiv (\chi, r)$. In this sense, these two notations represent exactly the same point \underline{X} . We also recall that the saddle point θ_q , contributes dominantly to the integration of (4.4) when evaluated by the SDP method.

Thus, one analyses the intrinsic field of equation (4.4), as the observation point \underline{X} moves along the wedge towards the branch point θ_c (i.e. as the local thickness T diminishes).

In moving θ_q from one side of the branch point θ_c to the other, difficulties with branch cuts might be anticipated. These difficulties do not arise when θ_q is bound by the interval

$\theta_{oq} < \theta_q < \theta_c$, corresponding to the Adiabatic mode in the guided wave region as defined by equation (3.27); for the steepest descent path contours do not capture the branch point according to our convention for choosing branches.

The integral signs which are mathematically used to compute the SDP contour appear not only in the main integration (4.4); but also in the expression of the coefficient $Q(\chi, \theta)$, present in the integrand of (4.4) and which is given by equation (3.21). This double appearance of the integral sign complicates numerically the computation of (4.4). In order to systematically evaluate (4.4), a computer program is also developed in this chapter and consists of computing (4.4) simultaneously with the steepest descent path in (4.6). The integrals involved directly or indirectly in (4.4) and (4.6) are carried out by use of the Simpson-numerical method.

Appendix F gives a flow chart of the computer program 'Integration', developed to implement (4.4).

Figs.4.3 compare both the Intrinsic modes as introduced by equation (4.4) and the Adiabatic modes as defined analytically by (3.27), for the four lowest modes of the single layer structure.

For a given local normalised thickness $k_0 T$; Figs.4.3 represent the variation of the cross angle χ (in radians) of the mode across the tapered waveguide, versus the normalised modulus of the Adiabatic and Intrinsic modes. For simplicity and convenience, each mode has been normalised with respect to a constant. However, there is no representation of the phase of each mode, for there is no absolute reference for the phases.

As the purpose of this chapter is to describe the field

inside the tapered waveguide; the polar angle variation χ must be confined to the interval $0 \leq \chi \leq \alpha$, where α is the wedge angle of the tapered waveguide.

Three different locations of saddle point θ_q are depicted in each diagram of Figs.4.3, in relation to θ_c .

Dealing first with the lowest mode, Fig.4.3a considers three distinct locations of the saddle point corresponding to three different thicknesses as illustrated in each diagram.

(i) $k_0 T = 10$, locates the saddle point θ_q much smaller than the branch point θ_c (located at a normalised critical thickness $k_0 T = 1.75$). One notices the good agreement between both Intrinsic and Adiabatic fields.

(ii) $k_0 T = 5$, positions the saddle point fairly distant from θ_c ; yet still a good agreement is obtained between both fields.

(iii) $k_0 T = 1.8$, locates the saddle point θ_q near the transition region. The confluence of θ_q and θ_c restricts the comparison of both fields within 10%. This error margin is a serious discrepancy as compared to the wedge angle α .

One notices in Fig.4.3a that as the thickness T approaches the critical region, the amplitude of the waves increases.

The mode is bound inside the tapered waveguide, undergoing multiple reflection at each interface. Energy is confined within the inner structure of the tapered waveguide. Thus, there is no loss, for the saddle points are real in such a region. It is

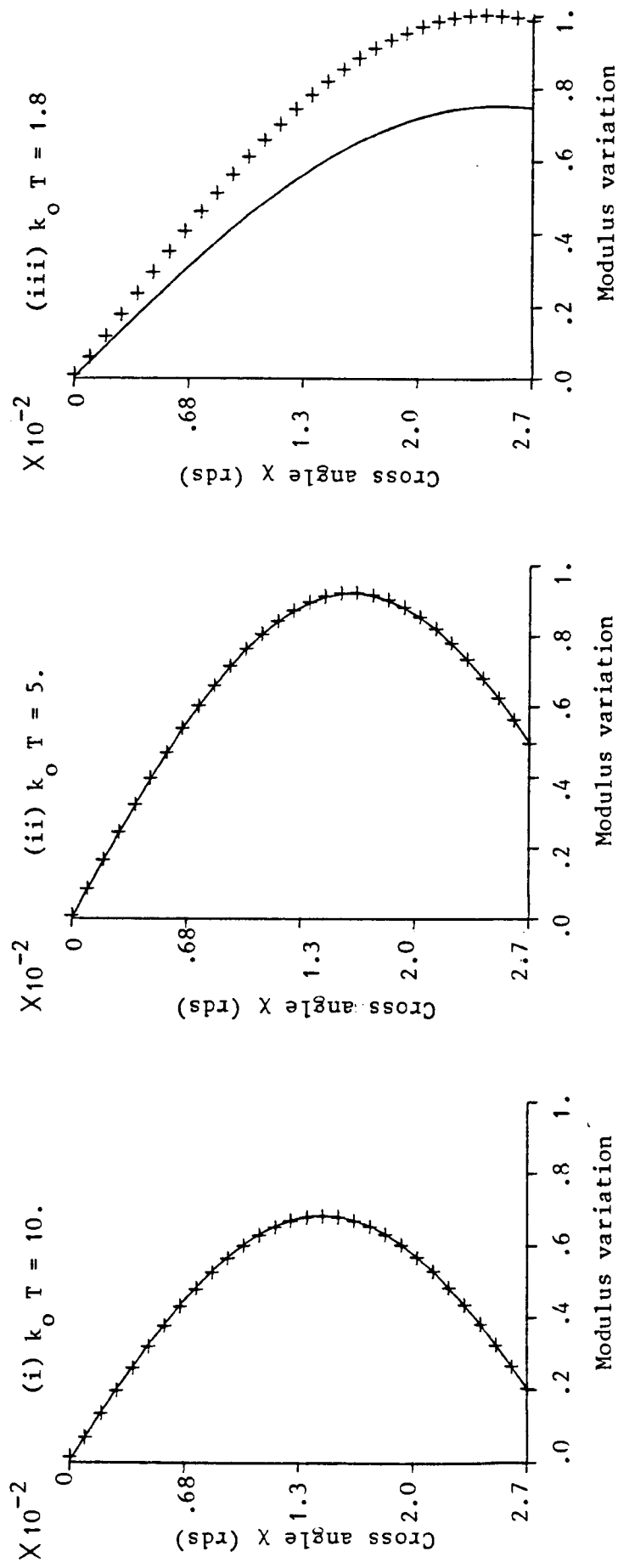


Fig.4.3a. Comparison of the normalised cross section Intrinsic and Adiabatic fields in the tapered waveguide, for the single layer structure. The saddle points in (i), (ii) and (iii) are located in the guided wave region. Mode 1, normalised critical thickness = 1.75, $\alpha = 0.027$ rds. The refractive indices in each medium are : $n_1 = 2$; $n_2 = 1.76$; $n_3 = 1$. + Intrinsic field, — Adiabatic field.

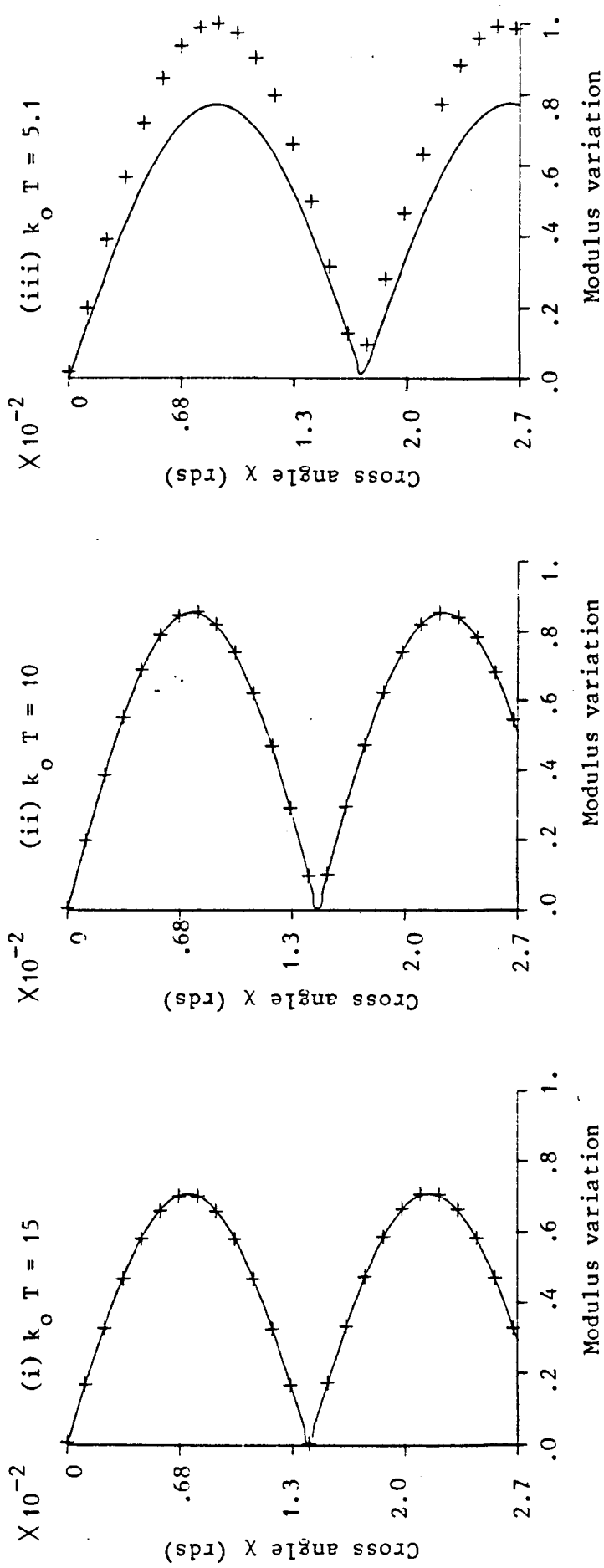


Fig.4.3b. Mode 2. Normalised critical thickness = 5.

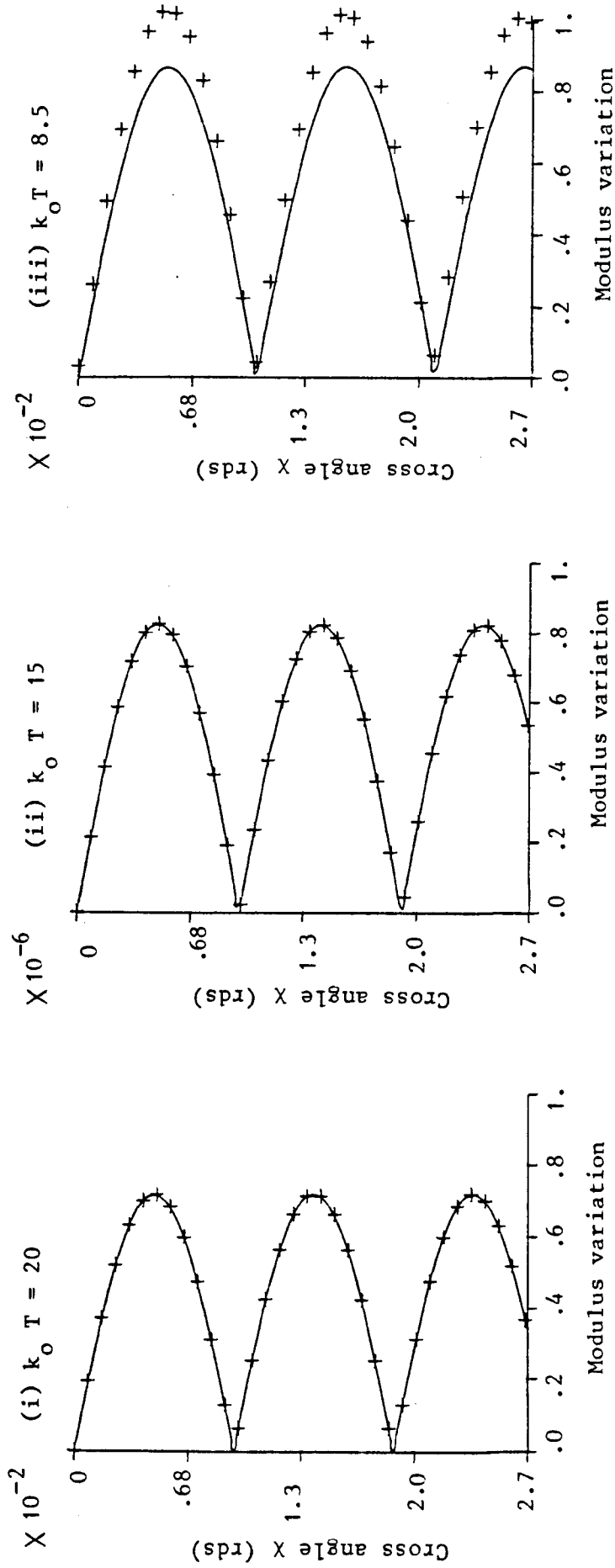


Fig.4.3c. Mode 3. Normalised critical thickness = 8.5

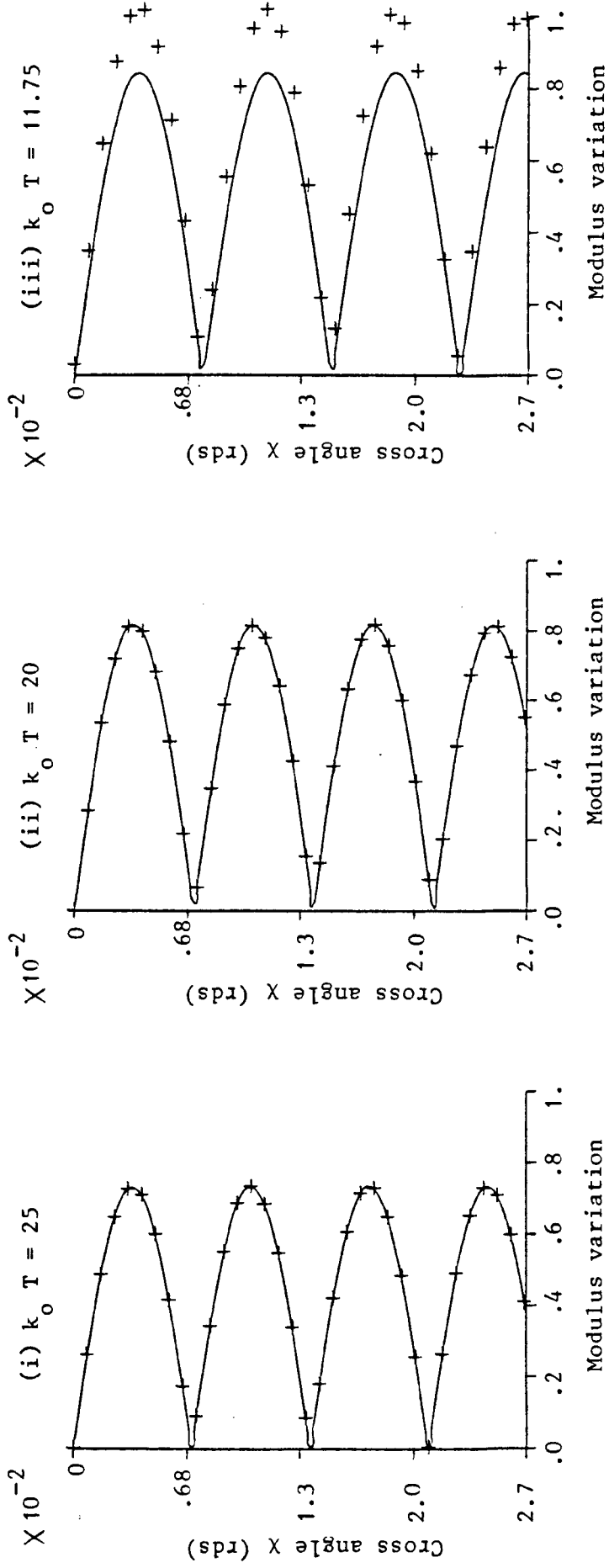


Fig.4.3d. Mode 4. Normalised critical thickness = 11.75

only in a region close to the transition region, that the amplitude of waves begin to diminish, because that is when the wave starts leaking out of the tapered waveguide. Energy is then lost by radiation as the saddle point θ_q becomes complex.

A similar reasoning holds for higher order modes as illustrated by Figs.4.3b, 4.3c and 4.3d.

The computation of the Intrinsic and Adiabatic fields for many modes of the single layer structure shows clearly that the Intrinsic field agrees to a good approximation with the Adiabatic field, when the latter is strongly guided. This identification motivates the important conclusion that the Intrinsic Integral calculated by the saddle point method, yields the Adiabatic mode approximation. However, as the saddle point θ_q approaches the branch point θ_c , the local mode indexed by q approaches its corresponding cut off and the Adiabatic mode theory breaks down. This failure of the Adiabatic mode near the branch point (critical thickness) is associated with the failure of the steepest descent method used in subsection 3.8.1. to define the Adiabatic mode. But the Intrinsic Integral (4.4) itself, from which each Intrinsic mode is constructed, remains well defined. Although the saddle point method can no longer be used to approximate it, because of the confluence of θ_q and θ_c , it can be evaluated by other numerical methods to provide a canonical transition function, valid through and beyond the transition. Hence, one can evaluate the Intrinsic Integral $I(\chi, \theta)$ by attempting to deform the original contour of integration (C) of equation (4.1) onto another contour, when proper account of any singularity of the phase in (4.1) is taken

according to the theory of functions of complex variable.

The identification of Intrinsic and Adiabatic fields in the guided wave region however, permits us to push the saddle point θ_q further (that is by reducing further T) across and beyond the branch point θ_c in order to describe the field behaviour in the leaky wave region, by analytic continuation.

Before moving onto the next section, which analyses the Intrinsic field in the leaky wave region, we must be aware that the Adiabatic field no longer exists in that region. As far as the Intrinsic field is concerned, it cannot easily be carried out along the SDP because of reasons stated earlier. In order to be able to systematically evaluate the field in the leaky wave region, the method suggested is to deform the contour (C') of Fig.4.1 to lie along the real axis, instead of deforming it into the SDP, as long as the convergence of the integration is maintained. The justification of integrating (4.4) along the real axis will be fully explained and accounted for on physical grounds in the next chapter.

Although the Intrinsic fields of Figs.4.3 have all been carried out along the SDP, they are the same as if they had to be carried out along the real axis. This important identification, which follows from Cauchy's theorem [36] allows us to really analyse the field distribution beyond the branch point θ_c by integrating (4.4) along the real axis. In this case, any restriction due to branch points or poles (if any) will be automatically taken care of.

4.2.4. Intrinsic field in the leaky wave region

The observation point \underline{X} can be allowed to move through and beyond the critical range . The saddle point θ_q , as defined by the eigenvalue equation (2.11) becomes complex with a negative imaginary part, which accommodates the loss due to the leaky wave when $\text{Real}(\theta_q) > \theta_c$ for a time convention $\exp(-i \omega t)$.

The transition around the branch point θ_c is mathematically described by the term $(\theta - \theta_c)^{\frac{1}{2}}$. According to earlier convention, one chooses the branch which lies in a single Riemann sheet, so as to ensure vanishing waves along the tapered waveguide, when the motion of θ_q is towards the apex.

In the leaky wave region, the Adiabatic field no longer holds. Bearing in mind now that the contour of integration is the real axis, Figs.4.4 show the computational result of the Intrinsic field only, versus the cross angle χ , for the four lowest modes of the single layer structure, as the observation point \underline{X} moves down the tapered waveguide towards the apex.

Referring first to mode 1 of Fig.4.4a, the normalised thickness $k_o T$ is reduced further from the normalised critical thickness in each diagram. The Intrinsic field still remains well determined and propagates along the tapered waveguide. The saddle point θ_q becomes more and more strongly complex, characterised by an increasing imaginary component.

As the mode is pushed down onto the bottom interface of the tapered waveguide ($\chi = \alpha$), the amplitude of the wave decays along the taper. All energy which initially was bound inside the tapered waveguide, radiates into the bottom adjacent medium (n_2). It is the positive imaginary part of $\beta = n_1 k_o \cos \theta_q$

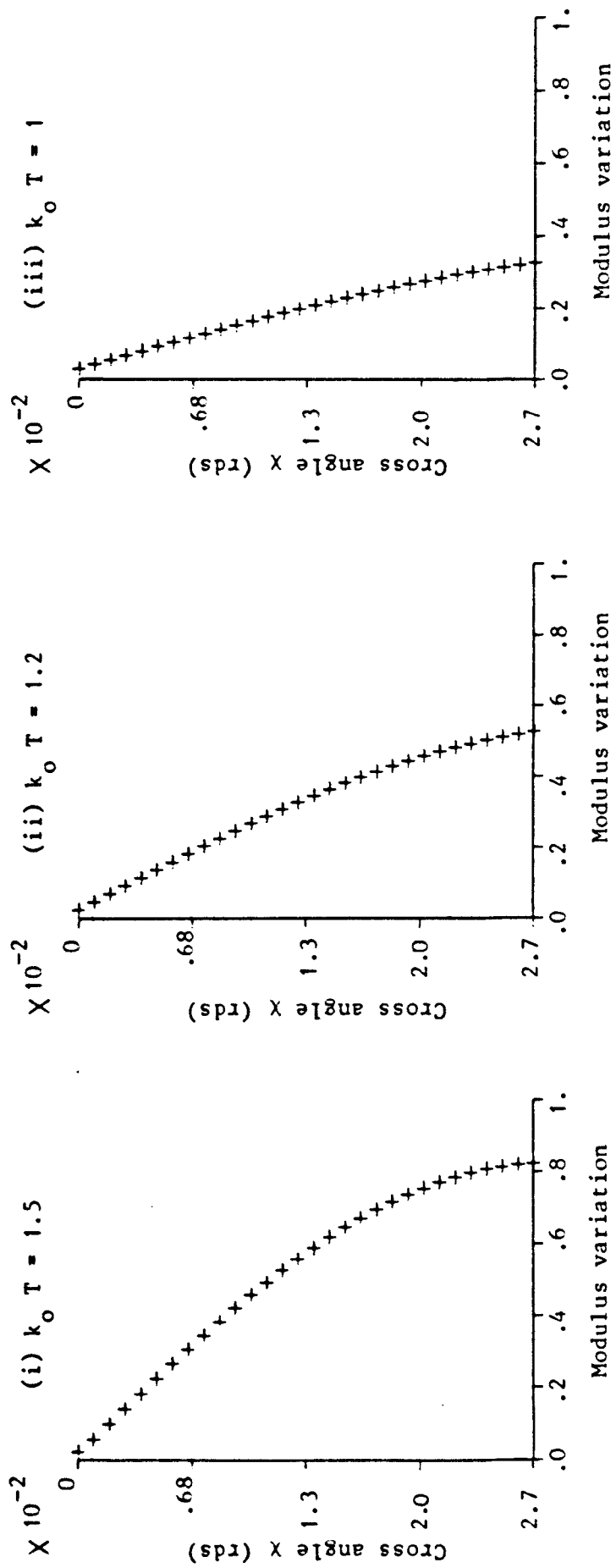


Fig.4.4a. Computation of the normalised cross section Intrinsic field in the tapered waveguide, for the single layer structure. The saddle points in (i), (ii) and (iii) are located in the leaky wave region. Mode 1, normalised critical thickness = 1.75, $\alpha = 0.027$ rds. The refractive indices in each medium are : $n_1 = 2$; $n_2 = 1.76$; $n_3 = 1$.

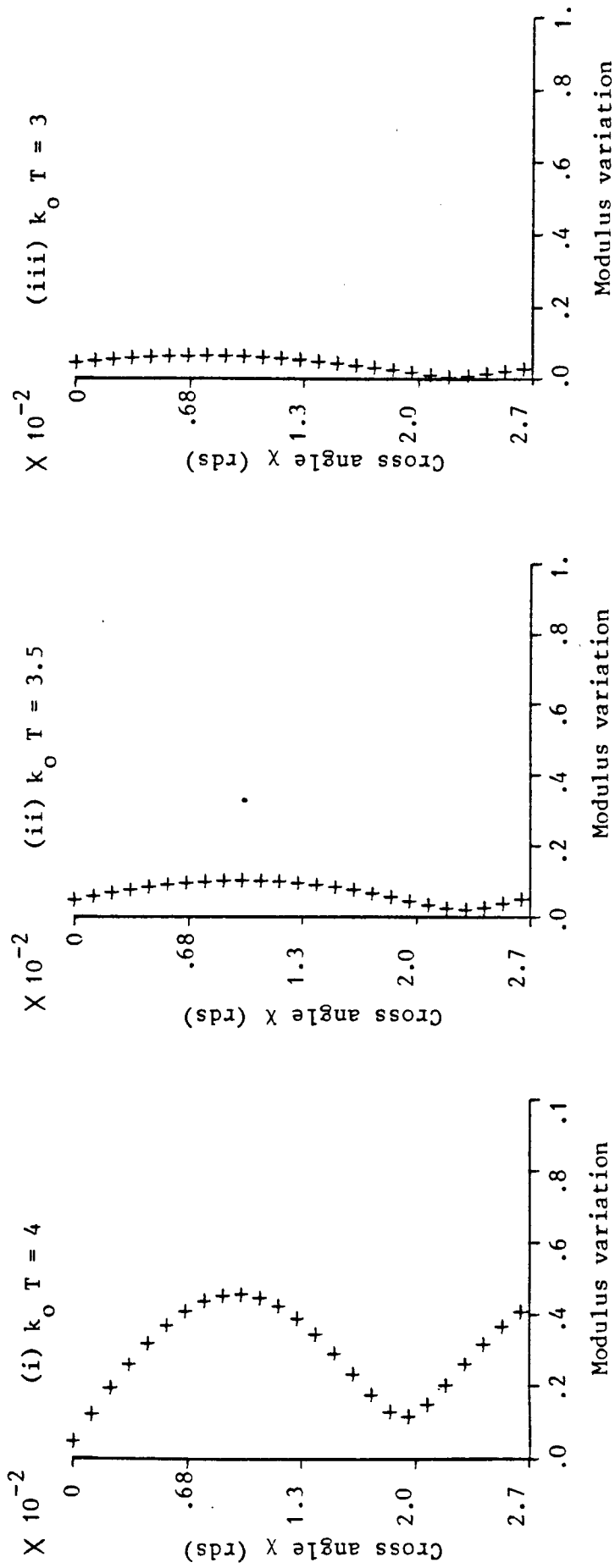


Fig.4.4b. Mode 2. Normalised critical thickness = 5.

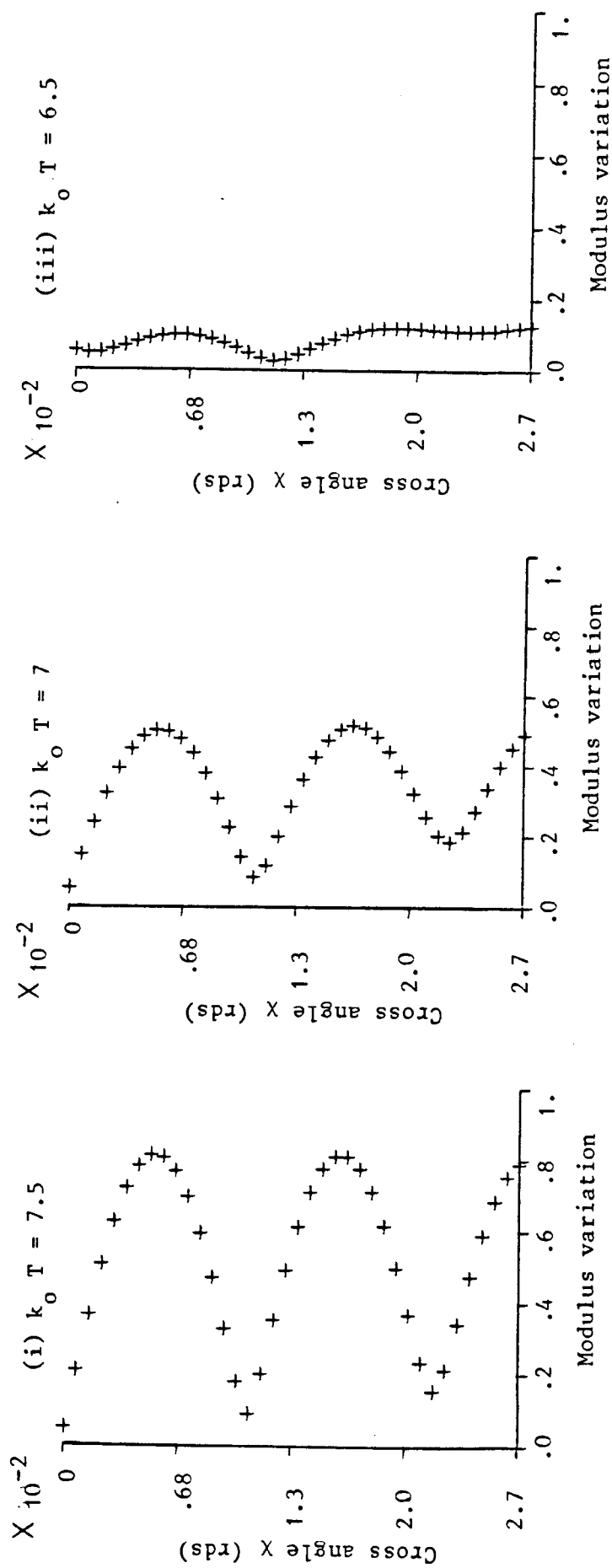


Fig.4.4c. Mode 3. Normalised critical thickness = 8.5

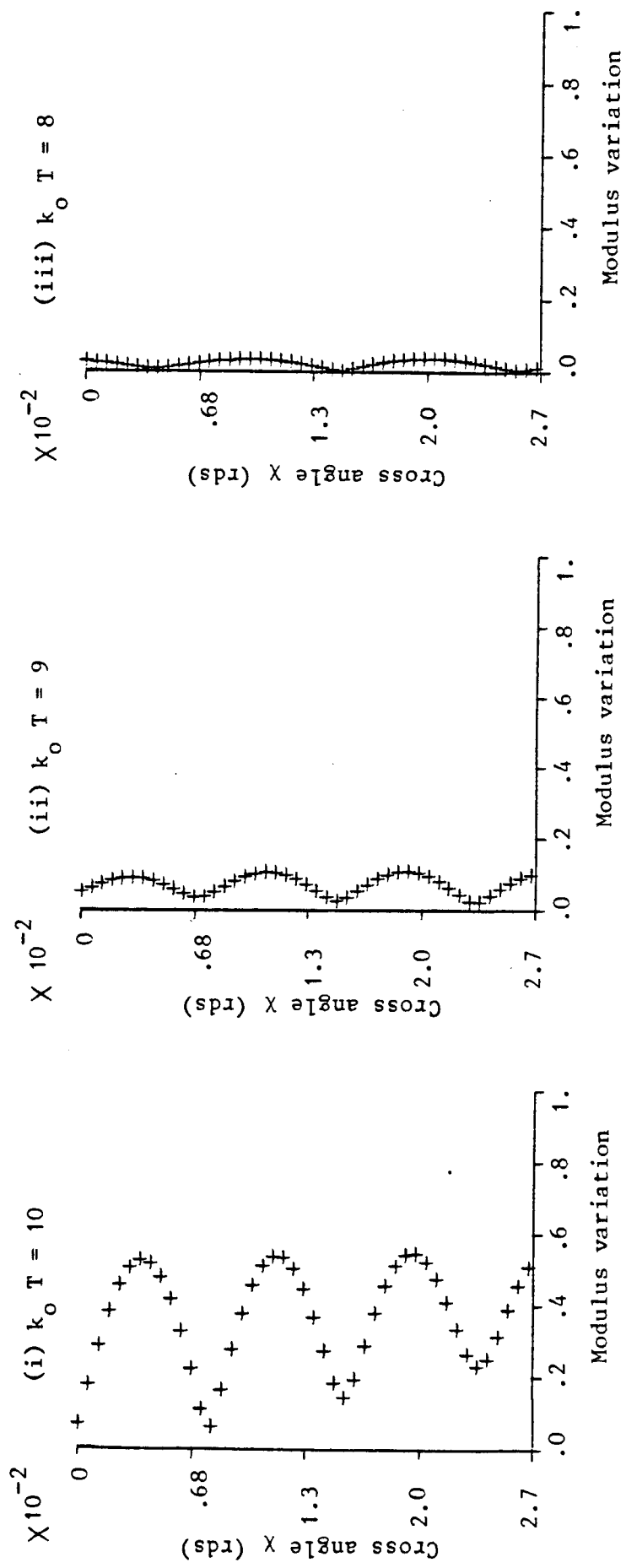


Fig.4.4d. Mode 4. Normalised critical thickness = 11.75

that is responsible for the amplitude decay, as the observation point \underline{X} moves towards the apex (as T diminishes), for a time convention $\exp(-i \omega t)$. This is clearly seen in the computation of eigenvalue equations (2.11), whose plotting is illustrated by Fig.2.5 and Fig.2.6 as dealt with in Chapter 2.

Similar treatment holds for higher order modes as illustrated by Figs.4.4b; 4.4c and 4.4d.

As this chapter is meant to deal with the field inside the tapered waveguide only, the radiation mechanism in medium (n_2) will be treated in the next chapter concerning the propagation outside the tapered waveguide for the single layer problem.

4.3. Application of Intrinsic Integral to the Double Layer Structure

Inserting the expression of phase change $\phi(\theta)$ given by Appendix D into (4.4), yields the Intrinsic Integral describing the mode propagation for the double layer problem. A close look at (4.4) will then prove that it has poles involved in its integrand. This complicates much more the analysis of (4.4), when evaluated by means of the saddle point method. However, this complication does not arise as long as (4.4) is carried out along the real axis and not along the SDP. Consequently, in the guided wave region as well as in the coupled wave region, all singularities (poles and branch point) will be taken care of.

4.3.1. Location of saddle point and determination of SDP contour

Despite the fact that this subsection is not necessary for the evaluation of the Intrinsic field (4.4) for the double layer structure, we shall after all introduce it as a supplement,

similar to the single layer problem. Here too, we require the exact location of the saddle point θ_q in order to evaluate the steepest descent path contour related to the phase integrand of (4.4).

The saddle points θ_q are roots of the derivative of the phase function $Q(\chi, \theta)$ in (4.4), which happens to yield the eigenvalue equation similar to the characteristic equation (2.18) already treated and computed in subsection 2.4.2.

The saddle points turn out to be real after the transition as well as before.

As will be explained in the next subsection, the double layer structure has two critical angles, θ_c and θ'_c , hence two critical thicknesses for each mode. In addition to branch conventions already chosen for θ_c , the same convention holds for θ'_c so as to keep all θ 's in a single Riemann sheet and to guarantee convergence of integral (4.4) in the case of the double layer problem. This constitutes the main differences between the single layer structure discussed in the previous section and the double layer structure.

Once the saddle point θ_q is known, one could depict the SDP contour of the phase function in (4.4), corresponding to the double layer problem.

Appendix E gives the flow chart of the computer program 'Saddle point - SDP' elaborated for this purpose.

For a specified θ_q at a given local thickness T , as well as a given mode number and a given transverse coordinate χ (we choose $\chi = 0$ to place an observation point at the top boundary B_{31} of the tapered waveguide) the SDP can be obtained in a similar

manner to that elaborated in subsection 4.2.1 for the single layer structure. In addition, one must specify the normalised thickness of the uniform film (n_2), $k_0 d$. For numerical purposes one chooses $k_0 d$ so as to permit a sufficient number of modes to be propagated in the tapered waveguide as well as in the uniform film (n_2).

Fig.4.5 illustrates the SDP for three different positions of the saddle point and for the first mode of the double layer structure. The first normalised critical thickness is at $k_0 T = 2.15$ (related to θ_c) and the second normalised critical thickness at $k_0 T = 0.63$ (related to θ_c').

Fig.4.5a corresponds to the SDP contour in the guided wave region, located at a local normalised thickness $k_0 T = 10$. One obtains a $\frac{\pi}{4}$ line crossing the real axis. The real saddle point θ_q denoted by the x sign in the figure, satisfies $\theta_q < \theta_c < \theta_c'$. The critical angle θ_c is denoted by the ∇ sign in the figure.

Fig.4.5b represents the SDP near the first critical thickness ($k_0 T = 2.15$): At this location, the saddle point θ_q tends to encompass the critical angle θ_c . It is at this stage, when θ_q and θ_c coalesce, that the modes exit the guided wave region and enter a new region known as the coupled wave region.

Fig.4.5c locates θ_q beyond the critical angle θ_c ($k_0 T = 1.3$) with $\theta_c < \theta_q < \theta_c'$ (the branch point θ_c' is not represented in this figure). The saddle point θ_q still remains real for the double layer structure. Continuity of the SDP across θ_c is ensured. It is only past the branch point θ_c' that the saddle point θ_q will become complex. This will not be treated here, for it would be

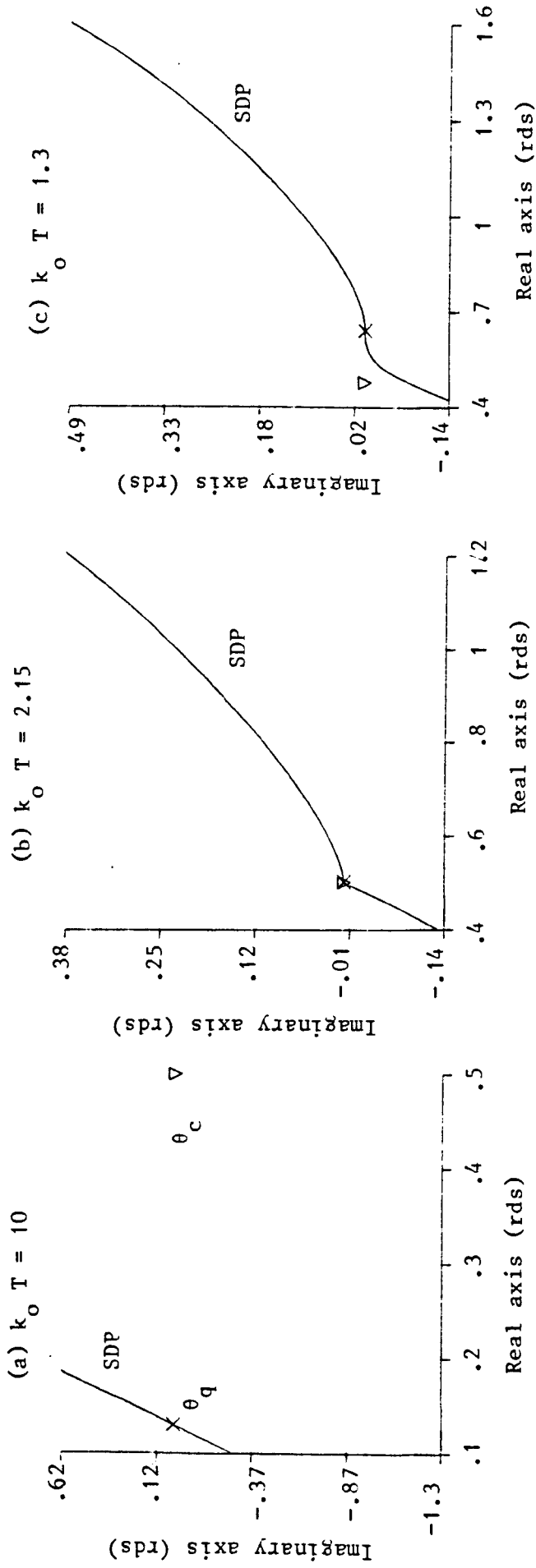


Fig.4.5. Plot in the complex θ -plane of the computed steepest descent path (SDP) for Intrinsic Integral of the double layer structure. Three different positions of the observation point are considered : (a) Saddle point located in the guided wave region, (b) Saddle point located near transition region, (c) Saddle point located in the coupled wave region. The refractive indices in each medium are : $n_0 = 1.5$; $n_1 = 2$; $n_2 = 1.76$; $n_3 = 1$. First normalised critical thickness = 2.15, second normalised critical thickness = 0.63 x Saddle point θ_q , ∇ critical angle θ_c , Mode 1, $\chi = 0$ rds, $\alpha = 0.027$ rds, $k_0 d = -5$.

exactly similar to the single layer case, elaborated when θ_q was located in the leaky wave region.

4.3.2. Intrinsic field in the guided wave region

Here, the saddle point θ_q is also bound in the interval $0 < \theta_q < \theta_c$. A similar treatment as done for the single layer problem in subsection 4.2.2 leads to the computational plotting of Figs.4.6, concerning the double layer problem. There, the four lowest modes of both Adiabatic and Intrinsic fields are respectively compared. The former is deduced from (3.27) and the latter is given by (4.4), after substitution of the appropriate expression for $\phi(\theta)$ from Appendix D.

One notices from Figs.4.6, that due to the presence of the uniform film (n_2), all critical thicknesses are shifted with respect to their counterpart in the single layer problem. This is physically due to the d -dependence of the characteristic equation (2.18) governing the double layer structure.

Dealing first with mode 1, Fig.4.6a evaluates three distinct locations of θ_q related to three different thicknesses as mentioned in each diagram.

(i) $k_0 T = 10$, locates a saddle point θ_q much smaller than both critical angles θ_c and θ_c' (corresponding to the first and second critical thickness respectively). Notice the good agreement between Adiabatic and Intrinsic fields.

(ii) $k_0 T = 5$, positions θ_q not too far from, but still smaller than θ_c . Yet again a good agreement is obtained between both fields.

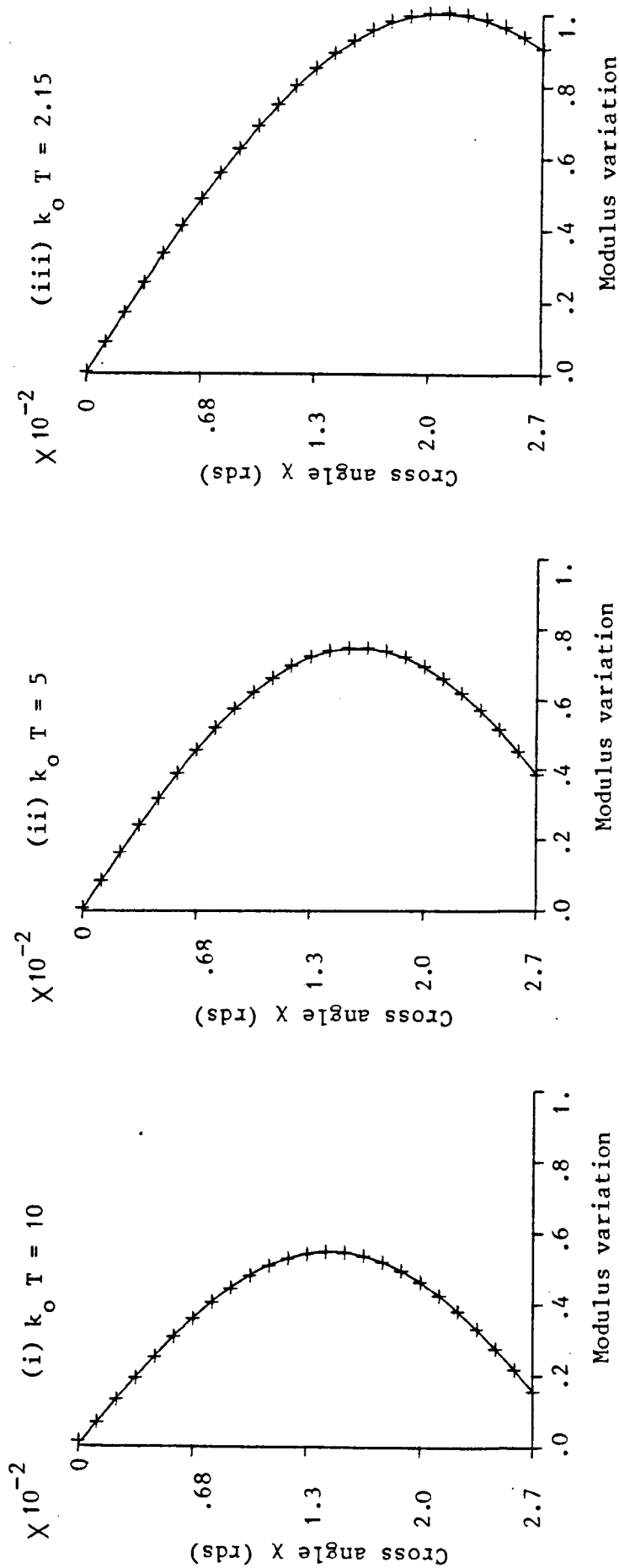


Fig.4.6a. Comparison of the normalised cross section Intrinsic and Adiabatic fields in the tapered waveguide, for the double layer structure. Mode 1. The saddle points in (i), (ii) and (iii) are located in the guided wave region. First normalised critical thickness = 2.15, second normalised critical thickness = 0.63. The refractive indices in each medium are : $n_0 = 1.5$; $n_1 = 2$; $n_2 = 1.76$; $n_3 = 1$. + Intrinsic field, — Adiabatic field. The normalised thickness of the uniform film (n_2) is : $k_0 d = -5$, $\alpha = 0.027$ rds.

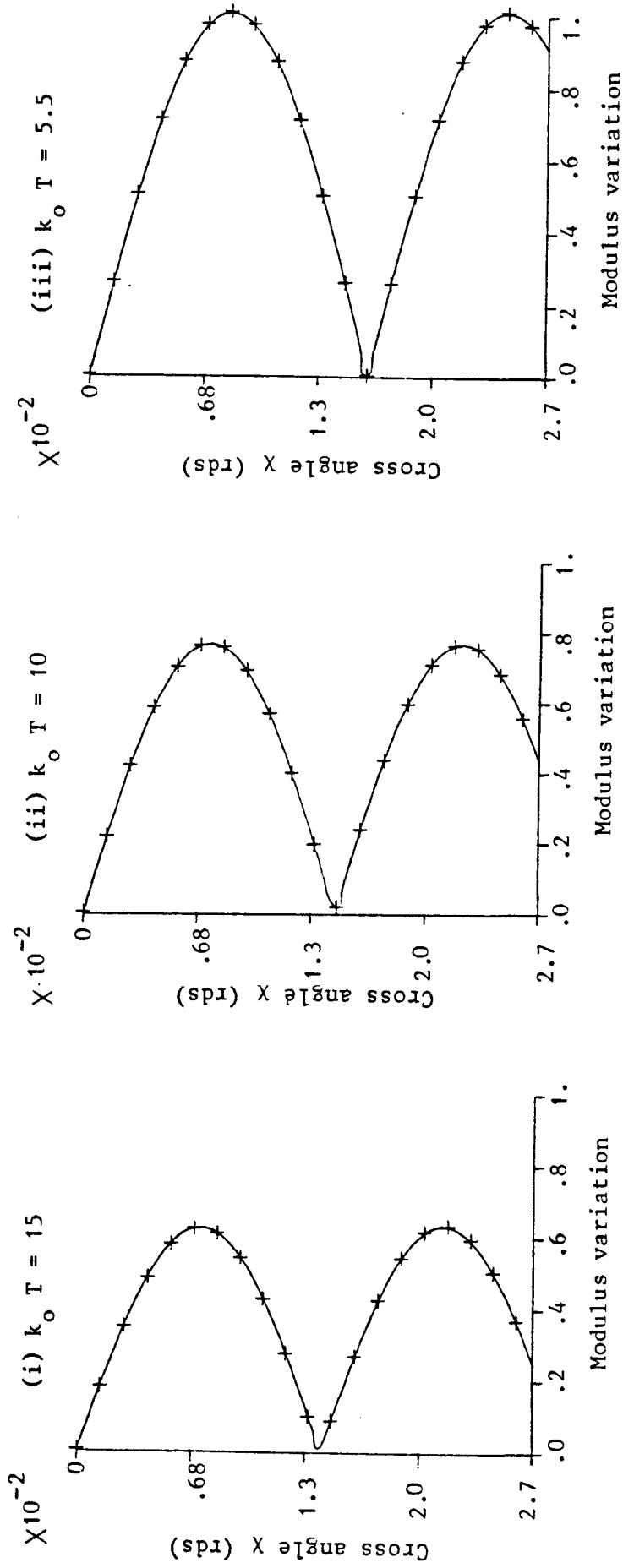


Fig.4.6b. Mode 2. First normalised critical thickness = 5.46, second normalised critical thickness = 3.01.

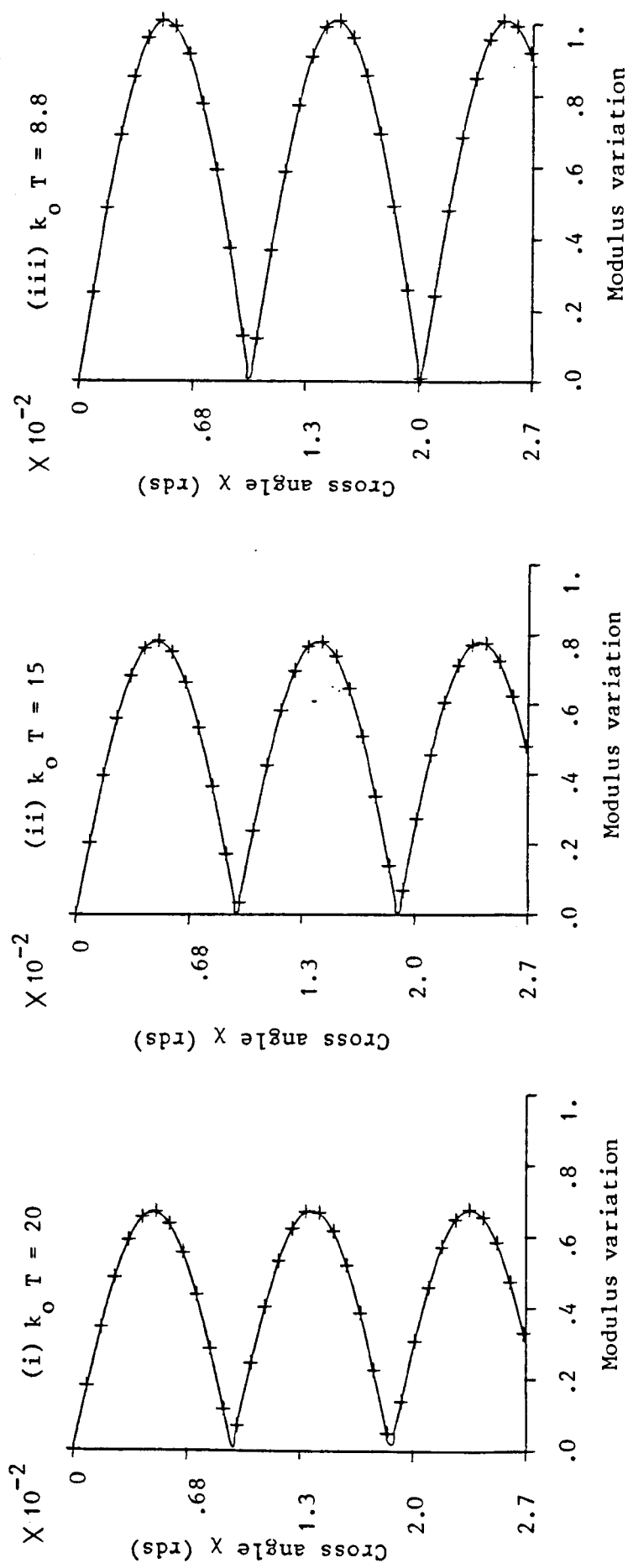


Fig.4.6c. Mode 3. First normalised critical thickness = 8.76, second normalised critical thickness = 5.38

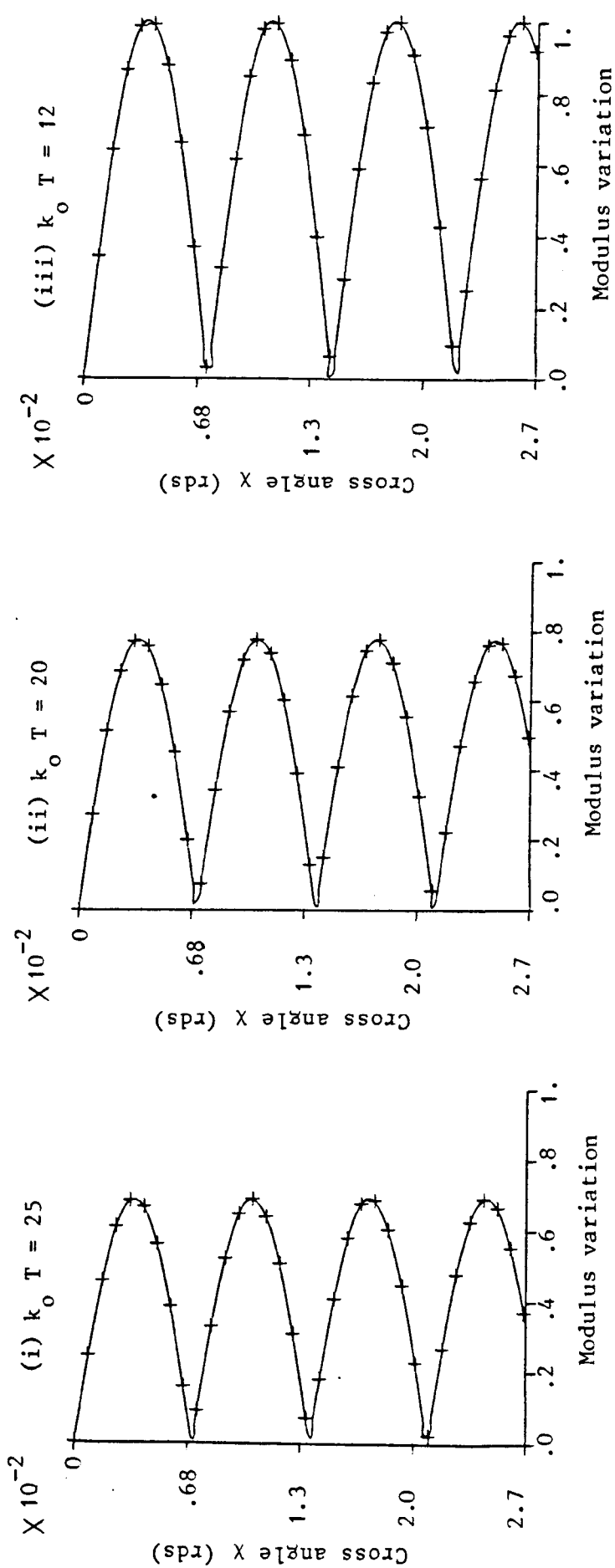


Fig.4.6.d. Mode 4. First normalised critical thickness = 12.07, second normalised critical thickness = 7.76

(iii) $k_0 T = 2.15$, places θ_q very near the critical angle θ_c . Unexpectedly, unlike the single layer problem, there is once again a good agreement between Adiabatic and Intrinsic fields.

One notices from Fig.4.6a that the amplitude of the wave increases as the local thickness T approaches the first critical thickness; this is due to the fact that, in such a guided wave region, energy is still bound inside the tapered waveguide following total reflection; and no wave is radiated or coupled out of the tapered waveguide yet. Hence, no loss is manifested, for all saddle points in the guided wave region are real.

A similar reasoning holds for higher order modes as depicted by Figs.4.6b, 4.6c and 4.6d. The good agreement between Adiabatic and Intrinsic fields for all modes of the double layer structure permits us once again to identify both fields in the guided wave region. The Adiabatic field however, does not break down at the first transition region (critical thickness), for the saddle points θ_q remain real without branching. Such important conclusions allow us to push the saddle point θ_q further beyond θ_c in order to investigate the mode propagation in the coupled wave region.

4.3.3. Definition of branch point θ_c'

Before moving onto the next subsection, we reconsider the Adiabatic field for the double layer structure as an addendum. By inspection of eigenvalue equation (2.18), elaborated earlier in subsection 2.4.2, we recall that the saddle points are real even beyond the first transition region corresponding to the first

critical angle $\theta_c = \text{Arccos} \left(\frac{n_2}{n_1} \right)$. As the existence of real saddle points in the coupled wave region motivates the necessary condition for the existence of Adiabatic modes; there is hence a discrete set of Adiabatic modes, bound and propagating locally not only between top and bottom interfaces of the tapered waveguide, but also between top and bottom interfaces of the uniform film (n_2).

Unlike the single layer problem, the Adiabatic modes in the double layer problem, still persist beyond the critical angle θ_c . According to the computation of (2.18) in subsection 2.4.2, there is another transition region corresponding to another critical angle $\theta'_c = \text{Arccos} \left(\frac{n_0}{n_1} \right)$. This second transition region manifests itself physically in the cut-off region for the double layer structure, corresponding to the interface B_{20} ; see Fig.2.1a. This proves that the double layer problem has, so to speak, two critical angles θ_c and θ'_c . We recall that θ_c is not a branch point for $\phi(\theta)$, whereas θ'_c is. It is only past the second transition region (related to θ'_c) that solutions of eigenvalue equation (2.18) become complex; at this stage only, the Adiabatic field breaks down. Then, for a more systematic analysis of the double layer problem, one ought to push the saddle point θ_q further beyond θ'_c ($\theta'_c > \theta_c$) in order to analytically continue the Intrinsic mode. We shall restrict ourselves to the first critical angle θ_c because, beyond the second critical angle θ'_c , one will obtain leaky mode propagation and the problem reduces to the one already tackled for the single layer structure in the leaky wave region.

4.3.4. Intrinsic field in the coupled wave region

During the transition from guided wave to coupled wave region the saddle point θ_q crosses the critical angle θ_c but remains real, because of the mathematical nature of the eigenvalue equation governing the double layer structure. Consequently, the Adiabatic field is still valid in this region, as the saddle point is confined in the region $\theta_c < \theta_q < \theta_c'$. In such a region beyond the first transition θ_c , one expects some difficulties to arise. These difficulties are essentially due to the more complicated field in the layer, as well as the presence of poles in the expression of $\phi(\theta)$ given by Appendix D. Such restrictions are easily overcome as Integral (4.4) is carried out along the real axis. In this case, all singularities are safely taken care of.

Figs.4.7 compare the normalised cross section variation of the Adiabatic and Intrinsic fields versus the variation of the cross angle χ , as the saddle point moves along the tapered waveguide in a region where θ_q is beyond the critical angle θ_c .

Four of the lowest modes of the double layer structure are considered.

Let us deal first with the lowest mode of Fig.4.7a, which illustrates the distinct location of θ_q relating to three different local normalised thicknesses as shown in each diagram.

(i) $k_o T = 2.1$, places a saddle point θ_q slightly higher than θ_c . A good agreement between Adiabatic and Intrinsic fields is obtained.

(ii) $k_o T = 1.5$, places θ_q halfway in the interval $\theta_c < \theta_q < \theta_c'$.

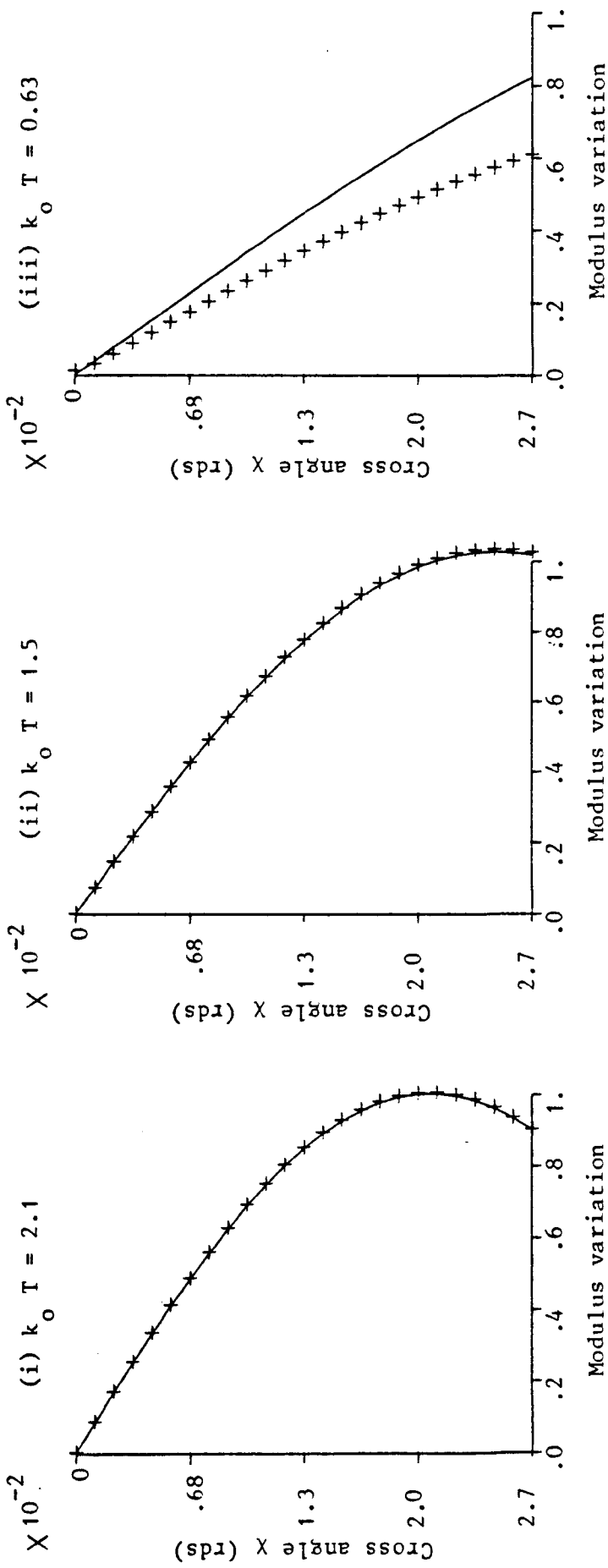


Fig.4.7a. Comparison of the normalised cross section Intrinsic and Adiabatic fields in the tapered waveguide, for the double layer structure. Mode 1. The saddle points in (i), (ii) and (iii) are located in the coupled wave region. Normalised first critical thickness = 2.15, second normalised critical thickness = 0.63. The refractive indices in each medium are : $n_0 = 1.5$; $n_1 = 2$; $n_2 = 1.76$; $n_3 = 1$. + Intrinsic field, — Adiabatic field. The normalised thickness of the uniform film (n_2) is : $k_0 d = -5$, $\alpha = 0.027$ rds.

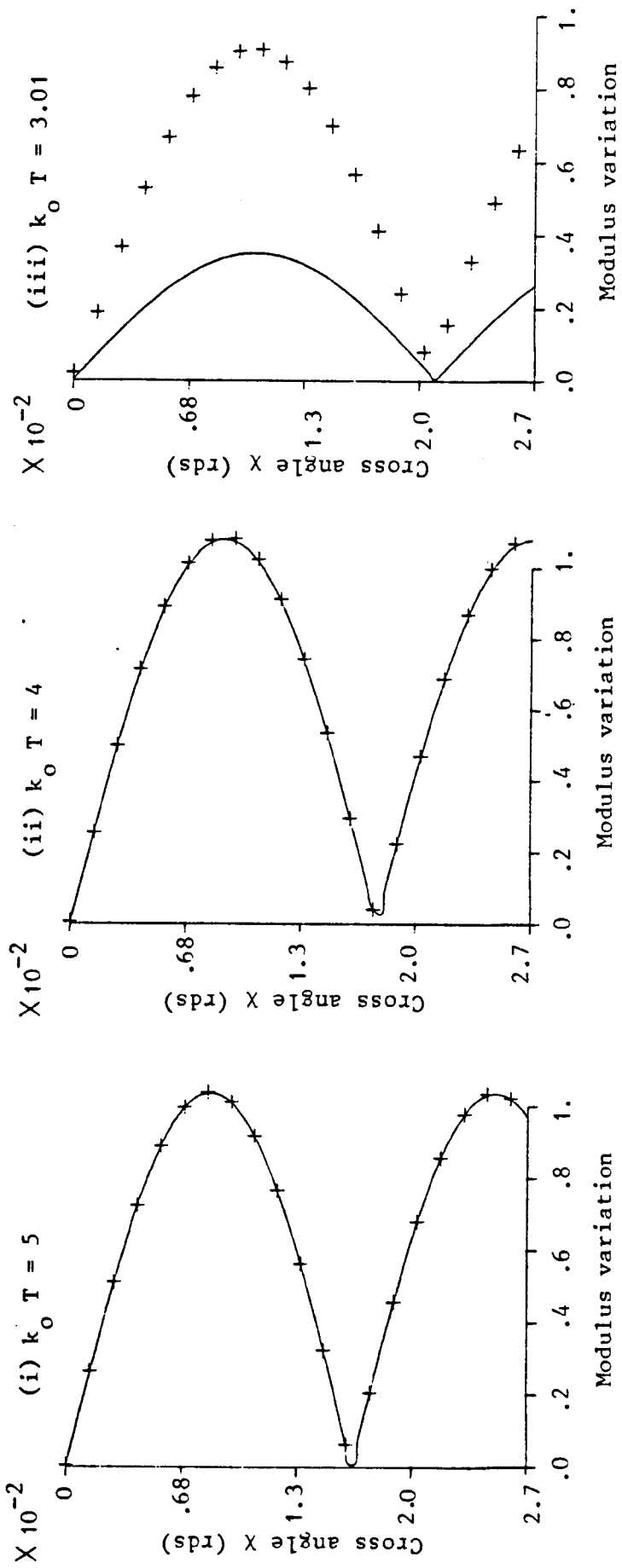


Fig.4.7b. Mode 2. First normalised critical thickness = 5.46, second normalised critical thickness = 3.01

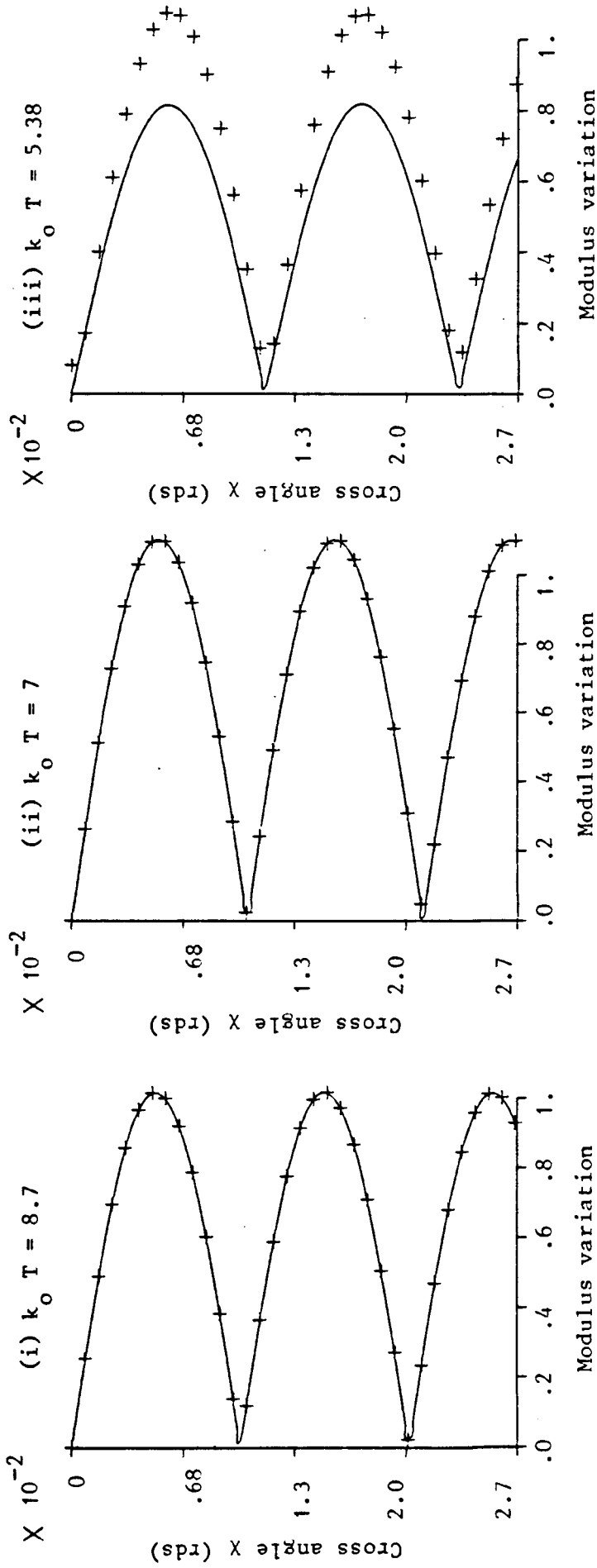


Fig.4.7c. Mode 3. First normalised critical thickness = 8.76, second normalised critical thickness = 5.38

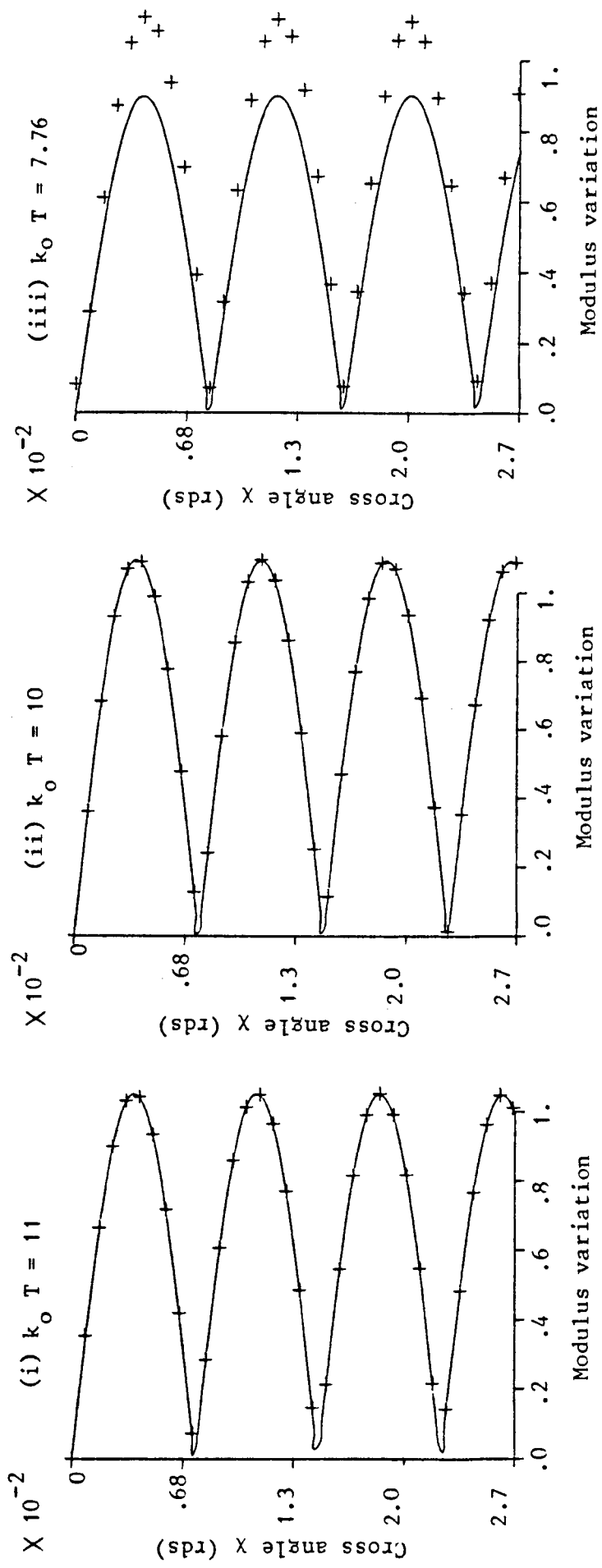


Fig.4.7d. Mode 4. First normalised critical thickness = 12.07, second normalised critical thickness = 7.76

The branch point θ_c' is located at the second critical thickness. Still a good identification of both fields is observed.

(iii) $k_0 T = 0.63$, positions θ_q very near to θ_c' . In this case, the confluence of θ_q and θ_c' restricts the comparison of both fields. The discrepancy is due to the fact that the saddle point θ_q starts becoming complex and the Adiabatic field begins to break down.

A further increase of θ_q beyond θ_c' (or diminishing further T beyond the second critical thickness), will cause leaky wave propagation in the waveguide, and the problem will be similar to the case already treated for the single layer structure in the leaky wave region.

A quite similar treatment holds for higher order modes of Figs.4.7b, 4.7c and 4.7d.

In each diagram of Figs.4.7, one can see that the modes are pushed down onto the bottom interface of the tapered waveguide ($\chi = \alpha$), and the amplitude of the waves increases, then decays abruptly as the saddle point θ_q moves along the tapered waveguide (as T diminishes).

Unlike the single layer structure, when modes are pushed down towards the uniform film (n_2); they are not radiated away but are rather coupled to that adjacent bottom uniform film (n_2). Such phenomena, characterises the coupling mechanism, hence the name of this region. Energy in the tapered waveguide couples to a mode in the uniform film (n_2); whereby, waves are once again trapped, undergoing total internal reflection.

The analysis of such coupled waves in the uniform film (n_2) shall be dealt with in the next chapter, which treats the propagation process outside the tapered waveguide for the double layer problem.

CHAPTER FIVE

RADIATION SPECTRAL INTEGRALS

5.1. Introduction

5.1.1. Definition of the Radiation Integral

In order to analyse the field distribution outside the tapered waveguide, it is necessary to track the motion of the observation point \underline{X} , not only along the tapered waveguide itself, but also across the cross section of its adjacent bottom medium too.

Physically, the rays of the spectrum undergo bottom reflections at the vicinity of the critical angle θ_c , when total internal reflections prevail. But, for observation points \underline{X} located beyond the critical transition range, rays reaching \underline{X} begin to radiate through the interface which adjoins the wedge. This could either be, the open medium (n_2) in the case of the single layer structure, or the uniform film (n_2) in the case of the double layer structure.

It is the purpose of this chapter to investigate the mode propagation in the adjacent bottom medium. To achieve this, it will be necessary to introduce a Radiation Integral which governs fields in the medium adjoining the wedge angle, and which will describe the radiation mechanism taking place in the structures. Of course, the following treatment could also apply to the top adjacent medium (free-space), see Fig.2.1. But we restrict ourselves to the radiation process occurring at the bottom medium only.

The Radiation Integral in an open region can be defined by a spectral integral representation $R(\chi, \theta)$. This is accomplished by extending the preceding plane wave spectral analysis, developed in Chapter 4.

One defines :

$$R(\chi, \theta) = (2\alpha)^{-\frac{1}{2}} \int_{C'} \exp [i k S(\chi, \theta)] d\theta \quad (5.1)$$

where (C') is still the integration contour given by Fig.4.1.

The phase $S(\chi, \theta)$ will explicitly be defined later. The wavenumber k in here refers to the bottom medium ($k = n_2 k_0$). Equation (5.1) must satisfy the boundary conditions at B_{31} (if it represents the radiation at B_{31} interface) or at B_{12} (if it represents the radiation at B_{12} interface). That is at $\chi = 0$ or $\chi = \alpha$, respectively (see Fig.2.1).

In this respect, one constructs the Radiation Integral $R(\chi, \theta)$, by tracking the spectrum of a particular and appropriate species of wave, that radiates by refraction into the corresponding boundary, and which satisfies that boundary condition.

5.1.2. Radiation Integral at bottom interface B_{12}

To present the Radiation Integral referred to the bottom boundary B_{12} we consider only one type of wave out of the four, introduced in Chapter 3; which is characterised by the phase $S_0^u(\chi, \theta)$ given by equation (3.19b). This choice is justified by the fact that $\exp[i k S_0^u(\chi, \theta)]$ is a wave which is destined to be refracted at the bottom medium.

Multiplying the downward propagating plane waves in the Intrinsic mode in (5.1), by the transmission coefficient at B_{12}

interface, which is $1+\exp[i \phi(\theta)]$; one obtains the Radiation Integral governing the field in the adjacent bottom medium :

$$R(\chi, \theta) = (2 \alpha)^{-\frac{1}{2}} \int_{C'} \{1+\exp[i \phi(\theta)]\} \exp\{i [-n_2 k_0 r \cos(\theta''-\alpha+\chi) - \frac{1}{2} \phi(\theta) + \frac{1}{2 \alpha} \int_{\theta_c}^{\theta} \phi(\theta') d\theta' + \frac{\pi \theta}{2 \alpha} - \frac{\pi \theta q_1}{\alpha}]\} d\theta \quad (5.2)$$

In (5.2), we have omitted terms due to the source point $\underline{X}_0 \equiv (\chi_0, r_0)$ in (3.19b), as was done in the previous Intrinsic mode construction. We also recall that the incidence angle θ becomes θ'' corresponding to the direction of propagation of the refracted wave in the adjacent bottom medium. These angles are both inter-related by Snell's law, which stipulates that :

$$n_1 \cos \theta = n_2 \cos \theta'' \quad (5.3)$$

The phase change $\phi(\theta)$ at the bottom boundary B_{12} is straightaway given by the Fresnel equation in the case of the single layer structure, through equation (3.25), or by Appendix D in the case of the double layer structure.

Combining (5.2) and (5.3), after expanding the cosine term in the integrand of (5.2), we obtain after neglecting terms which vanish as $\alpha \rightarrow 0$:

$$R(\chi, \theta) = (2 \alpha)^{-\frac{1}{2}} \int_{C'} 2 \cos \frac{\phi(\theta)}{2} \exp[i k S(\chi, \theta)] d\theta \quad (5.4)$$

with

$$k S(\chi, \theta) = \frac{1}{2 \alpha} \int_{\theta_c}^{\theta} \phi(\theta') d\theta' - \frac{\pi \theta}{2 \alpha} (2 q-1) - \frac{k r}{n_1} [n_1 \cos \theta \cos(\chi-\alpha) - \sin(\chi-\alpha) (n_2^2 - n_1^2 \cos^2 \theta)^{\frac{1}{2}}] \quad (5.5)$$

One also recalls that θ_c is the critical angle and is defined as :

$$\theta_c = \text{Arccos } n_2/n_1 \quad (5.6)$$

5.2. Parametric eigenvalue equation of the Radiation Integral (5.4)

To evaluate (5.4) asymptotically by means of the saddle point method one ought to reconsider the new eigenvalue equation; by finding zeroes of the derivative of the phase function in (5.5), one sets :

$$\frac{\partial S}{\partial \theta} (\chi, \theta_q) = 0 \quad (5.7)$$

Combining (5.5) and (5.7), yields the new characteristic equation, which is :

$$2 r \alpha k \sin \theta_q \cos(\chi - \alpha) + \phi(\theta_q) - \pi (2q - 1) + \frac{n_1 \sin \theta_q \cos \theta_q}{(n_2^2 - n_1^2 \cos^2 \theta_q)^{1/2}} = 0 \quad (5.8)$$

One notices the dissimilarity between (5.8) and the original eigenvalue equation (3.24b) treated in section 3.7 of Chapter 3. The additional terms are due to the χ -dependent quantity in (5.8), which mathematically accounts for the dependence on depth in the adjacent bottom medium; and which appears here to behave as a parameter.

At interface B_{12} , say at $\chi = \alpha$, equations (5.8) and (3.24b) are identical. Hence, they engender the same saddle points. For at $\chi = \alpha$, matching boundary values are necessarily required between, the construction of the Radiation Integral $R(\chi, \theta)$, whose

eigenvalue equation is given by (5.8); and that of the Intrinsic Integral $I(\chi, \theta)$ whose eigenvalue equation is given by equation (3.24b). One recalls that $I(\chi, \theta)$ describes the field inside the tapered waveguide, and it is analytically expressed in section 4.1.

A proper substitution of $\phi(\theta)$ in (5.8), by the phase of the Fresnel's coefficient in the case of the single layer problem, or by its counterpart expression given by Appendix D in the case of the double layer problem, leads to their corresponding eigenvalue equations which respectively engender the saddle points θ_q . Both eigenvalue equations obtained are similar analytically; that is why, in what follows in this subsection, we shall restrict attention to that characterising the single layer structure only. The treatment of that of the double layer structure would be analogous.

The saddle points θ_q are then located for each observation point \underline{X} defined by the polar coordinates $\underline{X} \equiv (\chi, r)$.

In the case of the single layer structure, the parametrically computed eigenvalue equation (5.8) is depicted in Fig.5.1 for 3 successive values of the transverse variable $\chi (\chi \gg \alpha)$ and for the first mode only. In other words, Fig.5.1 shows the physical effect on the eigenvalue equation (5.8), of moving the observation point \underline{X} outside the tapered waveguide and away from the bottom boundary B_{12} .

Fig.5.1a illustrates a plot corresponding to the parameter $\chi = \alpha$ (one wedge angle), where the observation point is located on the bottom interface B_{12} . One notes that such a parametrical case has already been treated via the eigenvalue equation (3.24b), whose numerical plotting is illustrated by Fig.2.5 in Chapter 2.

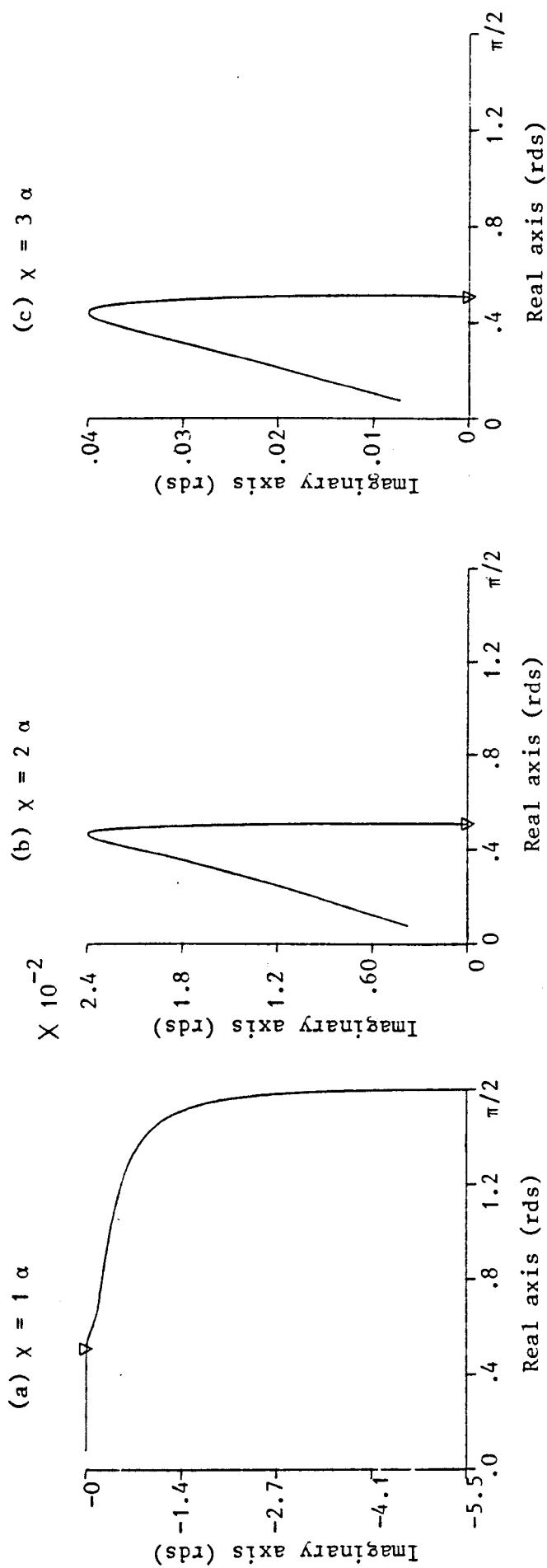


Fig. 5.1. Computation of eigenvalue equation (5.8) of the Radiation Integral, for the single layer structure. Solutions are the complex incident angle θ_q (saddle points) for the First lowest mode, as the thickness T is arbitrary reduced. Three multiple values of the wedge angle α are considered for the cross variable χ . The refractive indices in each medium are : $n_1 = 2$; $n_2 = 1.76$; $n_3 = 1$ ∇ Branch point θ_c .

Locating an observation point \underline{X} at $\chi = 2\alpha$ or at $\chi = 3\alpha$, as illustrated by Fig.5.1b or Fig.5.1c respectively, has the effect of shifting up the solutions (saddle points θ_q) of (5.8), particularly those lying beyond the transition region, to a region near the branch point θ_c , which is denoted by the ∇ sign in figures. For those solutions, which are situated in the guided wave region, they exhibit a slight positive imaginary component. In this case ($\chi = 2\alpha$ or $\chi = 3\alpha$), all solutions which are supposed to lie in the leaky wave region seem to be coinciding with the branch point θ_c . In other words, choosing a thickness T beyond the transition region, will have the effect of bringing all complex saddle points to coalesce with θ_c . Such an effect, exhibited by Fig.5.1b and Fig.5.1c, can geometrically be explained by reference to Figs.5.2.

In the guided wave region, as depicted by Fig.5.2a, the saddle points θ_q are within the interval $0 < \theta_q < \theta_c$. Consequently, all rays inside the tapered waveguide undergo total multiple reflections at B_{12} and B_{31} interfaces. For any observation point \underline{X} , located outside the tapered waveguide and within the guided wave region, there are evanescent waves accommodated by the complex θ_q . As \underline{X} moves away from B_{12} interface (as χ increases), the transverse propagation constant $(n_2^2 - n_1^2 \cos^2 \theta_q)^{\frac{1}{2}}$, of that evanescent wave becomes more complex and entails a strongly decaying evanescent field. Hence, one expects the imaginary part of the saddle point to increase.

In the leaky wave region in contrast, Fig.5.2b shows how the rays are refracted into medium (n_2), once the branch point θ_c is exceeded by θ_q . In this case, any observation point \underline{X} outside

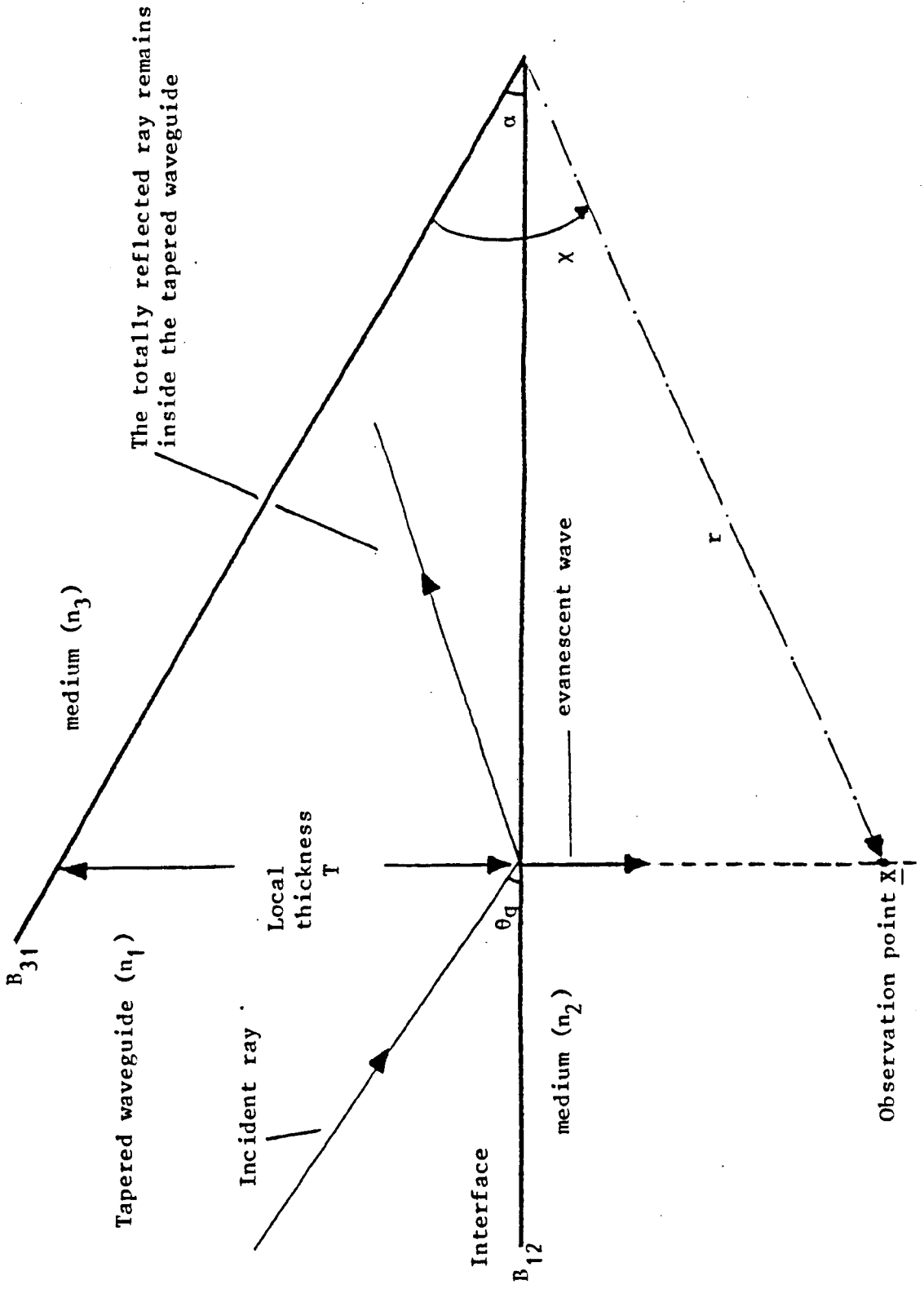
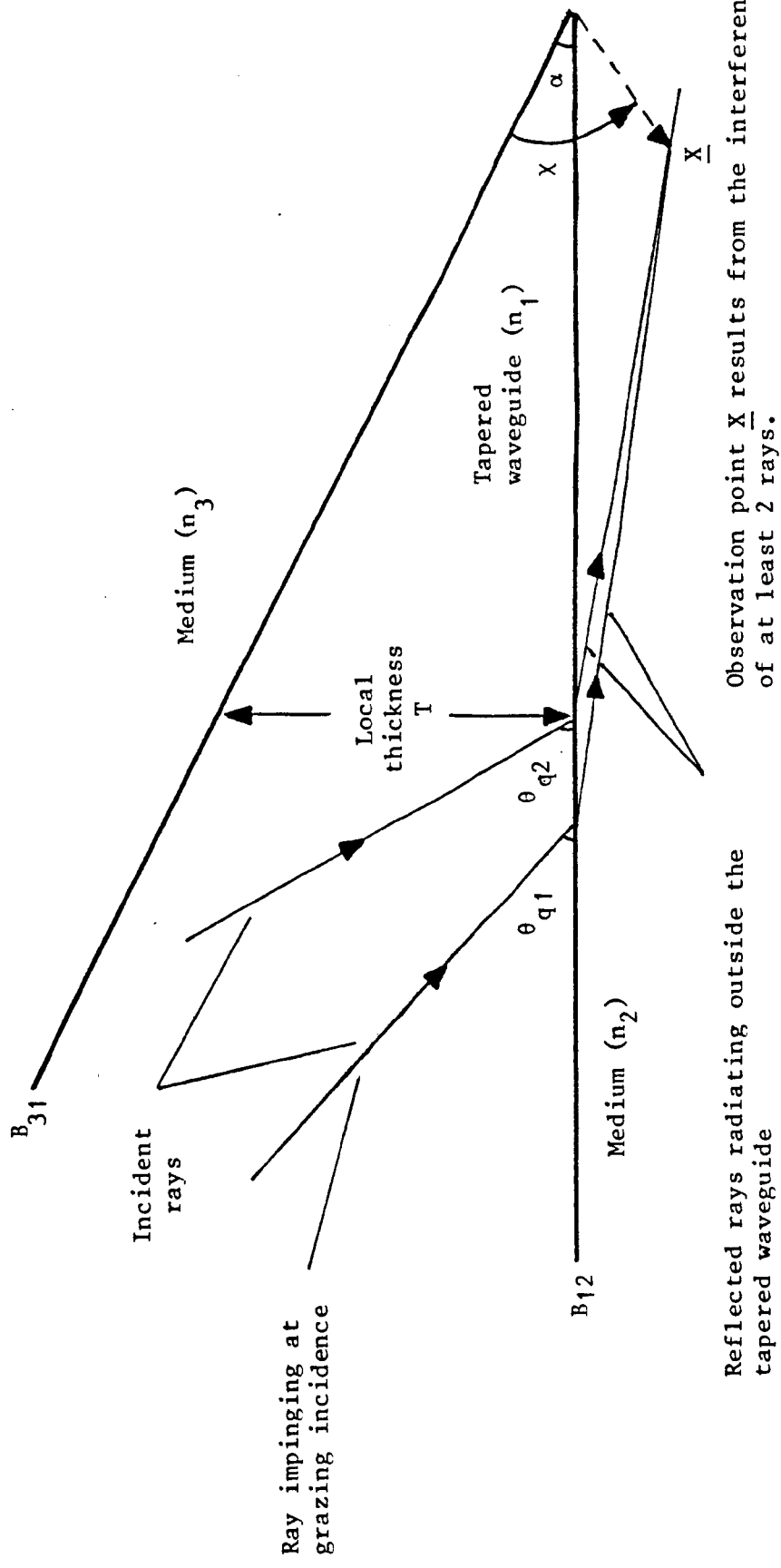


Fig.5.2a : Geometrical configuration of rays in the guided wave region outside the tapered waveguide



Reflected rays radiating outside the tapered waveguide

Observation point X results from the interference of at least 2 rays.

Fig. 5.2b. Configuration of rays beyond the transition region outside the tapered waveguide

the tapered waveguide receives the contribution of 2 distinct rays impinging at B_{12} interface, from 2 angles of incidence, θ_{q1} and θ_{q2} . Therefore, 2 saddle points (θ_{q1} and θ_{q2}) are required at a given thickness T and at a given transverse variable $\chi(\chi > \alpha)$. Because one of these is at an incident angle near to θ_c , the corresponding ray refracts from the tapered waveguide to the open medium (n_2), with a near grazing refraction angle. As the saddle point is condensed near the singularity θ_c it is very difficult (if not impossible) to numerically assess absolutely the branch cut contribution. Such an effect, which manifests itself strongly when the observation point \underline{X} is located outside the tapered waveguide ($\chi > \alpha$) and beyond the transition region, complicates the evaluation of the Integral (5.4) by the saddle point method.

5.3. Integrand variation of the Radiation Integral (5.4) along the real axis

To circumvent those above difficulties, and to achieve integration of (5.4) systematically, we suggest another method, already used in the previous chapter, which is to keep the undeformed original contour (C') and to abandon the saddle point integration method.

The original contour (C') is given by Fig.4.1 and has a path coinciding with the real axis. We omit however the two lower tails because computational results have shown that their evanescent contributions are negligible compared to the real axis integration.

We shall in the next subsections, for both single and double layer structures, show how the real axis integration can further be

limited to an integration over a restricted interval, namely

$$0 < \theta < \frac{\pi}{2}.$$

5.3.1. Single layer structure

Let us plot the variation of the phase $S(\chi, \theta)$ of the integrand in Integral (5.4) along the real axis at a given observation point \underline{X} situated on the bottom boundary B_{12} ($\chi = \alpha$). Only the first lowest mode of the single layer structure is considered. We recall that for such a structure, $\phi(\theta)$ in (5.4) is given through equation (3.25).

(a) θ_q in the guided wave region

Fig.5.3a illustrates the complex variation of $S(\chi, \theta) - S(\chi, \theta_q)$, versus the incidence angle θ varying on the real axis. The real saddle point θ_q is located in the guided wave region at $k_0 T = 5$. $\text{Real} \{S(\chi, \theta) - S(\chi, \theta_q)\}$ has an extremum at the chosen saddle point θ_q , which is denoted by the x sign in figures. Its imaginary part is zero for all Real θ 's lying in the region $\theta < \theta_c$, where θ_c is the branch point for the phase $S(\chi, \theta)$, and is denoted by the ∇ sign in figures. This means that $\text{Imag} \{S(\chi, \theta)\}$ is constant in the guided wave region. However when $\theta > \theta_c$, the imaginary part increases in magnitude, then leakage occurs; it is that very imaginary part of $S(\chi, \theta)$ that accounts for the amplitude decay of the field in the leaky wave region. In contrast, $\text{Real} \{S(\chi, \theta)\}$ decreases towards the constant $\text{Real} \{S(\chi, \theta_q)\}$ as θ tends to θ_q , and increases as θ tends to θ_c and beyond.

Fig.5.3 continued, shows the complex variation of the integrand of (5.4), when the incidence angle θ varies on the real

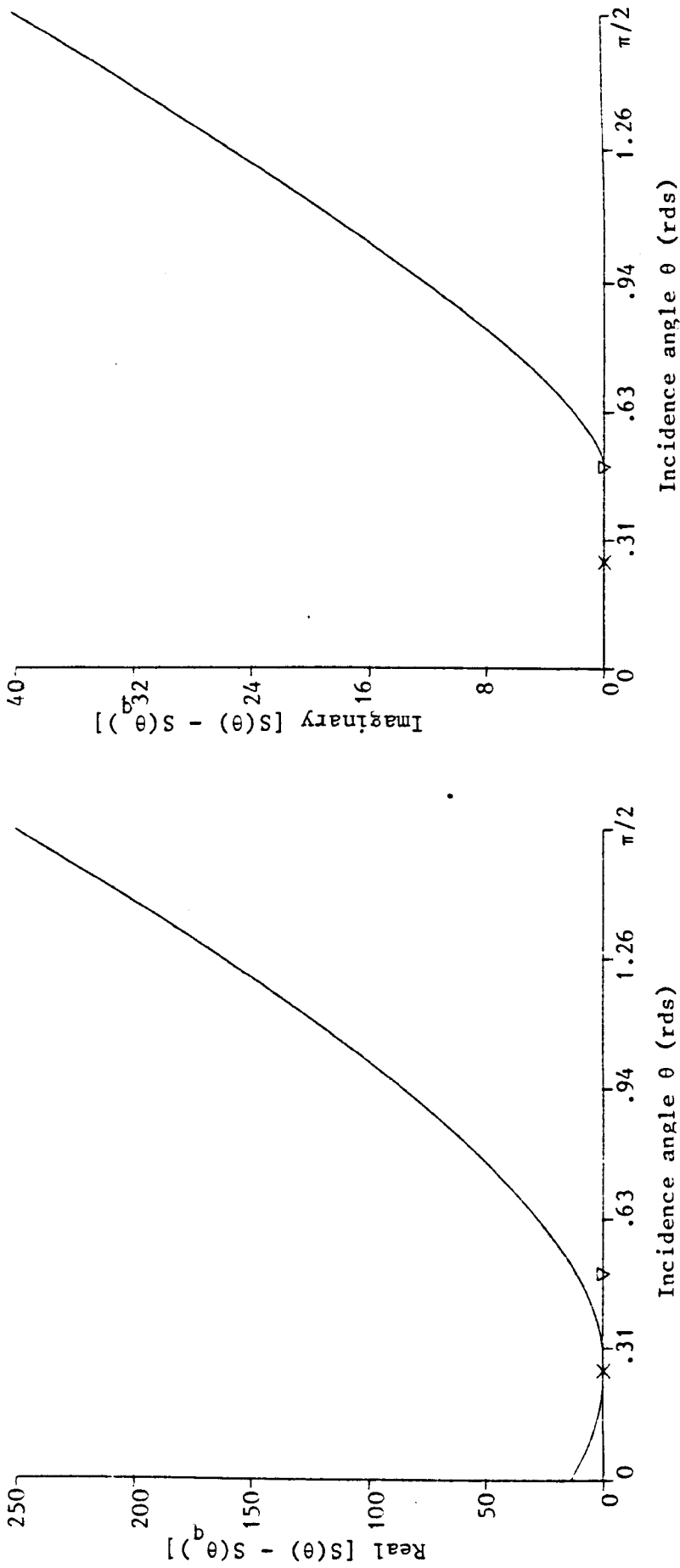


Fig. 5.3a. Computation of the phase in the Radiation Integral (5.4) versus the incidence angle θ varying along the real axis, for the single layer structure. The saddle point is located in the guided wave region at $k_o T = 5$. Mode 1, normalised critical thickness = 1.75.
 x Saddle point θ_q , V Branch point θ_c , $\chi = \alpha = 0.027$ rds.
 The refractive indices in each medium are : $n_1 = 2$; $n_2 = 1.76$; $n_3 = 1$.

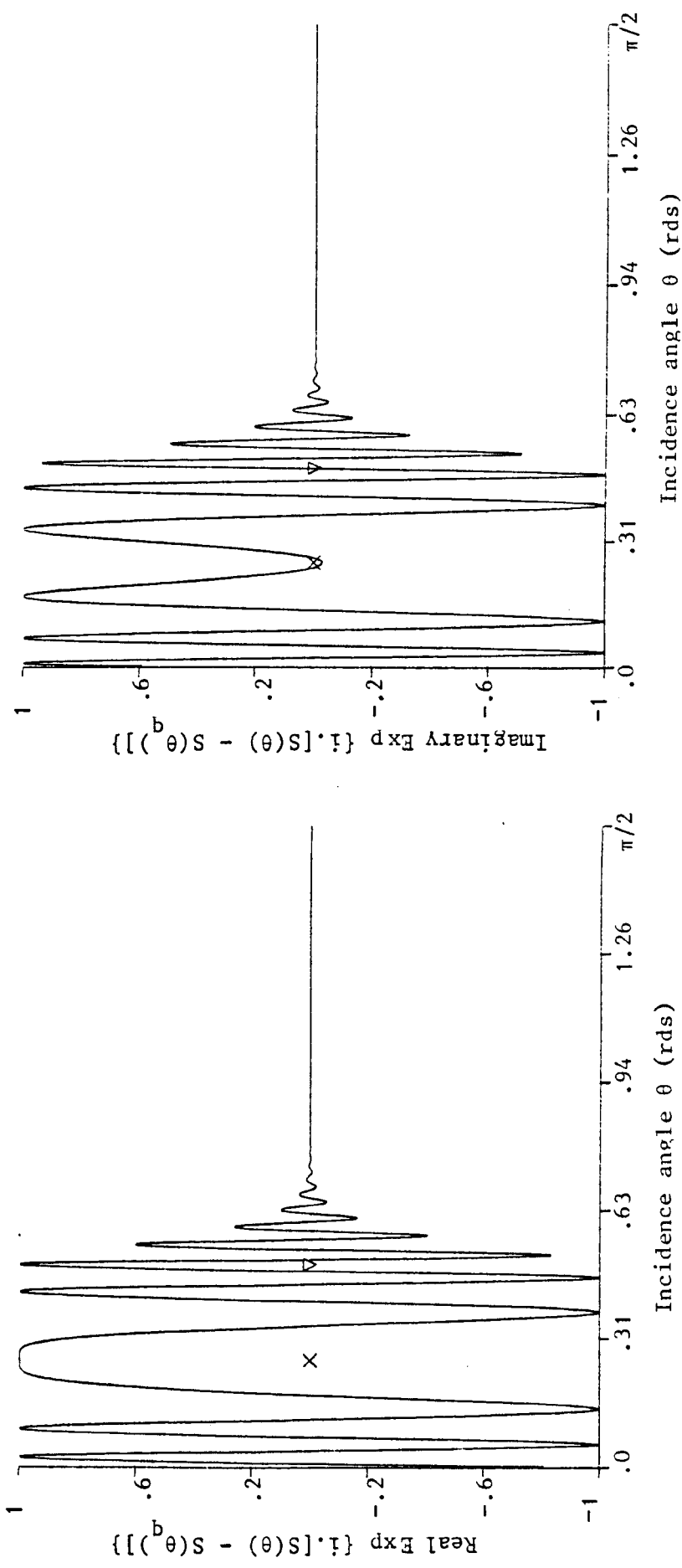


Fig.5.3a. continued. Computation of the integrand in the Radiation Integral (5.4) versus the incidence angle θ varying along the real axis.

axis. Both components exhibit extrema at the location of the saddle point. They oscillate initially, then decay exponentially as the incidence angle θ approaches $\frac{\pi}{2}$. This signifies that for $\theta > \frac{\pi}{2}$, the Radiation Integral (5.4) engenders a vanishing field. In other words, there is no contribution of rays whose incidence angle is higher than $\frac{\pi}{2}$. This important statement, justifies and accounts for the neglect of all types of subsequent rays in section 3.5.

(b) θ_q in the leaky wave region

Fig.5.3b shows the same phenomena for a saddle point θ_q located in the leaky wave region at $k_0 T = 1.2$. We notice that $S(\chi, \theta) - S(\chi, \theta_q)$, accommodates a shift due to the fact that the saddle point θ_q is complex in this leaky wave region. Therefore, any variation of θ on the real axis, will never coincide with θ_q . Henceforth, $S(\chi, \theta) - S(\chi, \theta_q)$, will never fall to zero. This explains why $S(\chi, \theta) - S(\chi, \theta_q)$ exhibits a shift in its real part. This shift is more accentuated as θ_q becomes strongly complex, that is to say, as the observation point \underline{X} tends towards the apex (or as T diminishes).

As for the variation of the integrand of (5.4), Fig.5.3b continued shows that initially it exhibits more rapid oscillation and then decays exponentially and faster than in Fig.5.3a continued. Here too, the field engendered by the Radiation Integral (5.4), vanishes as θ tends towards $\frac{\pi}{2}$.

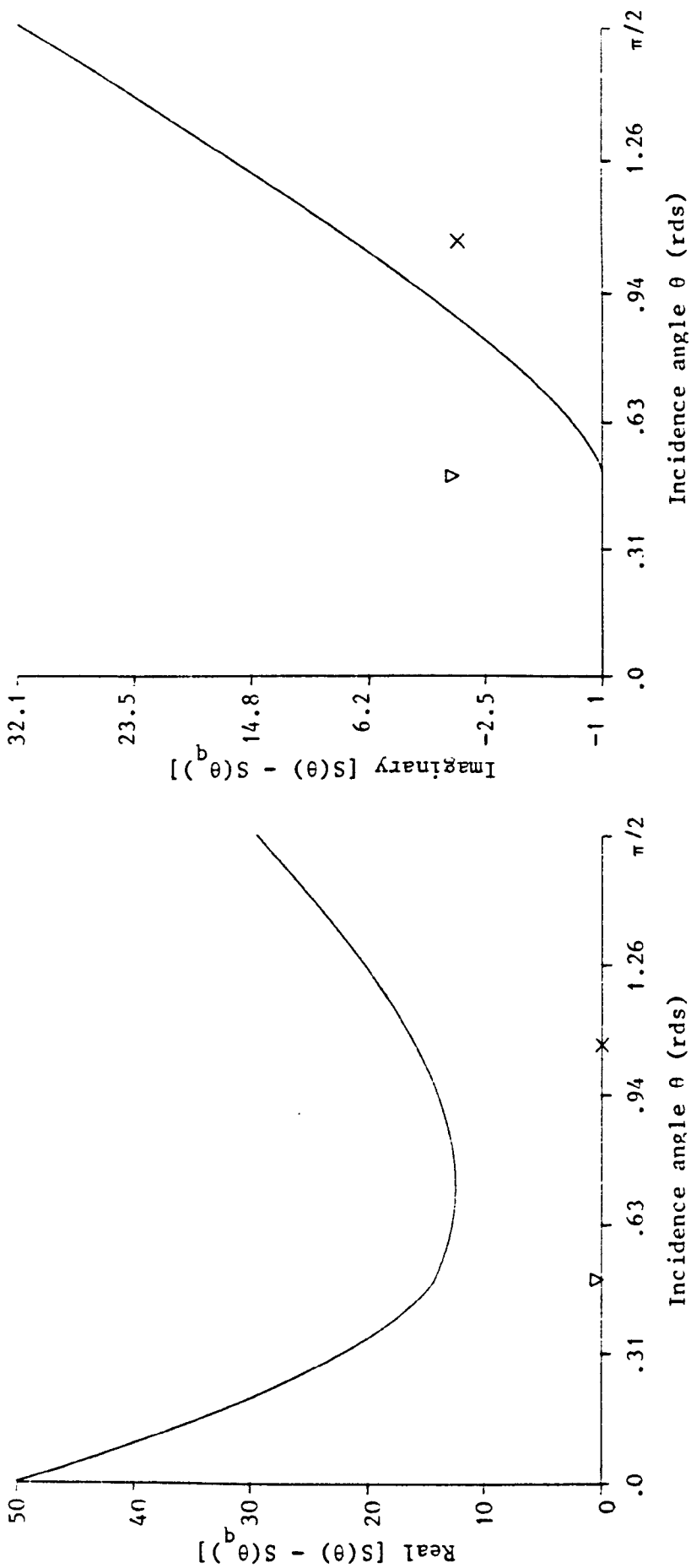


Fig.5.3b. Computation of the phase in the Radiation Integral (5.4) versus the incidence angle θ varying along the real axis, for the single layer structure. The saddle point is located in the leaky wave region at $k_c T = 1.2$. Mode 1, normalised critical thickness = 1.75.
 ∇ Saddle point θ_q^0 , ∇ Branch point θ_c , $x = \alpha = 0.027$ rds.

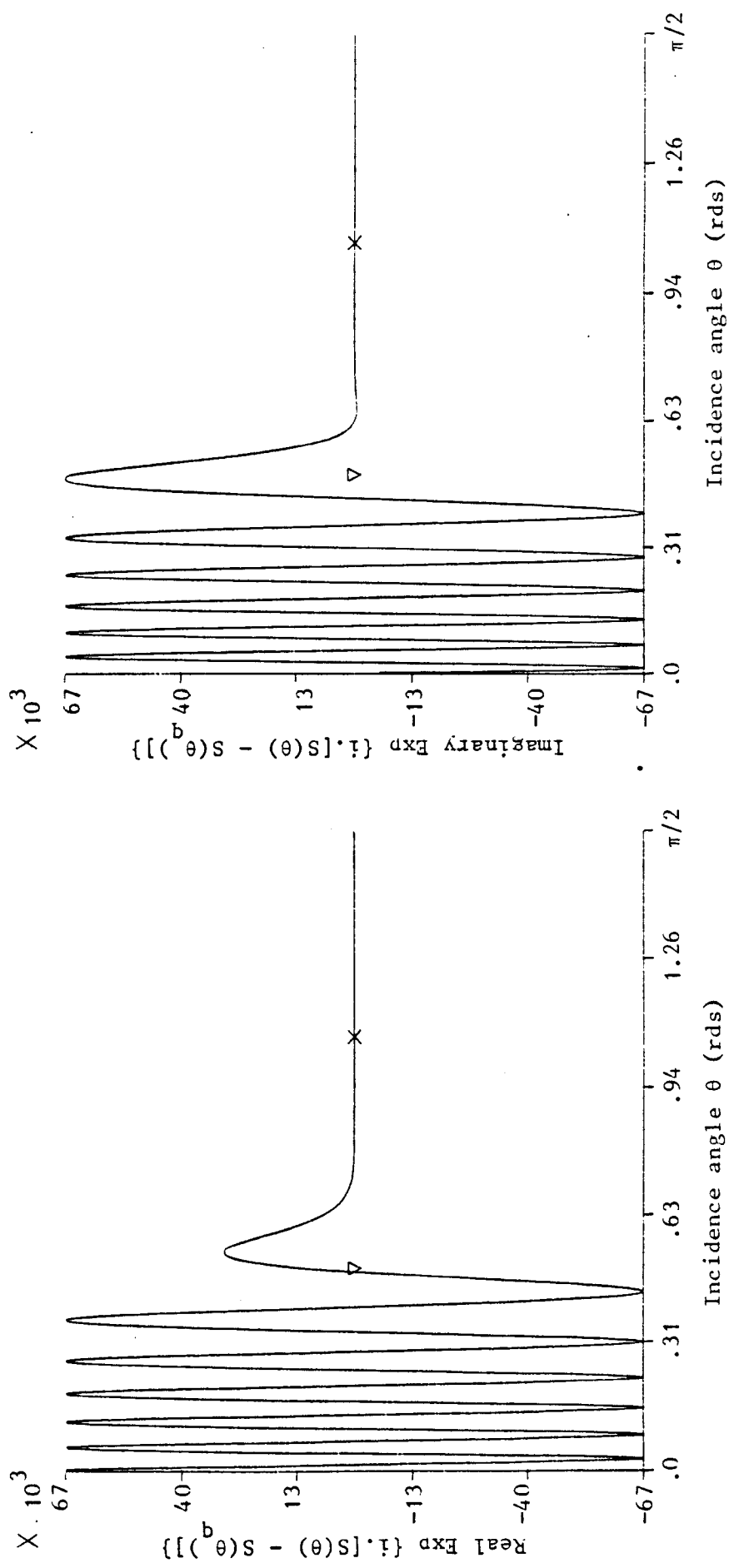


Fig. 5.3b. continued. Computation of the integrand in the Radiation Integral (5.4) versus the incidence angle θ varying along the real axis.

5.3.2. Double layer structure

In this case, $\phi(\theta)$ in (5.4) is given by Appendix D. Here too we position an observation point \underline{X} on the bottom boundary B_{12} ($\chi = \alpha$).

In fact, in order to be more rigorous, the Radiation Integral (5.4) does not apply to the double layer problem, for reasons which will be explained later on in this chapter. But as we have voluntarily chosen an observation point \underline{X} at the interface B_{12} , it happens that (5.4) and the exact Radiation Integral of the double layer structure, are identical in form but with differing Fresnel phase $\phi(\theta)$. In this case, and at this stage, one can safely use (5.4), provided it is understood that $\chi = \alpha$.

A similar treatment as in subsection 5.3.1, leads to the results presented in Figs.5.4, concerning only mode 1 of the double layer structure.

(a) θ_q in the guided wave region

In Fig.5.4a, the saddle point θ_q lies in the guided wave region at $k_0 T = 5$. The results here are qualitatively similar to those in Fig.5.3a. The only difference in this subsection is that the branch point θ'_c (characterised by the second critical thickness and which is defined in subsection 4.3.3 in Chapter 4) dominates, and not θ_c (characterised by the first critical thickness). The branch point θ'_c is denoted by the \square sign in figures.

Real $\{S(\chi, \theta) - S(\chi, \theta_q)\}$ behaves similarly as in Fig.5.3a. It falls to zero in here too, at the saddle point θ_q , which by definition is real. However unlike in Fig.5.3a, Fig.5.4a shows

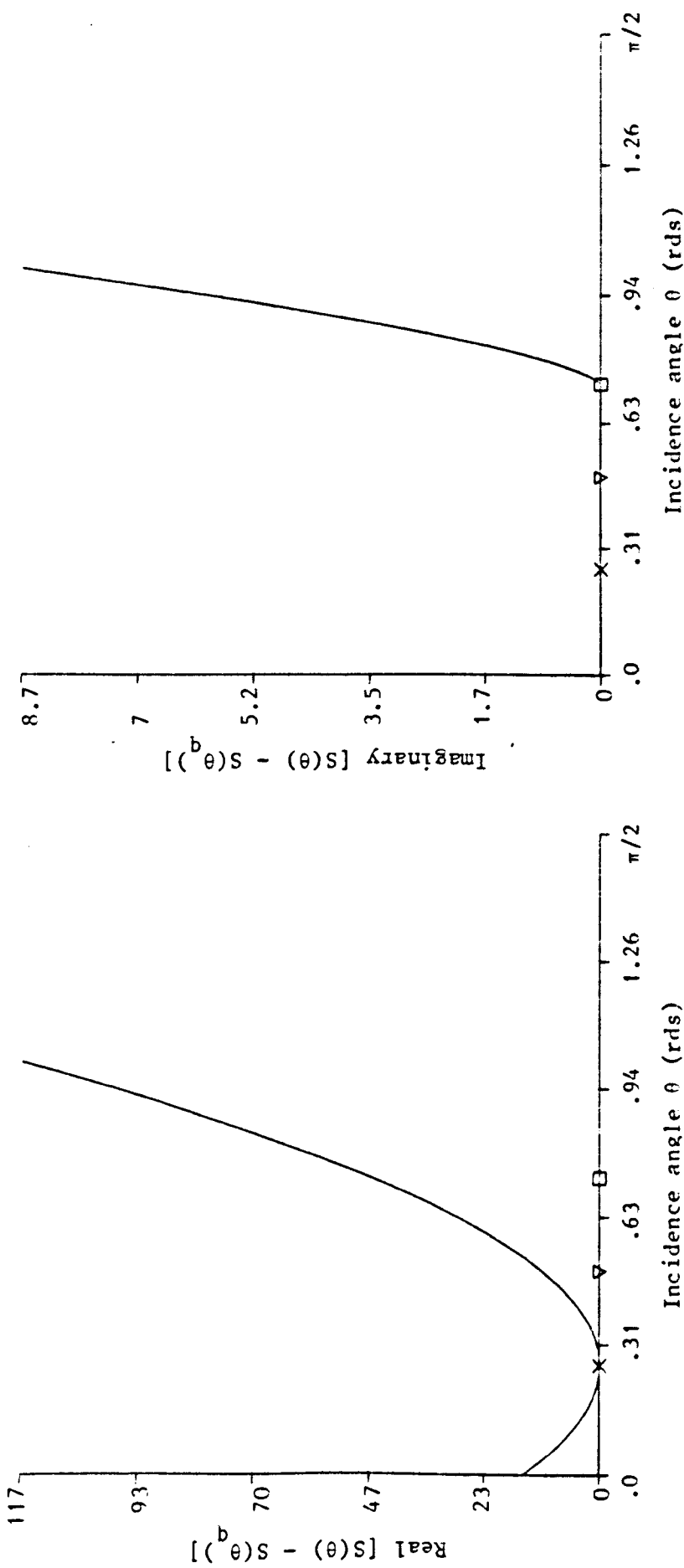


Fig. 5.4a. Computation of the phase in the Radiation Integral (5.4) versus the incidence angle θ varying along the real axis, for the double layer structure. The saddle point is located in the guided wave region at $k_0 T = 5$. Mode 1. First normalised critical thickness = 2.15, second normalised critical thickness = 0.63. x Saddle point θ , o Branch point θ_c , $\chi = \alpha = 0.027$ rds, $k_0 d = -5$. The refractive indices in each medium are : $n_0 = 1.5$; $n_1 = 2$; $n_2 = 1.76$; $n_3 = 1$.

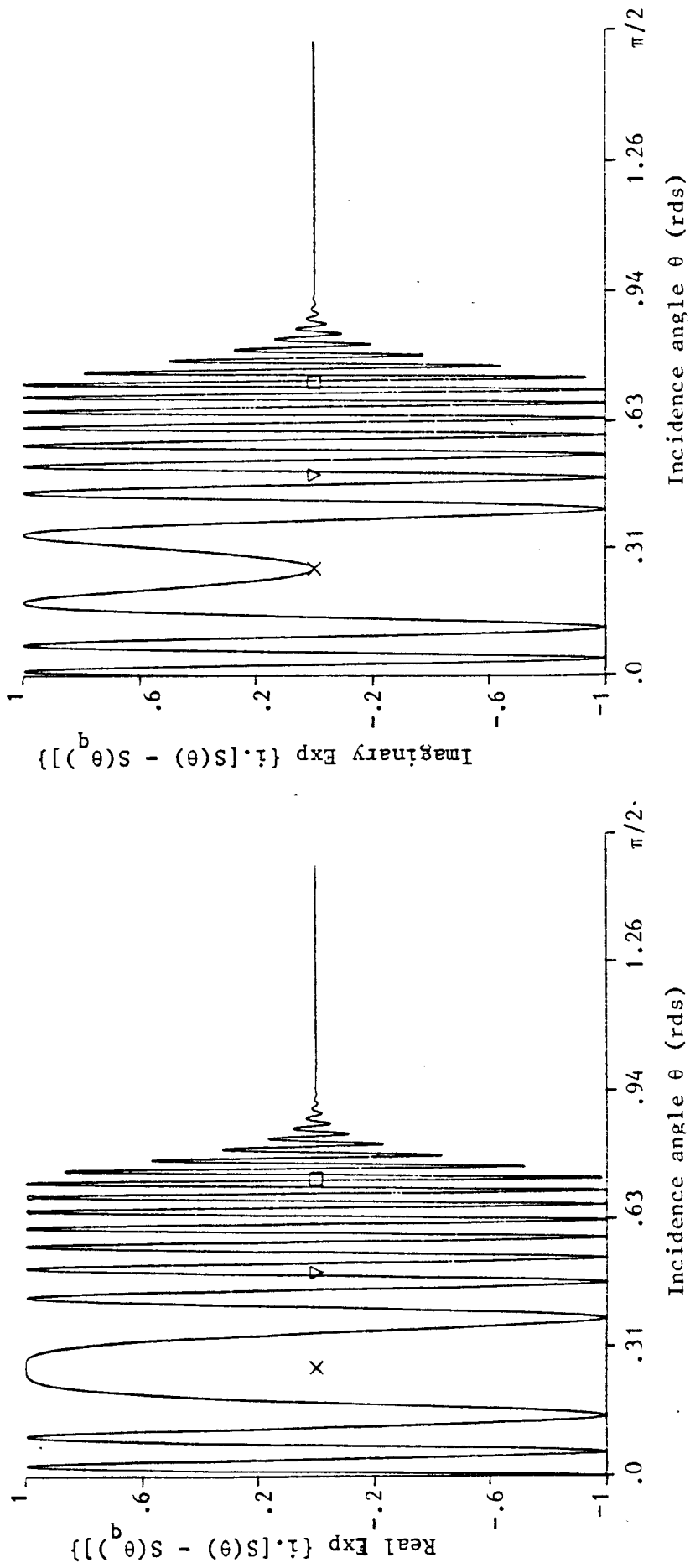


Fig.5.4a. continued. Computation of the integrand in the Radiation Integral (5.4) versus the incidence angle θ varying along the real axis

that $\text{Imag} \{S(\chi, \theta) - S(\chi, \theta_q)\}$ remains equal to zero even for θ beyond θ_c . It is only when θ exceeds θ'_c , that the imaginary part starts to increase. This is due to the fact that the eigenvalue equation for the double layer structure accommodates real solutions of θ_q even beyond θ_c . The solutions θ_q become complex only in the region beyond θ'_c .

The integrand variation of (5.4) is illustrated by Fig.5.4a continued. Both its components exhibit more rapid oscillations at one side of their respective extremum. They are qualitatively similar in variation to their counterpart in Fig.5.3a continued. But here, the decaying envelopes for both components seem to be faster. Hence, we can deduce that in the guided wave region, the single layer structure and the double layer structure behave in a quite similar manner for an observation point placed at B_{12} and for the same refractive indices of their respective medium. Consequently, as θ tends towards $\frac{\pi}{2}$ and beyond, the field magnitude vanishes.

(b) θ_q in the coupled wave region

In contrast, in Fig.5.4b, the saddle point θ_q is located in the coupled wave region at $k_0 T = 1.2$. Hence, even though θ_q is beyond the critical angle θ_c , it still remains real. This is due to the nature of eigenvalue equation governing the double layer structure. That is why $\text{Real} \{S(\chi, \theta) - S(\chi, \theta_q)\}$ falls to zero at θ_q . It is also noticed that both components of $\{S(\chi, \theta) - S(\chi, \theta_q)\}$ increase for θ past the branch point θ'_c . Such an increase of the imaginary part, represents the leakage taking place between the uniform film (n_2) and the substrate (n_0).

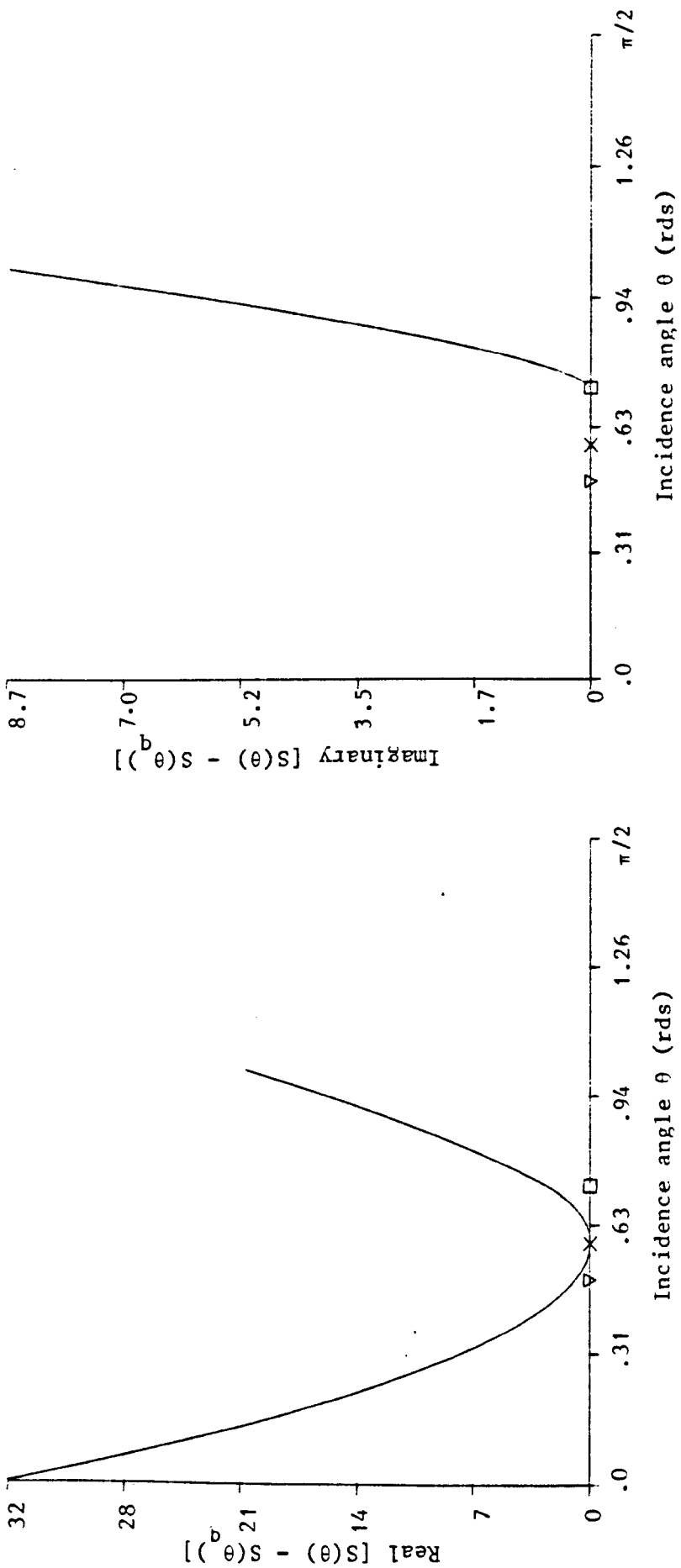


Fig.5.4b. Computation of the phase in the Radiation Integral (5.4) versus the incidence angle θ varying along the real axis, for the double layer structure. The saddle point is located in the coupled wave region at $k_0 T = 1.6$. Mode 1. First normalised critical thickness = 2.15, second normalised critical thickness = 0.63. \cdot Saddle point θ_c , ∇ critical angle θ_c' , \square Branch point θ_c'' , $\chi = \alpha = 0.027$ rds, $k_0 d = -5$.

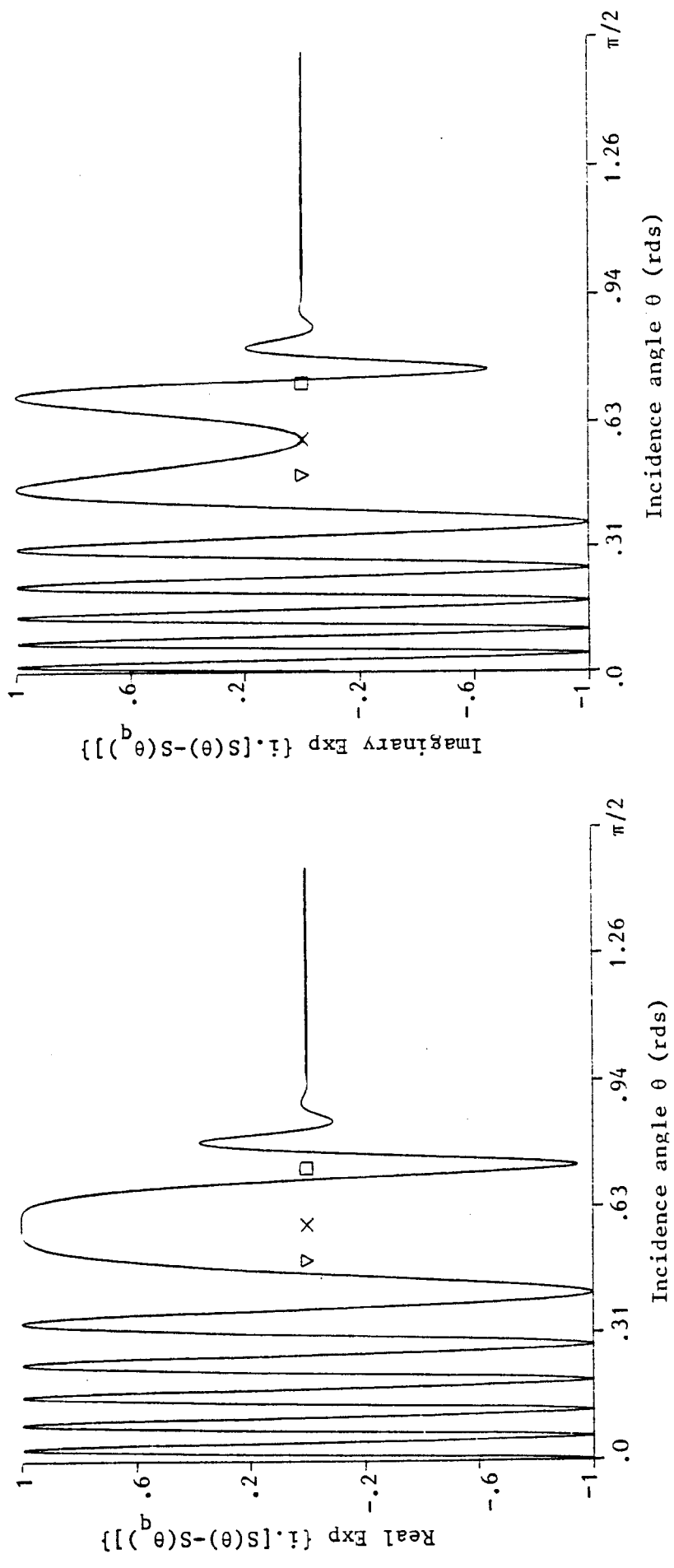


Fig.5.4b. continued. Computation of the integrand in the Radiation Integral (5.4) versus the incidence angle θ varying along the real axis

Finally, Fig.5.4b continued schematises how the integrand of (5.4) behaves, as θ varies along the real axis. Initially, real and imaginary parts manifest more rapid oscillations than in the case of the single layer problem, as reported by Fig.5.3b continued. There, as θ increases towards $\frac{\pi}{2}$, they are characterised by an exponentially vanishing envelope. Consequently, we have shown that, even for the double layer problem; the field exhibited for θ beyond $\frac{\pi}{2}$ is vanishingly small. Hence, we neglect all spectral plane waves exhibiting an incident angle higher than $\frac{\pi}{2}$.

5.3.3. Definition of integration contour along the real axis

For both structures we have shown in the previous subsections that for any location of the saddle point θ_q with respect to θ_c it is safe to neglect the field contribution outside the range $0 < \theta < \frac{\pi}{2}$.

Returning to the Radiation Integral (5.4), we shall then perform it along the real axis and in the interval $0 < \theta < \frac{\pi}{2}$. In this case, the presence of any branch point or pole (as may be the case for the double layer problem), will automatically be taken care of. The convergence of (5.4) is, however, guaranteed by taking an integration step length much smaller than the oscillating periods of Figs.5.3. and Figs.5.4. It is also necessary to maintain the same branch conventions for $(\theta - \theta_c)^{\frac{1}{2}}$ and $(\theta - \theta')^{\frac{1}{2}}$, defined earlier in the previous chapter.

In as far as we are not using the saddle point method to calculate (5.4), knowledge of the saddle point θ_q is not necessary. In spite of this, we still represent each observation point

$\underline{X} \equiv (\chi, r)$ by its equivalent notation $\underline{X} \equiv (\chi, \theta_q)$.

Note that Figs.5.3 and Figs.5.4 have been numerically carried out for an observation point \underline{X} at $\chi = \alpha$ and for the first mode $q = 1$ only. Similar qualitative results could have been obtained for any other parameter.

5.4. Application of the Radiation Integral to the single layer structure

5.4.1. Radiation field in the guided wave region

Let us now concentrate first on Fig.5.5a. It illustrates the variation of the normalised field modulus in medium (n_2) , versus the variable χ , for mode 1 of the single layer structure. Three locations of the observation point \underline{X} are considered, in the guided wave region, $\theta_q < \theta_c$. They correspond to the three distinct normalised thickness in (i), (ii) and (iii) of Fig.5.5a. Thereby, it is clear that, as θ_q approaches θ_c (that is to say, as $k_0 T$ approaches the critical thickness of the corresponding mode), the evanescent field decays less rapidly in the substrate (n_2) . The decay is more strongly evanescent, when \underline{X} is located far from θ_c , as in (i), than when it is near, as in (iii). This is mainly because, in such a region, the waves inside the tapered waveguide are totally guided. When θ_q approaches θ_c , as is the case in (iii), energy starts leaking out from the inside of the tapered waveguide to the medium (n_2) . As a matter of fact, this leakage near the transition region, makes the amplitude of the cross section field inside the tapered waveguide decrease in the guided wave region.

Of course, the above remarks hold for any higher mode,

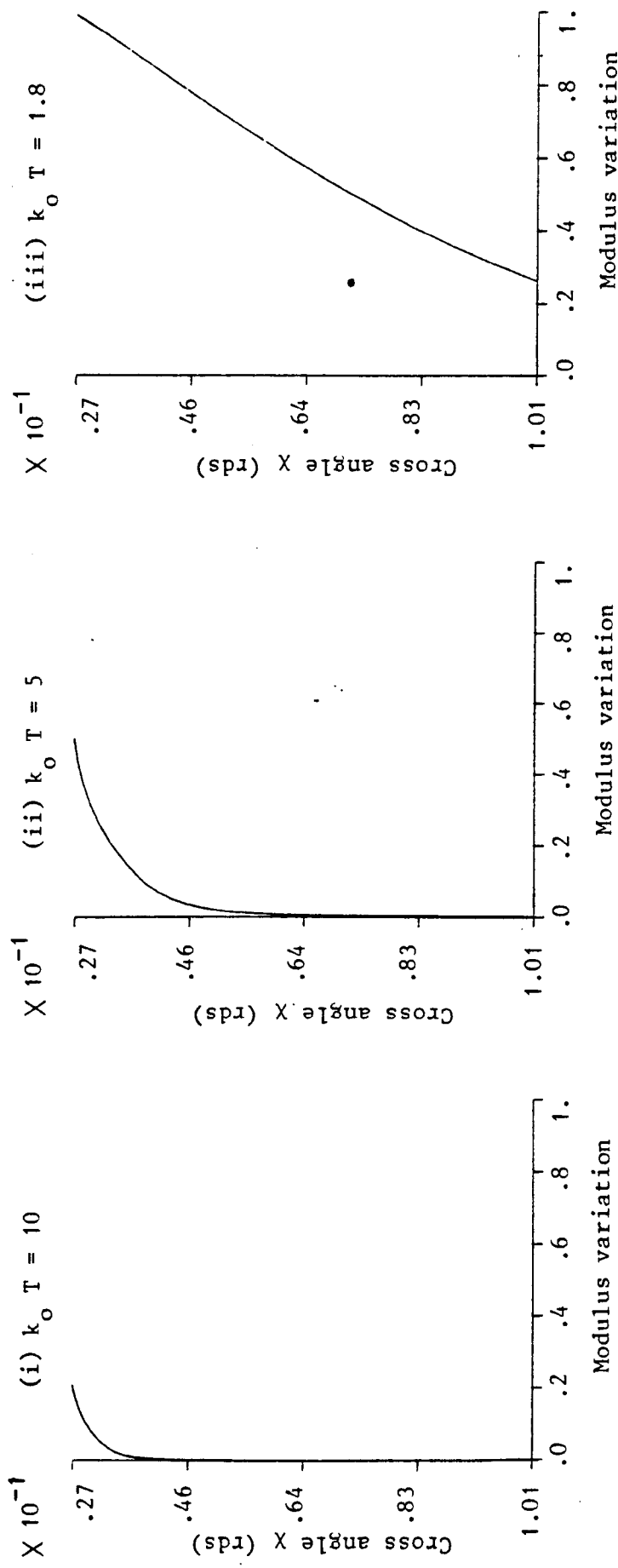


Fig. 5.5a. Computation of the normalised cross section radiation field in medium (n_2) versus the cross angle X , for the single layer structure. The saddle points in (i), (ii) and (iii) are located in the guided wave region. Mode 1, normalised critical thickness = 1.75, $\alpha = 0.027$ rds. The refractive indices in each medium are : $n_1 = 2$; $n_2 = 1.76$; $n_3 = 1$.

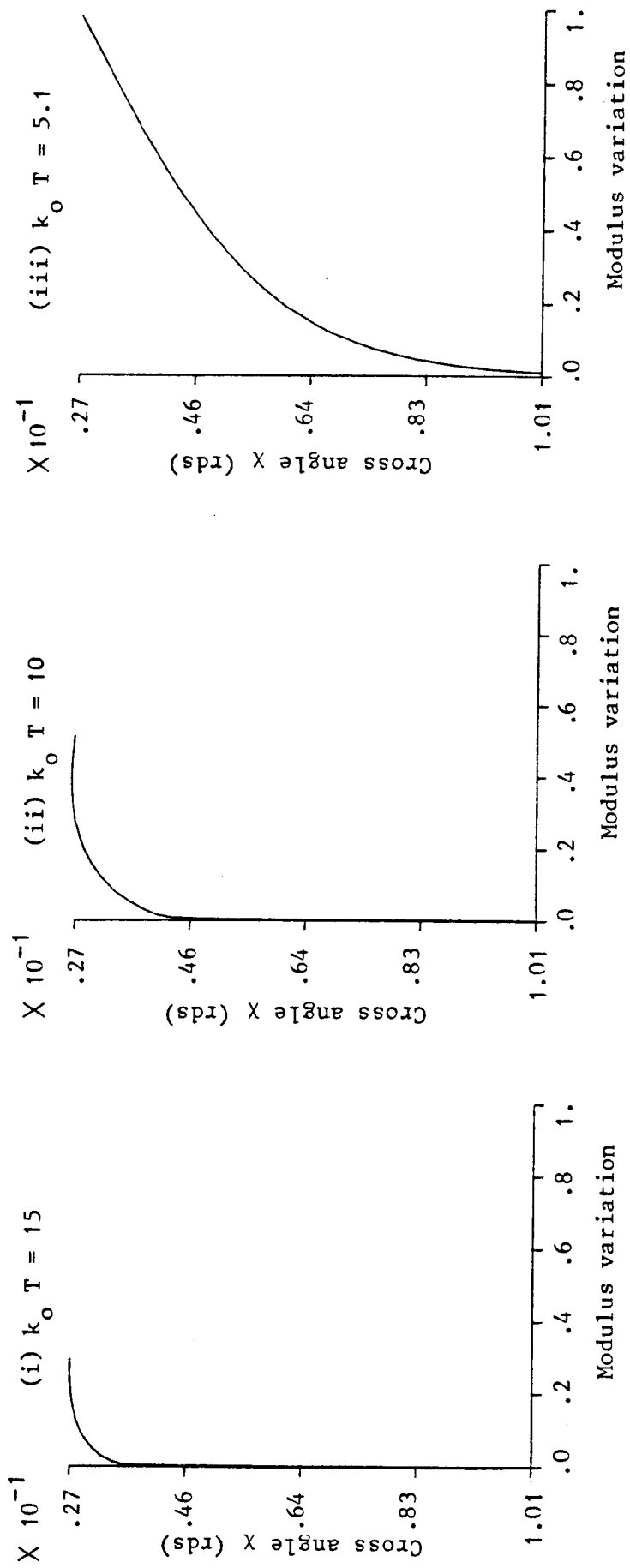


Fig.5.5b. Mode 2. Normalised critical thickness = 5

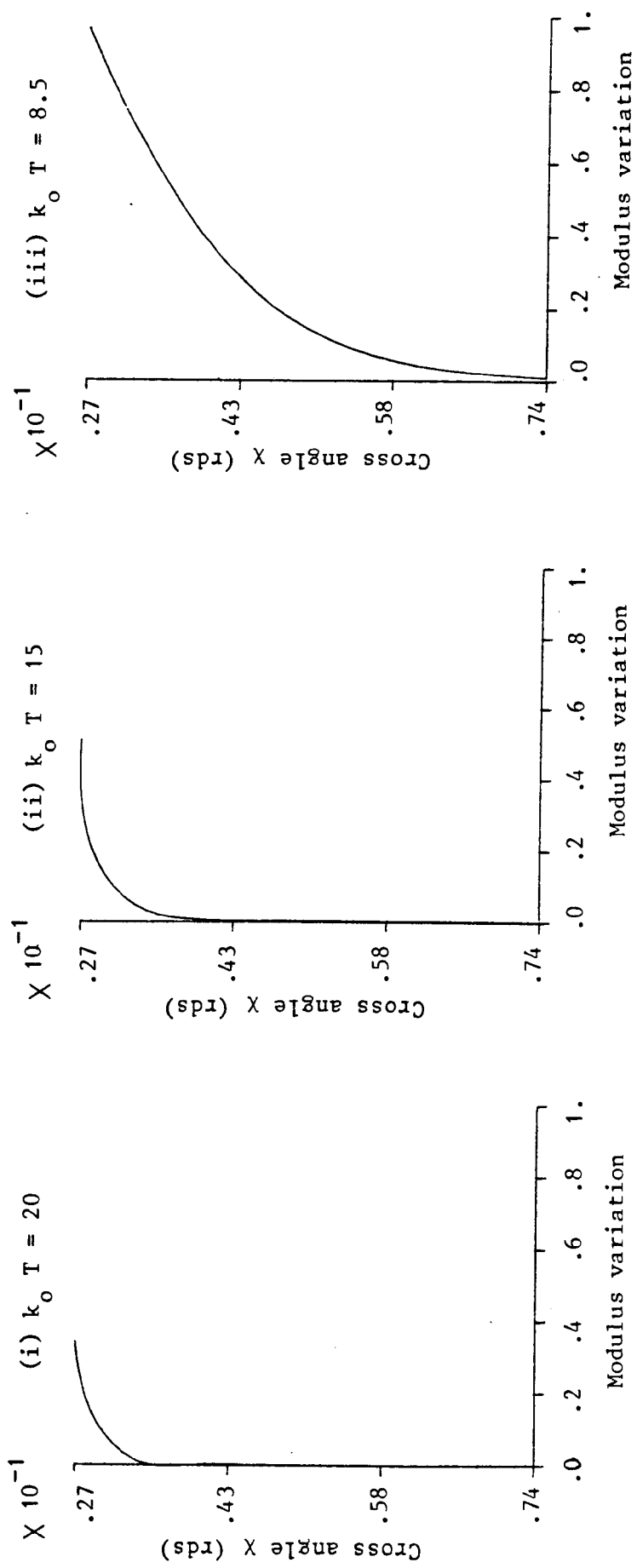


Fig.5.5c. Mode 3. Normalised critical thickness = 8.5

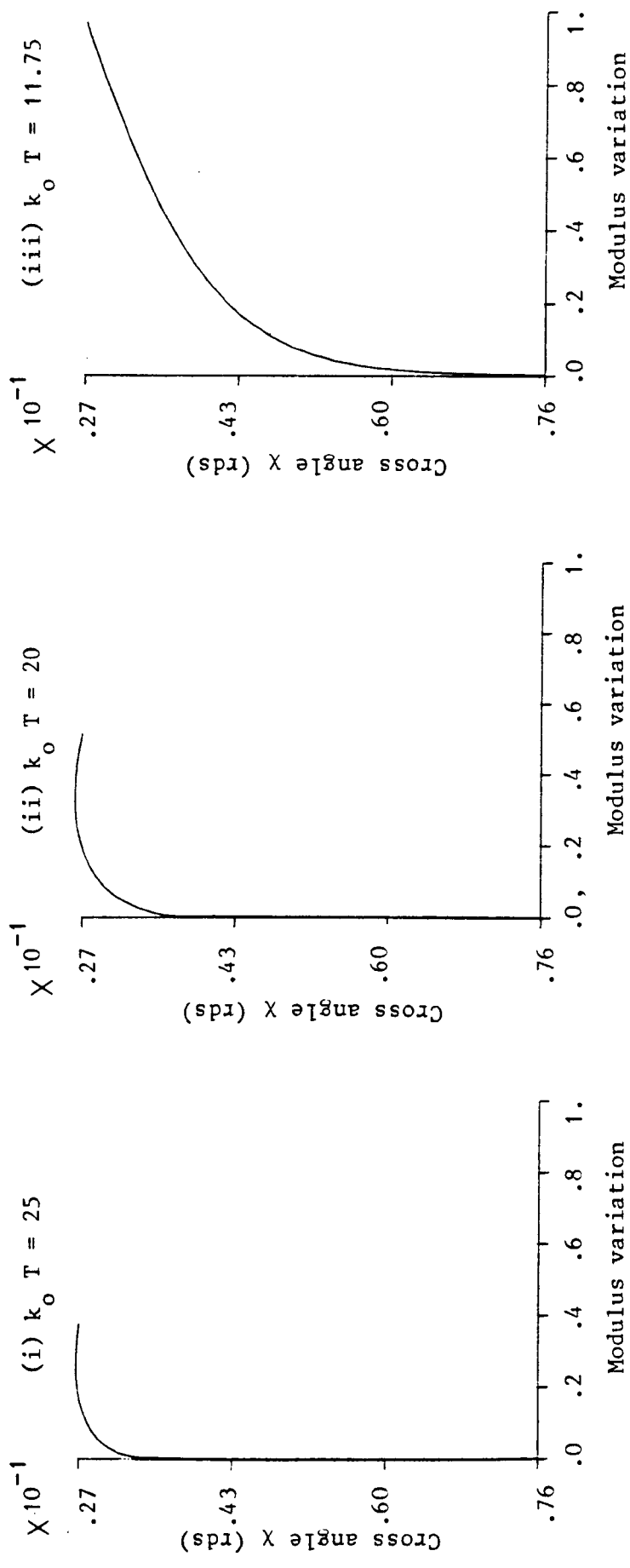


Fig.5.5d. Mode 4. Normalised critical thickness = 11.75

characterised by its own corresponding critical thickness, as illustrated by Figs.5.5b, 5.5c and 5.5d, corresponding respectively to mode 2, 3 and 4.

5.4.2. Radiation field in the leaky wave region

In this case, all observation points \underline{X} are located in the leaky wave region, such as $\theta_q > \theta_c$. In this region, energy is leaked out from the tapered waveguide to the medium (n_2). Such a leakage characterises the radiation process taking place at the bottom interface B_{12} . The light rays then are no longer totally reflected back into the tapered waveguide, but are partially transmitted into medium (n_2) as refracted waves.

Figs.5.6 show the variation of the normalised modulus of the radiated field, versus the angular variable χ , for the four lowest mode of the single layer structure. There too, we consider three positions of the observation point \underline{X} , for each mode, but each one is located in the leaky wave region.

Dealing first with mode 1, as illustrated by Fig.5.6a, it is seen in each plotting that the field oscillates to a maximum, then decays exponentially because of the continuous refraction taking place in medium (n_2). Also, in each diagram, the locus engendered by each maximum of the radiated field describes a caustic whose gradient with respect to the bottom interface B_{12} , corresponding to $\chi = \alpha$, represents the directionality of the beam of the radiation pattern. It is the existence of this caustic that causes the field (in each diagram of Fig.5.6a) to oscillate in one part of the cross section pattern, and decay exponentially in the other. We also notice that the amplitude

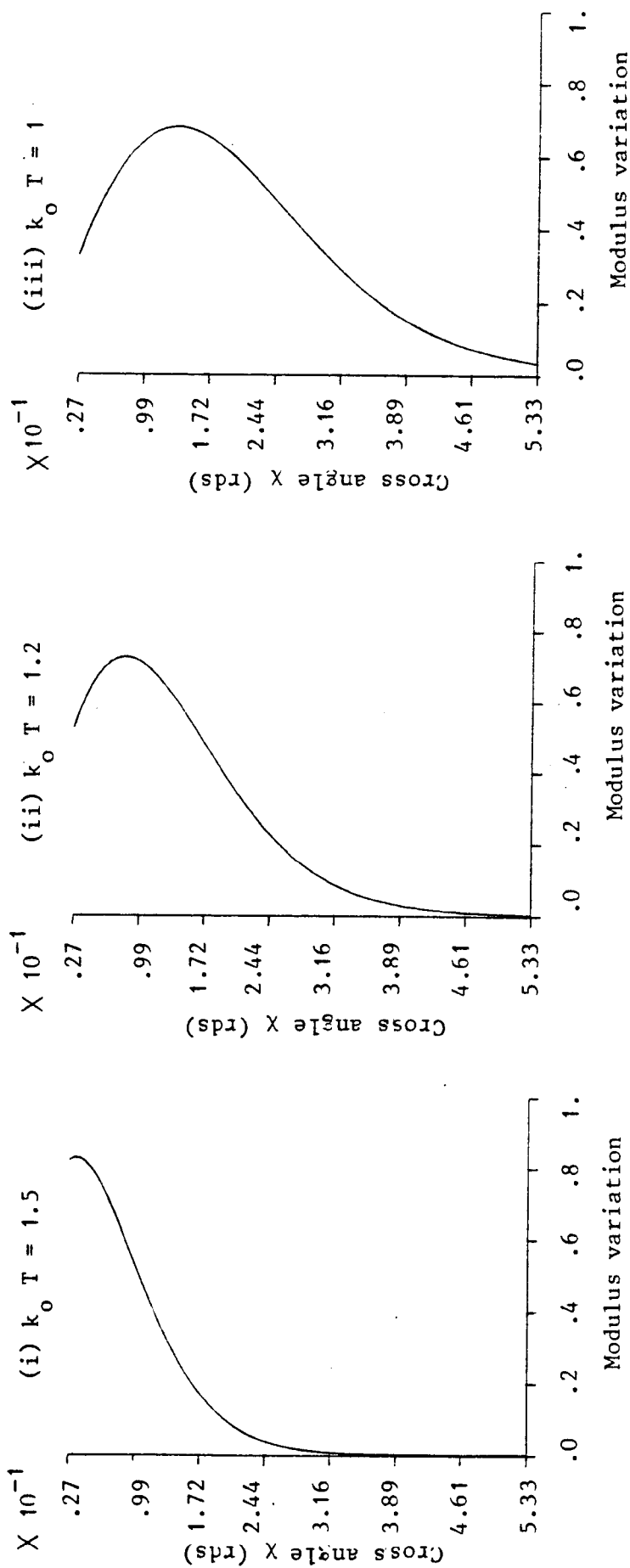


Fig.5.6a. Computation of the normalised cross section radiation field in medium (n_2) versus the cross angle X , for the single layer structure. The saddle points in (i), (ii) and (iii) are located in the leaky wave region. Mode 1, normalised critical thickness = 1.75, $\alpha = 0.027$ rds. The refractive indices in each medium are : $n_1 = 2$; $n_2 = 1.76$; $n_3 = 1$.

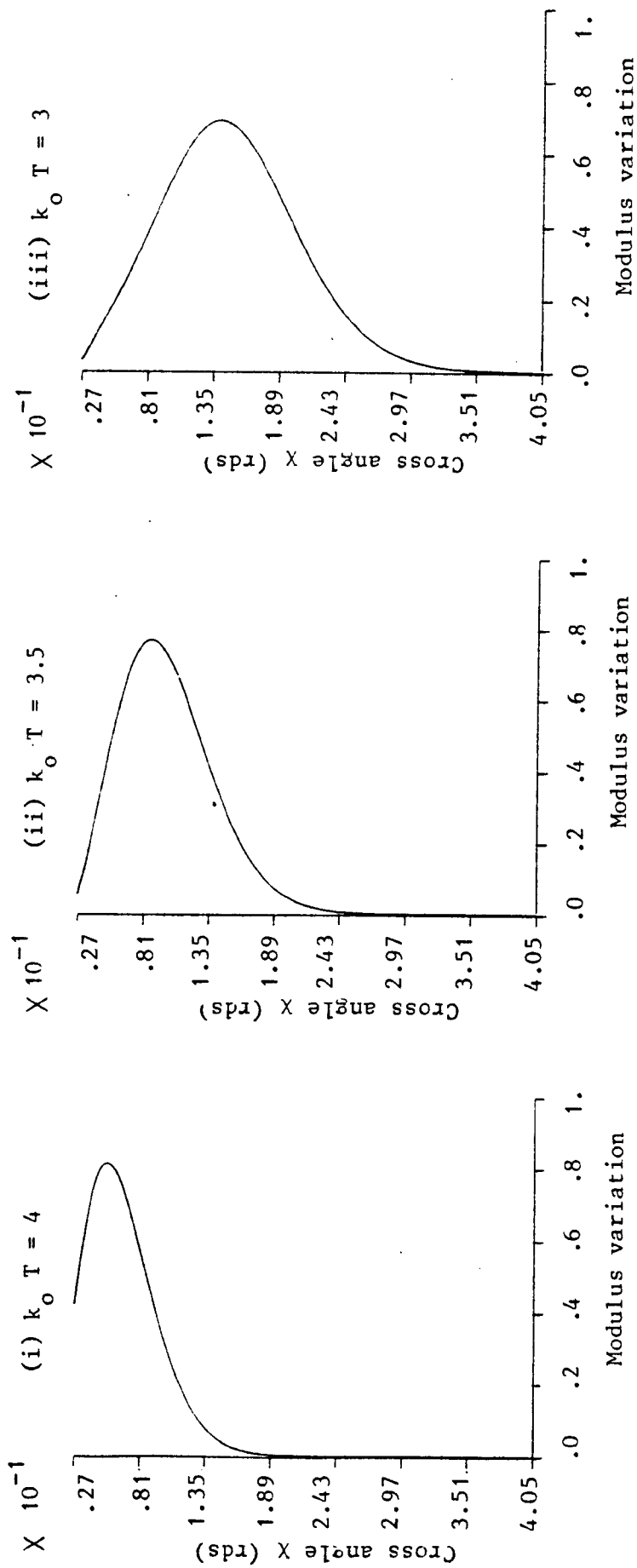


Fig.5.6b. Mode 2. Normalised critical thickness = 5

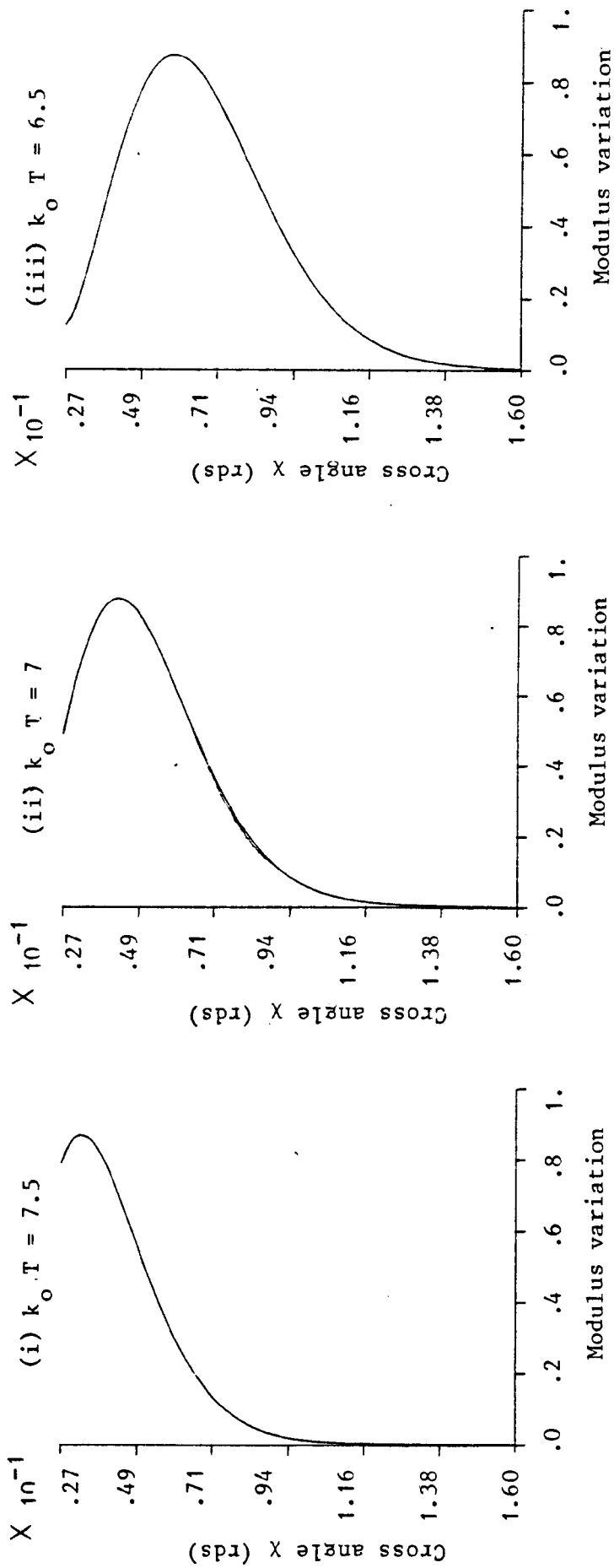


Fig.5.6c. Mode 3. Normalised critical thickness = 8.5

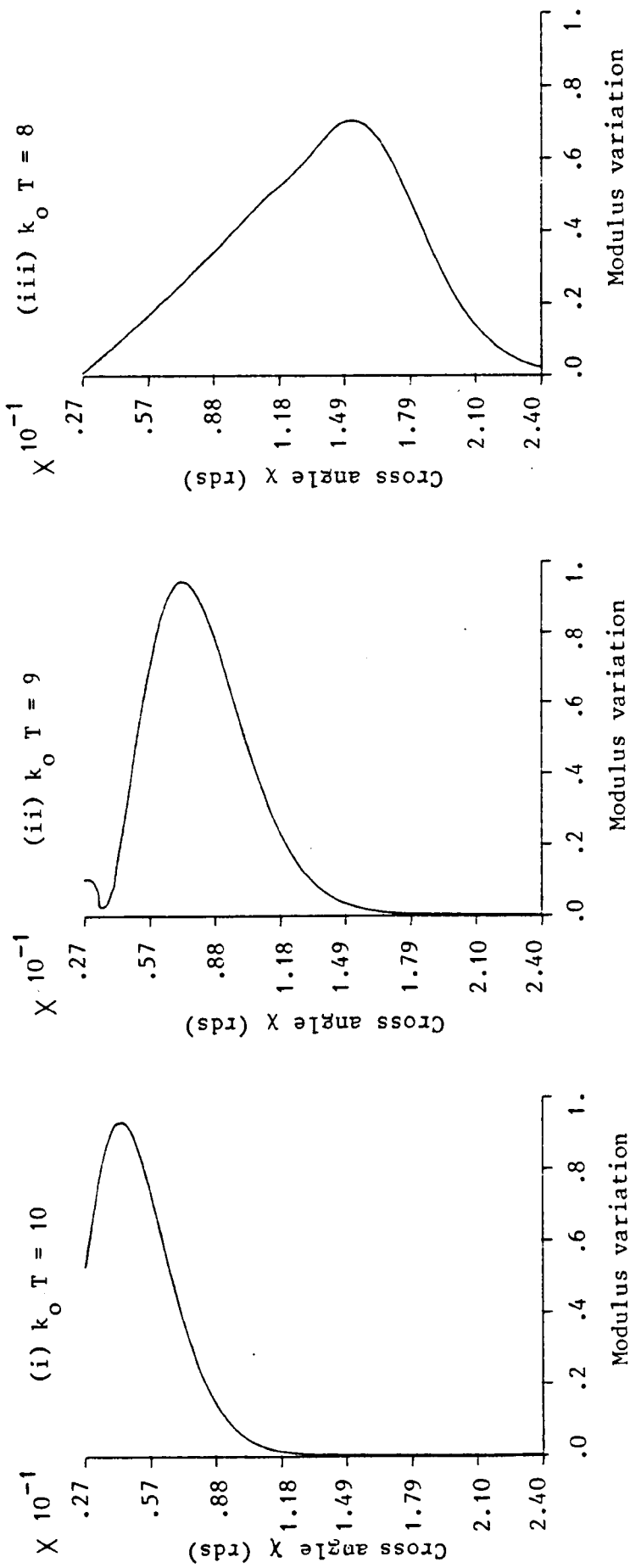


Fig.5.6d. Mode 4. Normalised critical thickness = 11.75

of the field maximum becomes smaller as the thickness $k_0 T$ diminishes from one diagram of Fig.5.6a to another. This emphasises the fact that as θ_q moves in the leaky wave region, away from θ_c and towards $\frac{\pi}{2}$, the field tends to vanish. The same remarks apply to any higher mode as presented by Figs .5.6b, 5.6c and 5.6d, respectively illustrating mode 2, 3 and 4.

However, spurious numerical discrepancies appear on some diagrams such as in Fig.5.6d, for $k_0 T = 9$. There, the field should be continuous for χ very near to $\alpha = 0.027$ rds. It is believed that these are small numerical errors due to the neglect of terms having the same order of magnitude as the wedge angle α in the analysis.

The computer program elaborated for implementing (5.4) is given by Appendix F.

5.5. Radiation Integral for the double layer structure

As far as the double layer structure is concerned, this section deals with the field distribution in the uniform film (n_2) only, which is confined by the constant thickness d (see Fig.5.8). It is actually the existence of that limited thickness d which causes some limitations in the model presented earlier for the construction of the Radiation Integral $R(\chi, \theta)$.

For observation point \underline{X} located in the highly guided wave region, where $\theta_q < \theta_c$, we can permit equation (5.4) to be used in order to describe the radiation mechanism taking place in the uniform film (n_2). In this case, all rays inside the tapered waveguide are totally reflected at interface B_{12} . In this sense only, the expected evanescent field in the uniform film (n_2)

would not react back from the boundary B_{20} into the boundary B_{12} , at least as long as $\theta_q < \theta_c$ (see Fig.5.8). But, as the observation point goes beyond the transition region (as T diminishes beyond the critical thickness corresponding to each mode) the Radiation Integral (5.4) can no longer be used to describe the radiation process taking place in the coupled wave region. The reason for this is that when coupling from the tapered waveguide to the uniform film (n_2) begins to manifest itself, the rays in the latter are reflected from B_{20} . These rays couple back from the uniform film (n_2) to the tapered waveguide and interfere with the already existing rays inside the tapered waveguide. One is then required to construct another model, in order to describe the coupling mechanism occurring in the uniform film (n_2), for an observation point located in the coupled wave region, which accounts for the above phenomenon.

5.5.1. Radiation field in the guided wave region

Locating an observation point such as $0 < \theta_q < \theta_c$, one can safely use equation (5.4) to predict the field in the uniform film (n_2). We substitute in (5.4), the expression of $\phi(\theta)$ given by Appendix D. We also bear in mind that the integration in (5.4) is along the real axis, $0 < \theta < \frac{\pi}{2}$. In this case, the existence of any pole through $\phi(\theta)$, will automatically be taken care of. To this purpose, Appendix F gives a brief presentation of the computer program used for such an implementation. Figs.5.7 represent the variation of the normalised field modulus, as given by (5.4), versus the cross variable χ , for a few of the lowest modes of the double layer structure. Thereby, in each figure, we

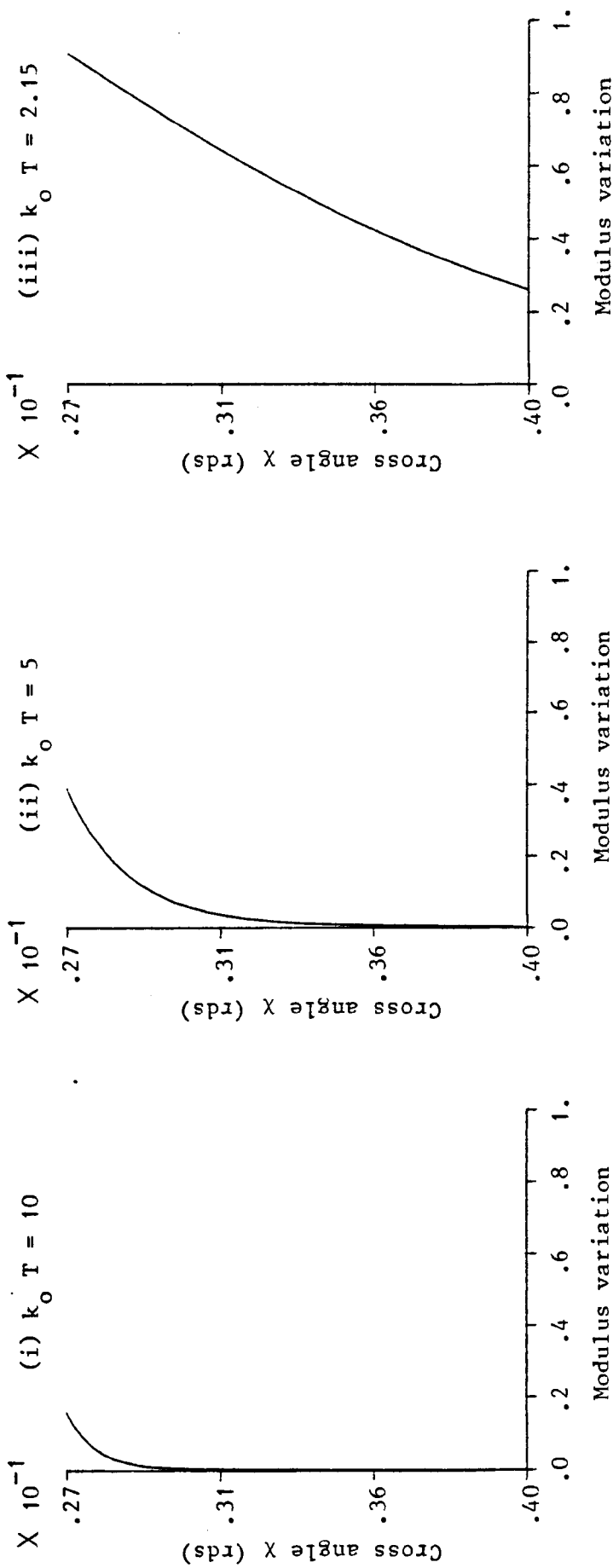


Fig.5.7a. Computation of the normalised cross section radiation field in the uniform film (n_2) versus the cross angle χ , for the double layer structure. The saddle points in (i), (ii) and (iii) are located in the guided wave region. First normalised critical thickness = 2.15, second normalised critical thickness = 0.63. The refractive indices in each medium are : $n_0 = 1.5$; $n_1 = 2$; $n_2 = 1.76$; $n_3 = 1$. Mode 1, $k_0 d = -5$, $\alpha = 0.027$ rds

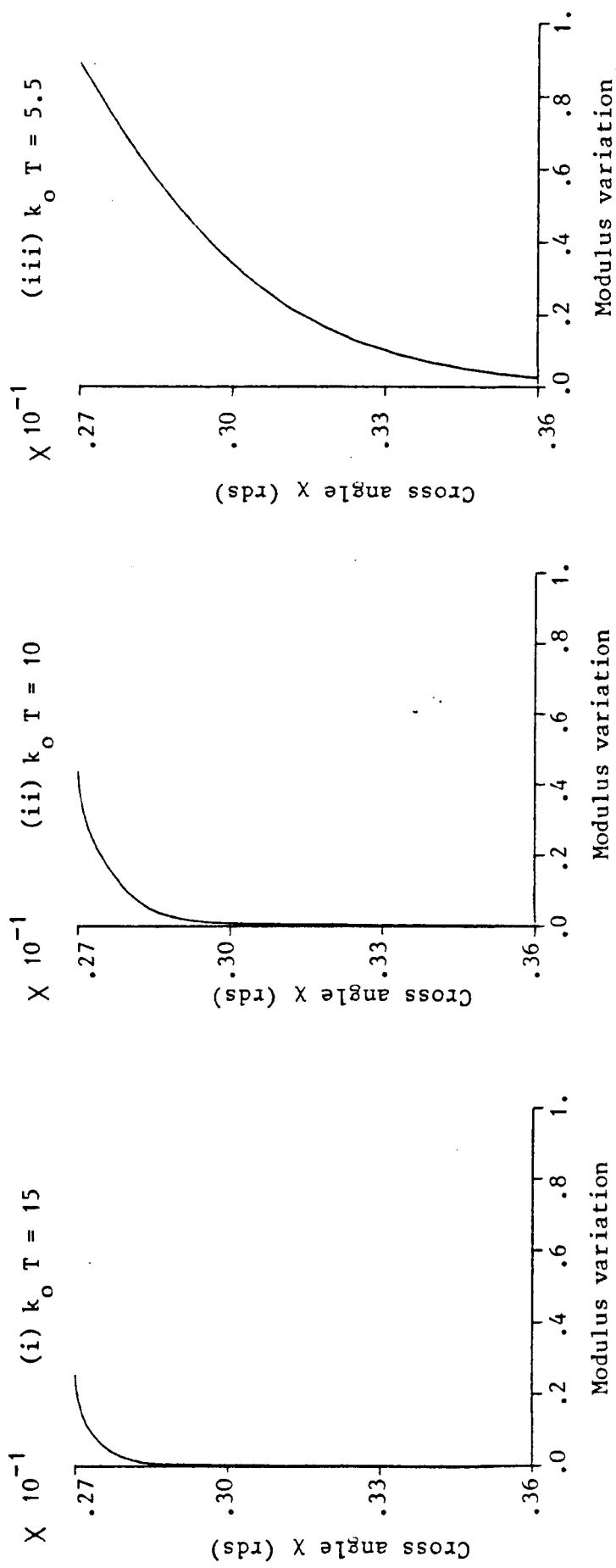


Fig.5.7b. Mode 2. First normalised critical thickness = 5.46, second normalised critical thickness = 3.07

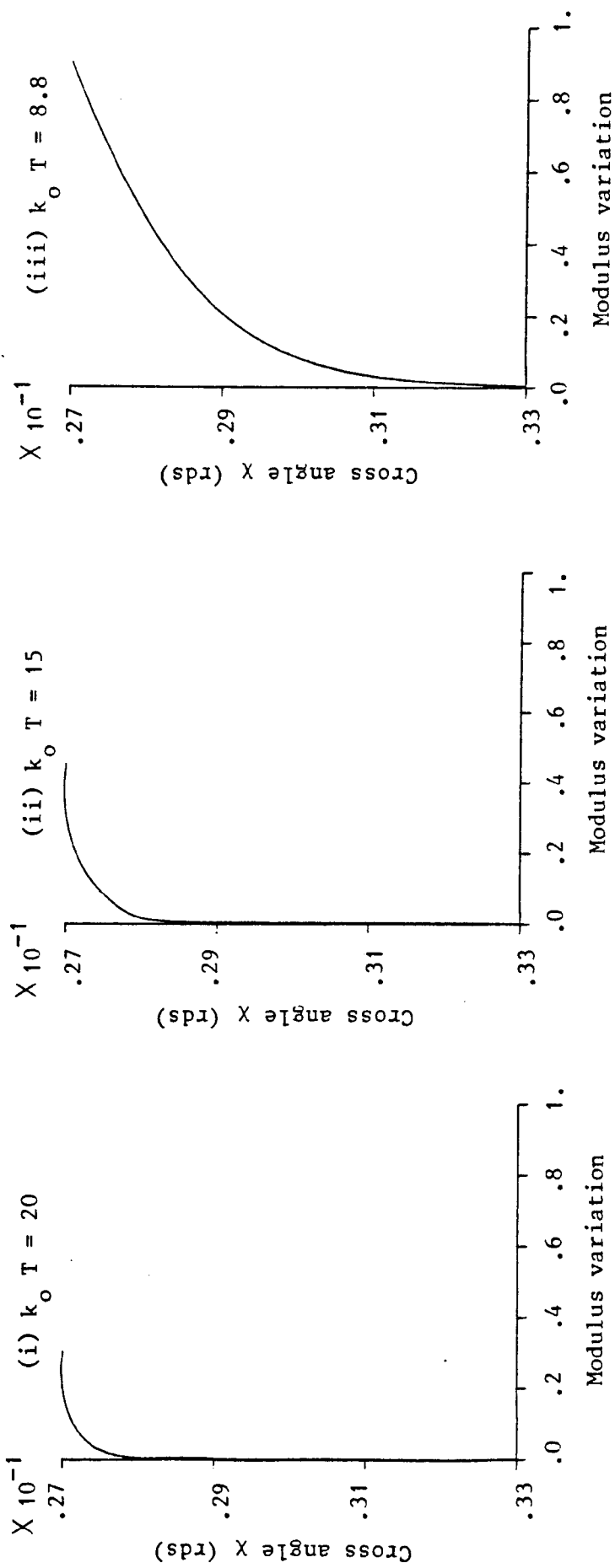


Fig. 5.7c. Mode 3. First normalised critical thickness = 8.76, second normalised critical thickness = 5.38

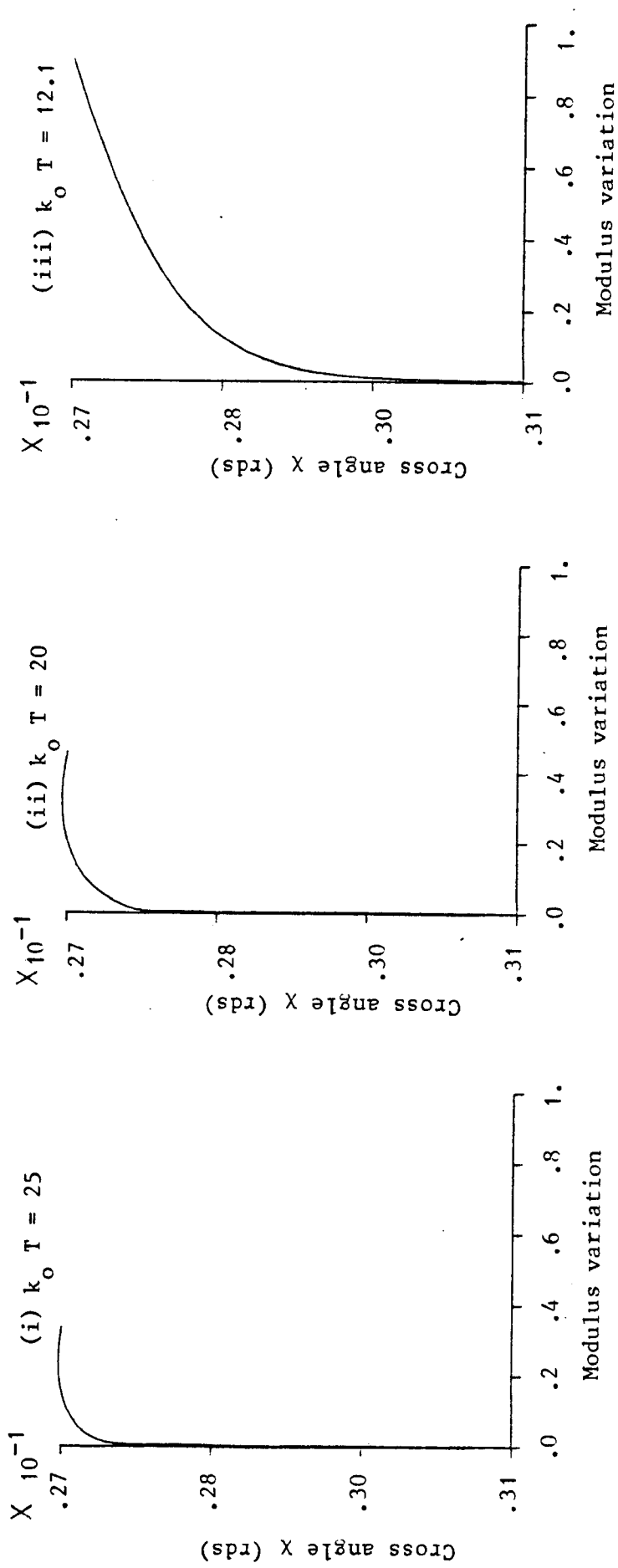


Fig.5.7d. Mode 4. First normalised critical thickness = 12.07, second normalised critical thickness = 7.76

consider 3 distinct normalised thicknesses $k_0 T$, corresponding to 3 saddle points θ_q , situated in the guided wave region, such as $0 < \theta_q < \theta_c$.

Let us consider Fig.5.7a first. It describes the normalised cross section field behaviour of mode 1, versus the cross variable χ , in the uniform film (n_2). In each diagram, the field exhibits an evanescent distribution, whose decay rate becomes smaller as $k_0 T$ approaches the first critical thickness (that is to say, from (i) to (iii) in the figure). For an observation point near the first critical thickness, as is the case in (iii), the slowest evanescent field is a consequence of the coupling beginning to take place, between the tapered waveguide and the uniform film (n_2).

A similar reasoning applies to higher modes, as illustrated by Figs.5.7b, 5.7c and 5.7d, respectively for mode 2, 3 and 4.

5.5.2. Radiation Integral in the coupled wave region

(a) Definition

For an observation point located in the coupled wave region, $\theta_q > \theta_c$, one cannot use equation (5.4) to simulate the radiation mechanism in the uniform film (n_2), for reasons stated earlier in this section. To circumvent this, one must find another model to comply with the requirement. Fig.5.8 illustrates the mechanism, when a downgoing wave inside the tapered waveguide, is refracted into a wave A_2 , inside the uniform film (n_2). The other upgoing wave A_2' results from the wave A_2 , after being reflected at interface B_{20} and also after travelling twice the optical path (2d), inside the film (n_2).

Continuity of fields at interface B_{12} , stipulates that :

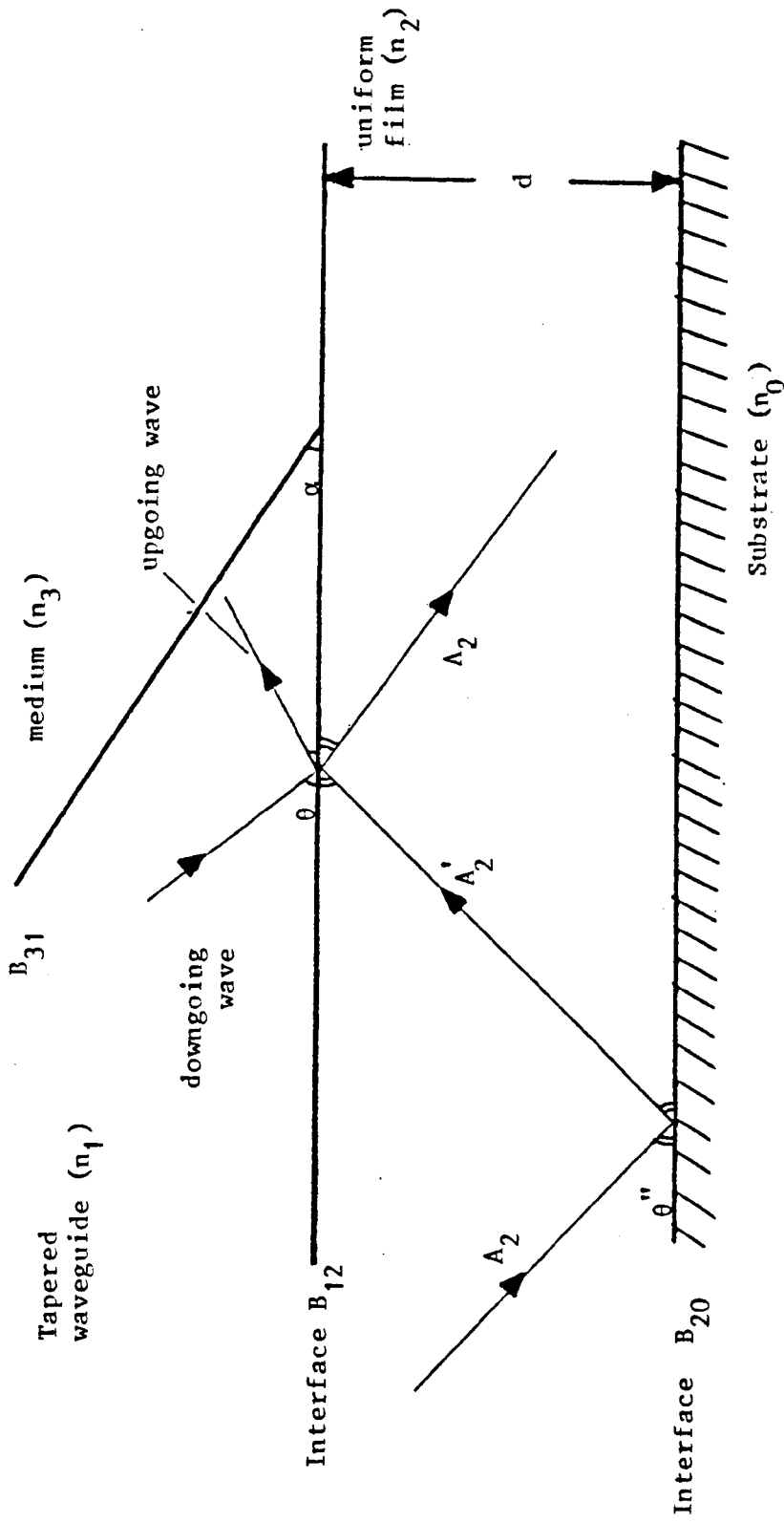


Fig.5.8 : Configuration of rays which contribute to the Radiation Integral for the double layer structure

$$A_2' + A_2 = 1 + \exp[i \phi(\theta)] \quad (5.9a)$$

where $\phi(\theta)$ is the phase of the reflection coefficient introduced at that interface; and which is given by Appendix D. Expression (5.9a) represents the composite transmitted wave in the uniform film (n_2). One can also deduce geometrically that :

$$A_2' = A_2 \exp[i \gamma(\theta'')] \quad (5.9b)$$

where :

$$\gamma(\theta'') = \phi_{20}(\theta'') + 2 k_0 d n_2 \sin \theta'' \quad (5.9c)$$

One recalls Snell's law :

$$n_1 \cos \theta = n_2 \cos \theta'' \quad (5.9d)$$

$\phi_{20}(\theta'')$ is the phase of the Fresnell reflection coefficient introduced at interface B_{20} , which is given by :

$$\phi_{20}(\theta'') = 2 \operatorname{Atan} \left\{ i \frac{(n_0^2 - n_2^2 \cos^2 \theta'')^{\frac{1}{2}}}{(n_2^2 - n_0^2 \cos^2 \theta'')^{\frac{1}{2}}} \right\} \quad (5.9e)$$

Combining expressions (5.9) gives :

$$A_2' = \frac{1 + \exp[i \phi(\theta)]}{1 + \exp[i \gamma(\theta)]} \exp[i \gamma(\theta)] \quad (5.10a)$$

and

$$A_2 = \frac{1 + \exp[i \phi(\theta)]}{1 + \exp[i \gamma(\theta)]} \quad (5.10b)$$

bearing in mind that :

$$\gamma(\theta) = 2 \operatorname{Atan} \left\{ \frac{i (n_0^2 - n_1^2 \cos^2 \theta)^{\frac{1}{2}}}{(n_2^2 - n_1^2 \cos^2 \theta)^{\frac{1}{2}}} \right\} + 2 k_0 d (n_2^2 - n_1^2 \cos^2 \theta)^{\frac{1}{2}} \quad (5.10c)$$

For simplicity, we shall assume that the substrate (n_0) is a perfectly reflecting medium, because of the relatively large index difference between n_2 and n_0 . That is to say, $\phi_{20}(\theta) = -\pi$. In this case, equation (5.10c) becomes :

$$\gamma(\theta) = -\pi + 2 k_0 d (n_2^2 - n_1^2 \cos^2 \theta)^{\frac{1}{2}} \quad (5.10d)$$

We can finally construct the Radiation Integral, which accounts for the contributions of the upgoing A_2' and for that of the downgoing wave A_2 , in the film (n_2), in the same manner as done in section 5.1. The result is :

$$R(\chi, \theta) = (2 \alpha)^{-\frac{1}{2}} \int_{C'} A_2' \exp[i k S_e^{u'}(\chi, \theta)] d\theta + \\ (2 \alpha)^{-\frac{1}{2}} \int_{C'} A_2 \exp[i k S_o^u(\chi, \theta)] d\theta \quad (5.11a)$$

The contour (C') in (5.11a) is given by Fig.4.1. But, as we have proved in earlier sections, this contour can safely be taken as the real axis and confined in the interval $0 < \theta < \frac{\pi}{2}$. The phase $S_o^u(\chi, \theta)$ in (5.11a) is given by equation (5.19b), with the amendment that the incident angle θ becomes θ'' ; the wave number $k = n_2 k_0$, refers to the film (n_2). As for the phase $S_e^{u'}(\chi, \theta)$ in (5.11a), it characterises the upgoing wave A_2' in the film (n_2), which suffers reflection less than the wave $\exp[i k S_e^u(\chi, \theta)]$ at interface B_{12} . In this case, one defines :

$$k S_e^{u'}(\chi, \theta) = k S_e^u(\chi, \theta) - \phi(\theta) \quad (5.11b)$$

where, $S_e^u(\chi, \theta)$ is given by equation (3.19a) with the same

above remarks as those concerning $S_o^u(\chi, \theta)$.

Bearing in mind the above remarks, recalling (3.19a) and (3.19b), with the omission of the source term, and inserting (5.10) into (5.11), one achieves the Radiation Integral which describes the coupling taking place in the uniform film (n_2) and which is :

$$R(\chi, \theta) = (2\alpha)^{-\frac{1}{2}} \int_{C'} 2 \cos \frac{\phi(\theta)}{2} \left\{ \frac{\cos[k_o r \sin(\alpha-\chi) (n_2^2 - n_1^2 \cos^2 \theta)^{\frac{1}{2}} + \frac{\gamma(\theta)}{2}]}{\cos[\frac{\gamma(\theta)}{2}]} \right\} \\ \times \exp \left\{ i \left[-k_o n_2 r \cos \theta \cos(\chi-\alpha) + \frac{1}{2\alpha} \int_{\theta}^{\theta} \phi(\theta') d\theta' + \frac{\pi\theta}{2\alpha} (1-2q) \right] \right\} \\ \times d\theta \quad (5.12)$$

We recall that $\gamma(\theta)$ and $\phi(\theta)$ are respectively stated in equation (5.10d) and Appendix D.

An important remark ought to be made at this point, which is that (5.12) matches perfectly the Intrinsic Integral (4.4) corresponding to the double layer structure at boundary B_{12} (at $\chi = \alpha$). This is to satisfy the boundary condition between the field inside the tapered waveguide and that in the uniform film (n_2) at interface B_{12} , for the structure. In addition, another important observation is that, for an observation point \underline{X} situated on interface B_{12} ($\chi = \alpha$) one can easily check that (5.12) yields the original Radiation Integral (5.4). Hence, this justifies the use of (5.4) earlier in subsection 5.3.2.

(b) Change from polar to Cartesian coordinates

Up until now, the cross section variable χ (in radians),

represents one of the polar coordinates of any observation point $\underline{X} \equiv (\chi, r)$ with respect to interface B_{31} . In order to be consistent with the physical geometry of the double layer geometry, particularly in the coupled wave region, we shall introduce a slight change of variable as shown in Fig.5.9. Thereby, the polar coordinate χ (referred to from top interface B_{31}), becomes a Cartesian coordinate x (referred to from bottom interface B_{12}). Consequently, in order to describe the field inside the film (n_2), the cross variable x (which also represents a depth) must be confined in the interval :

$$0 < x < d \quad (5.13a)$$

In terms of normalised variable, equation (5.13a) becomes :

$$0 < k_o x < k_o d \quad (5.13b)$$

From Fig.5.9, one can deduce the following change of variables :

$$\sin(\alpha - \chi) = \frac{k_o x}{k_o r} \quad (5.14a)$$

$$\cos(\alpha - \chi) = \frac{k_o T}{k_o r \tan \alpha} \quad (5.14b)$$

where the normalised range $k_o r$ is given by :

$$(k_o r)^2 = (k_o x)^2 + \left(\frac{k_o T}{\tan \alpha}\right)^2 \quad (5.14c)$$

Inserting (5.14) into (5.12), one obtains the final Radiation Integral describing the radiation mechanism for the double layer problem in the coupled wave region, which is :

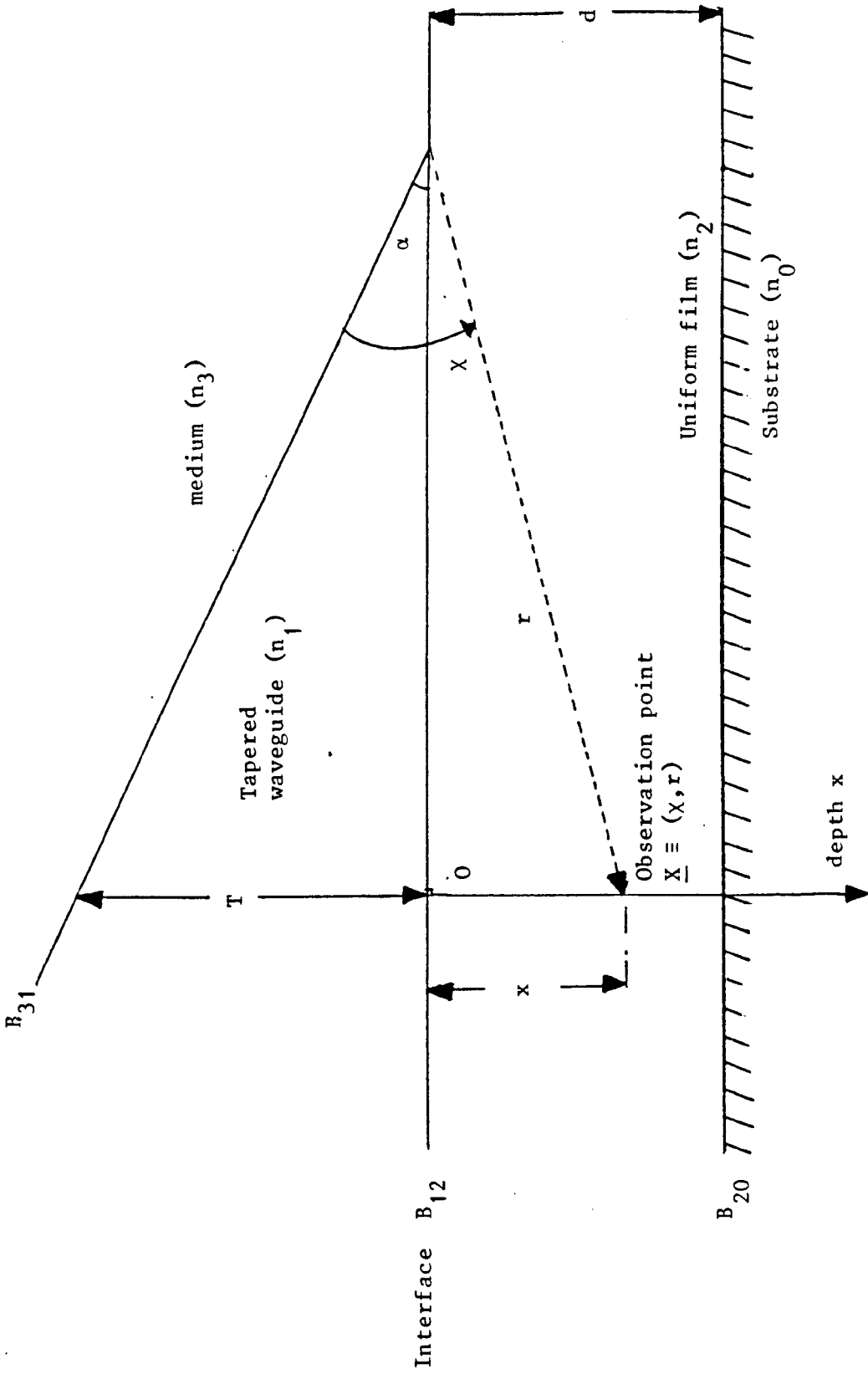


Fig.5.9 : New reference system

- $0 < x < \alpha$ or $x < 0$: observation point \underline{X} inside the tapered waveguide
- $x > \alpha$ or $x > 0$: observation point \underline{X} outside the tapered waveguide

$$R(\chi, \theta) = (2\alpha)^{-\frac{1}{2}} \int_{C'} \cos \frac{\phi(\theta)}{2} \left\{ \frac{\sin[(d-x) k_o (n_2^2 - n_1^2 \cos^2 \theta)^{\frac{1}{2}}]}{\sin[k_o d (n_2^2 - n_1^2 \cos^2 \theta)^{\frac{1}{2}}]} \right\} \\ \exp \left\{ i \left[\frac{n_1 \cos \theta k_o T}{\tan \alpha} + \frac{1}{2\alpha} \int_{\theta_c}^{\theta} \phi(\theta') d\theta' + \frac{\pi \theta (1-2q)}{2\alpha} \right] \right\} d\theta \quad (5.15)$$

The integral (5.15) exhibits poles located at :

$$k_o d (n_2^2 - n_1^2 \cos^2 \theta)^{\frac{1}{2}} = \pi, 2\pi, \dots \quad (5.16)$$

As long as (5.15) is performed on the real axis in the range $0 < \theta < \frac{\pi}{2}$, the contribution of all poles including those due to $\phi(\theta)$ which is given by Appendix D, will automatically be taken into account. However, during the integration process in the computer program (whose flow chart is presented in Appendix F), θ is scanned from zero to $\frac{\pi}{2}$. Hence, one expects θ to coincide with the critical angle θ_c , at which the ratio of sines in (5.15) is undeterminate. This will cause (5.15) to tend to infinity as θ approaches θ_c . Such a computational difficulty is alleviated by adding an extra routine to the main program which consists of setting the limit of the ratio :

$$\lim_{\theta \rightarrow \theta_c} \left\{ \frac{\sin[(d-x) k_o (n_2^2 - n_1^2 \cos^2 \theta)^{\frac{1}{2}}]}{\sin[k_o d (n_2^2 - n_1^2 \cos^2 \theta)^{\frac{1}{2}}]} \right\} = \frac{d-x}{d} \quad (5.17)$$

by using L'Hopital's theorem.

(c) Radiation field in the coupled wave region

In this region, all observation points \underline{X} are chosen so that $\theta_q > \theta_c$. Consequently, the normalised thickness $k_o T$ must be smaller than the first critical thickness corresponding to each mode.

Unlike in the guided wave region, the choice of d here is crucial, for it allows the selection of the modes which are to be coupled and guided along the uniform film (n_2). The selection of d and that of the mode q to couple into the uniform film (n_2) are inter-related via the characteristic equation appropriate to the film (n_2), which is approximately :

$$2 k_0 d n_2 \sin\theta'' + \phi_{21}(\theta'') + \phi_{20}(\theta'') - 2 \pi q = 0 \quad (5.18)$$

where

$$\phi_{21}(\theta'') = 2 \operatorname{Atan} \frac{i n_1 \sin\theta}{n_2 \sin\theta''} \quad (5.19a)$$

and

$$\phi_{20}(\theta'') = 2 \operatorname{Atan} \frac{i n_0 \sin\theta'}{n_2 \sin\theta''} \quad (5.19b)$$

Snell's law states :

$$n_2 \cos\theta'' = n_1 \cos\theta = n_0 \cos\theta' \quad (5.19c)$$

The configuration of each angle in (5.19) is given by Fig.5.8.

By virtue of (5.15), Figs.5.10 represent the cross variation of the normalised field modulus, versus the normalised depth $k_0 x$ for a few modes of the double layer structure and for their corresponding value of d .

Let us concentrate first on mode 1, as illustrated by Fig.5.10a. In each diagram, the saddle point θ_q is restricted in the range $\theta_q > \theta_c$ corresponding to different normalised thickness $k_0 T$ in (i), (ii), and (iii). The diagrams of Fig.5.10a clearly show how the mode propagates and how it is trapped from (i) to (iii). The field behaviour is Adiabatic and adapts smoothly to the presence

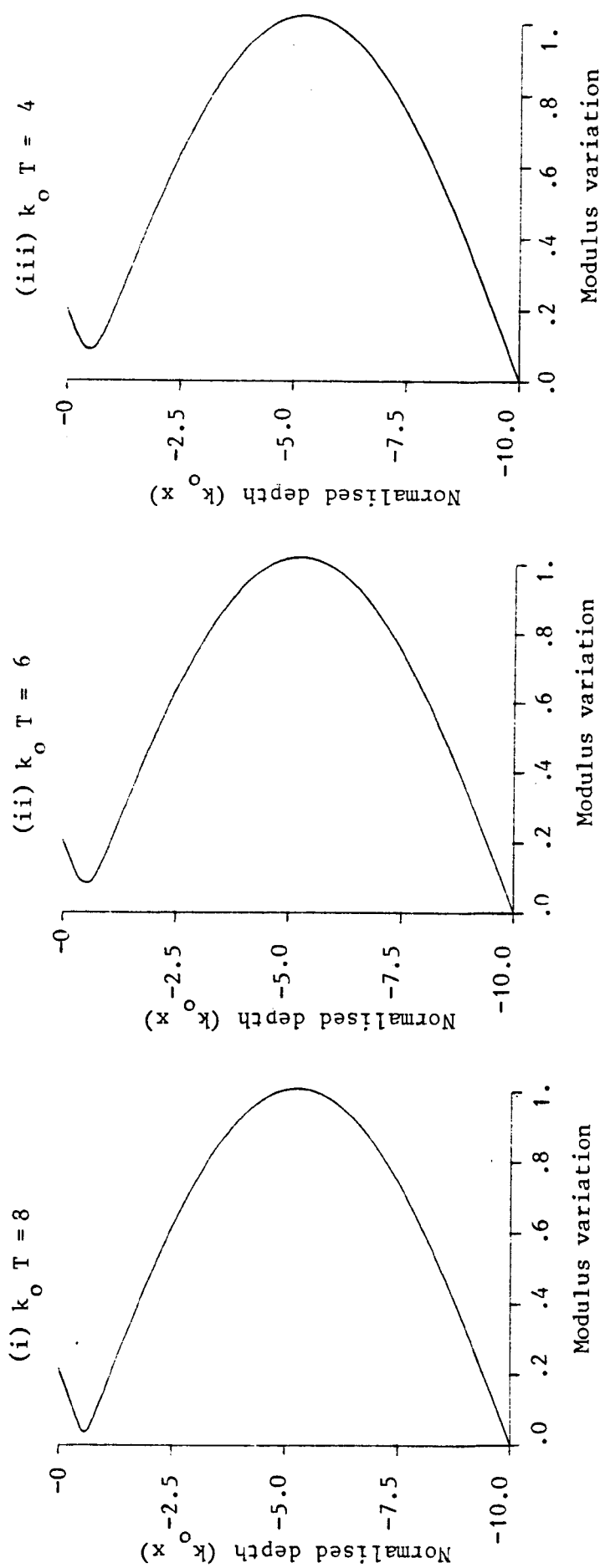


Fig. 5.10a. Computation of the normalised cross section radiation field in the uniform film (n_2) versus the normalised depth ($k_0 x$), for the double layer structure. The saddle points in (i), (ii) and (iii) are located in the coupled wave region. First normalised critical thickness = 11.5, second normalised critical thickness = 9.25. The refractive indices in each medium are : $n_0 = 1.5$; $n_1 = 2$; $n_2 = 1.98$; $n_3 = 1$. Mode 1, $k_0 d = -10$, $\alpha = 0.027$ rds.

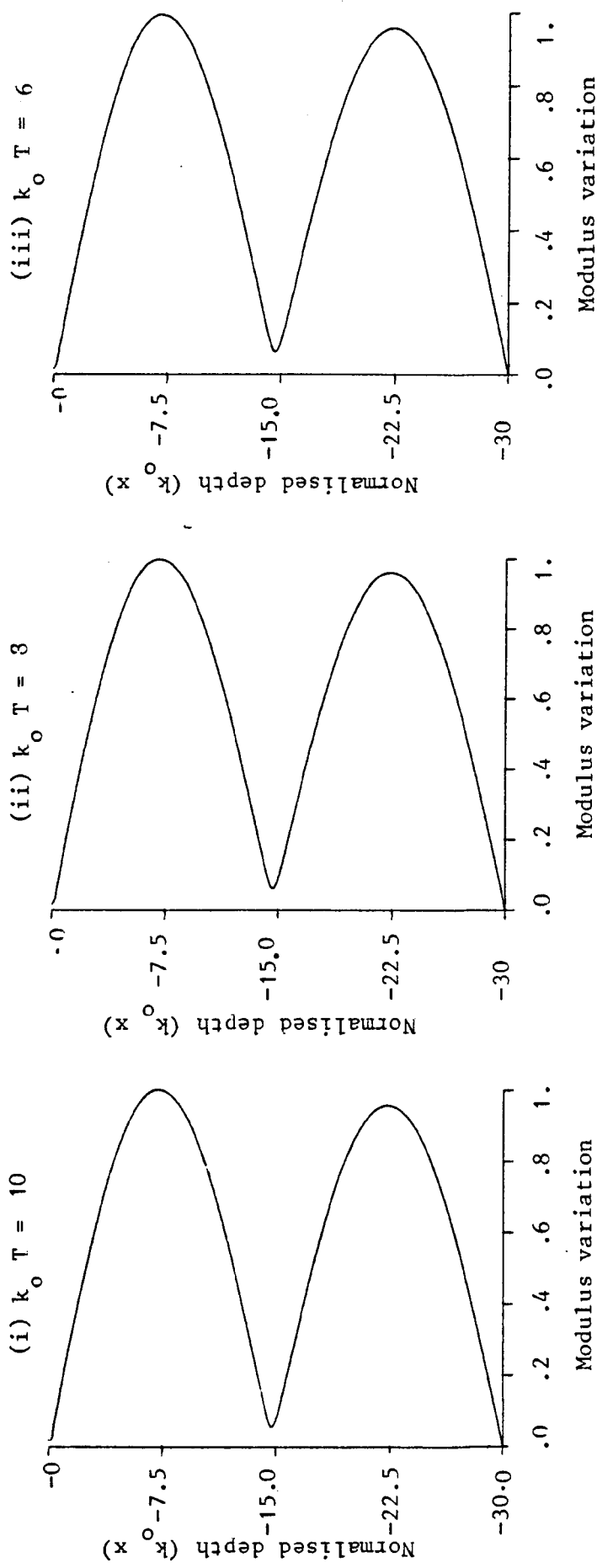


Fig. 5.10b. Mode 2, $k_0 d = -30$.
thickness = 17.5

First normalised critical thickness = 28.75, second normalised critical

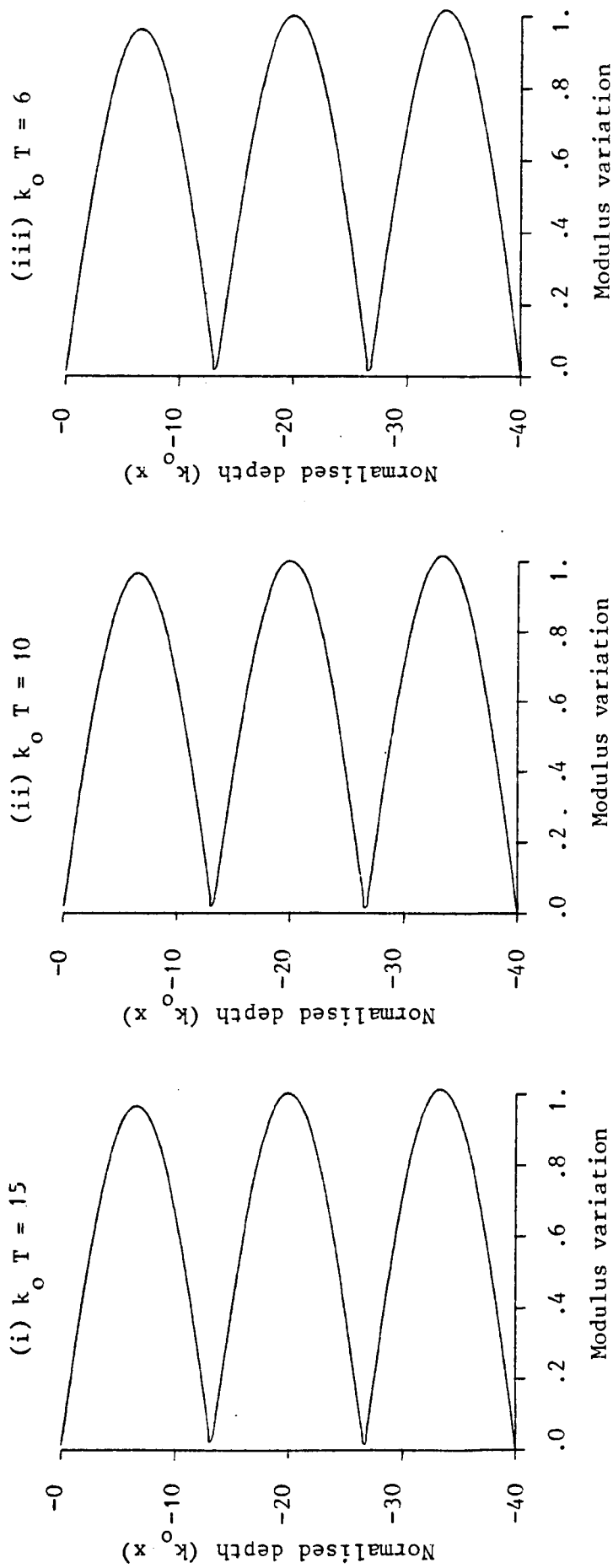


Fig.5.10c. Mode 3, $k_0 d = -40$. First normalised critical thickness = 44.75, second normalised critical thickness = 33.

of the uniform film (n_2); which is confined within the range $0 < k_0 x < k_0 d$. The amplitude of the mode remains nearly constant as it is bound along the film (n_2), emphasising the guiding mechanism.

Note also that at the boundary B_{20} , that is to say at $k_0 x = k_0 d$, the field vanishes to zero. This is of no surprise, for we have assumed earlier that the substrate (n_0) is perfectly reflecting.

Some numerical errors however, like those exhibited in Fig.5.10a arise. There, the field should increase continuously at the top interface ($k_0 x = 0$). These small errors are due to the neglect of all terms of the same magnitude as the wedge angle α in the analysis.

Similar conclusions hold for other higher modes as presented by Figs.5.10b and 5.10c, corresponding respectively to mode 2 and 3.

In this sense, we have been able to obtain (at least for the few lowest modes) an assessment of the mode coupling occurring within the coupled wave region, for the double layer case. For higher order modes, one ought to increase d ; undoubtedly, mode conversion will manifest itself again.

CHAPTER SIX

COMPARISON OF SOME RESULTS WITH OTHER PAPERS

6.1. Introduction

In order to assess and guarantee the accuracy of the method based on the spectral analysis we must compare some of our computed results with other independent calculations performed via different techniques.

To our knowledge , in connection with integrated optics applications there are almost no reported theoretical results on either of the structures dealt with in this thesis, except Bassi et al [18], who also use the coupled mode theory, just like Evans [20], to analyse a monomode taper. Besides, for the single layer structure in connection with underwater acoustic propagation in shallow ocean water some interesting papers were published by Kamel and Felsen [22], who make use of a numerical Green's function; and by Pierce [21] and Jensen and Kuperman [24], who explore the concept of the parabolic approximation. They analyse the propagation of waves in shallow ocean water, on a physical model similar to that of the single layer structure. The wedge angle α (equal to 0.027 rds) in their problem, is taken the same as in ours. Therefore, their problems and ours are mathematically similar.

The analytical model applied to the single layer structure in the previous chapters, and which is compatible with integrated optics, will be applied to the same structure, but for underwater acoustic application, in this chapter. To this purpose,

we must then scale our mathematical model with respect to the free-space wave number k_0 , so as to be able to use the same parameters, the same geometrical dimensions, under the same reference system as other papers.

6.2. Coordinate system appropriate to underwater acoustic applications

We shall in this section define the coordinate system appropriate to underwater acoustic applications. To achieve this, we introduce a change of coordinates which is illustrated in Fig.6.1. Thereby, each observation point $\underline{X} \equiv (\chi, r)$ is instead denoted by its Cartesian coordinates (ϵ, μ) ; where ϵ is the range in metres, referred to a coordinate axis passing by an arbitrary source \underline{X}_0 , and μ , also in metres, characterises the depth with respect to the bottom interface B_{12} .

We obtain from Fig.6.1 the change of coordinates given by the following equations :

$$r^2 = \mu^2 + \left(\frac{200}{\tan\alpha} - \epsilon\right)^2 - T^2 \quad (6.1a)$$

$$\sin(\chi - \alpha) = \frac{\mu}{r} \quad (6.1b)$$

$$\cos^2(\chi - \alpha) = \left(\frac{200}{\tan\alpha} - \epsilon\right)^2 - T^2 \quad (6.1c)$$

The arbitrary source \underline{X}_0 , corresponding to $\epsilon = 0$, is located at a thickness equal to 200 m in the tapered waveguide, according to the papers referred to in section 6.1.

We also need to normalise the refractive indices in our model in accordance with the papers as follows :

$$k_0 n_j = 2 \pi \frac{f}{v_j} \quad j = 1, 2, 3 \quad (6.2)$$

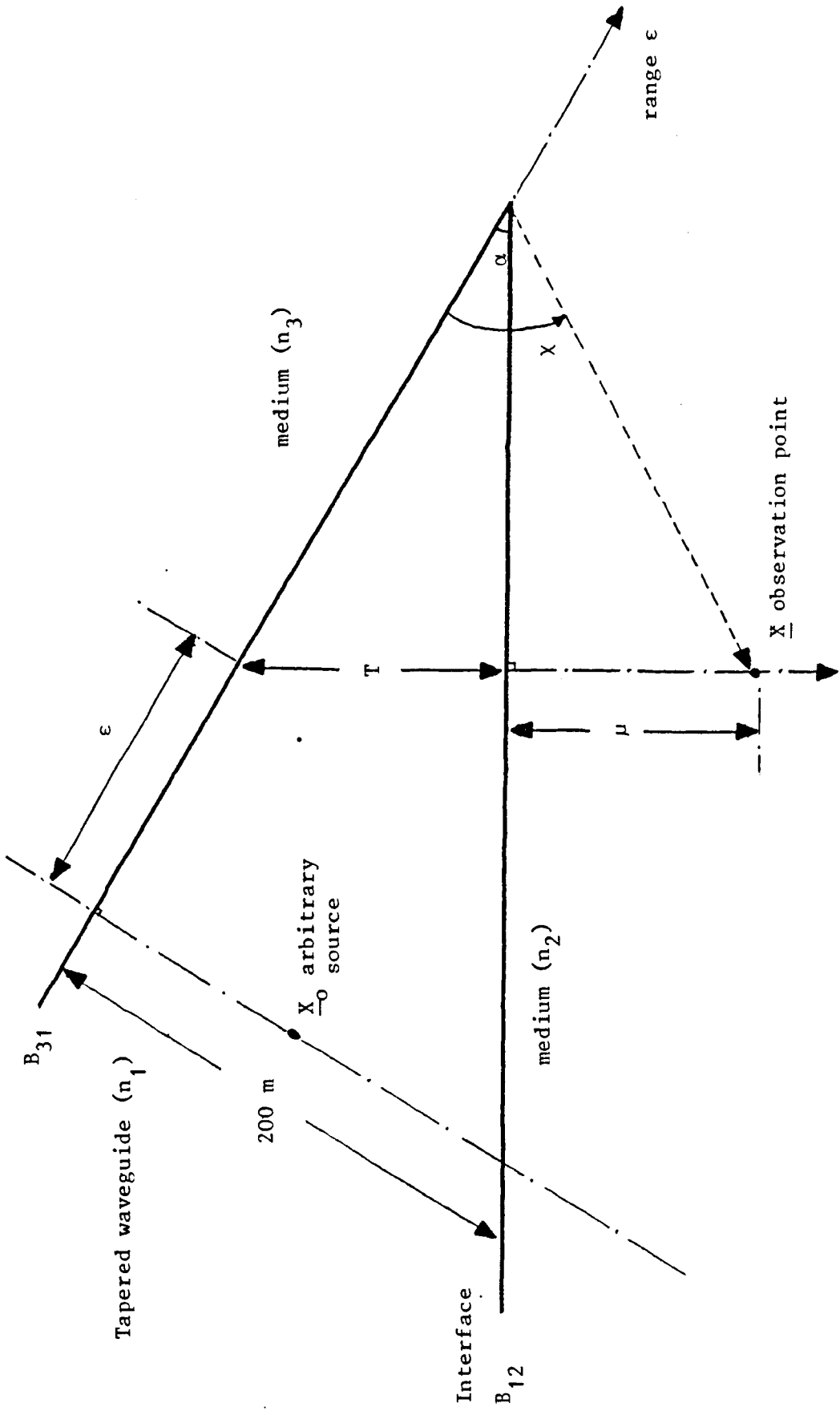


Fig.6.1 : Reference system appropriate to underwater acoustic applications
 $\underline{X} \equiv (\epsilon, \mu)$

where n_j are the refractive indices of each medium (n_j); v_j is the velocity of the acoustic waves in the same medium (n_j), and f represents the excitation frequency of waves.

For numerical applications to underwater acoustic, $f = 25$ Hz, $v_1 = 1500$ m/s, $v_2 = 1701.4$ m/s and $v_3 = 330$ m/s, as in [21], [22] and [24].

According to the normalisation of the refractive indices in equation (6.2), the geometrical variables such as T , r , ϵ and μ may be scaled in metres. That is why such a change of reference system makes the model compatible with underwater acoustic applications.

Besides this change of variables introduced in the computer program (whose flow chart is presented in Appendix F) one needs to incorporate propagation loss in medium (n_2) as in the references. Such a loss can be simulated in our model, by adding a small negative imaginary part to the refractive index (n_2) which is given by the following attenuation :

$$20 \log[\lambda \text{Imag}(k_0 n_2)] = 0.5 \text{ dB/wavelength} \quad (6.3)$$

where λ is the wavelength of the wave in the relevant medium (n_2). For $j = 2$ only, equation (6.3) gives the imaginary part of (n_2). Its real part is already given by equation (6.2).

6.3. Co-ordinate system appropriate to integrated optics applications

As far as integrated optics applications are concerned, the reference system used so far consists of normalising with respect to k_0 all geometrical variables such as T , r and x .

In this case, the refractive indices remain unnormalised. We shall remain with the same refractive indices as in previous

chapters, that is to say, $n_1 = 2$, $n_2 = 1.76$ and $n_3 = 1$. Notice that the ratios $(\frac{n_1}{n_2})$ and $(\frac{v_2}{v_1})$, have been chosen the same.

The fact of normalising all geometrical variables with respect to k_o makes the model universally applicable to any frequency in integrated optics. We recall that the reference system appropriate to integrated optics applications could be taken as the one illustrated by Fig.5.9 whereby each observation point $\underline{X} \equiv (\chi, r)$ is characterised by its normalised thickness $k_o T$, and by the cross variable χ (in rds). The latter polar co-ordinate χ can further be replaced by a normalised depth $k_o x$, as one recalls from Fig.5.9 :

$$(k_o r)^2 = (k_o x)^2 + \left(\frac{k_o T}{\tan\alpha}\right)^2 \quad (6.4a)$$

$$\sin(\chi-\alpha) = \frac{k_o x}{k_o r} \quad (6.4b)$$

$$\cos(\chi-\alpha) = \frac{k_o T}{k_o r \tan\alpha} \quad (6.4c)$$

6.4. Total field behaviour inside and outside the tapered waveguide

In this section, we shall endeavour to present some computed results for the single layer structure which describe the field variation inside and outside the tapered waveguide at the same time.

To this end, we consider Figs.6.2, 6.3 and 6.4, which illustrate for modes 1, 2 and 3 respectively the behaviour of the normalised field modulus versus the normalised depth $k_o x$ (or versus the depth μ in metres) as the observation point \underline{X} moves along the tapered waveguide. In each of the figures, the upper

horizontal scaling of the normalised depth $k_o x$ is appropriate to integrated optics applications, whereas the lower horizontal scaling of the depth μ (in metres) is appropriate to underwater acoustic applications.

Also, in each figure, the observation point \underline{X} is located by the normalised thickness $k_o T$ for integrated optics applications, whereas for underwater acoustics it is referred to by the range ϵ (in metres).

The variables $k_o T$ and ϵ are inter-related by a simple expression which can be found by reference to Fig.6.1. There, knowing the position ϵ , one can geometrically work out the value of T ; then (after normalising it with respect to k_o) one obtains the equation which relates $k_o T$ to ϵ , which is :

$$k_o T = 55 (0.2 - \alpha \epsilon) \quad (6.5)$$

Of course, equation (6.5) is only valid for a point source \underline{X}_o , situated at $\epsilon = 0$ as such is Fig.6.1. This is according to the [21,22,24] referenced papers. Also, to use (6.5) one must express ϵ in km and α in radians.

The transition region of each mode is characterised in each plot by a critical thickness in integrated optics; in underwater acoustics it is featured by a cut-off range.

As far as the field moduli are concerned, they all have been normalised with respect to a constant. This constant depends on each mode and it is selected in such a manner as to have a largest field modulus equal to unity for each plotting of Figs.6.2a, 6.3a and 6.4a, corresponding to mode 1, 2 and 3 respectively.

Fig.6.2a locates an observation point \underline{X} at $k_0 T = 2.83$ ($\epsilon = 5500$ m) with respect to the normalised critical thickness 1.75 (cut-off = 6224 m) of mode 1. That is to say, \underline{X} belongs to a guided wave region. For negative depth, the field magnitude exhibited corresponds to the inside of the tapered waveguide. It oscillates sinusoidally and has an Adiabatic behaviour. For positive depth, the field magnitude describes the behaviour of the mode outside the tapered waveguide, which is the open medium (n_2). It has an exponentially decaying distribution, for the observation point \underline{X} is located in the guided wave region. There is no leakage occurring yet. One notices the perfect continuity of the field and its derivative at the interface B_{13} (zero depth).

Fig.6.2b corresponds to an observation point situated near the transition region at $k_0 T = 2.09$ ($\epsilon = 6000$ m). For negative depth, the field still behaves Adiabatically, as it is pushed towards the interface B_{12} (zero depth). For positive depth, the field remains evanescent in nature, but decays less rapidly than in Fig.6.2a. It is at this stage that leakage will begin to occur.

A further move of the observation point \underline{X} beyond the transition region, exhibits a field distribution given by Fig.6.2c , where \underline{X} is located in the leaky wave region at $k_0 T = 1.34$ ($\epsilon = 6500$ m). For negative depth, we notice that the amplitude of the field diminishes as it is pushed towards the interface B_{12} (zero depth). Thus, such a field inside the tapered waveguide is no more Adiabatic in behaviour, because of the leakage taking place from the tapered waveguide to its adjacent bottom medium (n_2). In contrast, for positive depth, the field oscillates to a maximum then decays exponentially due to the existence of a caustic in

Observation point at $k_0 T = 2.83$ ($\epsilon = 5500$ m). Mode 1.

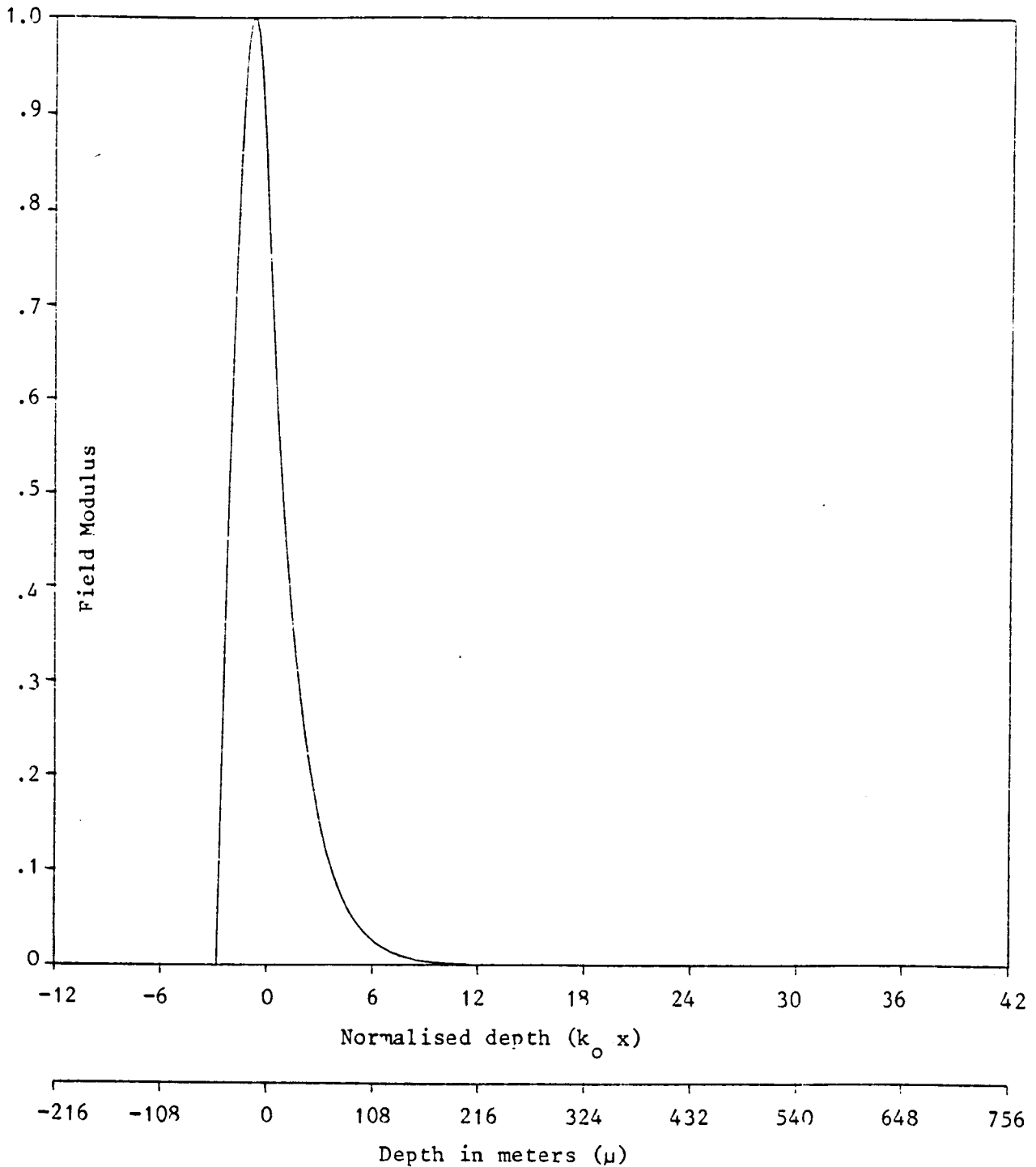


Fig.6.2a : Computation of the normalised field modulus versus the normalised depth ($k_0 x$). Normalised critical thickness = 1.75 (cut-off at 6224 m). Depth < 0 : describes the field inside the tapered guide. Depth > 0 : describes the field in medium (n_2).

Observation point at $k_0 T = 2.09$ ($\epsilon = 6000$ m). Mode 1.

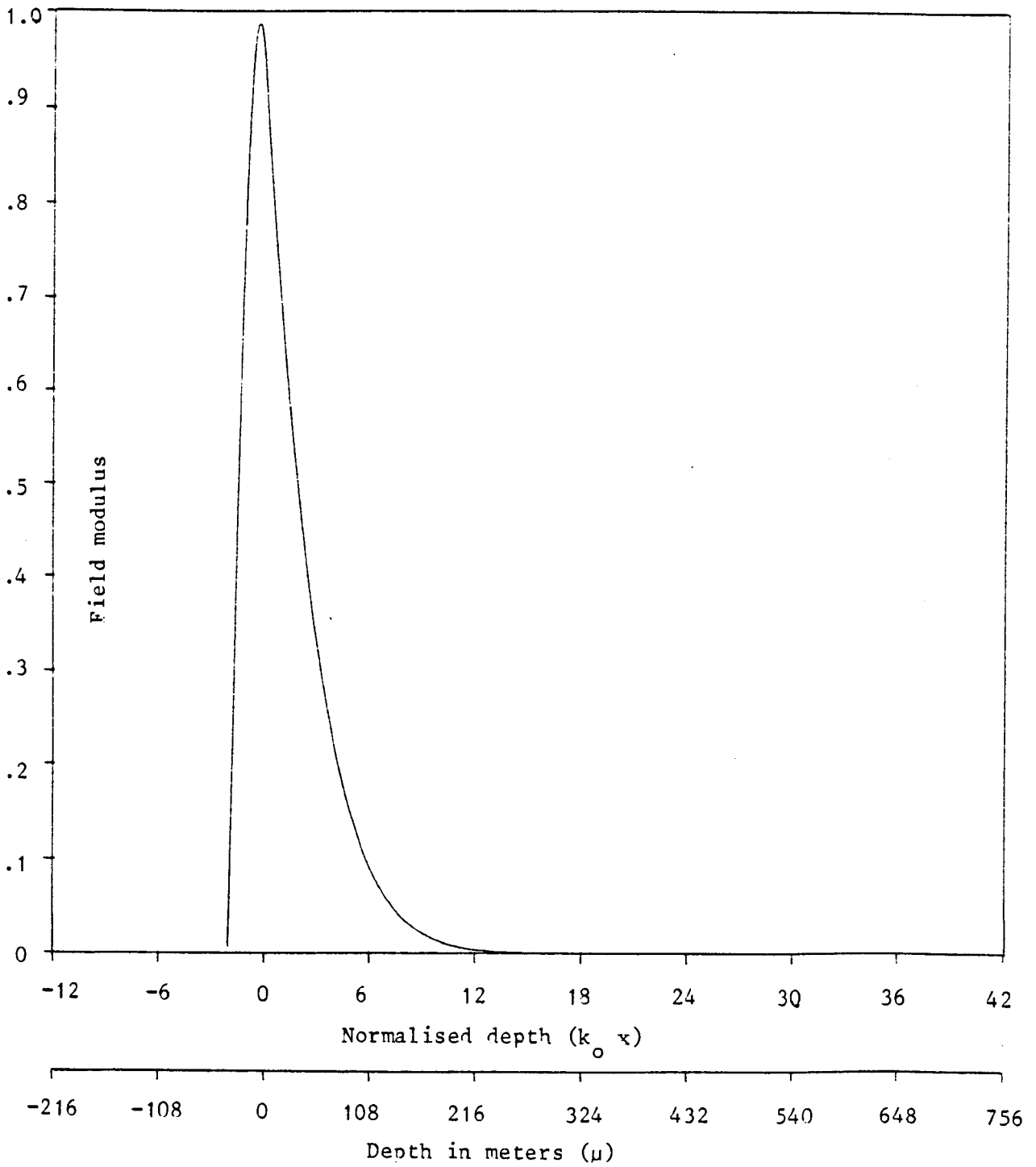


Fig.6.2b

Observation point at $k_0 T = 1.34$ ($\epsilon = 6500$ m). Mode 1.

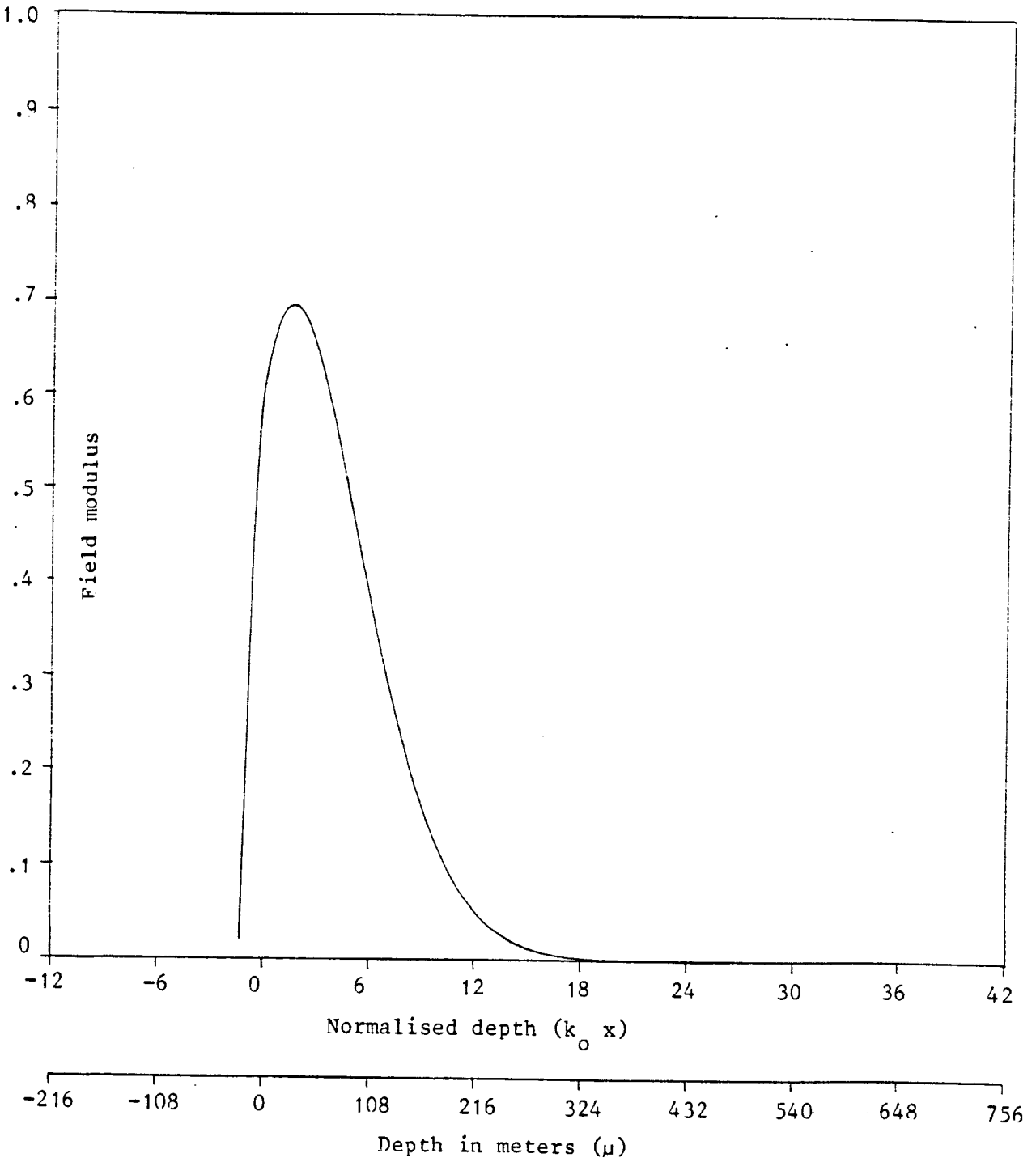


Fig.6.2c

Observation point at $k_0 T = 0.6$ ($\epsilon = 7000$ m). Mode 1.

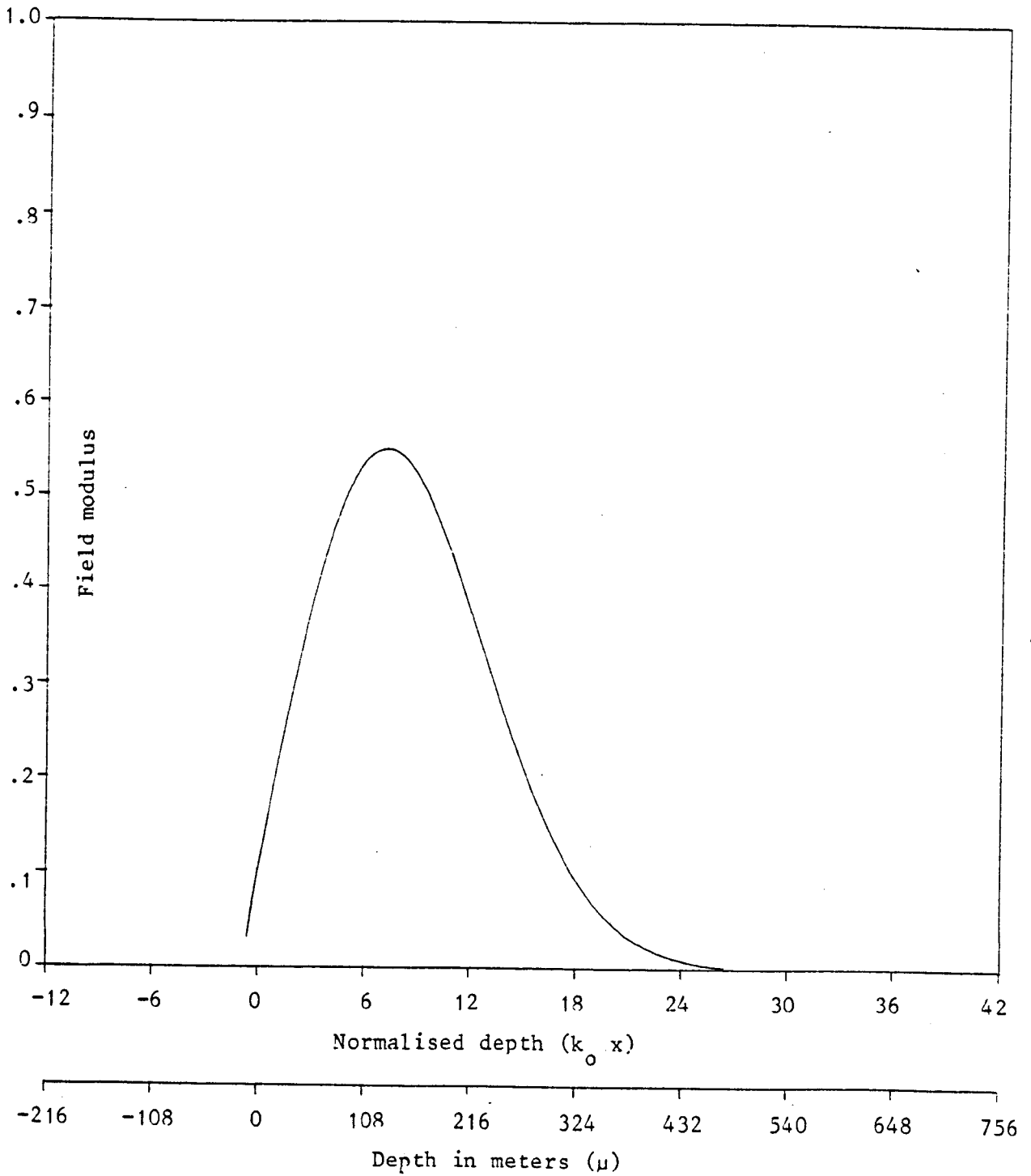


Fig.6.2d

Observation point at $k_0 T = 5.85$ ($\epsilon = 3500$ m). Mode 2.

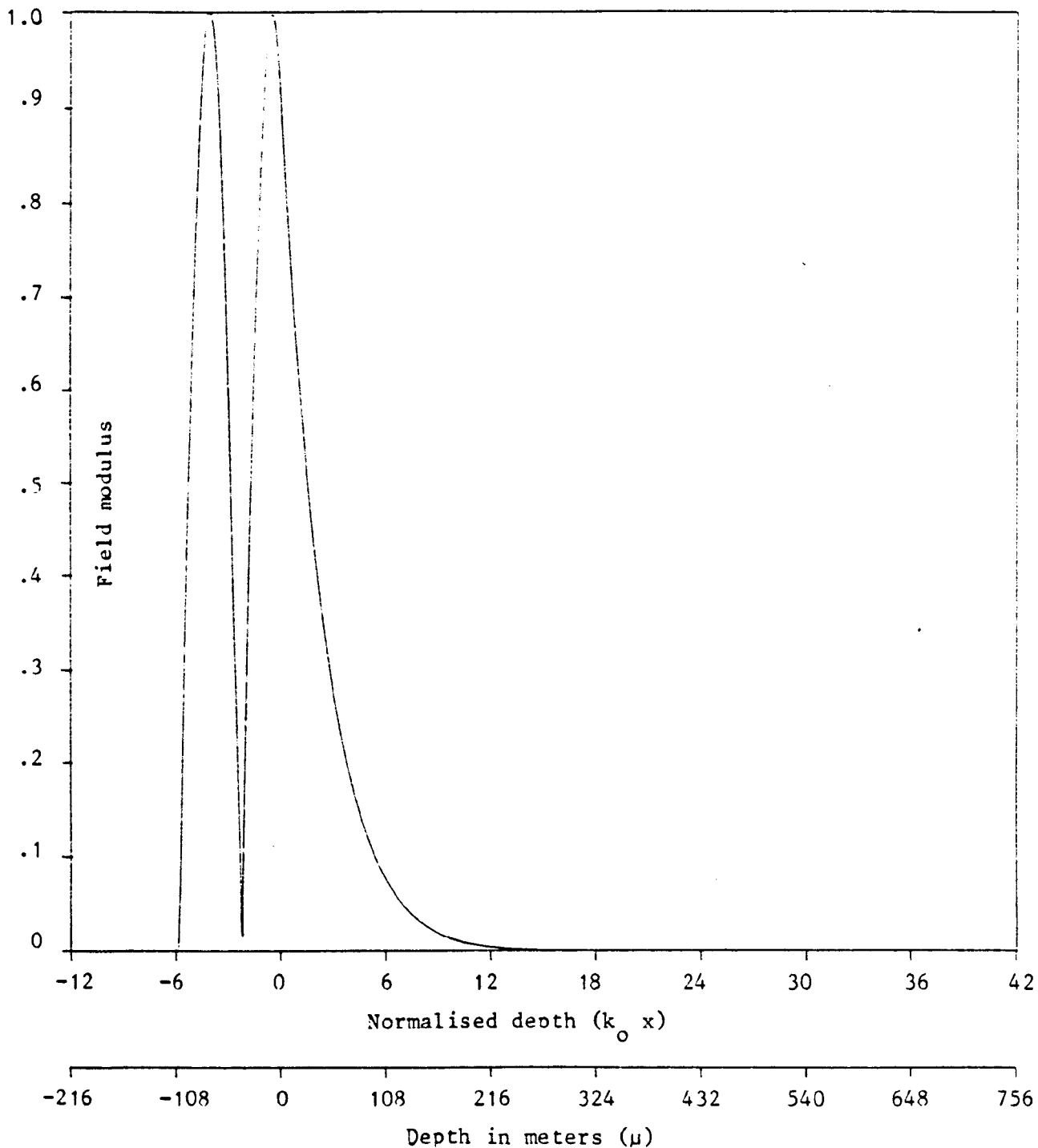


Fig.6.3a : Computation of the normalised field modulus versus the normalised depth ($k_0 x$). Normalised critical thickness = 5 (cut-off at 4000 m).
 Depth < 0 : describes the field inside the tapered guide.
 Depth > 0 : describes the field in medium (n_2).

Observation point at $k_0 T = 5.06$ ($\epsilon = 4000$ m). Mode 2.

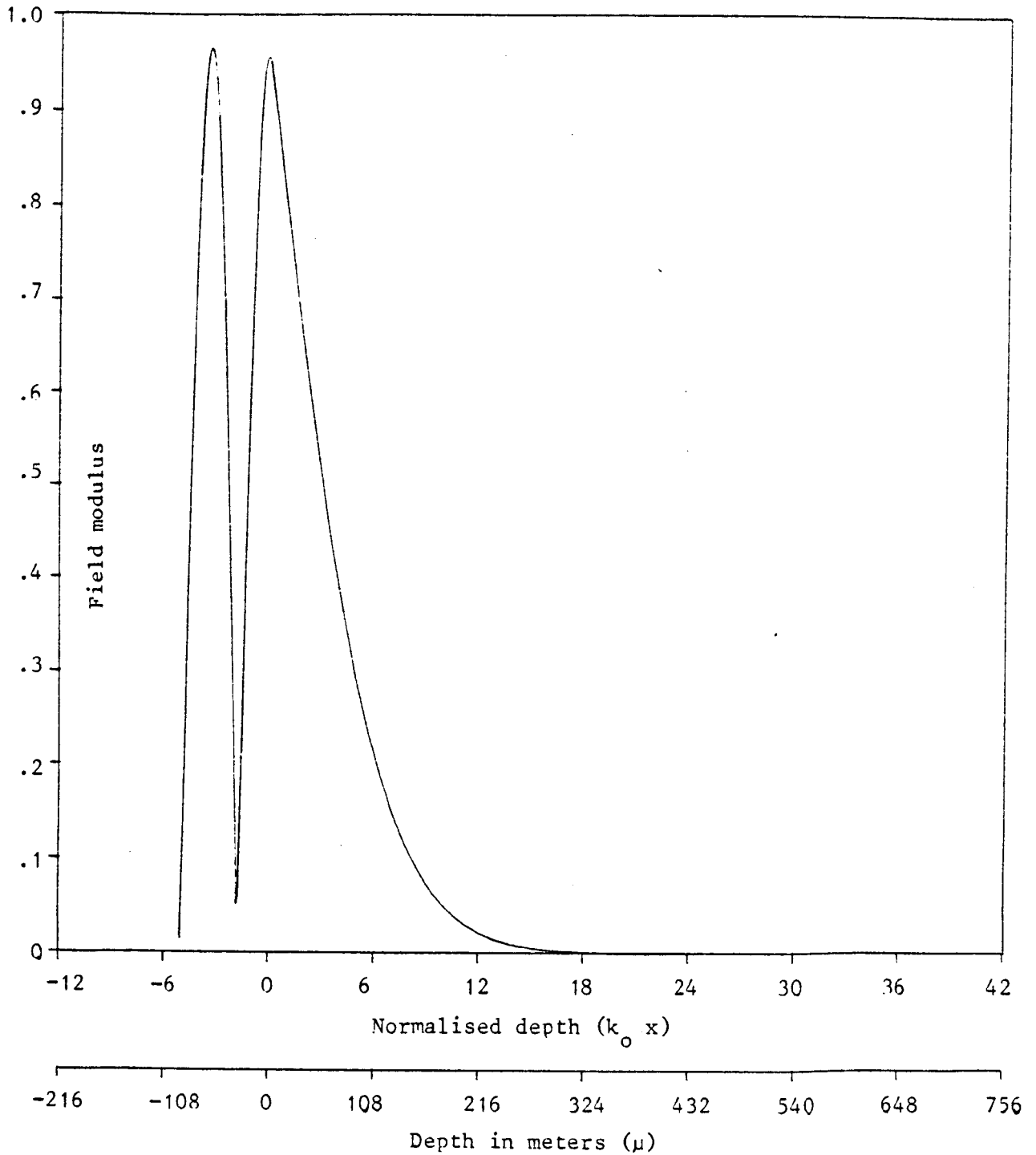


Fig.6.3b

Observation point at $k_0 T = 4.31$ ($\epsilon = 4500$ m). Mode 2.

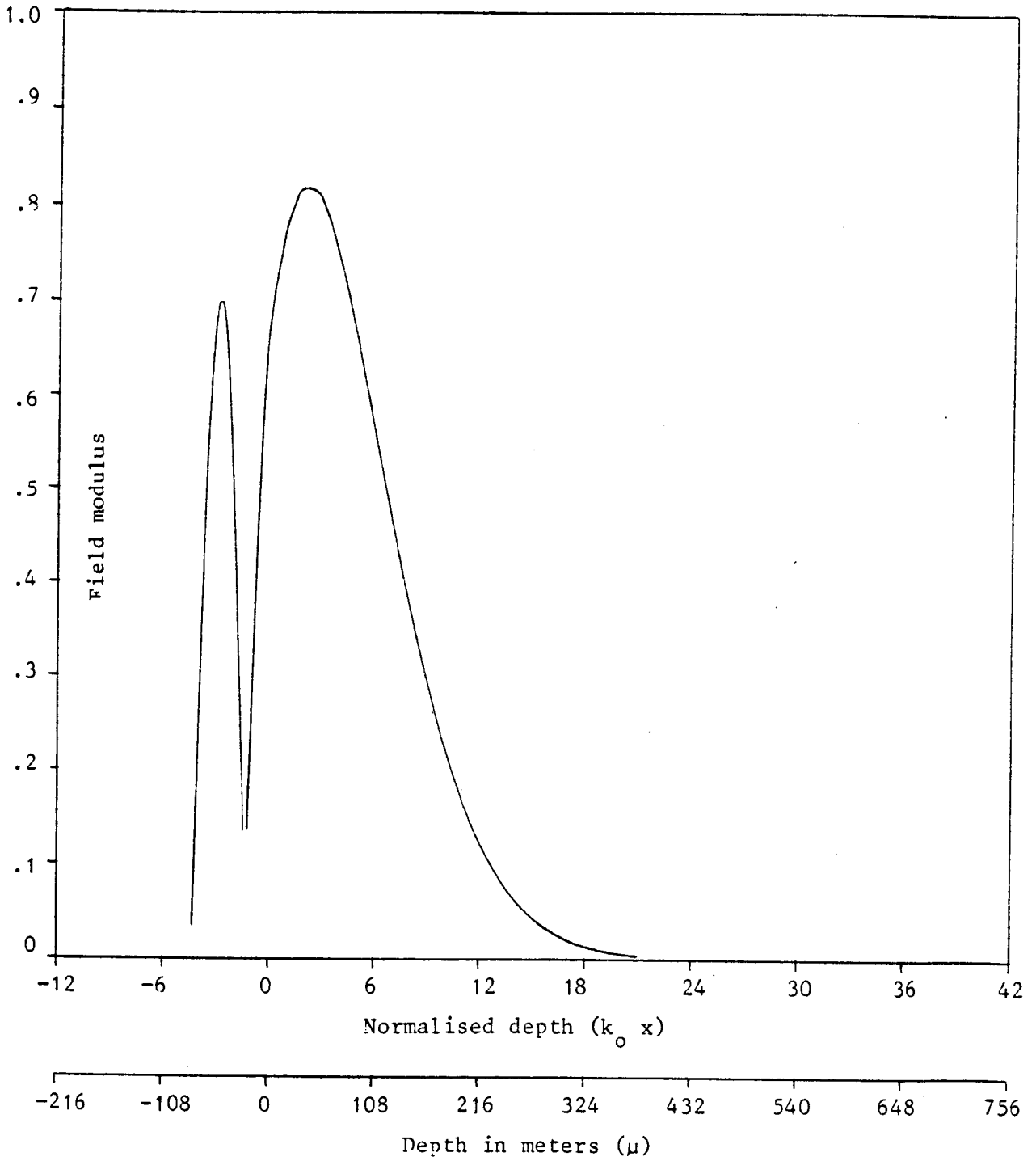


Fig.6.3c

Observation point at $k_0 T = 3.57$ ($\epsilon = 5000$ m). Mode 2.

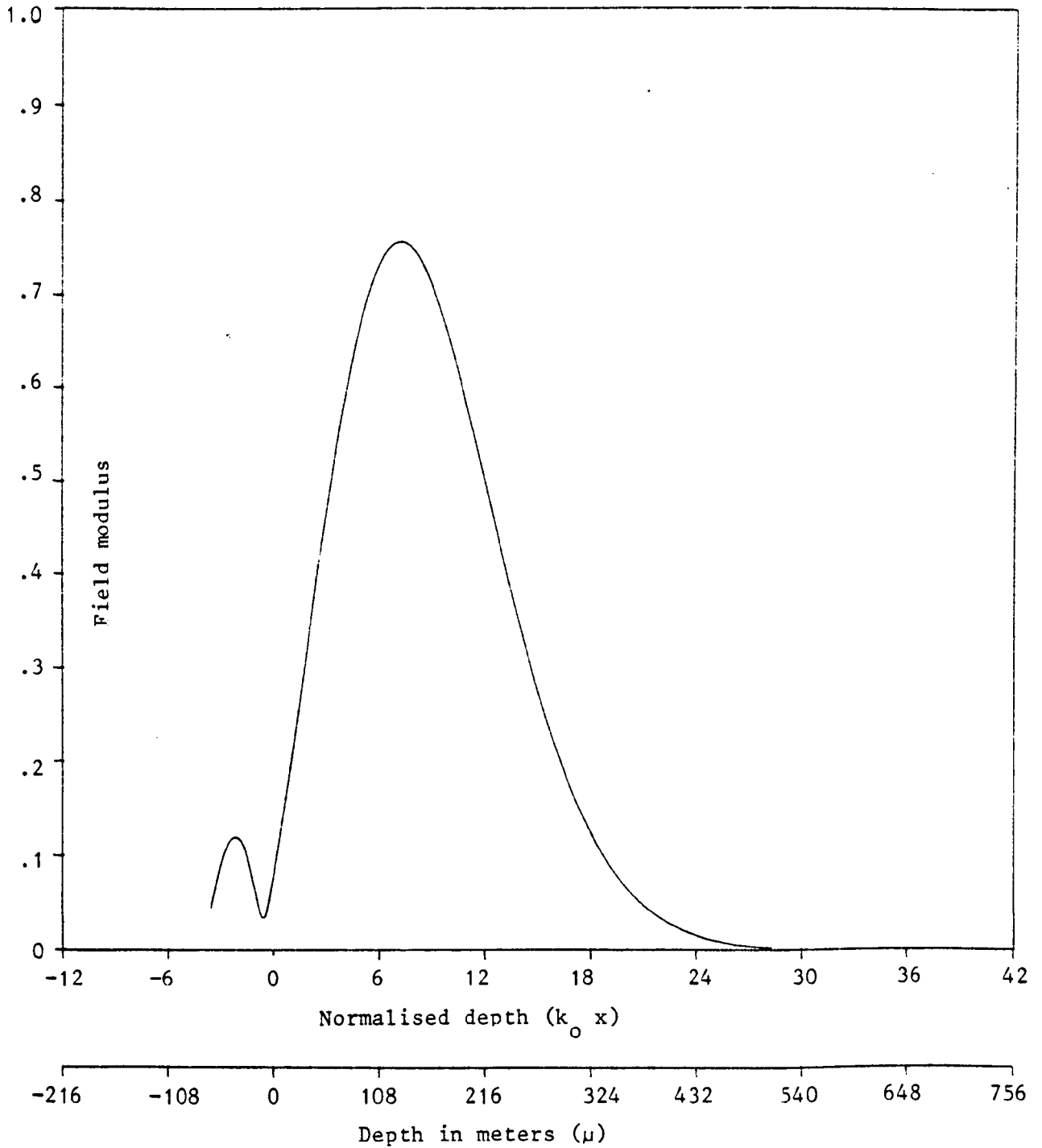


Fig.6.3d

Observation point at $k_0 T = 9.51$ ($\epsilon = 1000$ m). Mode 3.

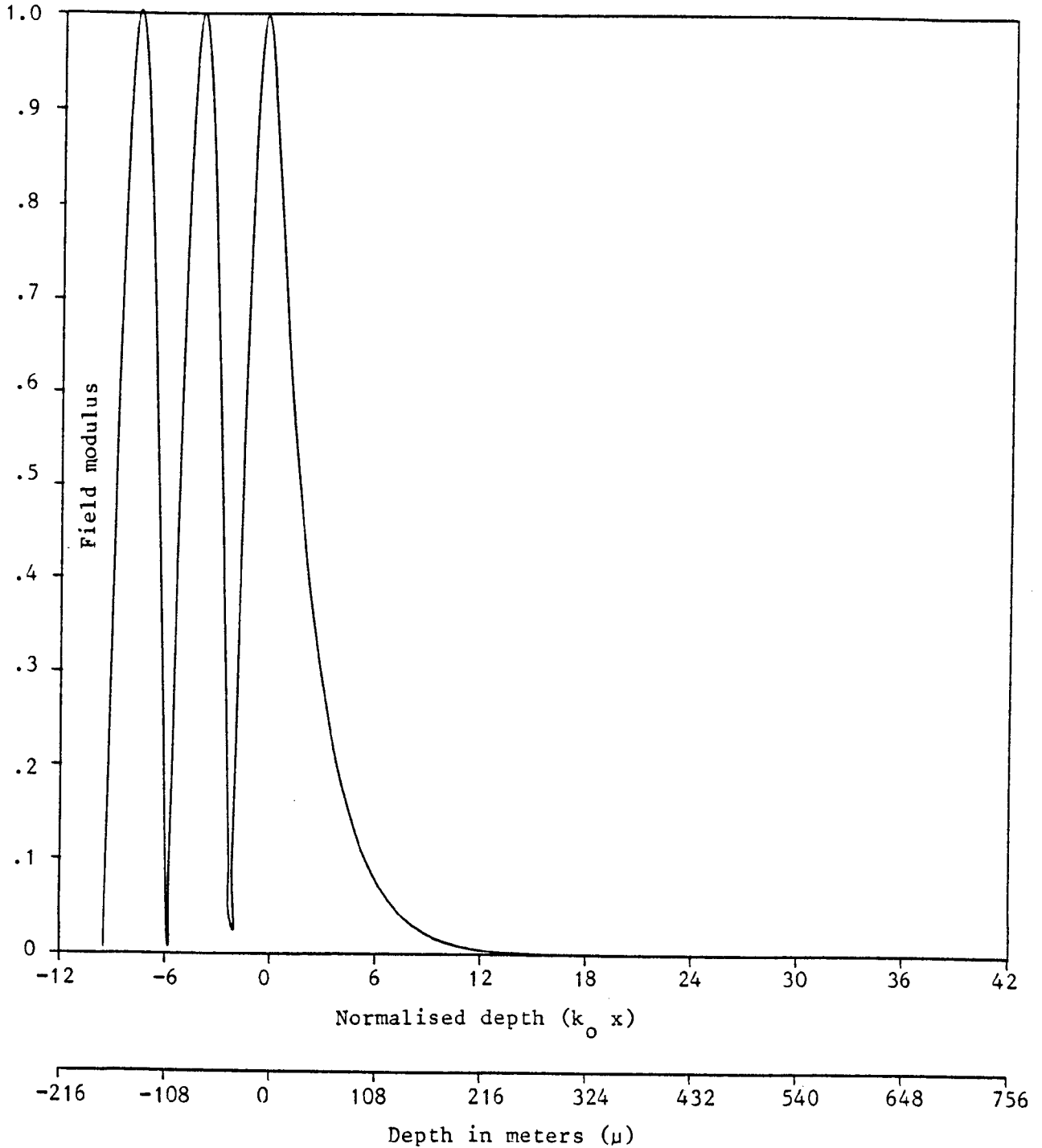


Fig.6.4a : Computation of the normalised field modulus versus the normalised depth ($k_0 x$). Normalised critical thickness = 8.6 (cut-off at 1555 m).
Depth < 0 : describes the field inside the tapered guide
Depth > 0 : describes the field in medium (n_2)

Observation point at $k_0 T = 8.7$ ($\epsilon = 1500$ m). Mode 3.

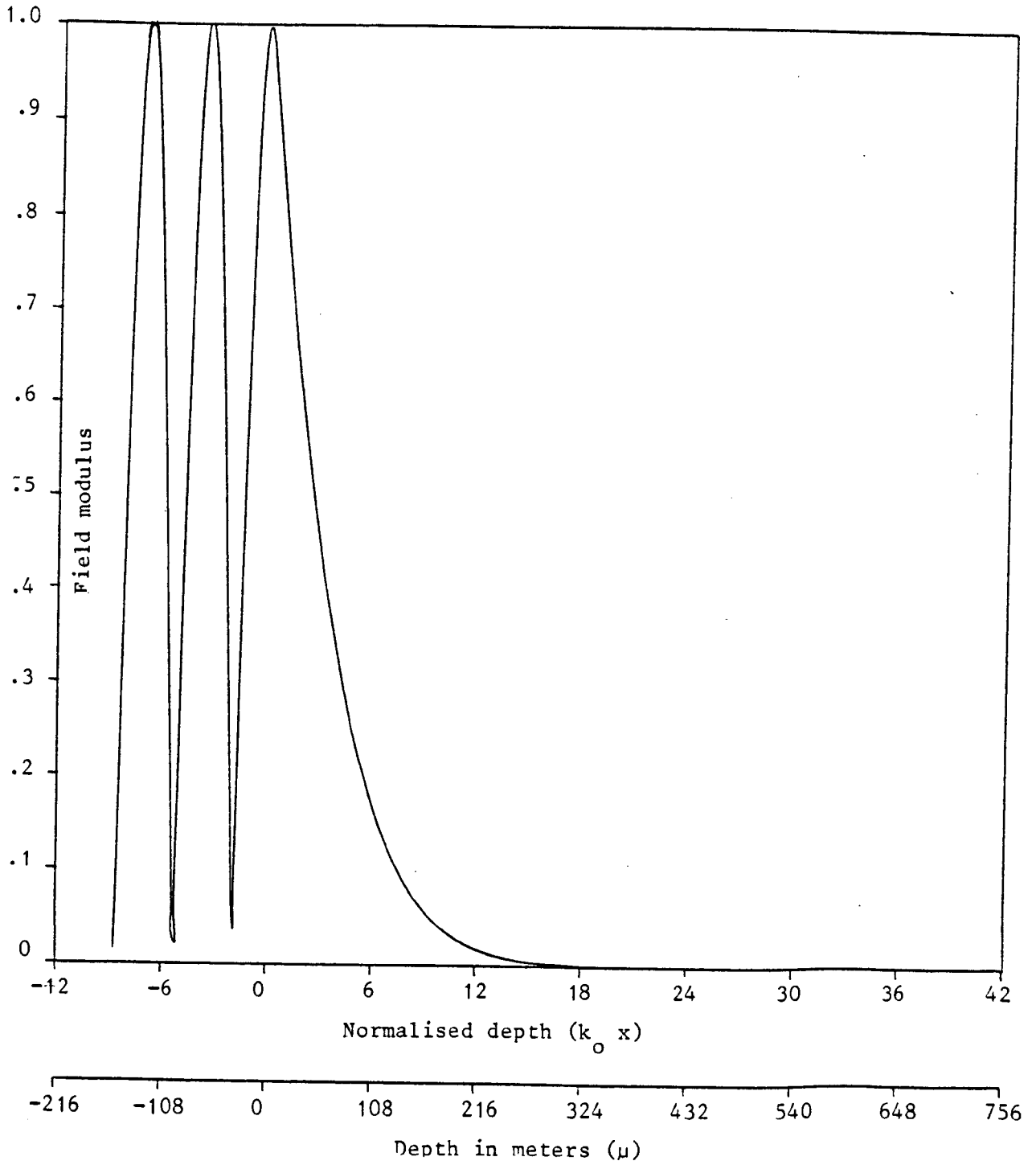


Fig.6.4b

Observation point at $k_0 T = 8.03$ ($\epsilon = 2000$ m). Mode 3.

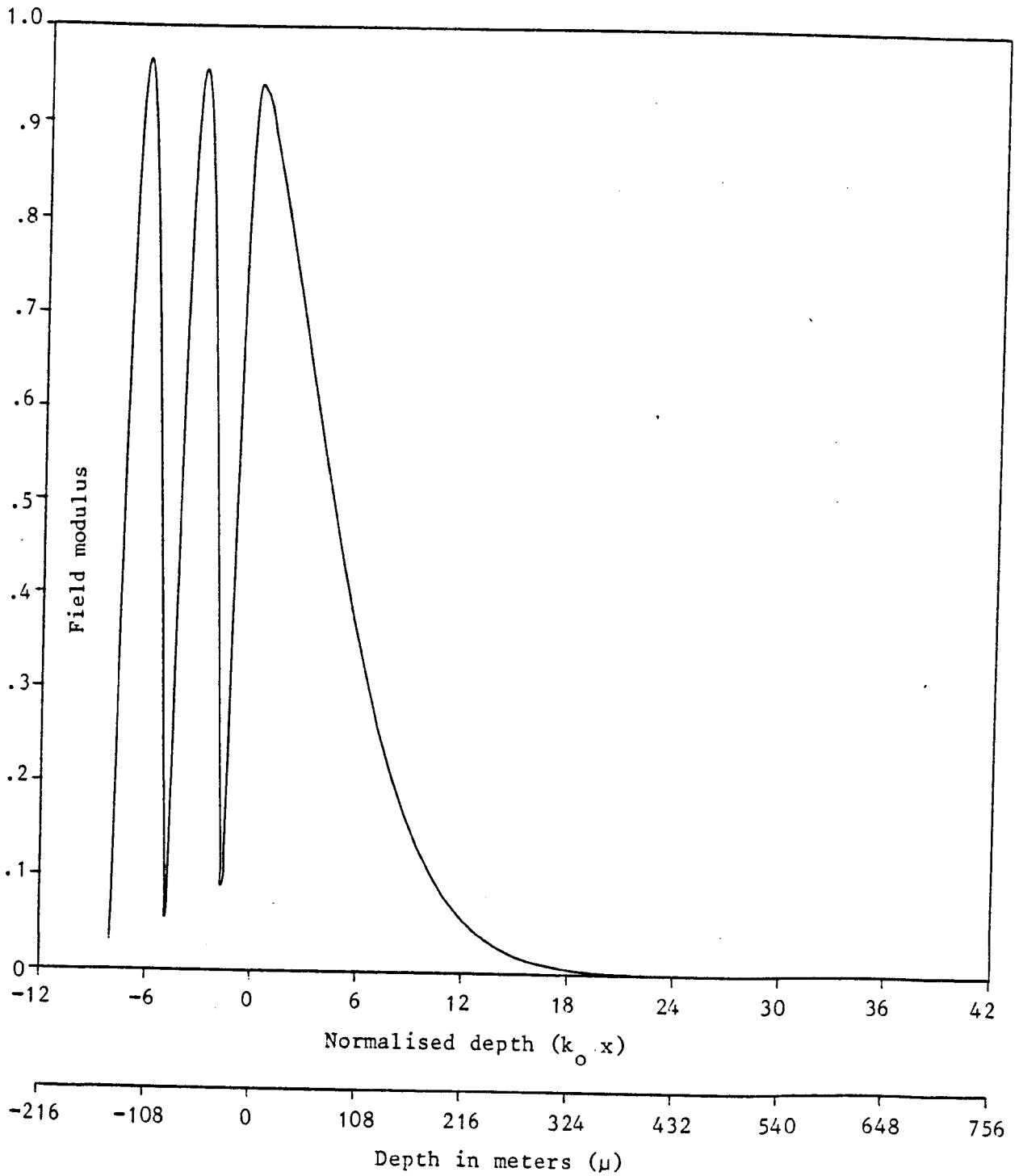


Fig.6.4c

Observation point at $k_0 T = 7.28$ ($\epsilon = 2500$ m). Mode 3.

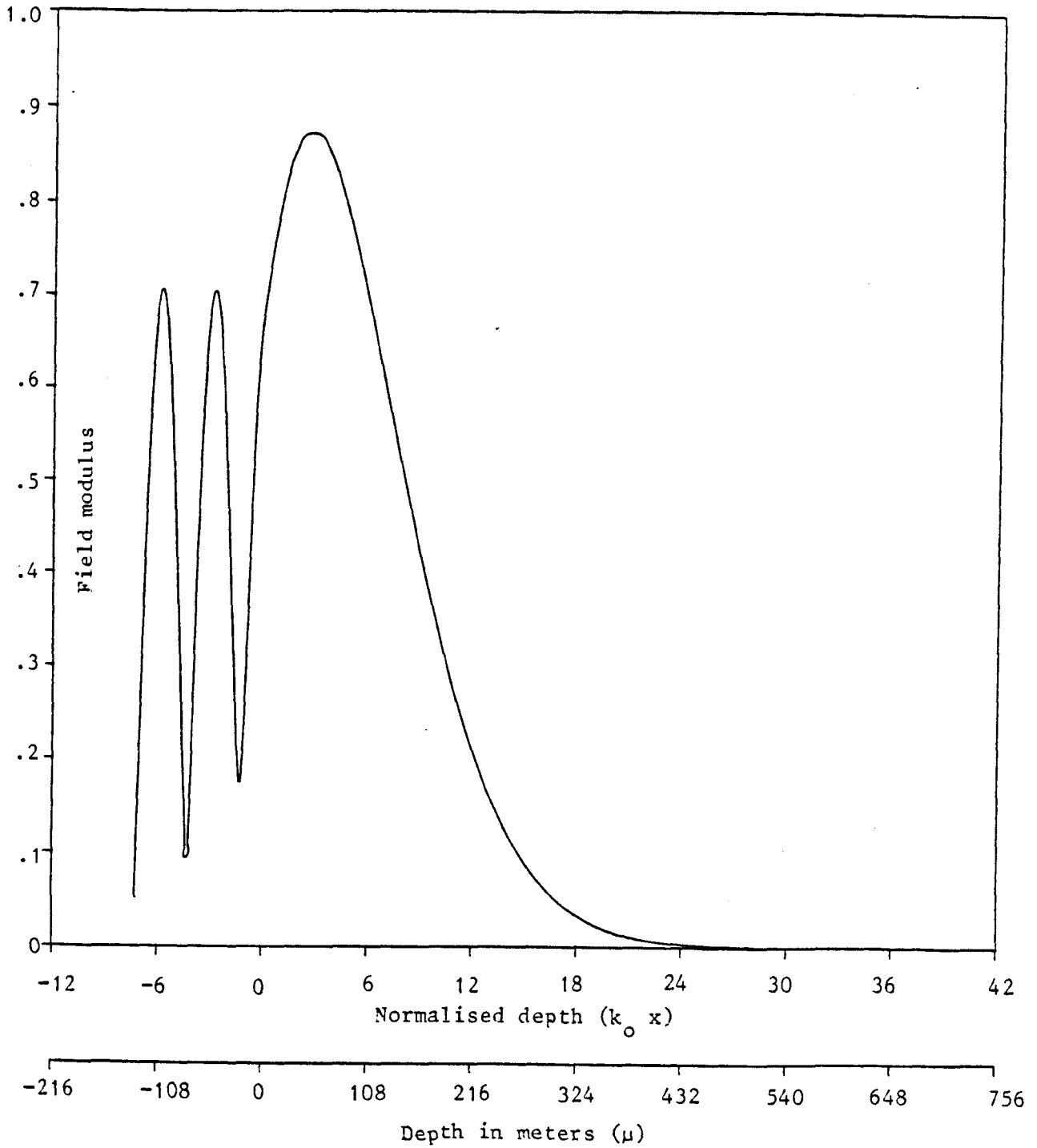


Fig.6.4d

medium (n_2). This distribution obtained in medium (n_2), characterises the radiation mechanism of the structure.

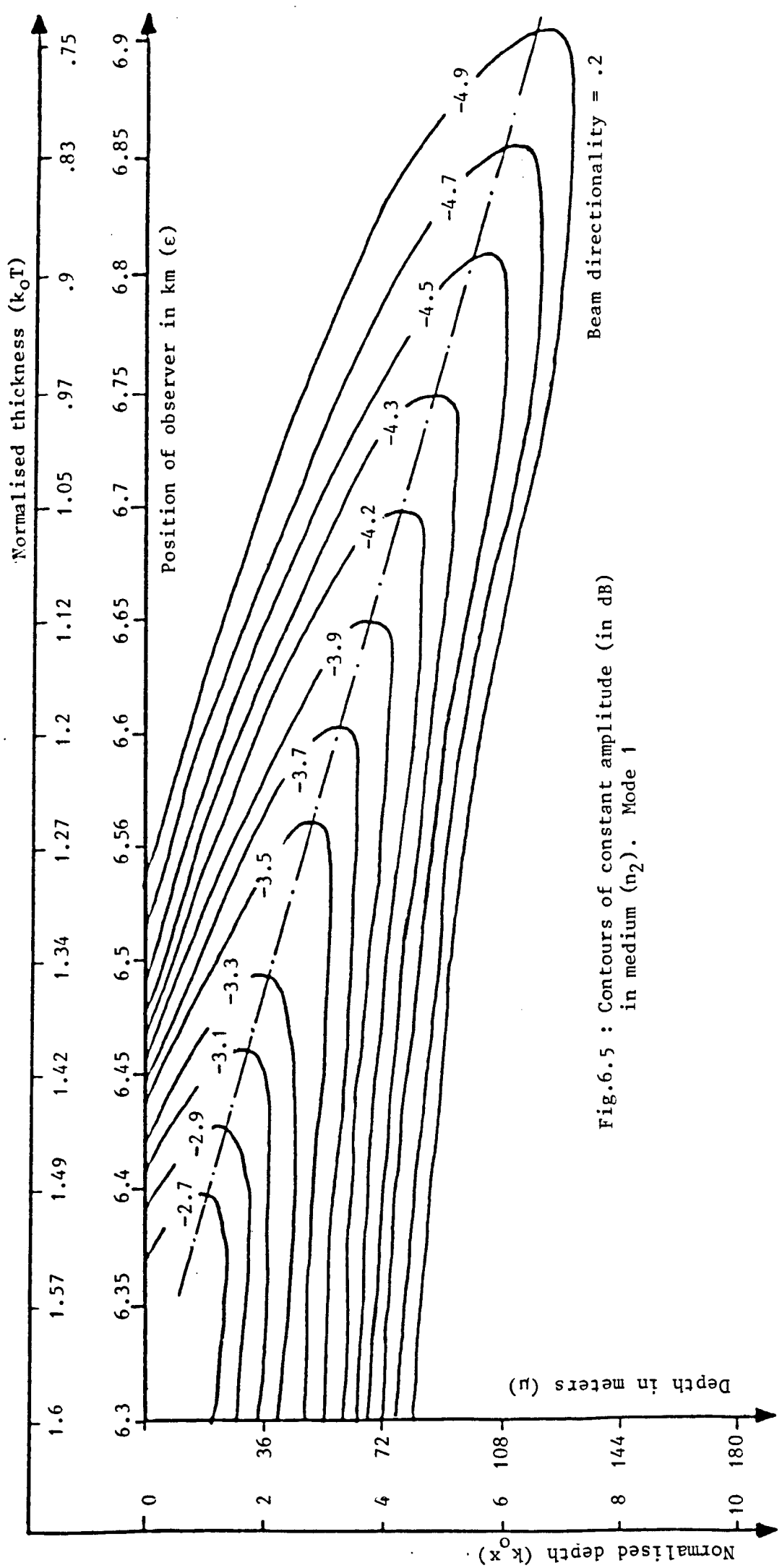
Fig.6.2d locates an observation point \underline{X} also in the leaky wave region, but further down towards the apex at $k_0 T = 0.6$ ($\epsilon = 7000$ m). For negative depth, the field is nearly vanishing. For positive depth, the radiated field pattern behaves as in Fig.6.2c but with a smaller magnitude. Also, the maximum of the cross section field is shifted away from the boundary B_{12} (zero depth). This is a consequence of the existence of the caustic in medium (n_2). One expects, then, the radiation pattern to vanish as \underline{X} moves towards the apex.

Similar reasoning holds for mode 2 and mode 3, represented by Figs.6.3 and 6.4 respectively.

However, one may notice in Figs.6.2c, 6.2d, 6.3c, 6.3d, 6.4c and 6.4d, that the field at $k_0 x = -k_0 T$ (Top interface B_{31}) is not zero, as it should be because we have assumed B_{31} interface perfectly reflecting. This is due to the fact that terms having the same order of magnitude as the wedge angle α are neglected in the analysis.

6.5. Contours of constant amplitude patterns

In this section, we use the same results as in section 6.4, but we shall reconsider, for each mode, and for each figure presented earlier in section 6.4; the field variation which corresponds only to positive depth. In addition to those already computed results, one can represent the cross section variation of the normalised field modulus (this time in dB) as a contour plot of constant amplitude, as shown in Figs.6.5, 6.6



Beam directionality = .2

Fig.6.5 : Contours of constant amplitude (in dB) in medium (n_2). Mode 1

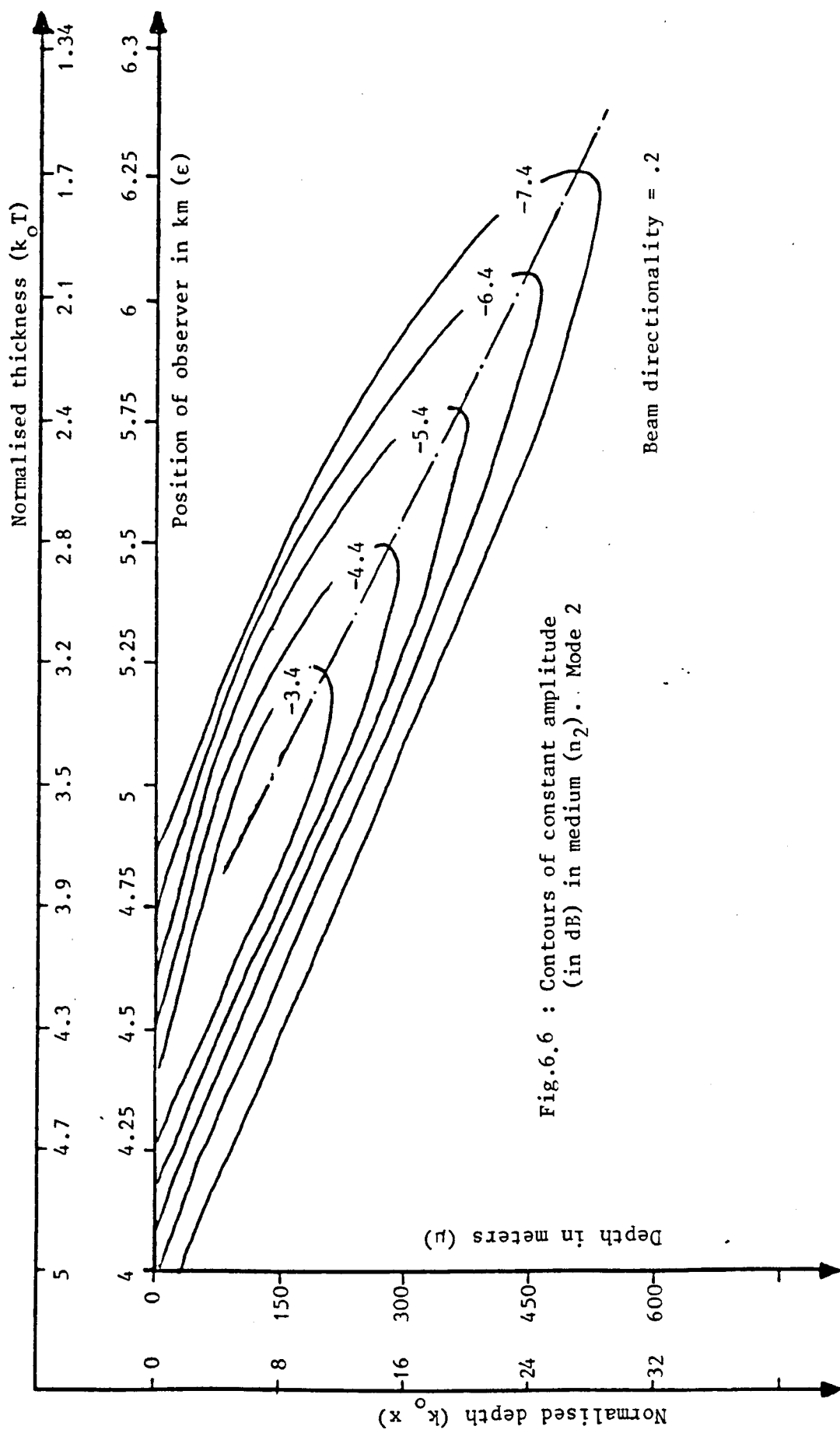
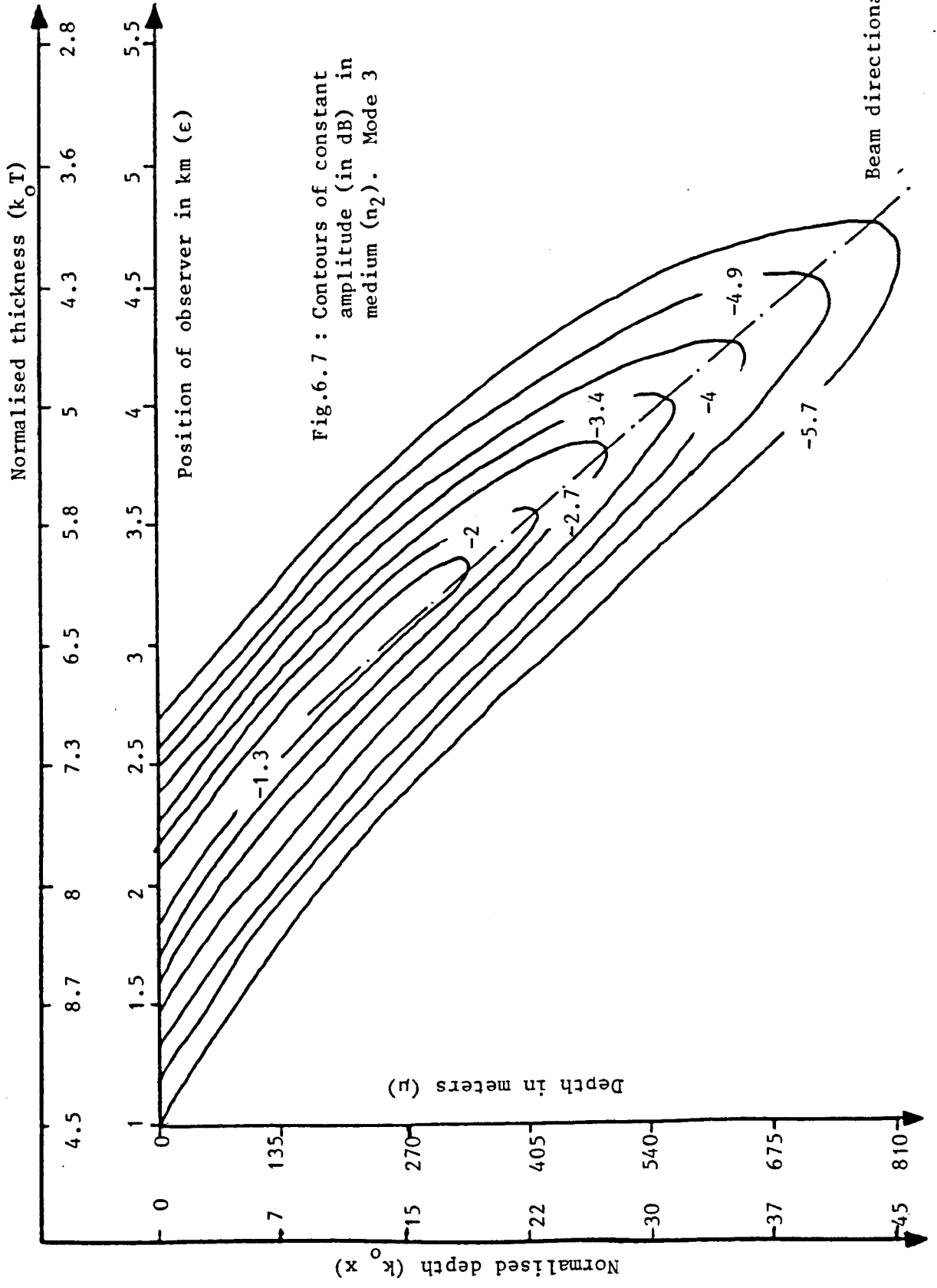


Fig.6.6 : Contours of constant amplitude (in dB) in medium (n_2).. Mode 2



and 6.7 for mode 1, 2 and 3 respectively.

Here too we use an upper horizontal scaling and a left vertical scaling, appropriate to integrated optics applications, whereas the lower horizontal scaling and the right vertical scaling are appropriate to underwater acoustic applications.

By way of emphasising the main features in Figs.6.5, 6.6 and 6.7 we have displayed contour levels between -2.7 and -4.9 dB for mode 1; between -3.4 and -7.4 dB for mode 2; and between +1.3 and -5.7 dB for mode 3. Thus, the region inside the tapered waveguide, which is uncountoured, represents a field magnitude higher than -2.7 dB for mode 1, higher than -3.4 dB for mode 2, and higher than +1.3 dB for mode 3. As for the uncountoured region in medium (n_2), it indicates a field magnitude lower than -4.9 dB for mode 1, lower than -7.4 dB for mode 2 and lower than -5.7 dB for mode 3.

In references [21], [22] and [24], unlike in our theory, their fields have been constructed with reference to a source X_0 ; whereas our fields are constructed from source-free Intrinsic and Radiation spectral Integrals. Therefore, the field magnitudes of each pattern in Figs.6.5, 6.6 and 6.7, do not contain reference to the source. In order to account for that, a constant (in dB) could be added to all contours illustrated by Figs.6.5 6.6 and 6.7.

Comparing the results of Figs.6.5, 6.6 and 6.7 (with their appropriate scaling) to Kamel and Felsen's [22] and Jensen and Kuperman's [24] good agreement is obtained. The prediction of directionality for the 3 modes (though one could obtain it for any higher mode) is in accord with the referenced papers. It is believed that the most prominent feature which enables us to

compare quantitatively our results of Figs.6.5, 6.6 and 6.7, with the earlier papers is the beam directionality, defined as the 'average' gradient of the direction of the beam. The word 'average' here is to emphasise the fact that all 3 modes show a beam directionality bending away from the tapered waveguide for observation points approaching the apex, in accordance with [24]. With guidance from reference [24], one derives a beam direction of 16 degrees for each mode. This value agrees well with the prediction from Figs.6.5, 6.6 and 6.7.

6.6. Discussion

The numerical values of the refractive indices n_1 and n_2 , may not be exactly suitable to Integrated optics devices, but their choice is mainly justified in order to obtain a similar ratio between $\frac{n_1}{n_2}$ and $\frac{v_2}{v_1}$, and to permit direct comparison of our model for underwater acoustics. That is why it is necessary to report [38] similar results to those illustrated in section 6.4 corresponding to the single layer case but for a structure more intended to be typical of Integrated optics devices. Such reported results [38] we hope will constitute a basic standard for further research to develop on the single layer problem in Integrated optics.

CHAPTER SEVEN

CONCLUSION

7.1. Summary of results

The object of this thesis was to develop reliable methods of evaluating, describing and analysing the tapered waveguide, which is considered as the main body for both structures in connection with integrated optics applications.

Five chapters were devoted to this end. In chapter 2, a conventional method was used. It mainly postulates the field distributions in each region of each type of structure.

By demanding appropriate boundary conditions at each interface, characteristic eigenvalue equations have been deduced. They provide eigenvalue solutions in terms of incident angles (saddle point θ_q), or in terms of normalised propagation constants $(\frac{\beta}{k_0})$.

All solutions correspond to different arbitrary thickness of the tapered waveguide. In the case of the single layer problem, solutions are real only in the guided wave region; in the leaky wave region, they manifest an imaginary part which accounts for the radiation loss. In the double layer case, solutions are real in the coupled wave region as well as in the guided wave region.

Chapter 3, describes an alternative method for obtaining the field distribution in terms of a Green's function, inside the tapered waveguide only. For that purpose, a hybrid ray-mode concept was formulated, subject to asymptotic considerations

which have been employed to clarify the mechanism of Adiabatic mode propagation, from its trapped to its radiating regime.

Ignoring coupling between different Adiabatic modes, the field spectrum obtained contains all the spectral information (continuous and discrete) for propagation along the tapered waveguide from an arbitrary source point \underline{X}_0 to an observation point \underline{X} . The assumption just cited is accommodated by the fact that mode coupling is unimportant for sufficiently weak wedge angle α , which is the case here. In regions where the Adiabatic mode propagates, one obtains agreement with the Adiabatic mode theory. The characteristic eigenvalue equations established by the spectral hybrid ray-mode analysis agree with those found by the conventional method of Chapter 2.

Chapter 4 was devoted to a concept of Intrinsic field; which satisfies the boundary conditions and describes systematically the field distribution inside the tapered waveguide, before and after the transition region. Such an Intrinsic formalism is defined via a plane wave spectral Integral, independent of any source configuration exciting it.

The field obtained has a local mode behaviour and it was achieved from an initial ray formulation by constructing a uniformly valid Integral representation for the field excited along and inside the tapered waveguide. Identification for any mode in the guided wave region, between the Intrinsic and Adiabatic field which was introduced in Chapter 3, permits us to extend the Intrinsic field concept beyond the transition region, when the Adiabatic mode theory fails. In that case, we have been able to explore the characteristics of local modes

even in regions where the conventional Adiabatic mode theory is not valid. Thus, the Intrinsic Integral concept is simply a uniformisation of the Adiabatic concept. For that, only suitable contours of integrations need be computationally sought. It turns out that in regions immune from any singularity, the Integral can be approximated asymptotically by the saddle point method. In this case, one need only deform the original contour of integration into a contour of steepest descent. Consequently, numerical evaluation of the Integral requires the exact knowledge of the computed steepest descent path.

However, in regions beyond the singularity, difficulties due to branch cut contribution are anticipated. For both structures, we have been able to circumvent those difficulties. The trick was to keep the original undeformed contour of integration and accomplish calculation of all spectral Integrals through integration along the real axis, more precisely between $\theta = 0$ and $\theta = \frac{\pi}{2}$. The spectral Integrals, once formulated and calculated, describe perfectly the field behaviour for any mode of both structures and in both regions with respect to the singularity.

As a result, the Intrinsic Integral, which itself is a plane wave representation of the modes, can be obtained for any general range-dependent environment other than the simple tapered waveguide, just by appropriate choice of reference system.

In this way, the singularity of the Adiabatic mode theory can be alleviated uniformly and systematically for any type of non-separable problem.

Chapter 5 also describes a Radiation Integral, which satisfies the boundary conditions and matches the Intrinsic Integral at the

bottom interface (B_{12}) of the tapered waveguide. Such a mathematical model was mainly introduced in order to analyse the field behaviour outside the tapered waveguide for observation points located before and after the transition region as well as across the structures.

In this sense, one has been able to present for any mode in integrated optics the field behaviour in medium (n_2) and in the uniform film (n_2). The former describes the leakage mechanism; whereas the latter describes the coupling transfer, respectively, for the single layer structure and the double layer structure.

Chapter 6, was mainly devoted to two purposes. On the one hand, it sums-up some computational results in connection with the single layer problem only, under two different scalings. One scaling is appropriate to integrated optics, the other is appropriate to underwater acoustic applications.

On the other hand, it compares these results appropriate to underwater acoustics with other referenced papers in order to lend confidence in the validity of the spectral analysis developed for small wedge angle α . This is achieved by numerical evaluation of the radiated field in medium (n_2), corresponding to positive depth only. The comparison of its cross section depth with the results obtained independently by the Parabolic equation method [21,24] and by the Green's function concept [22] have confirmed its validity in the guided wave region as well as in the leaky wave region for the same characteristic parameters.

This study clearly demonstrates the power of the spectral analysis method in handling propagation, not only restricted to the tapered waveguide in integrated optics but also to any type

of range dependent environment, such as underwater acoustic propagation, tropospheric ducts etc.

In this sense, the accuracy of the method inherently increases with decreasing wedge angle α .

Finally, we have been able to fully predict the mode behaviour of tapered structures, particularly in the integrated optics domain, by implementing the numerical simulation of the model based on the spectral analysis.

To this purpose, Appendix F elaborates a brief flow chart of the computer program developed for the implementation of such spectral analysis.

We thus hope that these predictions will form basic material in terms of a standard model, for further work to be carried out, in connection with any range-dependent environment.

As for the choice of the refractive indices, in connection with the single layer structure, they can be arbitrary as long as they are subject to the practicality of the structure and they satisfy the inequality given by (2.1).

In connection with the double layer structure, its choice is very relevant particularly when investigating the field behaviour outside the tapered waveguide and in the coupled wave region. Typical index differences should be in the range between 0.01 and 0.10, provided that (2.1) is met.

7.2. Suggestions and Further Work

The work presented in this thesis provides an initial investigation into the tapered waveguide also known as the tapered coupler. More work needs to be done to establish its full

significance as well as the limitation of the generalised spectral analysis.

One of the most important limitations of the model is due to the fact that the range variable should not extend past the apex of the tapered waveguide. In this sense, the location of any observation point across each structure is perfectly determined, whereas for observation points beyond the apex, it is physically impossible to envisage because of the analysis in the model. Also as T approaches zero, diffraction phenomena might be anticipated. Such an effect could be simulated by investigating a diffraction integral, which could be appended to the model in order to account for the diffraction occurring at the apex. However, this effect can safely be neglected for weak wedge angle and for observation points quite distant from the apex.

In addition one should explore to what extent the spectral Integral accommodates the propagation when the source is located beyond the cut-off region for any desired mode. Furthermore, if the source location is in a mode cut-off region, a different asymptotic analysis is required, where in here it is assumed that the source point and the transition region are far distant.

One could expand the work and investigate the propagation for curved bottom interfaces of the tapered waveguide. Such a complication might lead to a three-dimensional problem.

Also, propagation in inhomogeneous media should be tackled, a more complicated problem which involves mode coupling phenomena. Besides, particularly in the double layer case, one ought to investigate more thoroughly the coupling mechanism in regions beyond the singularity θ_c .

APPENDIX A

1. Poisson-sum-formulae

Consider a function $G(t)$, continuous and bounded in the interval $0 < t < 1$. Then, the theory of Fourier series [33] gives :

$$G(0) + G(1) = 2 \sum_{q=-\infty}^{+\infty} \int_0^1 G(t) \exp[-i 2 \pi q t] dt \quad (\text{A.1})$$

The series in (A.1) is convergent; summing over the integer value of m , one gets the Poisson-sum-formulae :

$$2 \sum_{m=1}^M G(m) = G(1) + G(M) + 2 \sum_{q=-\infty}^{+\infty} \int_1^M G(m) \exp[-i 2 \pi q m] dm \quad (\text{A.2})$$

Using equation (3.7) which gives the mapping between m and the incident angle θ , (A.2) becomes :

$$\sum_{m=1}^M G(m) = \frac{1}{2} [G(\theta_0) + G(\theta_M)] + \sum_{q=-\infty}^{+\infty} \int_{\theta_0}^{\theta_M} G(\theta) \exp[-i 2 \pi q m] \frac{d\theta}{2 \alpha} \quad (\text{A.3})$$

θ_0 and θ_M correspond to the first ($m = 1$) and the maximum ($m = M$) reflections respectively.

Neglecting the end points of the integral (A.3) is valid, for as long as M tends to infinity.

2. Euler Mac-Laurin formulae

Recalling (A.1), the Euler Mac-Laurin formula, which transforms a discrete sum into a continuous integral is derived as :

$$\sum_{m=1}^M G(m) = \frac{1}{2} [G(1)+G(M)] + \int_1^M G(m) dm + \text{Error} \quad (\text{A.4})$$

Where

$$\text{Error} = 2 \sum_{q=-\infty}^{+\infty} \int_1^M G(m) \cos(2\pi q m) dm \quad (\text{A.5})$$

As for the case one is concerned with, $G = \phi(\theta)$ is the phase change introduced at the bottom interface B_{12} of the tapered waveguide. The Error term in (A.4), which is usually [35] expressed in terms of the derivative of G , is neglected as α is small, in comparison with other dominant terms [23].

Another justification of the neglect of the Error term in (A.5), could be explained by using the Riemann-Lebesgue theorem [33]. The factor $2\pi qm$, which depends on α according to equation (3.7), becomes infinite as α is small. This, in addition to the fact that M tends to infinity, states the conditions which require that the integral in (A.5) vanishes.

APPENDIX B

This appendix works out the double integrals of equations (3.18) in a region where the two saddle points θ_{oq} and θ_q defined by (3.22) and (3.23) respectively, are far from the singularity θ_c . In other words, this analysis is limited to an observation point \underline{X} located in the guided wave region. Therefore, evaluation of (3.18) is amenable to the application of the saddle point method [36].

We concentrate first on the double integral (3.18a); its corresponding phase function is given by (3.20a).

The two saddle points are given by recalling (3.22) and (3.23) as :

$$\frac{\partial S_e^u}{\partial \theta_o} (\theta, \theta_{oq}) = 0 \quad (B.1)$$

$$\frac{\partial S_e^u}{\partial \theta} (\theta_q, \theta_o) = 0 \quad (B.2)$$

By expanding the phase $S_e^u(\theta, \theta_o)$ to second order in θ_o and θ , about θ_{oq} and θ_q respectively, and also using (B.1) and (B.2), equation (3.18a) becomes, after neglecting its end-points as M tends to infinity :

$$g_e^u(\underline{X}, \underline{X}_o) = \pi \exp[i k S_e^u(\theta_{oq}, \theta_q)] A(\chi, \theta_q) A(\chi_o, \theta_{oq}) \quad (B.3)$$

A similar treatment of other species of waves in equations (3.18) gives :

$$g_o^u(\underline{X}, \underline{X}_o) = \pi \exp[i k S_o^u(\theta_{oq}, \theta_q)] A(\chi, \theta_q) A(\chi_o, \theta_{oq}) \quad (B.4)$$

$$g_e^d(\underline{X}, \underline{X}_o) = \pi \exp[i k S_e^d(\theta_{oq}, \theta_q)] A(\chi, \theta_q) A(\chi_o, \theta_{oq}) \quad (\text{B.5})$$

$$g_o^d(\underline{X}, \underline{X}_o) = \pi \exp[i k S_o^d(\theta_{oq}, \theta_q)] A(\chi, \theta_q) A(\chi_o, \theta_{oq}) \quad (\text{B.6})$$

Where the coefficients $A(\chi, \theta_q)$ and $A(\chi_o, \theta_{oq})$ are defined as follows :

$$A(\chi, \theta_q) = \{r \alpha k \cos \theta_q + \frac{1}{2} \frac{\partial \phi}{\partial \theta}(\theta_q)\}^{-\frac{1}{2}} \quad (\text{B.7a})$$

$$A(\chi_o, \theta_{oq}) = \{r_o \alpha k \cos \theta_{oq} + \frac{1}{2} \frac{\partial \phi}{\partial \theta_o}(\theta_{oq})\}^{-\frac{1}{2}} \quad (\text{B.7b})$$

APPENDIX C

This appendix evaluates the double integrals of equations (3.18), in a region near and beyond the singularity θ_c .

We shall here too, concentrate only on the double integrals (3.18a), whose phase function is also defined in (3.20a). This phase function is characterised by the general behaviour of the dominant term $\alpha^{-1}Q(\chi, \theta)$ and $\alpha^{-1}Q(\chi_o, \theta_o)$. The function $Q(\chi, \theta)$ defined in (3.21) has a saddle point θ_q and a branch point θ_c of order $\frac{1}{2}$. Therefore, mapping the θ -plane into the s -plane, where $s = (\theta - \theta_c)^{\frac{1}{2}}$, takes the singularity θ_c into a new saddle point $s = 0$, because :

$$\frac{\partial Q}{\partial s} [\chi, \theta(s)] = \frac{\partial Q}{\partial \theta} (\chi, \theta) \quad \frac{\partial \theta}{\partial s} = \frac{\partial Q}{\partial \theta} (\chi, \theta) \quad 2s = 0 \quad (C.1)$$

which proves that $\theta = \theta_q$ and $s = 0$ are saddle points to $Q(\chi, \theta)$, in the θ -plane and s -plane respectively.

As θ_q is near (or beyond) the branch point θ_c , evaluation of the θ -integration in (3.18a) cannot be performed by the saddle point method, although the θ_o -integration can be performed by the saddle point method, because θ_{oq} is always maintained distant from any singularity. Therefore, another method must be sought to work out the θ -integration in (3.18a) in such a region. For that, we ought to map the function $Q(\chi, \theta)$ into a cubic polynomial by a suitable change of variable s into t , using the method of Chester-Friedman-Ursell [33]. (The variable t here is not to be confused with the time variable).

One can then, write $Q(\chi, \theta)$ in (3.20a) as [23] :

$$\alpha^{-1} Q(\chi, \theta) = Q_0(\chi) + Q_1(\chi) \frac{t^2}{2} - i \frac{t^3}{3} \quad (C.2)$$

where

$$Q_0(\chi) = \alpha^{-1} Q(\chi, \theta_c) \quad (C.3)$$

$$Q_1(\chi) = \{6 \alpha^{-1} Q(\chi, \theta_c) - 6 \alpha^{-1} Q(\chi, \theta_q)\}^{1/3} \quad (C.4)$$

The remaining term in the phase expression of (3.20a) has the form :

$$C = \frac{\partial Q}{\partial \theta}(\chi, \theta) + r \chi k \sin \theta \quad (C.5a)$$

Consequently :

$$\frac{\partial \theta}{\partial t} \exp [i C] = B_1 t \quad (C.5b)$$

and after some intermediate calculations, it is established that the general form of the leading coefficient is :

$$B_1 = 2 D(\chi) \exp[i r \chi k \sin \theta_c] \quad (C.6a)$$

and

$$D(\chi) = Q_1(\chi) \{\alpha^{-1} \frac{\partial^2 Q}{\partial s^2}(\chi, \theta_c)\}^{-1} \quad (C.6b)$$

Finally, evaluation of (3.18a) by the saddle point method for the θ_0 -integration and by the Chester-Friedman-Ursell method for the θ -integration leads to the result [23] :

$$g_e^u(\underline{X}, \underline{X}_0) = N \exp[i r_0 \chi_0 k \sin \theta_{oq}] \exp[-i r \chi k \sin \theta_c] \quad (C.7)$$

where

$$N = 2 \pi^{1/2} (2 \alpha)^{-1/2} e^{-j \frac{\pi}{4}} A(\chi_0, \theta_{oq}) D(\chi) \exp[i \alpha^{-1} Q(\chi_0, \theta_{oq})] \\ \int_{-\infty}^{+\infty} e^{2 \pi \frac{i}{3} t} \exp[i Q_1(\chi) \frac{t^2}{2} + \frac{t^3}{3}] dt \quad (C.8)$$

A similar reasoning leads to the result of the other species of waves in (3.18) :

$$g_o^u(\underline{X}, \underline{X}_o) = -N \exp[i r_o \chi_o k \sin\theta_{oq}] \exp[i r \chi k \sin\theta_c] \quad (C.9a)$$

$$g_e^d(\underline{X}, \underline{X}_o) = N \exp[-i r_o \chi_o k \sin\theta_{oq}] \exp[i r \chi k \sin\theta_c] \quad (C.9b)$$

$$g_o^d(\underline{X}, \underline{X}_o) = -N \exp[-i r_o \chi_o k \sin\theta_{oq}] \exp[-i r \chi k \sin\theta_c] \quad (C.9c)$$

where the coefficient N , $D(\chi)$, $Q_1(\chi)$, $A(\chi_o, \theta_{oq})$ and $Q(\chi_o, \theta_{oq})$ are respectively given by (C.8), (C.6b), (C.4), (B.7b) and (3.21).

The coefficients $D(\chi)$ and $Q_1(\chi)$, can be further approximated. For this purpose, one must bear in mind that θ_q lies near θ_c , as is the case just past the transition region. One can define :

$$\Delta = 2 \alpha^{-1} (2 \cotg\theta_c)^{\frac{1}{2}} \quad (C.10a)$$

$$\eta = r_c - r \quad (C.10b)$$

$$Z = k \eta \sin\theta_c \quad (C.10c)$$

Where r_c is the critical range corresponding to the critical thickness ($T_c = r_c \alpha$); which gives an incident angle $\theta = \theta_c$. It is at this stage, when $r = r_c$ that the Adiabatic mode defined in subsection 3.8.1 becomes cut-off. The critical range is defined by :

$$k \alpha r_c \sin\theta_c = \pi (q - \frac{1}{2}) \quad (C.10d)$$

Using (C.3), (C.4), (C.6) and (C.10) it is shown in [23] that one can approximate the expression $Q_1(\chi)$ by :

$$Q_1(\chi) \cong 2 Z \Delta^{-2/3} \quad (C.11a)$$

Consequently :

$$D(\chi) = \Delta^{-2/3} \quad (C.11b)$$

and

$$\frac{Q_1(\chi)}{D(\chi)} = \alpha^{-1} \frac{\partial^2 Q}{\partial s^2}(\chi, \theta_c) = 2 Z \quad (C.11c)$$

Beyond the critical region, where the saddle point θ_q becomes distant from the branch point θ_c , we require a distinct expression for the branch point contribution.

This arises in the t -plane, for the saddle point $t = 0$; it is easily found by standard asymptotic techniques. Equations (C.7) and (C.9) become , after using (C.11) :

$$g_e^u(\underline{X}, \underline{X}_0) = H \exp[i r_0 \chi_0 k \sin\theta_{oq}] \exp[-i r \chi k \sin\theta_c] \quad (C.12a)$$

$$g_o^u(\underline{X}, \underline{X}_0) = -H \exp[i r_0 \chi_0 k \sin\theta_{oq}] \exp[i r \chi k \sin\theta_c] \quad (C.12b)$$

$$g_e^d(\underline{X}, \underline{X}_0) = H \exp[-i r_0 \chi_0 k \sin\theta_{oq}] \exp[i r \chi k \sin\theta_c] \quad (C.12c)$$

$$g_o^d(\underline{X}, \underline{X}_0) = -H \exp[i r_0 \chi_0 k \sin\theta_{oq}] \exp[-i r \chi k \sin\theta_c] \quad (C.12d)$$

where

$$H = \pi A(\chi_0, \theta_{oq}) B(\chi, \theta_c) \exp[i \alpha^{-1} Q(\chi_0, \theta_{oq})] \exp[i \alpha^{-1} Q(\chi, \theta_c)] \quad (C.13)$$

and

$$B(\chi, \theta_c) = \alpha (k \eta \sin\theta_c)^{-5/2} (\cot\theta_c)^{\frac{1}{2}} \quad (C.14)$$

The coefficients $A(\chi_o, \theta_{oq})$ and $Q(\chi, \theta)$ are given by (B.7b) and (3.21) respectively.

At this stage of this Appendix, it is worth mentioning that equations (C.12), (C.13) and (C.14) describe exclusively the field behaviour (within the approximation of (C.11)) in a region not far from, but past the transition region. Such expressions are of use in subsection 3.8.3. As for equations (C.7), (C.8) and (C.9); they describe the field at the transition region, and they are of use in subsection 3.8.2.

APPENDIX D

In the case of the double layer problem, the insertion of the film (n_2) having a uniform thickness d as shown in Fig.D.1, does not allow the use of Fresnel's equation for the calculation of the reflection coefficient at the bottom interface (B_{12}) of the tapered waveguide. For the dimension of the medium (n_2) is no more supposed infinite, as was the case for the single layer structure. Consequently, the presence of the film (n_2) of finite thickness d makes the evanescent wave A_2 launched in it, undergo multiple reflections. These waves are coupled back into the tapered waveguide and interfere with the originally incident waves in the tapered waveguide. One is then inclined to work out the phase change $\phi(\theta)$ introduced at the bottom interface B_{12} by suggesting a method using the concept of the modified reflection coefficient $\Gamma(\theta)$, which represents the composite reflection coefficient at interface B_{12} , due only to one incident wave A_1 as it is schematised by Fig.D.1. This Appendix aims to calculate the total accumulated phase change $\phi(\theta)$ for the double layer structure, introduced at interface B_{12} as the light propagates along the tapered waveguide undergoing m reflections.

Each plane wave is individually tracked through successive reflections at the top (B_{31}) and bottom (B_{12}) interfaces using the appropriate Fresnel's coefficient at each reflection. See Fig.D.1.

One uses the conventional notation Γ_{ij} for the Fresnel reflection coefficients between medium (n_i) and medium (n_j) and are directly given by the Fresnel's equations for a TE type of

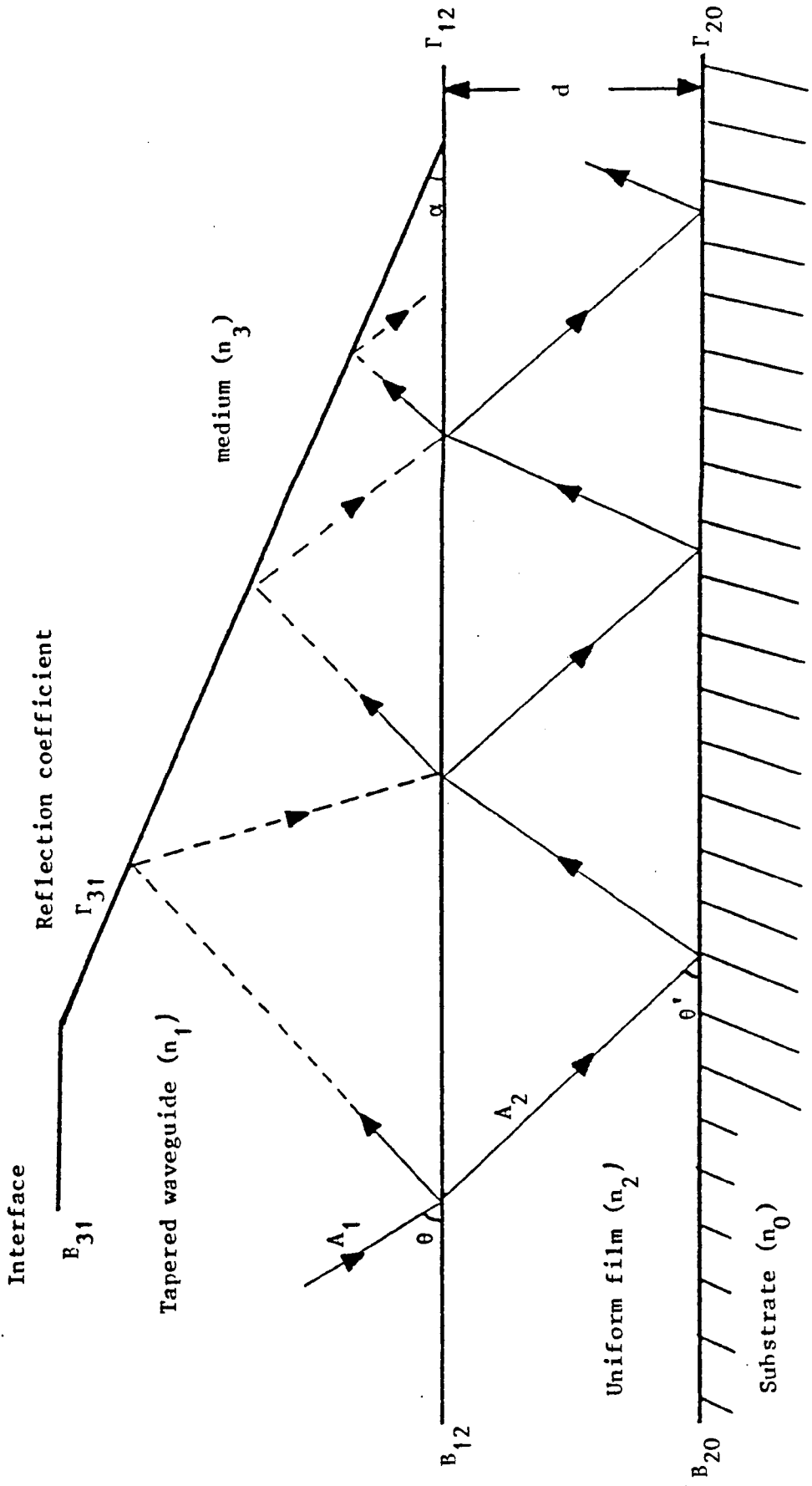


Fig.D.1 : Wave tracking for the modified reflection coefficient of the double layer structure

polarisation. They are :

$$\Gamma_{ij} = \exp \left\{ i \left[2 \operatorname{Atan} \left(\frac{n_j \sin \theta_j}{n_i \sin \theta_i} \right) \right] \right\} \quad (\text{D.1a})$$

where θ_i and θ_j are the incidence angle in medium (n_i) and (n_j) respectively. They are related via the Snell's law by :

$$n_i \cos \theta_i = n_j \cos \theta_j \quad (\text{D.1b})$$

We also define the T_{ij} which are the corresponding transmission coefficients. Assuming that there is no absorption in any medium, one recalls the equation :

$$T_{ij} - \Gamma_{ij} = 1$$

It can easily be demonstrated that after M reflections occur at B_{12} , after a laborious calculation to sum up a geometric progression, there results :

$$\Gamma(\theta) = \Gamma_{12}(\theta) + \Gamma_{20}(\theta') T_{12}(\theta) T_{21}(\theta') \exp(2 i \gamma) \left\{ \frac{1 - \Gamma_{20}^M(\theta') \Gamma_{21}^M(\theta') \exp(2 i \gamma M)}{1 - \Gamma_{20}(\theta') \Gamma_{21}(\theta') \exp(2 i \gamma)} \right\} \quad (\text{D.2})$$

as M tends to infinite and as :

$$\left| \Gamma_{20}(\theta') \Gamma_{21}(\theta') \exp(2 i \gamma) \right| < 1$$

(D2) becomes :

$$\Gamma(\theta) = \Gamma_{12}(\theta) + \Gamma_{20}(\theta') \exp(2 i \gamma) \left\{ \frac{T_{12}(\theta) T_{21}(\theta')}{1 - \Gamma_{20}(\theta') \Gamma_{21}(\theta') \exp(2 i \gamma)} \right\} \quad (\text{D.3})$$

where $\gamma = k_0 d (n_2^2 - n_1^2 \cos^2 \theta)^{\frac{1}{2}}$ (D.4)

At the m^{th} reflection at B_{12} interface, the incidence angle is θ ; then the total reflection coefficient is given by :

$$\prod_{\theta_l = \theta_0}^{\theta_M} \Gamma(\theta) = \Gamma_{31}(\theta_l + \alpha)$$

where α is the wedge angle and θ_l is defined by (3.7) and recalled here to be :

$$\theta_l = \theta_0 + 2 \alpha (l-1) \quad (\text{D.5b})$$

θ_0 and θ_M are the incident angles corresponding to the first and maximum reflection at B_{12} respectively.

Using (D.1), (D.2) and (D.5) the accumulated phase change $\phi(\theta)$ at B_{12} interface, after m reflections have taken place, is finally given by :

$$\phi(\theta) = \text{Argt} [\Gamma(\theta)] + \text{Argt} [\Gamma_{31}(\theta + \alpha)] \quad (\text{D.6})$$

where Argt denotes the argument.

As we assume for simplicity that medium (n_3) is perfectly reflecting, (D.6) becomes :

* In the guided wave region : $n_2 < \frac{\beta}{k_0} < n_1$

$$\phi(\theta) = -2 \text{Atan} \left\{ \frac{\tau_0 \gamma_2 - \gamma_2^2 \tanh(k_0 d \gamma_2)}{\gamma_1 \gamma_2 - \tau_0 \gamma_1 \tanh(k_0 d \gamma_2)} \right\} \quad (\text{D.7})$$

with
$$\gamma_2^2 = \left(\frac{\beta}{k_0}\right)^2 - n_2^2 \quad (\text{D.8})$$

* In the coupled wave region : $n_0 < \frac{\beta}{k_0} < n_2$:

$$\phi(\theta) = -2 \operatorname{Atan} \left\{ \frac{\tau_0 \gamma_2 + \gamma_2^2 \tan(k_0 d \gamma_2)}{\gamma_2 \gamma_1 - \tau_0 \gamma_1 \tan(k_0 d \gamma_2)} \right\} \quad (\text{D.9})$$

$$\text{with} \quad \gamma_2^2 = n_2^2 - \left(\frac{\beta}{k_0}\right)^2 \quad (\text{D.10})$$

In both cases, d is negative in order to be consistent with the same choice of d as in Chapter 2. We also define :

$$\beta = k_0 n_1 \cos\theta \quad (\text{D.11a})$$

$$\tau_0^2 = \left(\frac{\beta}{k_0}\right)^2 - n_0^2 \quad (\text{D.11b})$$

$$\tau_3^2 = \left(\frac{\beta}{k_0}\right)^2 - n_3^2 \quad (\text{D.11c})$$

$$\gamma_1^2 = n_1^2 - \left(\frac{\beta}{k_0}\right)^2 \quad (\text{D.11d})$$

The general expression of $\phi(\theta)$ can either be characterised by (D.7) or (D.9). However, declaring either equations to be complex in the computer program leads to the same result of $\phi(\theta)$, as β moves from the guided wave region to the coupled wave region.

APPENDIX E

This Appendix gives the flow chart, of the developed computer program 'Saddle point - SDP', to compute the steepest descent path (SDP) of any phase function $S(\chi, \theta)$ of integral (4.4).

The procedure locates first the saddle point θ_q for a fixed local thickness T (observation point \underline{X}) by means of the Newton-Raphson numerical algorithm. θ_q could be real or imaginary, depending on which region with respect to the critical angle θ_c one is dealing with, and also depending on which of the waveguiding structures one is concerned with.

The computation of the SDP is via equation (4.6). It implements the 'False Position' algorithm on each complex variable θ defined with respect to the origin (0,0) (see Fig.E.1).

Initially, one fixes α_{inc} positive so as to depict the upper part of the (SDP) contour, and chooses 2 arbitrary points θ_{01} and θ_{02} as initial guesses, whose values are very close to θ_q 's.

Iterating θ_{01} and θ_{02} so as to have :

$$\text{Real} [S(\chi, \theta)] = \text{Real} [S(\chi, \theta_q)] \quad (\text{E.1})$$

satisfied to a certain approximation ($\leq 10^{-8}$) leads to a root of equation (E.1) (see Figs.E.1 and E.2).

Incrementing α_{inc} and starting again from θ_{01} and θ_{02} close to θ (previous root), we repeat the procedure until the upper part of the SDP is completed. That is to say, when the total number of points θ is equal to N , where N is the arbitrary specified number of points in each part of the SDP.

For computation of the lower part of the SDP, we repeat the same procedure, bearing in mind that α_{inc} is negative. Of course,

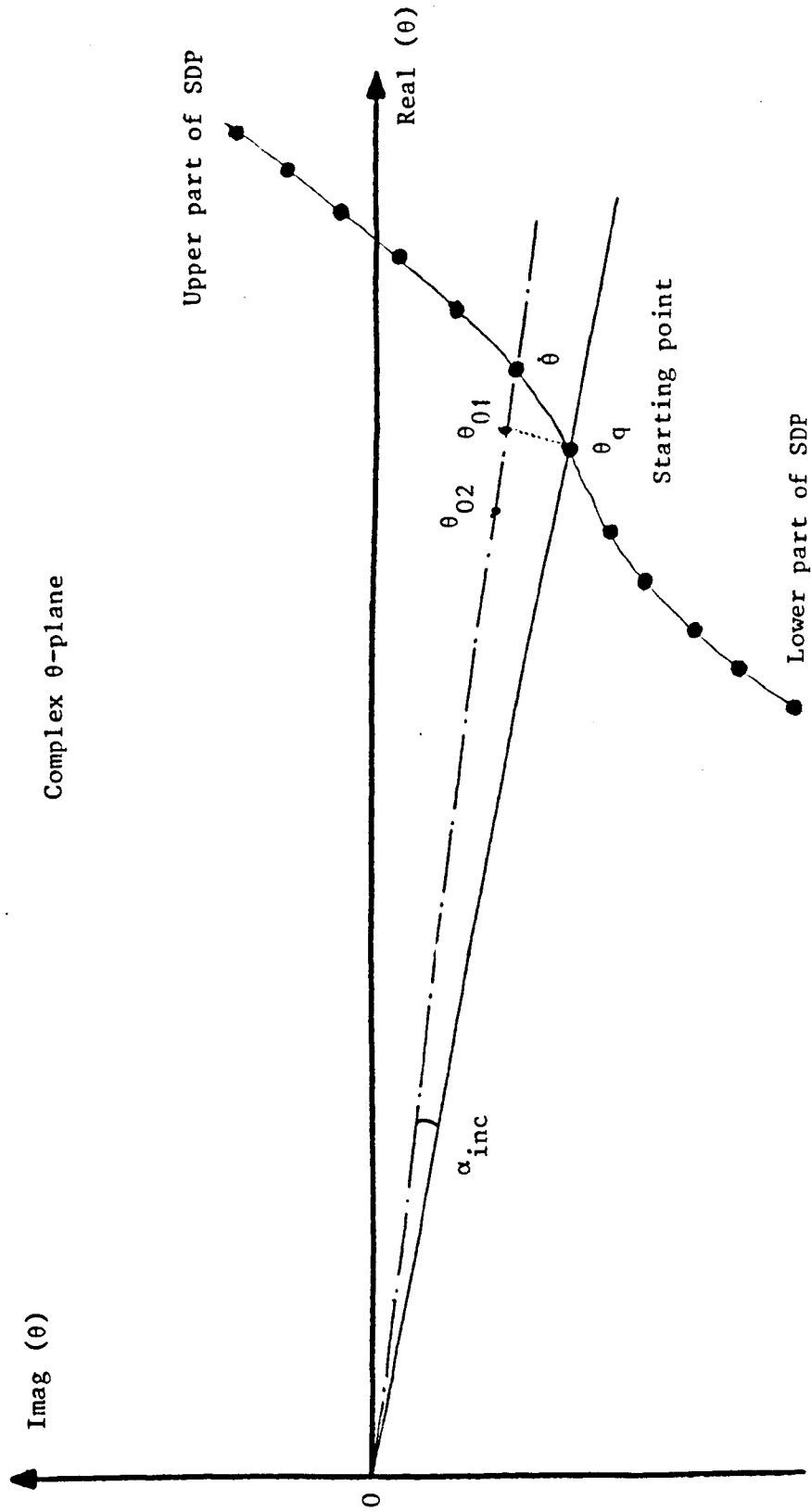


Fig.E.1 : Discrete representation of the steepest descent path (SDP) in the complex θ -plane

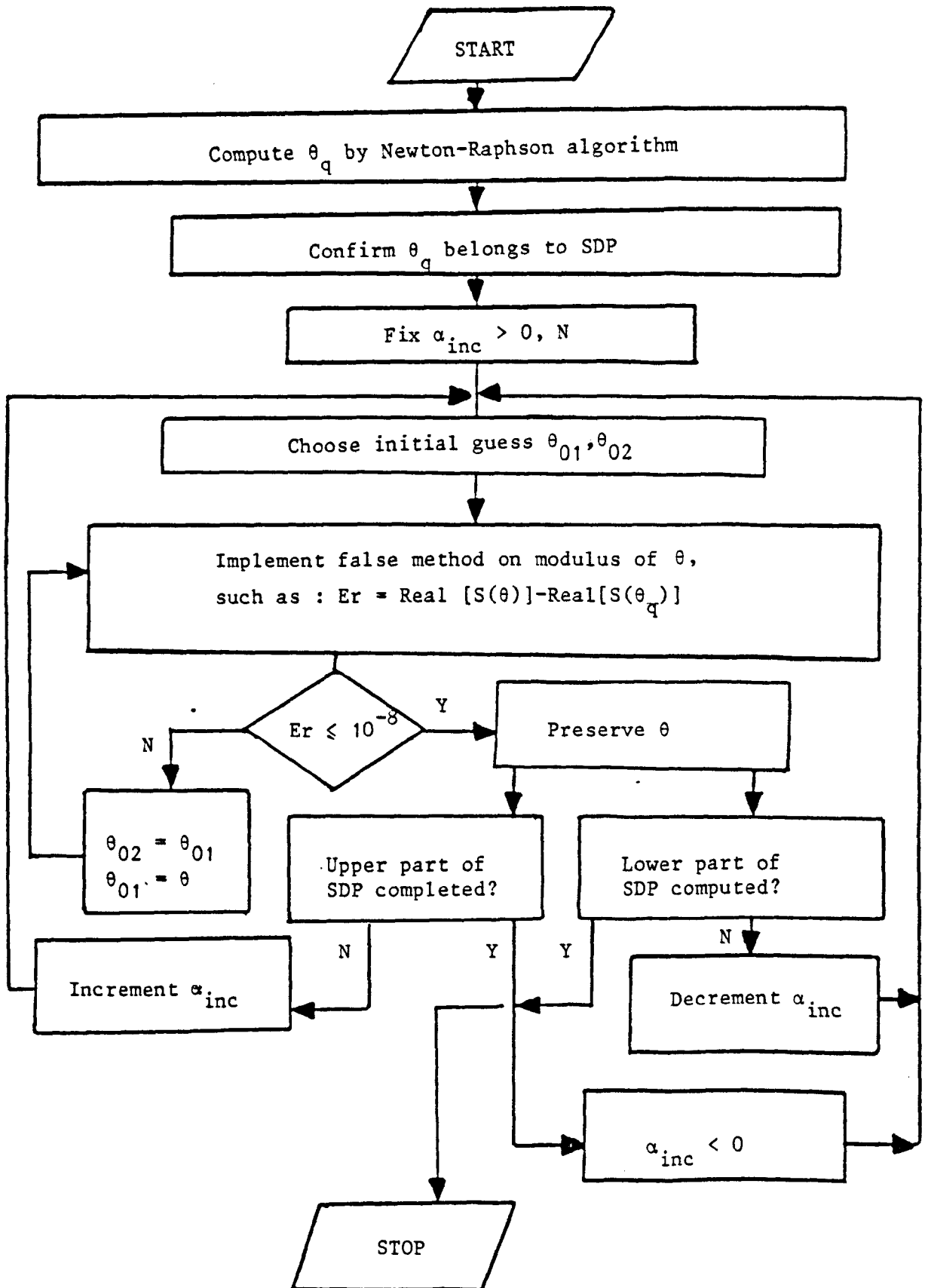


Fig.E.2 : Flow chart of program 'Saddle point - SDP'

the running time will automatically depend on the number of points N making up each part of the SDP. By taking α_{inc} within the wedge angle α ($\alpha_{inc} = \pi \cdot 10^{-2}$) and a quite small number of points N (20 points), one can get away very efficiently with a good approximation of Integral (4.4). In this case, the running time to implement 'Saddle point - SDP' is 5 seconds on an ICL-2900 computer.

As a matter of fact, only a few points near the saddle point θ_q , contribute significantly to the asymptotic evaluation of any integral by the saddle point method.

The drawback of this program, however, is that it works perfectly well in a region where $\theta_q < \theta_c$ (guided wave region), but beyond any singularity where $\text{Real}(\theta_q) > \theta_c$ it becomes very difficult to compute the SDP. For, past the transition region, the SDP tends to surround the singularity θ_c . Consequently, the computer program predicts points on the steepest ascent path instead of points on the steepest descent path. For this reason, one must find another method of evaluation of the integrals in a region past the singularity. This is dealt with in Chapters 4 and 5.

APPENDIX F

This Appendix aims to present a brief flow chart of the main computer program, used to implement the mathematical model which describes the field behaviour $f(\chi, \theta)$ defined as follows :

$$f(\chi, \theta) = I(\chi, \theta) \quad 0 < \chi < \alpha \quad (\text{depth} < 0) \quad (\text{F.1a})$$

$$f(\chi, \theta) = R(\chi, \theta) \quad \chi > \alpha \quad (\text{depth} > 0) \quad (\text{F.1b})$$

For both structures, $I(\chi, \theta)$ is given by equation (4.4), whereas $R(\chi, \theta)$ is given by (5.4) for the single layer structure and by (5.15) for the double layer structure. $I(\chi, \theta)$ and $R(\chi, \theta)$ are recalled to represent the field distribution inside and outside the tapered waveguide respectively.

One should refer to Fig.F.1, whereby we start by supplying the data, which consists of locating an observation point \underline{X} at a thickness T , for a specific mode number. We also give the appropriate expression of $\phi(\theta)$, whether dealing with the single layer structure or the double layer structure.

We fix the maximum of the cross variable χ (or depth). In the double layer case, this maximum is restricted by the thickness d of the uniform film (n_2).

In Fig.F.1, one can perform the contour integrals in $f(\chi, \theta)$ either by following the sequence in 'path 1', which consists of integrations along the real axis and in the interval $0 < \theta < \frac{\pi}{2}$; or by following the sequence in 'path 2', which makes use of the program 'Saddle point - SDP' presented in Appendix E, and then performing integrations on the steepest descent path (SDP).

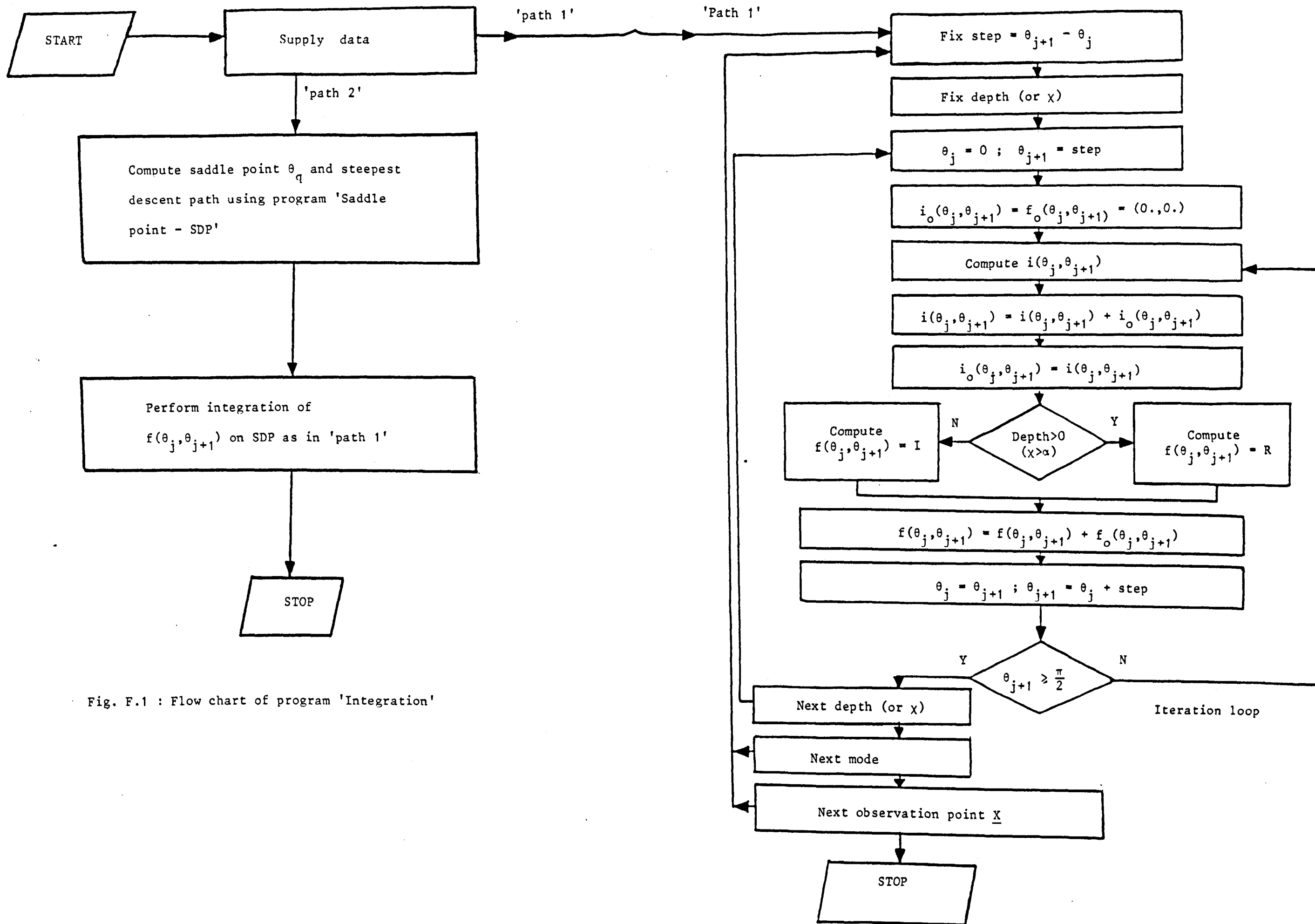


Fig. F.1 : Flow chart of program 'Integration'

Returning to 'path 1' in Fig.F.1, it is necessary to supply the integration step $\theta_{j+1} - \theta_j$, which must be smaller than the oscillations periods of the phases in $f(\chi, \theta)$. According to section 5.3, such oscillation periods are on the order of 10^{-2} radians.

We fix the cross variable χ (or depth) as well as two arbitrary initial points, θ_{j+1} and θ_j , such as $\theta_{j+1} - \theta_j = \text{step}$. These two points belong to the interval $0 < \theta < \frac{\pi}{2}$ and they both depart from zero.

We set the initial complex quantities as :

$$f_o(\theta_j, \theta_{j+1}) = i_o(\theta_j, \theta_{j+1}) = (0, 0) \quad (\text{F.2})$$

We compute in the interval (θ_j, θ_{j+1}) , the integral :

$$i(\theta_j, \theta_{j+1}) = (2\alpha)^{-\frac{1}{2}} \int_{\theta_j}^{\theta_{j+1}} \phi(\theta) d\theta \quad (\text{F.3})$$

Equation (F.3) is carried out by means of Simpson's numerical rule.

We update $i(\theta_j, \theta_{j+1})$, by adding to it $i_o(\theta_j, \theta_{j+1})$, which initially is zero, in order to accumulate the contributions of all $i(\theta_j, \theta_{j+1})$ from $\theta_j = 0$ to θ_{j+1} . It is also necessary to refresh the quantity $i_o(\theta_j, \theta_{j+1})$ by storing once again $i(\theta_j, \theta_{j+1})$ into it. This quantity will be used in the next iteration, so as to reduce the computing time, and also for the integral in (F.3) to cover the whole range from zero to θ_{j+1} . We test whether $\alpha > \chi > 0$ or $\chi > \alpha$ (depth negative or positive respectively). In the former case $f(\theta_j, \theta_{j+1}) = I(\chi, \theta)$, which describes the field inside the tapered waveguide; in the latter case, $f(\theta_j, \theta_{j+1}) = R(\chi, \theta)$, which describes the field in the bottom adjacent medium. In either case, the integration of $f(\theta_j, \theta_{j+1})$ is also performed by the

Simpson's rule in the interval (θ_j, θ_{j+1}) and at the same time as $i(\theta_j, \theta_{j+1})$ in (F.3).

We need to add to $f(\theta_j, \theta_{j+1})$ the previous value $f_o(\theta_j, \theta_{j+1})$, which corresponds to the preceding iterations and which initially is zero. We then increment θ_j and θ_{j+1} by a step length and repeat the same process until θ_{j+1} reaches $\frac{\pi}{2}$. The same integration routines are repeated over, for the next cross variable χ (depth), the next mode and the next observation point \underline{X} .

Of course, the computer running time depends on the number of χ (depth), integration step, number of modes as well as the number of points \underline{X} . However, for a fixed integration step of 10^{-2} rds and for 50 values of χ (depth), at each range of each contributing mode, it requires approximately 60 s of CPU running time or an ICL-2900 computer.

For underwater acoustic applications, the program still holds, but it is necessary to introduce the appropriate change of variable as given in section 6.2.

As far as the sequencies in 'path 2' of Fig.F.1 are concerned, the θ_j are represented by the discrete values of points making up the SDP, each of them stored in an array from program 'saddle point - SDP' presented in Appendix E. Thus, to perform the integrations along the SDP, one could follow the same procedure as in 'path 1', but the incrementation and the selection of the θ_j 's are restricted to those constituting the SDP. The integration along the SDP works perfectly well in the guided wave region, and achieves the same results as if integrating along the real axis and in a shorter time. Unfortunately, in regions past the singularity, difficulties due to branch cut contributions arise.

For this reason, we drop the integration along the SDP and concentrate only on the integration along the real axis; this works adequately in both regions with respect to the singularity.

REFERENCES

1. TIEN, P. K., and MARTIN, R. J.,
'Modes of propagating light waves in thin film deposited semiconductor films',
Appl. Phys. Letters, Vol.14, No.9, May (1969), pp.291.
2. DAKSS, M. L., KUHN, L., HEIDRICH, R. F. and SCOTT, B. A.,
'Grating coupler for efficient excitation of optical guided waves in thin films',
Appl. Phys. Letters, Vol.16, No.12, June (1970), pp.523.
3. ULRICH, R.,
'Optimum excitation of optical surface wave',
J. Opt. Soc. Am., Vol.61, No.11, November (1971), pp.1467.
4. TIEN, P. K. and MARTIN, R. J.,
'Experiments on light waves in a thin tapered film and a new light wave coupler',
Appl. Phys. Letters, Vol.18, No.9, May (1971), pp.398.
5. OSTROWSKY, D. B., POIRIER, R., REIBER, L. M. and DEVERDUM, C.,
'Integrated optical photodetector',
Appl. Phys. Letters, Vol.22, No.9, May (1973), pp.463.
6. BURNS, W. K. and MILTON, A. F.,
'Mode conversion in planar dielectric separating waveguides',
IEEE, J.QE, Vol.QE11, No.1, January (1975), pp.33.
7. HALL, D., YARIV, A. and GARMIRE, E.,
'Observation of propagation cut off and its control in thin optical waveguides',
Appl. Phys. Letters, Vol.17, No.3, August (1970), pp.127.
8. HUNTER, W. R.,
'Physics of thin films',
Vol.7, 1973, edited by Georg Hass, Academic Press, N.Y. and London.
9. MAISSEL, L. I. and FRANCOMBE, M. H.,
'An introduction to thin films',
Gordon and Breach, N.Y., 1973.
10. HAMMER, J. M. and PHILLIPS, W.,
'Low loss single mode optical waveguides and efficient high speed modulators of $\text{LiNb}_x\text{Ta}_{1-x}\text{O}_3$ on LiTaO_3^+ ',
Appl. Phys. Letters, Vol.24, No.11, June (1974), pp.545.
11. LINDHAND, J. and SCHARFF, M.,
'Energy dissipation by ions in the Kev region',
Phys. Rev., Vol.124, No.1, October (1961), pp.128.
12. MIYAZAWA, S.,
'Growth of LiNbO_3 single crystal film for optical waveguides',
Appl. Phys. Letters, Vol.23, No.4, August (1973), pp.198.

13. TAMIR, T.,
Optik 37, 269 (1973).
14. TAMIR, T. and BERTONI, H. L.,
'Lateral displacement of optical beams at multilayered and periodic structures',
J. Opt. Soc. Am., Vol.61, No.10, October (1971), pp.1397.
15. RUTHERFORD, S. and HAWKER, K.,
'Consistent coupled mode theory of sound propagation for a class of non-separable problems',
J. Acoust. Soc. Am., Vol.70, No.2, August (1981), pp.554.
16. PIERCE, A. D.,
'Extension of the mode of normal modes to sound propagation in an almost stratified medium',
J. Acoust. Soc. Am., Vol.37, No.1, January (1965), pp.19.
17. MILDER, D. M.,
'Rays and wave invariant for SOFAR channel propagation',
J. Acoust. Soc. Am., Vol.46, No.5 (part 2), 1969, pp.1259.
18. BASSI, P., ZANG, D. Y. and OSTROWSKY, D. B.,
'Near field radiation pattern of tapered monomode optical waveguides',
Opt. Comm., Vol.41, No.2, March 1982, pp.95.
19. SPORLEDER, F. and UNGER, H. G.,
'Waveguide tapers transitions and couplers',
1979, IEE electromagnetic wave, series 6, Peter Peregrin Ltd.
20. EVANS, R. B.,
'A coupled mode solution for acoustic propagation in a waveguide with stepwise depth variations of a penetrable bottom',
J. Acoust. Soc. Am., Vol.74, No.1, July (1983), pp.188.
21. PIERCE, A. D.,
'Guided mode disappearance during upslope propagation in variable depth shallow water overlying a fluid bottom',
J. Acoust. Soc. Am., Vol.72, No.2, August (1982), pp.523.
22. KAMEL, A. and FELSEN, L. B.,
'Spectral theory of sound propagation in an ocean channel with weakly sloping bottom',
J. Acoust. Soc. Am., Vol.73, No.4, April (1983), pp.1120.
23. ARNOLD, J. M. and FELSEN, L. B.,
'Rays and local modes in a wedge-shaped ocean',
J. Acoust. Soc. Am., Vol.73, No.4, April (1983), pp.1105.
24. JENSEN, F. B. and KUPERMAN, W. A.,
'Sound propagation in a wedge-shaped ocean with a penetrable bottom',
J. Acoust. Soc. Am., Vol.67, No.5, May (1980), pp.1564.

25. ANDERSON, W. W.,
'Mode confinement and gain in junction lasers',
IEEE, J.QE, Vol.QE1, No.6, (1965), pp.228.
26. REISINGER, A.,
'Characteristics of optical guided modes in lossy waveguides',
Appl. Opt., Vol.12, No.5, May (1973), pp.1015.
27. KAMINOW, I. P., MAMMEL, W. L. and WEBER, H. P.,
'Metal-clad optical waveguides : Analytical and experimental
study',
Appl. Opt., Vol.13, No.2, February (1974), pp.396.
28. NELSON, D. F. and MCKENNA, J.,
'Electromagnetic modes of anisotropic dielectric waveguide
at p-n junctions',
J. Appl. Phys., Vol.38, No.10, September (1967), pp.4057.
29. YAMAMOTO, S., KOYAMADA, Y. and MAKIMOTO, T.,
'Normal mode analysis of anisotropic and gyrotropic thin
film waveguides for integrated optics',
J. Appl. Phys., Vol.43, No.12, December (1972), pp.5090.
30. RAMASWAMY, V.,
'Propagation in asymmetrical anisotropic film waveguide',
Appl. Opt., Vol.13, No.6, June (1974), pp.1363.
31. RAMASWAMY, V.,
'Ray model of energy flow in anisotropic film waveguides',
J. Opt. Soc. Am., Vol.64, No.10, November (1974), pp.1313.
32. MARCUSE, D.,
'Theory of dielectric optical waveguide',
Chapter 1, Academic Press, N.Y. and London, 1974.
33. TITCHMARSH, E. L.,
'Introduction of the theory of Fourier Integral',
Oxford University Press, London, 1948.
34. BREKHOVSKIH, L. M.,
'Wave in layered media',
Academic N.Y., 1960.
35. OLVER, F. W. J.,
'Asymptotic and special functions',
Academic, N.Y., 1974.
36. FELSEN, L. B. and MARCUVITZ, N.,
'Radiation and scattering of waves',
Prentice-Hall, Englewoods, Cliffs, N.J., 1973.
37. HOROWITZ, B. R. and TAMIR, T.,
'Lateral displacement of a light beam at a dielectric interface',
J. Opt. Soc. Am., Vol.61, No.5, May (1971), pp.586.
38. ARNOLD, J. M., BELGHORAF, A. and DENDANE, A.,
'Intrinsic mode theory of tapered optical waveguides',
submitted to the Proc. IEE, December 1984.

39. ARNOLD, J. M. and FELSEN, L. B.,
'Intrinsic modes in a non-separable waveguide',
J. Acoust. Soc. Am., Vol.76, 1984.
40. ARNOLD, J. M. and FELSEN, L. B.,
'Ray invariants, plane wave spectra and Adiabatic modes
for tapered dielectric waveguides',
Radio Sci., Vol.19, 1984, pp.1254.